UNIVERSITÀ DEGLI STUDI DI MILANO

Scuola di Dottorato in Fisica, Astrofisica e Fisica Applicata
Dipartimento di Fisica

Corso di Dottorato in Fisica, Astrofisica e Fisica Applicata
Ciclo XXXI

Search for CP violation in the angular distribution of $\Lambda_b^0 \to p\pi^-\pi^+\pi^-$ baryon decays and a proposal for the search of heavy baryon EDM with bent crystal at LHCb

Settore Scientifico Disciplinare FIS/01

Supervisore: Prof. Nicola NERI

Coordinatore: Prof. Francesco RAGUSA

Tesi di Dottorato di:
Andrea MERLI

Anno Accademico 2018/2019

Commission of the final examination:

Prof. Angelo CARBONE
Prof. Gianluca CAVOTO
Prof. Tim GERSHON

Referees:

Dott. Giovanni MARCHIORI
Dott. Matteo RAMA

Final examination:

Date 23^{rd} May 2019

Università degli Studi di Milano, Dipartimento di Fisica, Milano, Italy

To my parents Daniela and Stefano
and my sister Michela

MIUR subjects:

FIS/01

PACS:

11.30.Er, 13.30.Eg, 14.20.-c

Preface

The conjugation operator (C) exchange particles in antiparticles and viceversa, the parity operator (P) reverses the axis direction of the reference frame and the time reversal operator (T) inverts the time flow of a process. It would seem reasonable to expect that the physical properties of particles will not change with the application of either of these operators, and certainly not with the both the couple CP and T. How long a particle lives and the manner in which it decays should not depend on the charge, nor on its direction compared to, say, its own axis of spinning rotation. Physical measurable quantities should not depend on the direction of the arrow of time. However, in a series of experimental revelations first P and then CP/T symmetry were found to be violated under the weak nuclear force.

In 1957, a team of physicists (Wu et al.) found that a weak decay violated parity symmetry. In a magnet, they aligned the spin angular momentum of some very cold, radioactive cobalt nuclei and then observed that, as they decayed, the ejected electron was not emitted isotropically. The weak decay, somehow stipulated a particular direction, preferentially close to the direction of the spin vector. This absolute directional bias meant that the mirror image of the process does not occur. In direct contrast the other fundamental forces of nature, weak decays maximally violated P symmetry.

In 1964, another team (Cronin et al.) observed that long-lived "strange" mesons, assumed to consist equally of K^0 and $\overline{K}^0$ with a value of $CP = -1$, decayed 0.2% of the time into two pions which are definitely $CP = +1$. This demonstrated that, as the neutral kaons travelled through space, the quantum mechanical proportion of K^0 and $\overline{K}^0$ slightly altered such that a small portion of $CP = +1$ arose. The altering of K^0 and $\overline{K}^0$ proportions are possible only if their interactions by the weak force differ. This is why the term "CP violation" immediately implies a difference between matter and antimatter (K^0 and $\overline{K}^0$ in this case).

The cosmological relevance of a matter/antimatter asymmetry in particle interactions is clear. In an inflationary model of the Big Bang, equal particle production of matter and antimatter is expected. However at very early time a difference in behaviour must have been present to leave us with a Universe made exclusively of matter. In this context, the discovery made by Cronin et al. would seem to have astonishing significance. However, estimates done later show that the amount of CP violation in kaons is orders of magnitude too small to explain the Universe.

Over the following decades the Standard Model (SM) of particle physics was developed around three generation of quarks, three generations of leptons and three forces (gravity excluded). CP violation is introduced in the SM through the Cabibbo-Kobayash-Maskawa mechanism (CKM) which predict that all CP violating phenomena originate from the same complex phase in the CKM quark-mixing unitary matrix. In 1973, it not only predicted the third quark generation now known as the "top" and "bottom" quarks, but also that the matter/antimatter differences should be even more glaring in the decays of bottom particles. The validation of this prediction had to wait until 2001 when two competing experiments, Belle at KEK (Japan) and BaBar at SLAC (California) discovered a large difference in the time evolution of B^0 and $\overline{B}^0$ mesons. This *CP* violation is ~ 10 times greater than the effect first observed in kaons 37 years earlier; the long delay was mainly due to the difficulty in producing the much-heavier bottom mesons. In the first decade of the new millenium, *CP* violation was seen in a number of decay modes of the B^0, B^+ and B_s^0 mesons. The effects varied in size but all were consistent with the SM expectation. Nowadays we are in a regime where the SM *CP* violation must be tested to high precision by cross-comparing all the known effects to constraint the CKM matrix parameters and verify its unitarity. A deviation from the prediction would be a clear sign of new physics, and in particular new sources of *CP* violation.

The LHCb detector is a single-arm spectrometer situated on the Large Hadron Collider at CERN. It is optimised to select and reconstruct the b and c hadrons produced in high energy pp collisions, in order to study *CP*-violating processes and rare decays with unprecedented precision.

The unprecedented number of b baryons available with the data sample collected in LHCb will allow a completely new world class measurements. It opens a new unexplored sector in particle physics for precision measurements in b-baryon decays where also new physics effect could be observed. In particular, with the increase of the statistics, we could search for *CP* violation in heavy baryon decays where it has never been observed. It is extremely important to confirm the CKM mechanism in baryons, where it predicts sizeable effects in b baryons.

CP violation could manifest itself not only in dynamic processes such as decays, but also in static properties of the particles such as the electric dipole moment (EDM). The existence of permanents EDM requires the violation of P and T symmetries and thus, relying on the validity of the *CPT* symmetry, the violation of *CP* symmetry. In the SM, contributions to the EDM of baryons is highly suppressed but can be largely enhanced in some of its extensions. Hence, the experimental searches for the EDM of fundamental particles provide powerful probes for physics beyond the SM.

This thesis is composed by two parts, main subjects of the work of the author during the PhD, preceded by two chapters:

- the first chapter provides an introduction on the *CP* violation. After a short preamble on the flavour physics, the author lists the motivations why it is important to search for *CP* violation and what fundamental informations it could reveals. Our actual knowledge and how it manifests itself in all known phenomena up to date is described in the final part;

- the second chapter gives a short overview of the LHCb detector, the experimental apparatus used to perform the analysis described in the first part of this thesis;

- the first part of the thesis presents the search for *CP* violation in the angular distributions of $\Lambda_b^0 \to p\pi^-\pi^+\pi^-$ decay. The measurement is performed exploiting the full LHCb dataset, taken during Run 1 and Run 2 (from 2011 to 2017), and it is in review within the collaboration. The author has been responsible for the analysis from its early stages. Using the Run 1 dataset, taken during 2011 and 2012, the first evidence at 3.3σ of *CP* violation in a baryon decay was obtained in $\Lambda_b^0 \to p\pi^-\pi^+\pi^-$. The result was published in [Nature Physics 13, 391-396 (2017)].

The same technique has been applied also to other $\Lambda_b^0 \to ph^-h^+h^-$ baryon decays; the results are compatible with the *CP* symmetry and already published [JHEP 08 (2018) 039]. This was the first observation of these modes and the first time *CP* violation was searched for in baryon decays with this technique. I presented this analysis at the SIF National Congress and I've been awarded the first prize as the best presentation in the nuclear and subnuclear physics area. The prize consisted of a report of the analysis published in [Il Nuovo Cimento 39 C (2016) 273];

- the second part of the thesis describe the new proposal for searching a non-zero EDM of heavy and strange baryons at LHCb, extending the ongoing worldwide experimental program on the neutron, muon and atoms. The existence of a non-zero EDM in fundamental particles requires a breaking of the T and P symmetries and consequently, relying on the *CPT* theorem, the violation of the *CP* symmetry. The use of bent crystals is crucial to induce an appreciable spin precession in few centimeter before the decay occurs. With the same apparatus it is also possible to measure the magnetic dipole moment (MDM) of such particles. The proposed experiment would represents the first direct measurement of EDM and MDM for charmed baryons. The author demonstrated the feasibility of this proposal solving the equation of motion of the spin precession, calculating the expected sensitivity, determining the optimal parameters of the crystal, the occupancies of the detector and verifying the possibility of the LHCb detector to reconstruct the signal with good resolution and isolate it from the dangerous background. The proposal has already been published [Eur. Phys. J. C (2017) 77, 181] with also an update [Eur. Phys. J C (2017) 77, 828] where the analytical resolution of spin precession has been verified through simulations. I've been awarded the first poster prize for presenting this work at one of the most important conferences on the High Energy Physics: the XXVIII International Symposium on Lepton Photon conference in Guangzhou (China) during 2017.

During the writing of this thesis we submitted a new proposal for the direct measurement of the elusive τ MDM and EDM to PRL and arXiv [arXiv:1901.04003]. The experimental approach and setup is similar to the one proposed in this thesis for the heavy baryons, but an higher statistics is required to test the SM prediction of the τ MDM. However this novel method is not discussed here.

Contents

1 Introduction **1**
1.1 Physics motivations 2
  1.1.1 Baryogenesis 2
1.2 Standard Model 4
1.3 *CP* violation in the Standard Model 5
  1.3.1 Brief history of flavour physics and discrete symmetries violation 5
  1.3.2 The CKM matrix 7
1.4 *CP* violation in beauty baryons 9
  1.4.1 Motivation for searching *CP* violation in $\Lambda_b^0 \rightarrow p\pi^-\pi^+\pi^-$ 12
  1.4.2 Experimental technique and its sensitivity to *CP* violation 13
  1.4.3 Definition of the triple product observables 16
1.5 Electric and magnetic dipole moments 17
  1.5.1 Motivations and physics opportunities 17
  1.5.2 Electric dipole moments 18
  1.5.3 Magnetic dipole moments 25

2 LHC collider and LHCb detector **27**
2.1 The Large Hadron Collider 27
2.2 Beauty production at LHCb 28
2.3 LHCb Detector 30
2.4 The LHCb tracking system 34
  2.4.1 The Vertex Locator 34
  2.4.2 The Tracker Turicensis 36
  2.4.3 The tracking stations T1, T2 and T3 36
  2.4.4 The dipole magnet 38
  2.4.5 Tracking algorithm and performances 38
2.5 The LHCb particle identification system 40
  2.5.1 The Ring Imaging Cherenkov detectors 40
  2.5.2 The calorimetry system 41
  2.5.3 Muon detectors 42
2.6 The LHCb trigger 43
  2.6.1 Level-0 trigger 44
  2.6.2 The high level trigger 45

Part I : Measurement of *CP* violation in the angular distribution of $\Lambda_b^0 \to p\pi^-\pi^+\pi^-$ baryonic decay 51

3 Selection 51
3.1 Trigger requirements 51
3.2 Preselection requirements 53
3.3 Resonance vetoes 53
3.4 Offline selection 55
  3.4.1 Boosted decision tree selection 55
  3.4.2 PID optimisation for charged tracks 62
3.5 $\Lambda_b^0 \to \Lambda_c^+(\to pK^-\pi^+)\pi^-$ control sample 62

4 Fit Model 67
4.1 Signal shape 67
4.2 Sources of background 68
  4.2.1 Background fit model 69
4.3 Fit to the invariant mass distribution $m(p\pi^-\pi^+\pi^-)$ 71
4.4 Fit to the invariant mass distribution for $\Lambda_b^0 \to \Lambda_c^+(\to pK^-\pi^+)\pi^-$ control sample 71

5 Sensitivity studies for *CP* violation and optimisation of the analysis method 75
5.1 $\Lambda_b^0 \to p\pi^-\pi^+\pi^-$ decay model 75
  5.1.1 Helicity formalism 75
  5.1.2 Resonant contributions to the decay model 78
5.2 Binning scheme for optimised sensitivity to *CP* violation 79

6 Extraction of the asymmetries 87
6.1 Search for *CP* violation integrated over phase space 87
6.2 Search for localised *CP* violation in regions of the phase space 87

7 Systematics uncertainties 107
7.1 Experimental bias 107
7.2 Bias due to detector resolution on $C_{\widehat{T}}$ 108
7.3 Fit model 109
7.4 Summary of systematic uncertainties 110
7.5 Cross-checks 110
  7.5.1 Particle identification requirements 110
  7.5.2 Signal reconstruction efficiency on Monte Carlo events 110
  7.5.3 L0 trigger requirement 110
  7.5.4 Magnet polarities 111

8 Results 119
8.1 Measurement of the asymmetries integrated over the phase space 119
8.2 Measurement of the asymmetries in bins of the phase space 119

Part II : Proposal for the search of heavy baryon EDM with bent crystal at LHCb 127

9 Experiment concept and sensitivity 127
9.1 Experiment concept 127

9.2 Sensitivity reach 129
  9.2.1 Baryon and antibaryon production yields 130
  9.2.2 Efficiencies 132
  9.2.3 Spin polarization of baryons 133
  9.2.4 Sensitivity on EDM and MDM 134

10 Experimental setup **137**
10.1 Proof of principle 137
10.2 Experimental layout 137
10.3 Detector occupancies 140
10.4 Crystal parameters 141

11 Event reconstruction and identification **149**
11.1 Acceptance, signal reconstruction and setup positioning 149
11.2 Signal identification and background rejection 152
  11.2.1 Background from Λ_c^+ baryons 152
  11.2.2 Background from channeled charmed mesons 154

12 Results **159**

13 Conclusions **161**

Appendices **165**

A Part I **165**
A.1 Kinematic distributions comparison of $\Lambda_b^0 \to \Lambda_c^+(\to pK^-\pi^+)\pi^-$ control sample and $\Lambda_b^0 \to p\pi^-\pi^+\pi^-$ data 165
A.2 Kinematic distributions of $\Lambda_b^0 \to \Lambda_c^+(\to pK^-\pi^+)\pi^-$ control sample 170
A.3 Amplitude model description 171
A.4 Fit Model validation in each bin 174

B Part II **187**
B.1 Discrete ambiguities 187
B.2 Spin time evolution for positively charged baryons 187

Bibliography **193**

Acknowledgments **208**

CHAPTER 1

Introduction

In the past, flavour physics has driven indirect discoveries of new particles through precision measurements of other processes before the actual particles could be produced directly. For example the discovery of the differences in the behaviour of matter and antimatter, CP violation (CPV), has led to the explanation of flavour mixing with three families of quarks; the absence of the $K^0_L \to \mu^+\mu^-$ decay drove the prediction of the c quark trough the GIM mechanism; the measurement of the B^0 mixing allowed for the prediction of high mass of the t quark.

The asymmetry between matter and antimatter behaviour is related to the violation of the CP symmetry, where C and P are the charge-conjugation and parity operators. CPV is accommodated in the Standard Model (SM) of particle physics by the Cabibbo-Kobayashi-Maskawa (CKM) mechanism that describes the transitions between up- and down-type quarks, in which quark decays proceed by the emission of a virtual W boson and where the phases of the couplings change sign between quarks and antiquarks. A significant excess of CPV with respect to the theoretical predictions would represent a proof of new physics beyond the SM (BSM). The experiments BaBar and Belle have systematically studied the B^0 and $B^\pm$ mesons. The heavy baryon sector (*i.e.* containing the b quark) still remains largely unexplored. Given the large production of heavy baryons at LHCb, precision measurements have become possible in this field. Moreover, the interest of the scientific community is growing on heavy baryons: the last measurement on $|V_{ub}|$ in the channel $\mathit{\Lambda}^0_b \to p\mu^-\overline{\nu}$ and the discovery of the pentaquark in the channel $\mathit{\Lambda}^0_b \to J/\psi pK^-$ are only few relevant examples. Actually the theory describes very well, within the experimental error, the CPV mechanism so far observed in meson decays. Since in the mesons and baryons decays the quark transitions are the same, the CKM theory predicts CPV also in the baryon sector, which has never been observed so far. It is important to measure CPV also in baryons to check if the mechanisms through which it is generated is the same as mesons. We know that CPV is a key ingredient for baryogenesis, but the CKM mechanism cannot explain it quantitatively. New sources of CPV are necessary to explain baryogenesis.

The search for electric dipole moment (EDM) of baryons represents a powerful probe for new sources of CPV and new physics beyond the Standard Model. In particular, it is sensitive to flavour diagonal CPV contributions that are predicted to be minuscule in the SM. The existence of permanent EDMs requires the violation of parity (P) and time reversal (T) symmetries and thus, relying on the validity of the CPT theorem, the violation of CP symmetry. These measurements are not foreseen in the physics program of the LHCb experiment dedicated to the study of the CP violation of heavy hadron via flavour-changing observables, and require new instrumentation.

1.1 Physics motivations

The *CP* symmetry is minimally violated in nature. It is not only relevant for the understanding of a small set of rare weak processes but it actually bears on one of the most intriguing mysteries of cosmology, namely the fact that the universe contains only matter and not antimatter.

The fundamental and deep connection between particles and antiparticles which is expressed by the *CPT* symmetry, the only discrete symmetry which appears to be exactly valid in nature, could lead to the expectation that matter and antimatter are equally abundant in the universe. This appears, however, not to be the case and only one of the two, which we call matter, is present around us.

1.1.1 Baryogenesis

It is believed that at the time of the Big Bang, about 13.8 billion years ago, equal amounts of matter and antimatter were populating the early universe. Then, particles and antiparticles started to annihilate each other until a universe exclusively composed of matter was left. Such a phenomenon, called baryogenesis, can be explained if there exists some kind of asymmetry which differentiates the behaviour of matter and anti-matter particles.

The presence of antimatter in the observed universe is excluded [1], otherwise the amount of radiation produced in the regions where matter and antimatter annhilate will be much larger than what observed. Information on the presence of antimatter in the universe can be also obtained from extra galactic cosmic rays, searching for antiparticles with energies greater than $\mathcal{O}(100)$ PeV which are believed not to be of solar origin. The only antiparticles that are identified in cosmic rays are positrons and antiprotons in an amount that is consistent with the production through high energy collisions with ordinary matter. If antimatter exists, it must be separated from us at least by the observable universe [2, 3]. There seems to be no plausible way of separating baryons and antibaryons from each other on such large scales. The experimental evidence is that we live in a matter-dominated universe.

The present universe contains radiation, mostly in the form of the Cosmic Microwave Background (CMB). As the baryon number density evolves with the expansion of the universe, the excess of baryons over antibaryons is conveniently expressed by the dimensionless ratio

$$\eta = \frac{n_B - n_{\overline{B}}}{n_\gamma} \sim \frac{n_B}{n_\gamma} \approx 6 \cdot 10^{-10} \tag{1.1}$$

where $n_B, n_{\overline{B}}$ are the densities of baryons and antibaryons and n_γ the density of photons. The value of η is experimentally determined in two independent ways: from Big-Bang nucleosynthesis [4] and from the angular distribution of anisotropies of the CMB [5]. The quantity η is usually called the Baryon Asymmetry of the Universe (BAU), which corresponds to the matter-antimatter asymmetry. It means that, while today the baryon asymmetry is maximal (as no antibaryons are found), in the early universe it was very small: there was an excess of a single baryon for every $1/\eta \sim 10^9$ baryon-antibaryon pairs. It is interesting to note that in a homogeneous, baryon-symmetric universe, there would still be a few baryons and antibaryons left since annihilations aren't perfectly efficient, but the departure from equilibriumpredicts an abundance of $\eta \approx 10^{-18}$ [6], which is far too small for the measured value in Equation (1.1).

Sakharov pointed out in his paper [7] that a baryon asymmetry can actually arise dynamically during the evolution of the universe from an initial symmetric state if the following three necessary conditions hold:

Baryon number (B) violation

If every fundamental interaction conserves B-number individually, then it will always be conserved globally. Thus, there must exists a process of the form:

$$X \to Y + B \tag{1.2}$$

where X and Y have the same baryon number and B is the baryons excess.

***C* and *CP* violation**

C symmetry has to be violated otherwise every B-number violation reaction $X \to Y + B$ proceeds at the same rate as the C-conjugate reaction

$$\Gamma(X \to Y + B) = \Gamma(\overline{X} \to \overline{Y} + \overline{B}) \tag{1.3}$$

and the B-number is totally conserved. However if C symmetry is violated and CP symmetry holds

$$\Gamma(X \to Y_L B_L) = \Gamma(\overline{X} \to \overline{Y}_R \overline{B}_R) \tag{1.4}$$

$$\Gamma(X \to Y_R B_R) = \Gamma(\overline{X} \to \overline{Y}_L \overline{B}_L) \tag{1.5}$$

$$\Gamma(X \to Y_L B_L) + \Gamma(X \to Y_R B_R) = \Gamma(\overline{X} \to \overline{Y}_R \overline{B}_R) + \Gamma(\overline{X} \to \overline{Y}_L \overline{B}_L). \tag{1.6}$$

and by summing over helicities the equality of decay widths in Equation (1.6) still preserves baryon number. Then both C and CP symmetry has to be violated.

Departure from thermal equilibrium

If the process $X \to Y + B$ is in thermal equilibrium, then by definition:

$$\Gamma(X \to Y + B) = \Gamma(Y + B \to X) \tag{1.7}$$

and no net baryon asymmetry can be produced since the inverse process destroys B as fast as Equation (1.2) creates it.

The theoretical challenge has been to find out if SM support scenarios that yield to the correct order of magnitude of the BAU. In principle all the three Sakharov requirements are present in the SM.

The SM Lagrangian conserves B classically, but there are global anomalies under which B conservation can be violated [8]. SM baryon number violating processes are non-perturbative and violate B and Leptonic Number (L) by 3 units $\Delta B = \Delta L = \pm 3$ with the selection rules $\Delta B = \Delta L$. These processes are extremely suppressed and completely negligible in normal conditions, occurring with a probability $\sim \exp(-\frac{4\pi}{\alpha_W}) \sim 10^{-164}$ (where α_W is the weak gauge coupling constant) [6]. In the extreme conditions of the early universe such processes, often called *sphaleron processes*, become significant at temperatures $T > T_{EW} \sim 100\,\text{GeV}$, which the universe had at the time of the electroweak phase transition, when it was energetically favourable for the Higgs scalar field to acquire a non-zero expectation value [9].

The violation of C and CP symmetries are well incorporated in the SM, the former was firstly observed in the decay of muons and antimuons [10] while the latter in the $K^0_L \to \pi^+\pi^-$ decays [11]. The amount of CPV in the standard model could only account for $\eta \sim 10^{-20}$ [3, 6, 2, 12], far too small for the measured value in Equation (1.1). There is now a general consensus, among practitioners, that *CPV á la CKM* is irrelevant in the BAU. This means that other sources of CPV must be present beyond the SM and the aim of this thesis is to search for them.

1.2 Standard Model

The Standard Model is the theory that describes electromagnetic, weak and strong interactions which are responsible for the dynamics of all known sub-atomic particles. It is essentially a merger between two theories: the Glashow-Weinberg-Salam (GWS) model describing the electromagnetic and the weak interactions and Quantum Chromodynamics (QCD), describing the strong interaction. The particles contained in this model are divided into two families: fermions (with semi-integer spin) and bosons (with integer spin). Fermions are then further divided into leptons and quarks, depending on whether they interact via the electromagnetic and weak forces only, or also via the strong force. Moreover, leptons and quarks are then organized in 3 families which contain particles that couple with the same coupling constants to the fundamental forces and differ by the mass, as shown in Figure 1.1.

Each interaction has its own mediator: γ for the electromagnetic interaction, $W^{\pm}$ and Z for the weak interaction and 8 gluons for the strong interaction. Finally the Higgs boson is the result of the weak isospin symmetry breaking of the Higgs field that is also responsible for the non-zero mass of the $W^{\pm}$ and Z bosons and fermions. Their masses and their principal properties are shown in Figure 1.1.

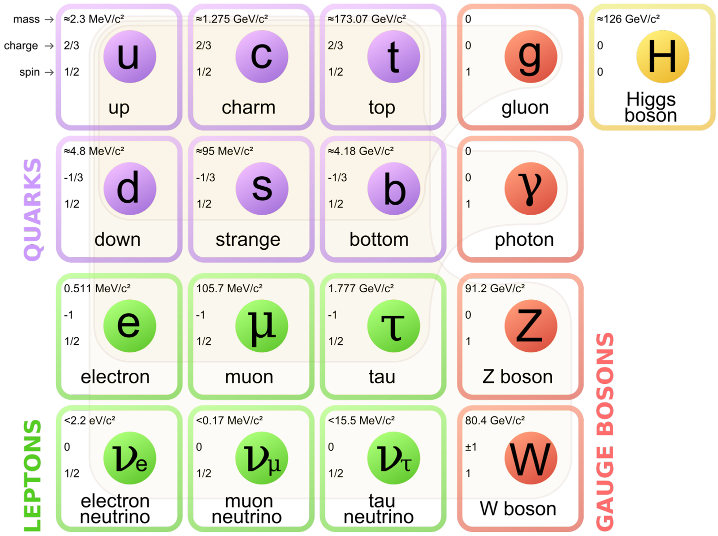

Figure 1.1: Elementary particles forming the Standard Model: 6 quarks (purple), 6 leptons (green), four gauge bosons (red) and the Higgs boson (yellow).

The Standard Model is formulated using the framework of the quantum field theory where the quarks, leptons and bosons are represented via quantum fields. The SM is described by a Lagrangian density that is invariant under a local gauge transformation.

The local gauge symmetry group for the SM is:

$$G_{SM} = \mathrm{SU}(3)_C \otimes \mathrm{SU}(2)_L \otimes \mathrm{U}(1)_Y. \tag{1.8}$$

The strong interactions, described by the QCD, are obtained requiring the local gauge invariance of the Lagrangian for $\mathrm{SU}(3)_C$ transformation, where C is the colour charge, while the request of invariance for transformations of the $\mathrm{SU}(2)_L \otimes \mathrm{U}(1)_Y$ group describes the electroweak interactions, where L refers to left-handed fermions while Y is the weak hypercharge.

1.3 *CP* violation in the Standard Model

The operation of *CP* is obtained combining the two discrete transformations of parity P and charge conjugation C. Under C, particles turn into antiparticles, by conjugation of their internal quantum numbers. Under P, spatial coordinates are reversed, changing the handedness of the reference frame.

The CPT theorem [13] establishes the invariance of any local quantum field theory when the three discrete symmetries C, P and T are applied. Following this theorem, observing *CP* violation, then T violation is implied and viceversa. But, if T is violated in fundamental processes, then the assertion that local past and future are not distinguishable falls down.

During the past years it has been verified experimentally that only gravitational, electromagnetic and strong interactions respect the C and P symmetries and, therefore, also their combination *CP*. Conversely, it has been found that weak interactions do not respect P and C symmetries. Before 1964 it was thought that all of the fundamental interactions had to respect the *CP* symmetry, but an experiment by Fitch and Cronin, involving neutral kaon decays, observed for the first time that also *CP* was violated [11]. From that moment, *CPV* has been deeply studied using decays of K, B, and D mesons. Up to date no evidence of *CPV* in baryons sector have been found.

CP violation can arise from three different sources, namely:

- the flavour mixing of neutral mesons, *i.e.* the transformation of a neutral meson to its *CP* counterpart
- directly from decay diagram, where the decay rate of a particle to a final state differs from the decay rate of the relative antiparticle to the charge conjugate final state
- in the interference between mixing and decay amplitudes.

It is relevant to note that, since the baryon number is conserved, only *CPV* in decay is possible in baryons.

CPV is still nowadays a very promising field of research, with an exhaustive programme of precision measurements being pursued by LHCb, and next by the Belle II experiment in Japan. In particular, charmless four-body *beauty* baryon decays proceed through loop-level quark transitions and are sensitive to potential contributions from physics beyond the SM.

1.3.1 Brief history of flavour physics and discrete symmetries violation

The SM was formulated in its current form at the beginning of the '70s and since then it has collected an extraordinary series of successes but to arrive at this point lots of experiments, measurements and discoveries were required. Until 60 years ago, it was believed that all laws in nature were invariant under the application of charge conjugation and parity transformations. It was clear that it was an incorrect assumption when C. S. Wu and her team, in 1957, found a clear evidence of P violation in the $^{60}Co\ \beta$ decay [14] and soon after a team led by Lederman observed C violation in the decays of muons and antimuons [10]. After this experimental evidence, the fact that P and C are violated by weak interactions was definitely established. A subsequent experiment made by Goldhaber *et al.* [15] in 1958 showed that the neutrino is *left-handed*, *i.e.* its spin is antiparallel with respect to its momentum. It was soon pointed out that the independent application of C and P operators to the *left-handed* neutrino (ν_L) led to physical states not observed in nature (*right-handed* neutrino (ν_R) and *left-handed* anti-neutrino ($\overline{\nu}_L$), respectively), but that the application of the *CP* operator to the ν_L led to the observed $\overline{\nu}_R$. For this reason it was thought that the *CP* symmetry was indeed conserved. However, in 1964, Cronin and Fitch discovered that *CP* symmetry was broken in a small fraction of K^0_L decays [11], yielding the first experimental evidence of CPV.

Murray Gell-Mann and George Zweig developed some years later a classification scheme for hadrons that soon became known as the quark model. This model initially comprised only the up, $down$ and $strange$ quarks. In 1963, to preserve the universality of weak interactions, *i.e.* the fact that the coupling constant was the same in all transitions, Nicola Cabibbo introduced a mixing angle θ_C (the so-called Cabibbo angle) and made the hypothesis that the state coupling to the up quark was a superposition of down-type quarks [16], *i.e.*:

$$d' = d\cos\theta_C + s\sin\theta_C. \tag{1.9}$$

Few years later, in 1970, Glashow Iliopoulos and Maiani proposed to explain the observed suppression of flavour-changing neutral currents (FCNC) processes with the hypothesis that the up quark coupled to a second superposition of down-type quarks, orthogonal to d' and defined as:

$$s' = -d\sin\theta_C + s\cos\theta_C. \tag{1.10}$$

Moreover, they also theorized the existence of a fourth quark, the c quark [17], which is necessary for a complete cancellation of the tree-level FCNC diagrams in $K^0_L \to \mu^+\mu^-$ decay. This prediction was experimentally confirmed four years later by two groups led by Samuel C. C. Ting at Brookhaven National Laboratory [18] and by Burton Richter at the Stanford Linear Accelerator [19], through the discovery of the first $c\bar{c}$ resonance, called the J/ψ meson.

We can write d' and s' combinations in matrix notation as

$$\begin{pmatrix} d' \\ s' \end{pmatrix} = \begin{pmatrix} \cos\theta_C & \sin\theta_C \\ -\sin\theta_C & \cos\theta_C \end{pmatrix} \begin{pmatrix} d \\ s \end{pmatrix}, \tag{1.11}$$

where the 2×2 matrix is known as the Cabibbo matrix.

By noting that CPV could not be explained in a four-quark model, Kobayashi and Maskawa generalized the Cabibbo matrix into the so-called Cabibbo-Kobayashi-Maskawa matrix (or CKM matrix)

$$\begin{pmatrix} d' \\ s' \\ b' \end{pmatrix} = \begin{pmatrix} V_{ud} & V_{us} & V_{ub} \\ V_{cd} & V_{cs} & V_{cb} \\ V_{td} & V_{ts} & V_{tb} \end{pmatrix} \begin{pmatrix} d \\ s \\ b \end{pmatrix}, \tag{1.12}$$

thus predicting the existence of another quark doublet [20]. This hypothesis was then confirmed with the discovery of the *bottom* quark in 1977 by Leon M. Lederman and collaborators at FermiLab [21] and with the discovery of the *top* quark in 1995 by the CDF [22] and DØ [23] collaborations. The CKM matrix is characterized by four free parameters: three mixing angles and one complex phase, the latter being responsible for the CPV. This formalism has proven to be very successful in explaining and predicting CPV in different decays. For their work, Kobayashi and Maskawa were awarded the Nobel Prize in 2008.

Since its discovery in 1964, systematic studies of CPV have been carried out by several experiments. Another important leap was made by the ARGUS collaboration in 1987 through the discovery of the B^0-$\overline{B}^0$ mixing [24]. It opened the venue for the measurement of CPV using mesons containing b quark. Some years ago the CDF Collaboration reported the first observation of B^0_s-$\overline{B}^0_s$ mixing [25], and recently the LHCb collaboration reported that of D^0-$\overline{D}^0$ mixing [26]. The existence of CPV in the decays of B^0 mesons was observed by the BaBar and Belle experiments [27, 28]. Finally, the first observation of CPV in the B^0_s decays was reported by LHCb [29].

1.3.2 The CKM matrix

In the SM, the CP symmetry is broken by a complex phase in the Yukawa couplings of quark fields with the Higgs scalar. When the symmetry group of the SM electroweak interaction $\mathrm{SU}(2)_L \otimes \mathrm{U}(1)_Y$ is broken, leading to a non-zero vacuum expectation value to the Higgs field, then mass terms for the quarks appear. The mass eigenstates are thus obtained diagonalizing the Yukawa matrix (Y^f) using four matrices (V^f_L, V^f_R):

$$M^f_{diag} = \frac{v}{\sqrt{2}} V^f_L Y^f V^{f\dagger}_R, \qquad f = u, d \tag{1.13}$$

where $\frac{v}{\sqrt{2}}$ is the vacuum expectation value of the Higgs field, with the requirement that the V matrices are unitary. As a consequence, in the new basis of mass eigenstates, the electroweak currents for quarks are given by

$$\mathcal{L}_{W^\pm} = \frac{g}{\sqrt{2}} \overline{U}_{Li} \gamma^\mu (V^u_L V^{d\dagger}_L)_{ij} D_{Lj} W^+_\mu + h.c. \tag{1.14}$$

$$\mathcal{L}_Z = \frac{g}{\cos\theta_W} c^F_H \overline{F}_{Hi} \gamma^\mu \underbrace{(V^F_H V^{F\dagger}_H)}_{=\mathbb{I}}{}_{ij} F_{Hj} Z_\mu + h.c., \quad F = U, D, \quad H = L, R \tag{1.15}$$

where g is the electroweak coupling constant, θ_W is the Weinberg angle, c^F_H is the coupling constant relative the fermion of type F and handedness H, $U_L(D_L)$ is the up (down) left-handed fermion field and W^+, Z are the weak fields, i and j run over the three families. The effect of Equation (1.15) is that the neutral current is still diagonal in flavour (in the SM there are no FCNC at tree level) while the charged current mixes up- and down- type quarks as shown in Equation (1.14). The product of the two V^f_L matrices contains the couplings of an up-type antiquark and a down-type quark to the charged W bosons and is called Cabibbo-Kobayashi-Maskawa (CKM) matrix:

$$V_{CKM} \equiv V^u_L V^{d\dagger}_L = \begin{pmatrix} V_{ud} & V_{us} & V_{ub} \\ V_{cd} & V_{cs} & V_{cb} \\ V_{td} & V_{ts} & V_{tb} \end{pmatrix}. \tag{1.16}$$

Properties of the CKM matrix

The first important feature of the CKM matrix is its unitarity, expression of the FCNC suppression and universality of the weak interaction. Such a condition determines the number of free parameters of the matrix. A generic $N \times N$ unitary matrix depends on $N(N-1)/2$ mixing angle and $N(N+1)/2$ complex phases. The SM Lagrangian allows us to redefine the phase of each quark field such that:

$$\begin{cases} U \to e^{-i\varphi_U} U \\ D \to e^{-i\varphi_D} D \end{cases} \Rightarrow V_{UD} \to e^{i\varphi_U} V_{UD} e^{-i\varphi_D}. \tag{1.17}$$

In this way $2N-1$ unphysical phases of the CKM cancel out. As a consequence any $N \times N$ complex matrix describing mixing between N generations of quarks has

$$\underbrace{\frac{1}{2}N(N-1)}_{\text{mixing angles}} + \underbrace{\frac{1}{2}(N-1)(N-2)}_{\text{physical complex phases}} = (N-1)^2 \tag{1.18}$$

free parameters. The case $N = 2$ leads to a mixing matrix with only one free parameter, known as the Cabibbo angle θ_C, with a mixing matrix V_C as defined in Equation (1.11). No complex phases appear and no *CPV* is possible in this case.

In the case $N = 3$, the resulting number of free parameters is four: three mixing angles and one complex phase. This phase alone is responsible for *CPV* in the weak interactions of the SM. The presence of a complex phase in the mixing matrix is a necessary but not sufficient condition for *CP* violation. As pointed out in Reference [30], another key condition is

$$(m_t^2 - m_c^2)(m_t^2 - m_u^2)(m_c^2 - m_u^2)(m_b^2 - m_s^2)(m_b^2 - m_d^2)(m_s^2 - m_d^2) \times J_{CP} \neq 0 \tag{1.19}$$

where

$$J_{CP} = \mid \Im(V_{i\alpha} V_{j\beta} V_{i\beta}^* V_{j\alpha}^*) \mid \quad (i \neq j, \alpha \neq \beta) \tag{1.20}$$

is the "Jarlskog parameter". This condition is related to the fact that according to Equation (1.17) it would be possible to remove the CKM phase if any of the two quarks with the same charge were degenerate in mass. As a consequence the origin of *CPV* is deeply connected to the origin of the quark masses hierarchy and the number of fermion generations. J_{CP} can be interpreted as a measurement of the amount of *CP* violation in the SM. Its value does not depend on the phase convention of the quark field as in Equation (1.17). Experimentally one has $J_{CP} = \mathcal{O}(10^{-5})$, which states that *CPV* in SM is suppressed due to the small mixing angles. Various extension of the SM foresee new sources of flavour mixing which could enhance the strength of the violation.

Experimental information lead to the following consideration: transition within the same generation imply V_{CKM} elements of $\mathcal{O}(1)$; those between the first and second generation are suppressed by a factor $\mathcal{O}(10^{-1})$; those between the second and third generations are suppressed by a factor $\mathcal{O}(10^{-2})$; and those between the first and the third generations are strongly suppressed by a factor $\mathcal{O}(10^{-3})$. The "Wolfenstein parametrization" [31] of the CKM matrix exploits these considerations

$$V_{CKM} = \begin{pmatrix} 1 - \frac{\lambda^2}{2} & \lambda & A\lambda^3(\rho - i\eta) \\ -\lambda & 1 - \frac{\lambda^2}{2} & A\lambda^2 \\ A\lambda^3(1 - \rho - i\eta) & -A\lambda^2 & 1 \end{pmatrix} + \mathcal{O}(\lambda^4) \tag{1.21}$$

written as a power expension of the parameter $\lambda = \frac{|V_{us}|}{\sqrt{|V_{ud}|^2 + |V_{us}|^2}} = \sin\theta_C$, where $A\lambda = \left|\frac{V_{cb}}{V_{us}}\right|$ and $A\lambda^3(\rho - i\eta) = V_{ub}$. The measured values are $A = 0.8403^{+0.0056}_{-0.0201}$, $\lambda = 0.224747^{+0.000254}_{-0.000059}$, $\overline{\rho} = \rho\left(1 - \frac{\lambda^2}{2}\right) = 0.1577^{+0.0096}_{-0.0074}$ and $\overline{\eta} = \eta\left(1 - \frac{\lambda^2}{2}\right) = 0.3493^{+0.0095}_{-0.0071}$.

Unitary triangles

The unitary of the CKM matrix $V_{CKM}V^{\dagger}_{CKM} = V^{\dagger}_{CKM}V_{CKM} = \mathbb{I}$, leads to a set of 12 equations relating the matrix elements: 6 for diagonal terms equal to 1 and 6 for the off-diagonal terms equal to 0. The equations for the off-diagonal terms can be represented as triangles in the complex plane, all having the same area $J_{CP}/2$

$$\underbrace{V_{ud}V^*_{us}}_{\mathcal{O}(\lambda)} + \underbrace{V_{cd}V^*_{cs}}_{\mathcal{O}(\lambda)} + \underbrace{V_{td}V^*_{ts}}_{\mathcal{O}(\lambda^5)} = 0, \tag{1.22}$$

$$\underbrace{V_{us}V^*_{ub}}_{\mathcal{O}(\lambda)^4} + \underbrace{V_{cs}V^*_{cb}}_{\mathcal{O}(\lambda^2)} + \underbrace{V_{ts}V^*_{tb}}_{\mathcal{O}(\lambda^2)} = 0, \tag{1.23}$$

$$\underbrace{V_{ud}V^*_{ub}}_{\mathcal{O}(\lambda^3)} + \underbrace{V_{cd}V^*_{cb}}_{\mathcal{O}(\lambda^3)} + \underbrace{V_{td}V^*_{tb}}_{\mathcal{O}(\lambda^3)} = 0, \tag{1.24}$$

$$\underbrace{V^*_{ud}V_{cd}}_{\mathcal{O}(\lambda)} + \underbrace{V^*_{us}V_{cs}}_{\mathcal{O}(\lambda)} + \underbrace{V^*_{ub}V_{cb}}_{\mathcal{O}(\lambda^5)} = 0, \tag{1.25}$$

$$\underbrace{V^*_{cd}V_{td}}_{\mathcal{O}(\lambda^4)} + \underbrace{V^*_{cs}V_{ts}}_{\mathcal{O}(\lambda^2)} + \underbrace{V^*_{cb}V_{tb}}_{\mathcal{O}(\lambda^2)} = 0, \tag{1.26}$$

$$\underbrace{V^*_{ud}V_{td}}_{\mathcal{O}(\lambda^3)} + \underbrace{V^*_{us}V_{ts}}_{\mathcal{O}(\lambda^3)} + \underbrace{V^*_{ub}V_{tb}}_{\mathcal{O}(\lambda^3)} = 0. \tag{1.27}$$

Only two out of the six unitary triangles have sides of the same order of magnitude resulting in non squashed triangles: they are represented by Equation (1.24) and (1.27). Normalizing to the common factor $A\lambda^3$, the former is usually called "The Unitary Triangle" (UT) and its fit is shown in Figure 1.2. Since the three sides and the three angles of each triangles must be measured experimentally, a class of tests of the SM is to check that each triangle closes, *i.e.* that Equations (1.22)-(1.27) are verified. This is the purpose of a modern series of experiments under way: Belle II at KEK (Japan) and LHCb at CERN (Switzerland).

1.4 *CP* violation in beauty baryons

In contrast with the study of *CP* violation in beauty meson decays, the sector of beauty baryons remains almost unexplored. Prior to the LHC era, only a measurement of direct *CP* asymmetries in $\Lambda_b^0 \to pK^-$ and $\Lambda_b^0 \to p\pi^-$ decays was available with $\mathcal{O}(0.1)$ precision [32]. Thanks to the large production cross-section of beauty baryons in pp collisions at the LHC, the LHCb experiment is capable of expanding our knowledge in this sector. This is more interesting considering the fact that these decays are not accessible at the e^+e^- KEK collider. To date a handful of *CP* asymmetries of Λ_b^0 decays have been measured by LHCb in $\Lambda_b^0 \to pK^0_S\pi^-$ [33], $\Lambda_b^0 \to J/\psi p\pi^-$, $\Lambda_b^0 \to J/\psi pK^-$ decays [34], $\Lambda_b^0 \to \Lambda K^+\pi^-$ and $\Lambda_b^0 \to \Lambda K^+K^-$ [35], $\Lambda_b^0 \to pK^-\mu^+\mu^-$ [36] and $\Lambda_b^0 \to pK^-$ and $\Lambda_b^0 \to p\pi^-$ [37]. The landscape of *CP* violation in the decays of beauty baryons is expected to change rapidly in the next few years.

The unprecedented number of beauty baryons available with the data sample collected in LHCb will allow for a precision measurement programme of *CP* violation observables in b-baryon decays. These studies can be seen as a complementary approach with respect to the study of B mesons, to probe the SM and search for new physics beyond. It is clear that analyses similar to those carried out with b-meson decays will also

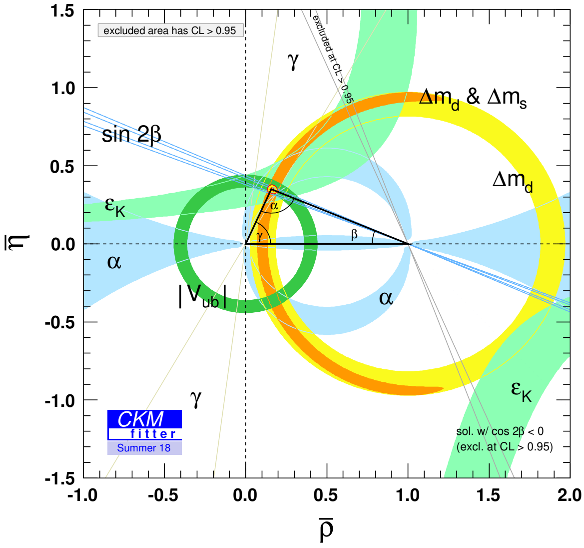

Figure 1.2: The Unitary Triangle fit overlayed with the experimental constraint at 68% of confidence level in the space parameter $(\overline{\rho}, \overline{\eta})$.

be possible with b-baryon decays.

A very interesting sector is the one of beauty baryons decaying to final states without a charm quark. These decays receive relevant contributions from $b \to d, s$ loop-level transitions, where new physics beyond the SM may appear. As for the case of B-meson decays, CP-violating observables should be measured in baryon decays. In Run 2 a statistical precision of $\mathcal{O}(10^{-2})$ or below is expected for the CP asymmetries of the $\Lambda_b^0 \to ph^-$ decays and for several multi-body final states of Λ_b^0 and Ξ_b^0 decays: $\Lambda_b^0 \to p\pi^-\pi^+\pi^-$ and $\Lambda_b^0 \to pK^-K^+K^-$ decays [38], $\Xi_b^0 \to pK^-\pi^+K^-$ decays [39]. In multi-body final states it is possible to perform measurements of CP-violating quantities over the phase space, characterised by a rich set of resonances. Unfortunately, as for the charmless decays of B mesons, the interpretation of these quantities in terms of CKM parameters is still unclear from the theoretical point of view. Hence, more theoretical work is crucial to exploit the full potential of beauty baryons.

From the experimental point of view, the main issues are represented by the determination of particle-antiparticle production asymmetries and detection asymmetries that could mimic CP violation effects. This task is generally more difficult to accomplish for heavy baryons, with respect to B mesons, since methods used for measuring meson production asymmetries [40] cannot be applied. In addition, different interactions of baryons and antibaryons with the detector material are difficult to calibrate. Nonetheless, several quantities can be measured in b-baryon decays that are sensitive to different manifestations of CP violation and are largely unaffected by experimental effects. A few examples are the difference of CP-violating asymmetries of particles decaying to similar final state, ΔA_{CP}, as measured in $\Lambda_c^+ \to pK^-K^+$ and $\Lambda_c^+ \to p\pi^-\pi^+$ decays [41], the triple-product asymmetries measured in $\Lambda_b^0 \to p\pi^-\pi^+\pi^-$ and $\Lambda_b^0 \to p\pi^-K^+K^-$ decays [38] and the energy-test [42] yet to be performed in multi-body baryon decays. The triple-product asymmetries used here is an important tool for the observation and discovery of *CP* violation in multi-body decays, while an amplitude analysis would be advantageous to study the origin of *CP* violation.

The first observation of *CP* violation in a baryon decay is potentially within the reach of LHCb with the data collected during the Run 2 of the LHC, considering that a first evidence for *CP* violation in baryon decays has been reported in $\Lambda_b^0 \to p\pi^-\pi^+\pi^-$ decays [38]. Searches for *CPV* are particularly suited to Λ_b^0 four-body decays to hadrons with no charm quark [43] thanks to the rich resonant substructure which is dominated by $\Delta(1232)^{++} \to p\pi^+$ and $\rho^0 \to \pi^+\pi^-$ resonances in the $\Lambda_b^0 \to p\pi^-\pi^+\pi^-$ final state. In four-body particle decays, the *CP* asymmetries may vary over the phase space due to resonant contributions or their interference effects, possibly cancelling when integrated over the whole phase space. In the previous reported measurement, measurements of asymmetries in the entire phase space did not show any evidence of *P* or *CP* violation [38]. The asymmetries were also measured in different regions of phase space for the $\Lambda_b^0 \to p\pi^-\pi^+\pi^-$ decay using two binning schemes, defined before examing the data, as shown in Figure 1.3. Scheme A was designed to isolate regions of phase space according to their dominant resonant contributions. Scheme B exploited in more detail the interference of contributions which could be visible as a function of the angle Φ between the decay planes formed by the $p\pi^-$ and the $\pi^+\pi^-$ systems. The overall significance for *CPV* in $\Lambda_b^0 \to p\pi^-\pi^+\pi^-$ decays from the results of the two schemes was determined by means of a permutation test, taking into account correlations among the results. A significance of 3.3 standard deviations was found including both statistical and systematic uncertainties. Alternative binning schemes were studied as a cross-check, such as using 8 or 12 bins in $|\Phi|$. For these alternative binning schemes, the significance of the *CPV* measurement was reduced to below 3σ.

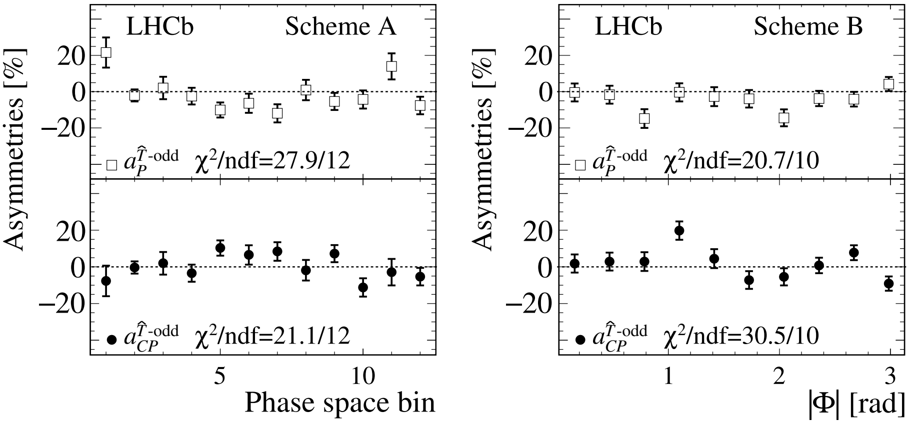

Figure 1.3: The results of the fit in each region of the two binning schemes A and B are shown for the previously published LHCb Run 1 analysis. The *P*-violating ($a_P^{\hat{T}\text{-odd}}$) and *CP*-violating asymmetries ($a_{CP}^{\hat{T}\text{-odd}}$) for $\Lambda_b^0 \to p\pi^-\pi^+\pi^-$ decays are represented by open boxes and filled circles, respectively. The error bars represent one standard deviation, calculated as the sum in quadrature of the statistical and systematical uncertainty. The values of the χ^2/ndf are quoted for the *P*- and *CP*-conserving hypotheses for each binning scheme, where ndf indicates the number of degrees of freedom.

1.4.1 Motivation for searching *CP* violation in $\Lambda_b^0 \to p\pi^-\pi^+\pi^-$

The study of matter-antimatter asymmetries in B-meson decays contributed to establishing the validity of the CKM mechanism for *CPV* in the SM. By contrast, no *CPV* has been observed in the baryon sector to date. However, sizeable *CP*-violating asymmetries of up to 20% are expected in certain b-baryon decays [44], and a systematic study will either confirm the CKM mechanism in baryon decays, or will bring insights into new sources of *CP* violation.

In this thesis, a search for *CP* violation based on triple-product asymmetries in charmless $\Lambda_b^0 \to p\pi^-\pi^+\pi^-$ decay is presented. This decay is mediated by the weak interaction and governed mainly by two amplitudes expected to be of similar magnitude, from different diagrams describing quark-level tree $b \to ud\overline{u}$ and penguin $b \to du\overline{u}$ transitions, shown in Figure 1.4 with a relative large weak phase, $\arg\left(-V_{td}V_{tb}^*/V_{ud}V_{ub}^*\right)$, that in the literature is referred to as the CKM angle α, depicted in Figure 1.4. *CPV* could arise from the interference of two amplitudes with relative phases that differ between particle and antiparticle decays, leading to differences in the Λ_b^0 and $\overline{\Lambda}_b^0$ decay rates. The main source of this effect in the SM would be the large relative phase α, between the product of the CKM matrix elements $V_{ud}V_{ub}^*$ and $V_{td}V_{tb}^*$, which are present in the different diagrams depicted in Figure 1.4. P violation is also expected in weak interactions, but has never been observed in the Λ_b^0 decays. In addition, new physics effects could be caused by new particles contributing to penguin loop diagrams. The study of triple product asymmetries in Λ_b^0 decays is particularly sensitive to new physics effects [45]. Triple product asymmetries which are expected to vanish in the SM can be very large (up to 50%) in the presence of new physics [45]. This technique is very promising in the baryon sector to search for *CP* violation also from an experimental point of view [43]. In the present analysis, the triple-product *CP*-violating asymmetries are measured integrated over all the phase space and in specific phase space regions. It is important to measure the size and nature of these *CP* asymmetries in as many decay modes as possible, to determine wheather they are consistent with the CKM mechanism or, if not, what extensions to the SM would be required to explain them [46, 45].

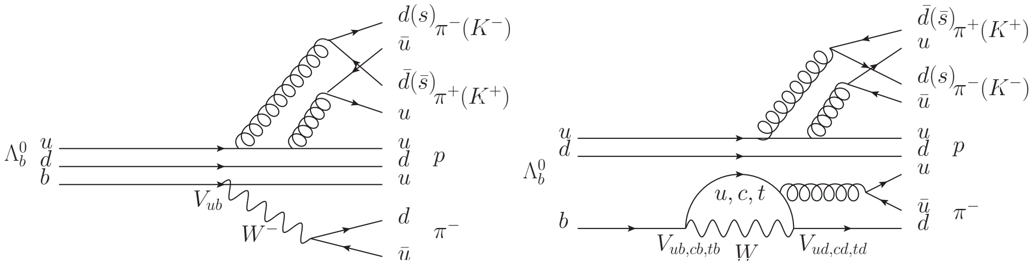

Figure 1.4: Examples of tree (left) and penguin (right) diagrams for $\Lambda_b^0 \to p\pi^-\pi^+\pi^-$ decays. The tree and penguin diagrams have the same magnitude and *CPV* effects can potentially arise from the interference of amplitudes with different weak phases.

The triple product asymmetries defined in Section 1.4.3 are by construction largely insensitive to production and detection asymmetries. These properties are particularly important in a pp collider where $\Lambda_b^0/\overline{\Lambda}_b^0$ production asymmetry can arise, and $p/\overline{p}$ interactions with matter are quite different for different energy regimes. The copious $\Lambda_b^0 \to pK^-\pi^+\pi^-$ and $\Lambda_b^0 \to \Lambda_c^+\pi^-$ control samples, roughly 3 and 15 times the $\Lambda_b^0 \to p\pi^-\pi^+\pi^-$ signal yield, are used to optimize the selection criteria and to determine the systematic uncertainties, respectively.

1.4.2 Experimental technique and its sensitivity to *CP* violation

Let us consider two transitions of amplitudes $\mathcal{M}\left(\{s_i, p_i\}\right)$ and $\overline{\mathcal{M}}\left(\{s_{\bar{i}}, p_{\bar{i}}\}\right)$. They involve an equal number of particles respectively labeled by i and $\bar{i}$, with helicities $s_{i,\bar{i}}$ and four-momenta $p_{i,\bar{i}}$.

If these two processes are *CP* conjugate of each other, with $\bar{i} = CP[i]$, CPV at any phase-space point takes the form of a difference between the squared moduli of $\mathcal{M}\left(\{s_i, p_i\}\right)$ and $\overline{\mathcal{M}}\left(\{s_i, \overline{p}_i\}\right)$ where $\overline{p} \equiv P[p]$ is the parity conjugate of the momentum p. Testing *CP* conservation phase-space point by phase-space point thus implies a comparison of the differential rates of two processes involving *CP*-conjugate particles of identical spins but opposite three-momenta.

It reveals useful to define an operator, denoted here by $\widehat{T}$, that reverts both momentum and spin three-vectors [47]. Its action on helicities and momenta is thus identical to that of *CP* and it can be viewed as the unitary component of the antiunitary time-reversal operator T. In general, the amplitudes above can then be decomposed into two pieces that are respectively $\widehat{T}$-even and $\widehat{T}$-odd

$$\begin{aligned}
\mathcal{M}\left(\{s_i, p_i\}\right) &= \mathcal{M}_e\left(\{s_i, p_i\}\right) + \mathcal{M}_o\left(\{s_i, p_i\}\right),\\
\overline{\mathcal{M}}\left(\{s_i, \overline{p}_i\}\right) &= \overline{\mathcal{M}}_e\left(\{s_i, \overline{p}_i\}\right) + \overline{\mathcal{M}}_o\left(\{s_i, \overline{p}_i\}\right),\\
&= \overline{\mathcal{M}}_e\left(\{s_i, p_i\}\right) - \overline{\mathcal{M}}_o\left(\{s_i, p_i\}\right).
\end{aligned} \tag{1.28}$$

Those two terms can receive several contributions whose absorptive parts take the form of *CP*-even phases δ. One can then write

$$\begin{aligned}
\mathcal{M}_e\left(\{s_i, p_i\}\right) &= a_e^j e^{i\left(\delta_e^j + \phi_e^j\right)},\\
\overline{\mathcal{M}}_e\left(\{s_i, p_i\}\right) &= a_e^j e^{i\left(\delta_e^j - \phi_e^j\right)},\\
\mathcal{M}_o\left(\{s_i, p_i\}\right) &= a_o^k e^{i\left(\delta_o^k + [\phi_o^k + \pi/2]\right)},\\
\overline{\mathcal{M}}_o\left(\{s_i, p_i\}\right) &= a_o^k e^{i\left(\delta_o^k - [\phi_o^k + \pi/2]\right)},
\end{aligned} \tag{1.29}$$

with implicit summation over the j, k indices, and real $a_{e,o}^{j,k}, \delta_{e,o}^{j,k}, \phi_{e,o}^{j,k}$ functions of the spins and momenta $\{s_i, p_i\}$. The above conventions imply that all *CP* violation is encoded in the *CP*-odd phases $\phi_{e,o}^{j,k}$. When they vanish,

$$\begin{aligned}
\overline{\mathcal{M}}_e\left(\{s_i, p_i\}\right) &= +\mathcal{M}_e\left(\{s_i, p_i\}\right),\\
\overline{\mathcal{M}}_o\left(\{s_i, p_i\}\right) &= -\mathcal{M}_o\left(\{s_i, p_i\}\right),
\end{aligned} \tag{1.30}$$

so that the *CP*-conjugate rates are identical, phase-space point by phase-space point.

For processes involving only scalars in their initial and final states, $\widehat{T}$ is actually equivalent to parity conjugation P. The measured differential rates of any pair of *CP*-conjugate processes can therefore be decomposed into four pieces of definite $\widehat{T}$ and *CP* transformation properties

$$\left.\frac{d\Gamma}{d\Phi}\right|_{CP\text{-}^{\text{even}}_{\text{odd}}}^{\widehat{T}\text{-}^{\text{even}}_{\text{odd}}} \equiv \frac{\mathbb{I} \pm \widehat{T}}{2}\,\frac{\mathbb{I} \pm CP}{2}\,\frac{d\Gamma}{d\Phi} \tag{1.31}$$

with the shorthand $\Phi \equiv \{s_i, p_i\}$.

For simplicity, let us assume there are respectively two and one contribution(s) to the $\widehat{T}$-even and $\widehat{T}$-odd parts of the amplitude in the process under scrutiny

$$\begin{aligned}\mathcal{M}\left(\{s_i, p_i\}\right) &= a_e^1 e^{i\left(\delta_a^1+\phi_a^1\right)} + a_e^2 e^{i\left(\delta_a^2+\phi_a^2\right)} + i a_o^1 e^{i\left(\delta_o^1+\phi_o^1\right)},\\ \overline{\mathcal{M}}\left(\{s_i, \overline{p}_i\}\right) &= a_e^1 e^{i\left(\delta_a^1-\phi_a^1\right)} + a_e^2 e^{i\left(\delta_a^2-\phi_a^2\right)} + i a_o^1 e^{i\left(\delta_o^1-\phi_o^1\right)}.\end{aligned} \tag{1.32}$$

All functions of the phase space are evaluated at $\{s_i, p_i\}$. Note the convention of Equation (1.29) causes the appearance of a factor i in front of the $\widehat{T}$-odd term. Up to a flux factor, the squared modulus of this expression and of its *CP* conjugate provides us with the differential rates which can be decomposed as prescribed in Equation (1.31)

$$\begin{aligned}\left.\frac{d\Gamma}{d\Phi}\right|_{CP\text{-even}}^{\widehat{T}\text{-even}} &\propto a_e^1 a_e^1 + a_e^2 a_e^2 + a_o^1 a_o^1 + 2 a_e^1 a_e^2 \cos\left(\delta_e^1 - \delta_e^2\right) \cos\left(\phi_e^1 - \phi_e^2\right),\\ \left.\frac{d\Gamma}{d\Phi}\right|_{CP\text{-even}}^{\widehat{T}\text{-odd}} &\propto 2 a_e^1 a_o^1 \sin\left(\delta_e^1 - \delta_o^1\right) \cos\left(\phi_e^1 - \phi_o^1\right) + 2 a_e^2 a_o^1 \sin\left(\delta_e^2 - \delta_o^1\right) \cos\left(\phi_e^2 - \phi_o^1\right),\\ \left.\frac{d\Gamma}{d\Phi}\right|_{CP\text{-odd}}^{\widehat{T}\text{-even}} &\propto -2 a_e^1 a_e^2 \sin\left(\delta_e^1 - \delta_e^2\right) \sin\left(\phi_e^1 - \phi_e^2\right),\\ \left.\frac{d\Gamma}{d\Phi}\right|_{CP\text{-odd}}^{\widehat{T}\text{-odd}} &\propto 2 a_e^1 a_o^1 \cos\left(\delta_e^1 - \delta_o^1\right) \sin\left(\phi_e^1 - \phi_o^1\right) + 2 a_e^2 a_o^1 \cos\left(\delta_e^2 - \delta_o^1\right) \sin\left(\phi_e^2 - \phi_o^1\right).\end{aligned} \tag{1.33}$$

The last two expressions above vanish in the *CP* symmetry limit. There are thus two distinct kinds of *CP*-violating differential rates: the presence of the $\widehat{T}$-even one requires nonvanishing differences in the *CP*-even phases δ while the $\widehat{T}$-odd-*CP*-odd does not. This can be understood as, in the absence of absorptive part to the amplitude, $\widehat{T}$ is equivalent to T so that CPT conservation imposes any *CP*-odd quantity to also be $\widehat{T}$ odd.

On the other hand, $\widehat{T}$-odd-*CP*-even piece of the differential rate could be used to isolate relatively small differences in the *CP*-even phases δ, in the absence of *CP*-odd phase ϕ. It can thus serve to better understand final-state interactions.

The total rate asymmetry is constructed upon the $\widehat{T}$-even-*CP*-odd differential rate

$$\int d\Phi \left.\frac{d\Gamma}{d\Phi}\right|_{CP\text{-odd}}^{\widehat{T}\text{-even}}. \tag{1.34}$$

A second family of observables can be obtained from integrals of its $\widehat{T}$-odd-*CP*-odd homologue

$$\int d\Phi f\left(\Phi\right) \left.\frac{d\Gamma}{d\Phi}\right|_{CP\text{-odd}}^{\widehat{T}\text{-odd}} \tag{1.35}$$

with some $\widehat{T}$-odd function $f\left(\Phi\right)$ without which the phase-space integral would vanish.

As a product of a $\widehat{T}$-odd kinematic function with a $\widehat{T}$-odd-*CP*-even differential rate, the observables of Equation (1.35) are $\widehat{T}$ even and *CP* odd but have not definite T transformation properties.

There are two tensors available to construct Lorentz invariants from spin and momenta four-vectors. The metric $g_{\mu\nu}$ leads to $\widehat{T}$-even contractions like invariant masses, and the completely antisymmetric $\epsilon_{\mu\nu\rho\sigma}$ produces $\widehat{T}$-odd combinations of four-vectors.

Dot products and antisymmetric contractions of four-momenta and Pauli-Lubański spin vectors (respectively denoted by p and w) have definite P parities. The P-even combinations are

$$p_1 \cdot p_2, \quad w_1 \cdot w_2 \tag{1.36}$$

$$\epsilon_{\mu\nu\rho\sigma} p_1^\mu p_2^\nu p_3^\sigma w_4^\rho, \quad \text{and} \quad \epsilon_{\mu\nu\rho\sigma} p_1^\mu w_2^\nu w_3^\sigma w_4^\rho \tag{1.37}$$

while the P-odd ones are

$$p_1 \cdot w_2 \tag{1.38}$$

$$\epsilon_{\mu\nu\rho\sigma} p_1^\mu p_2^\nu p_3^\sigma p_4^\rho, \quad \epsilon_{\mu\nu\rho\sigma} p_1^\mu p_2^\nu w_3^\sigma w_4^\rho, \quad \epsilon_{\mu\nu\rho\sigma} w_1^\mu w_2^\nu w_3^\sigma w_4^\rho \tag{1.39}$$

The completely antisymmetric Lorentz structure can originate directly from Lagrangian couplings like $i\epsilon_{\mu\nu\rho\sigma}F^{\mu\nu}F^{\rho\sigma}$, or arise in the presence of chiral fermions, since $\gamma^5 = \frac{i}{4!}\epsilon_{\mu\nu\rho\sigma}\gamma^\mu\gamma^\nu\gamma^\rho\gamma^\sigma$. Because it is completely antisymmetric, however, a necessary condition for the presence of a $\widehat{T}$-odd part $\mathcal{M}_o$ in an amplitude is the availability of four independent and distinguishable four-vectors. In a process involving scalars or particles of unmeasured spins, at least five external momenta are therefore required.

In a reference frame where $a^\mu = \left(a^0, \mathbf{0}\right)$, the completely antisymmetric combination of four four-vectors $\epsilon_{\mu\nu\rho\sigma}a^\mu b^\nu c^\sigma d^\rho$ reduces to $a^0 \boldsymbol{b} \cdot (\boldsymbol{c} \times \boldsymbol{d})$ scalar triple product (for $\epsilon_{0123} = +1$). The observables constructed from the $\widehat{T}$-odd parts of the differential rate are therefore customarily called triple-product asymmetries. A significant amount of effort, both theoretical and experimental has been devoted to their study. A triple product asymmetry has been measured in $K_L^0 \to \pi^+\pi^-e^+e^-$ and applications are also found in heavy meson, baryon, top, Z, Higgs, and BSM physics and the method is described in Reference [46, 45, 48].

The simplest triple product asymmetries are based on the sign of one of the constructible triple product (see Equation (1.35))

$$f\left(\Phi\right) = \text{sign}\{\epsilon_{\mu\nu\rho\sigma}a^\mu b^\nu c^\rho d^\sigma\}. \tag{1.40}$$

The usual quantities defined in the literature

$$\begin{aligned} A_{\widehat{T}} &= \frac{\int d\Phi f\left(\Phi\right)\left[\left.\frac{d\Gamma}{d\Phi}\right|_{CP\text{-even}}^{\widehat{T}\text{-odd}} + \left.\frac{d\Gamma}{d\Phi}\right|_{CP\text{-odd}}^{\widehat{T}\text{-odd}}\right]}{\int d\Phi\left[\left.\frac{d\Gamma}{d\Phi}\right|_{CP\text{-even}}^{\widehat{T}\text{-even}} + \left.\frac{d\Gamma}{d\Phi}\right|_{CP\text{-odd}}^{\widehat{T}\text{-even}}\right]} \\ \overline{A}_{\widehat{T}} &= \frac{\int d\Phi f\left(\Phi\right)\left[\left.\frac{d\Gamma}{d\Phi}\right|_{CP\text{-even}}^{\widehat{T}\text{-odd}} - \left.\frac{d\Gamma}{d\Phi}\right|_{CP\text{-odd}}^{\widehat{T}\text{-odd}}\right]}{\int d\Phi\left[\left.\frac{d\Gamma}{d\Phi}\right|_{CP\text{-even}}^{\widehat{T}\text{-even}} - \left.\frac{d\Gamma}{d\Phi}\right|_{CP\text{-odd}}^{\widehat{T}\text{-even}}\right]} \end{aligned} \tag{1.41}$$

are ratios of integrated $\widehat{T}$-odd and $\widehat{T}$-even differential rates and have no definite *CP* transformation properties. In the notations of Equation (1.29)

$$\begin{aligned} A_{\widehat{T}} &\propto 2a_e^j a_o^k \sin\left[\left(\delta_e^j - \delta_o^k\right) + \left(\phi_e^j - \phi_o^k\right)\right] \\ \overline{A}_{\widehat{T}} &\propto 2a_e^j a_o^k \sin\left[\left(\delta_e^j - \delta_o^k\right) - \left(\phi_e^j - \phi_o^k\right)\right]. \end{aligned} \tag{1.42}$$

As reported in References [49, 50], $A_{\widehat{T}}$ and $\overline{A}_{\widehat{T}}$ observables are affected by final state interaction effects and it is difficult to predict their value theoretically. On the contrary

$$a_{CP}^{\widehat{T}\text{-odd}} = \frac{1}{2}\left(A_{\widehat{T}} - \overline{A}_{\widehat{T}}\right) \tag{1.43}$$

is always *CP* odd.

The *CP*-violating asymmetry based on triple product $a_{CP}^{\widehat{T}\text{-odd}}$ is different and complementary observable with respect to the total rate asymmetry $\mathcal{A}_{CP}$ proportional to Equation (1.34) [51, 52, 50]. Following the notations used in Equation (1.29)

$$\mathcal{A}_{CP} \propto -2a_e^j a_e^k \sin\left(\delta_e^j - \delta_e^k\right)\sin\left(\phi_e^j - \phi_e^k\right) \tag{1.44}$$

The observable $a_{CP}^{\widehat{T}\text{-odd}}$ is sensitive to the interference of $\widehat{T}$-even and $\widehat{T}$-odd amplitudes with different *CP*-odd ("weak") phases. Unlike the overall asymmetry in the decay rate $\mathcal{A}_{CP}$ that is sensitive to the interference of $\widehat{T}$-even amplitudes, $a_{CP}^{\widehat{T}\text{-odd}}$ does not require a non-vanishing difference in the *CP*-invariant ("strong") phase between the contributing amplitudes [51, 53].

To avoid dilutions in the integral of Equation (1.35), the functions chosen should ideally change sign wherever the $\widehat{T}$-odd-*CP*-odd piece of the differential decay rate itself changes sign. The bins' boundaries should also be placed there.

The question of what set of $f(\Phi)$ functions would yield the best sensitivity to *CP* violation is nontrivial and depends on the process at hand. Actually, when the form of the differential decay rate is known with confidence, one may rely on an unbinned likelihood fit to the data for extracting *CP*-violating parameters as done in many amplitude analyses.

However in many hadronic decays of heavy baryons the decay rate in not known and no amplitude analyses has been carried out. Using tests of *CP* violation that have a limited reliance upon the process dynamics and its parametrization is therefore desiderable.

1.4.3 Definition of the triple product observables

We define the triple product of final-state particle in the Λ_b^0 centre-of-mass frame as $C_{\widehat{T}} \equiv \vec{p}_p \cdot \left(\vec{p}_{\pi^-_{fast}} \times \vec{p}_{\pi^+}\right)$, where π^-_{fast} identifies the π^- with the highest momentum in the Λ_b^0 frame. The triple product $\overline{C}_{\widehat{T}}$ is defined similarly for $\overline{\Lambda}_b^0$ using the momenta of the charge conjugate particles. The triple products observables $C_{\widehat{T}}$ and $\overline{C}_{\widehat{T}}$ are $\widehat{T}$-odd. Since they are constructed with final-state particle momenta, they are also P-odd. We analyse a four-body decay in order to have three $\widehat{T}$-odd independent quantities, *i.e.* three final state momenta, and experimentally define the asimmetries $A_{\widehat{T}}$ and $\overline{A}_{\widehat{T}}$

$$A_{\widehat{T}} = \frac{\Gamma(C_{\widehat{T}} > 0) - \Gamma(C_{\widehat{T}} < 0)}{\Gamma(C_{\widehat{T}} > 0) + \Gamma(C_{\widehat{T}} < 0)}, \tag{1.45}$$

$$\overline{A}_{\widehat{T}} = \frac{\bar{\Gamma}(-\overline{C}_{\widehat{T}} > 0) - \bar{\Gamma}(-\overline{C}_{\widehat{T}} < 0)}{\bar{\Gamma}(-\overline{C}_{\widehat{T}} > 0) + \bar{\Gamma}(-\overline{C}_{\widehat{T}} < 0)}, \tag{1.46}$$

where Γ ($\bar{\Gamma}$) is the decay rate for Λ_b^0 ($\overline{\Lambda}_b^0$) decay. These asymmetries are P-odd and $\widehat{T}$-odd and so change sign under P or $\widehat{T}$ transformation, that is, $A_{\widehat{T}}(C_{\widehat{T}}) = -A_{\widehat{T}}(-C_{\widehat{T}})$ or

$\overline{A}_{\widehat{T}}(\overline{C}_{\widehat{T}}) = -\overline{A}_{\widehat{T}}(-\overline{C}_{\widehat{T}})$. Consequently the asymmetry $A_{\widehat{T}}$ ($\overline{A}_{\widehat{T}}$) is sensitive to P violation in the Λ_b^0 ($\overline{\Lambda}_b^0$) decay. They could be summed to obtain a P-violating asymmetry for both the decays Λ_b^0 ($\overline{\Lambda}_b^0$), or subtracted to compare the P violation in Λ_b^0 and $\overline{\Lambda}_b^0$ decays. Then the P- and CP-violating observables are defined as

$$a_P^{\widehat{T}\text{-odd}} = \frac{1}{2}\left(A_{\widehat{T}} + \overline{A}_{\widehat{T}}\right), \qquad a_{CP}^{\widehat{T}\text{-odd}} = \frac{1}{2}\left(A_{\widehat{T}} - \overline{A}_{\widehat{T}}\right), \tag{1.47}$$

and a significant deviation from zero in these observables would indicate P violation and CP violation, respectively.

1.5 Electric and magnetic dipole moments

The experimental searches for permanent electric dipole moments (EDMs) of fundamental particles constitute a promising attempts to probe for physics beyond the Standard Model. We propose to search for the EDM of heavy and strange baryons at LHCb, extending the ongoing worldwide experimental program on the neutron, muon, atoms, molecules and light nuclei. For Λ_c^+, Ξ_c^+, $\overline{\Xi}^+$ and $\overline{\Omega}^+$ baryons and anti-baryons, to be produced in a fixed-target experiment using 7 TeV protons extracted from the LHC beam and channeled in a bent crystal in front of the LHCb detector, the spin precession is induced by the intense electromagnetic field between crystal atomic planes. Measurements of the magnetic dipole moment (MDM) for all these systems would provide experimental anchor points for testing non-perturbative QCD dynamics and further insight in our understanding of the internal structure of hadrons and heavy quarks. Here we discuss the physics motivations for this research opportunity, the experimental layout and the performance with the LHCb detector, along with the expected sensitivities.

1.5.1 Motivations and physics opportunities

The existence of permanent EDMs requires the violation of parity (P) and time reversal (T) symmetries and thus, relying on CPT invariance, the violation of CP symmetry. Since EDM searches started in the fifties [54, 55], there has been an intense experimental program, leading to limits on the EDM of leptons [56, 57, 58], neutron [59], heavy atoms [60], proton (indirect from ^{199}Hg) [61] and Λ baryon [62]. New experiments are ongoing and others are planned, including those based on storage rings for muon [63, 64], proton and light nuclei [65, 66, 67]. These searches are currently putting the most stringent bounds on new models of CP violation, being considered of first importance in model-building. In addition, any signal of an EDM in the upcoming years would be an undisputed sign of T violation, which has only been observed in K^0 decays and entangled $B^0\overline{B}^0$ systems [68, 69, 70]. Here, we propose to extend this worldwide program to heavy (charm and beauty) and strange baryons produced by interaction of 7 TeV protons extracted from the LHC beam on a fixed target and channeled in a bent crystal located in front of the LHCb detector. The initiative is based on previous works discussed in References [71, 72, 73].

The amount of CP violation induced by the CKM matrix cannot account for the observed baryon asymmetry η defined in Equation (1.1). BSM physics, also referred to as new physics, is needed and must bring new CP violation sources that need to be tested experimentally.

These sources can be probed not only through flavour-changing, CP-violating transitions (the core of the LHCb physics program and the topic of the first part of this thesis), but also via flavour-diagonal CP-violating processes where the SM represent a negligible background [74]. The EDM of a particle falls in the latter category, as in fact is the only static property that violates P, T and CP. In addition to that, since the SM contributions to EDMs are highly suppressed (at the third order of the perturbation theory), these provide a "background free" search for BSM physics, whose contributions can largely enhance EDMs.

As BSM models vary in their contributions to the effective Lagrangian, EDM searches in different systems are complementary to disentangle the underlying source of CP violation. In this context, free particles bring the most valuable and cleanest information. In the case of heavy baryons, the dominance of the valence heavy quark in the low-energy hadronic calculation allows a clear interpretation.

EDM searches of fundamental particles rely on the measurement of the spin precession angle induced by the interaction with an external electromagnetic field. For unstable particles this is challenging since the precession has to take place before the decay. A solution to this problem requires large samples of high-energy polarized particles traversing an intense electromagnetic field.

No direct limits exist for the EDM of heavy baryons, since negligibly small spin precession would be induced by magnetic fields used in current particle detectors. Any experimental observation of an EDM in a heavy or strange baryon would be an unambiguous indication of BSM physics.

A large spin precession angle for positively- charmed ($\mathit{\Lambda}_c^+$, $\mathit{\Xi}_c^+$) and strange ($\overline{\mathit{\Xi}}^+$, $\overline{\mathit{\Omega}}^+$) baryons and anti-baryons, channeled in a bent crystal, would be expected by exploiting the intense electromagnetic field between crystal atomic planes.

The spin precession phenomenon can also be exploited to measure the MDM of the baryons. The proof of principle of the spin precession of particles with bent crystals was obtained by the E761 experiment at Fermilab that measured the MDM of the $\mathit{\Sigma}^+$ baryon [75].

Searches for electric dipole couplings of heavy quarks can be carried out at hadron colliders through Higgs observables [76]. These indirect upper limits, however, are largely overtaken by the limits from EDM experiments [77, 78] and are not expected to improve significantly with Run 2 data since they are dominated by systematic uncertainties [79]. Exploiting the geometrical shape and the tracking system of the LHCb detector there is a unique opportunity to perform direct measurements of baryon EDMs requiring additional but rather minimal setup upstream to the pp collision point. The proposed program will make the LHC competitive in the field of direct EDM searches.

1.5.2 Electric dipole moments

EDM concept

Classically the EDM of a charge distribution $\rho(\boldsymbol{r})$ is defined as $\boldsymbol{\delta} = \int \boldsymbol{r}\rho(\boldsymbol{r})d^3r$ and quantifies the electric charge separation. As any vector-like quantity in a subatomic system, it must be either parallel or anti-parallel to the spin. The former transforms under parity and time-reversal as a polar vector, while the latter as an axial vector. Contrary to the MDM, the existence of an EDM in fundamental particles therefore requires the violation of both the P and T symmetries [80]. This can be seen also using the classical Hamiltonian, in which the term proportional to $\boldsymbol{\delta}$ changes sign under P and T, while the term proportional to $\boldsymbol{\mu}$ does not,

$$\mathcal{H} = -\boldsymbol{\mu}\cdot\mathbf{B} - \boldsymbol{\delta}\cdot\mathbf{E} \xrightarrow{P} \mathcal{H} = -\boldsymbol{\mu}\cdot\mathbf{B} + \boldsymbol{\delta}\cdot\mathbf{E}\,,$$
$$\mathcal{H} = -\boldsymbol{\mu}\cdot\mathbf{B} - \boldsymbol{\delta}\cdot\mathbf{E} \xrightarrow{T} \mathcal{H} = -\boldsymbol{\mu}\cdot\mathbf{B} + \boldsymbol{\delta}\cdot\mathbf{E}\,.$$

Hence, the existence of a $\boldsymbol{\delta} \neq 0$ requires a breaking of the T and P symmetries [74]. Figure 1.5 illustrates the effect of these two symmetries on a system with a magnetic and electric dipole moment.

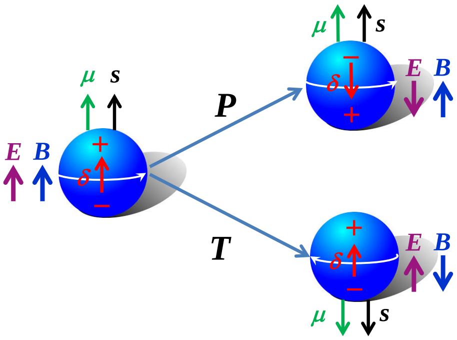

Figure 1.5: A particle with spin **s** is represented as a sphere with a spinning charge distribution. Its transformations under P and T operators are also shown, together with the corresponding particle magnetic moment $\boldsymbol{\mu}$ and the external magnetic $\mathbf{B}$ and electric $\mathbf{E}$ fields.

In the relativistic quantum field theory the EDM of any spin-$\frac{1}{2}$ particle is defined as the coupling constant δ of the operator

$$-\frac{i}{2}\,\delta\,\bar{\psi}\sigma^{\mu\nu}\gamma_5\psi F_{\mu\nu}\,, \tag{1.48}$$

where ψ is the Dirac field of the particle, $F^{\mu\nu} = \partial_\mu A_\nu - \partial_\nu A_\mu$ the electromagnetic tensor, and γ_5 and $\sigma^{\mu\nu}$ are the commonly defined products of Dirac matrices. It can be shown that only this operator in the non-relativistic limit induces the spin of the particle (ψ) to change direction in a way that breaks *CP* symmetry according to the classical equations of motion of an electric dipole moment subjected to an external electric field ($F^{\mu\nu}$).

Electromagnetic Form Factors

Being electromagnetic properties, the EDM and MDM of a particle are described, within quantum field theory, as the couplings of the particle with an external photon. These type of couplings appear in the transition amplitude of the baryon with the electromagnetic current J^μ_{em}, and can be parametrized by four linearly independent operators [81][1], whose coefficients are the so-called electromagnetic form factors $F_i(q^2)$ $(i = 1, 2, 3, 4)$. The form factors only depend on a Lorentz-invariant quantity, chosen to be q^2, the transferred momentum (i.e the momentum of the photon).

---

[1] This parametrization is done in the most general way through a linear combination of all the terms that respect the symmetries of J^μ and are linearly independent. There are three requirements [81]: Lorentz covariance, hermiticity ($J^\mu = J^{\mu\,\dagger}$) and gauge invariance ($\partial_\mu J^\mu = 0$).

For baryons[2] with spin-1/2, the matrix element is [82]

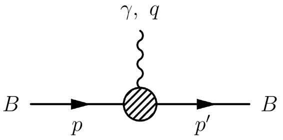

$$= \langle B(p')|J^{\nu}_{\text{em}}|B(p)\rangle \tag{1.49}$$

$$= \bar{u}(p')\left\{\gamma^{\nu}F_1\left(q^2\right) - \frac{i\,F_2\left(q^2\right)}{2m_B}\sigma^{\mu\nu}q_{\mu} - \frac{F_3\left(q^2\right)}{2m_B}\sigma^{\mu\nu}q_{\mu}\gamma_5 + i\left(\gamma^{\nu}q^2\gamma_5 - 2m_B q^{\nu}\gamma_5\right)F_A\left(q^2\right)\right\}u(p)\,,$$

where m_B is the baryon mass.

Each of these form factors describes one specific coupling of the particle to a photon, and together they contain all its electromagnetic properties. In particular [81], $F_1(0) = Q$ is the electric charge of the baryon; $\frac{1}{2m_B}[F_1(0) + F_2(0)] = \mu$ is the magnetic moment; $F_A(0)$ is the anapole moment; and $\frac{1}{2m}F_3(0) = \delta$ is the electric dipole moment, which corresponds to the unique term in Equation (1.49) that violates *CP* symmetry. Being a static property, the EDM coupling δ is defined using an external photon that is on-shell, i.e. at $q^2 = 0$. This requirement can only be met in direct measurements as the one proposed in this work. Other searches use dynamical observables with large q^2 values [83, 84] or even with q^2 integrated over all momenta inside the loops [85].

Baryon EDMs

In the case of baryons, the EDM arises from their inner structure of quarks and gluons. Any process involving an external photon and a flavour-conserving *CP*-violating vertex within the bound state would contribute to the overall EDM of the baryon. All of these *CP*-violating operators behind the EDM of a baryon are accounted in the *CP*-odd flavour

---

[2] This expression is still valid for any fermion with spin 1/2 including quarks and leptons.

diagonal effective Lagrangian, here at 1 GeV,

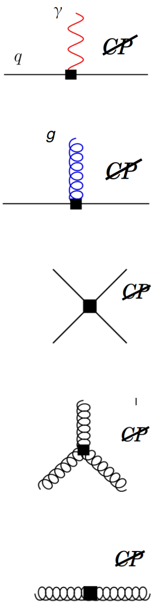

$$\begin{aligned}
\mathcal{L}_{\text{eff}}^{\not{P}\not{T}} = &- \frac{i}{2} \sum_{q=u,d,s,c,b} \delta_q \, \bar{q} \sigma^{\mu\nu} \gamma_5 q \, F_{\mu\nu} && \text{qEDM} \\
&+ i \sum_{q=u,d,s,c,b} \tilde{\delta}_q \, \bar{q} \sigma^{\mu\nu} \gamma_5 t_a q \, G^a_{\mu\nu} && \text{qCEDM} \\
&+ \sum_{i,j,k,l=u,d,s,c,b} C_{ijkl} \, \bar{q}_i \Gamma q_j \, \bar{q}_k \Gamma' q_l && \text{4q op.} \qquad (1.50) \\
&+ \frac{d_W}{6} f_{abc} \varepsilon^{\mu\nu\alpha\beta} G^a_{\alpha\beta} G^b_{\mu\rho} G^{c\,\rho}_{\nu} && \text{gCEDM (Weinberg op.)} \\
&- \bar{\theta} \frac{g^2}{64\pi^2} \epsilon^{\mu\nu\alpha\beta} G^a_{\mu\nu} G^a_{\alpha\beta} && \theta\text{-QCD term,}
\end{aligned}$$

where the notation has been taken from Reference [86], except for the δ symbol, referred to as d therein. We can easily recognize Equation (1.48) in the qEDM term. The qCEDM (quark chromo-EDM) term is the analogous term when the external photon is replaced by a gluon. Overall, a measurement of a heavy or strange baryon EDM is directly sensitive to the qEDM and qCEDM couplings, as the other contributions are either suppressed because the involved operators are of higher dimension (4q and gCEDM) or are constrained by the neutron EDM (θ-QCD term).

This effective Lagrangian plays an intermediate role between the fundamental theories and the EDM of baryons. The various extensions of the SM present very different contributions to these operators , which in turn do not contribute in equal amounts to the EDM of baryons. Evaluating the contribution of these operators at the quark-gluon scale to the hadronic EDM requires the calculation of nonperturbative matrix elements, which is not trivial since QCD cannot be analytically solved at low energy. Different approaches exist such as naive dimensional analysis, chiral theories, QCD sum rules or lattice QCD. The reliability of these techniques can be tested experimentally through low-energy observables among which the magnetic moment of charm baryons could play an important role [87], as discussed in Section 1.5.3.

With the exception of the neutron and the proton, only few theoretical works have developed expressions for the EDM of baryons in terms of the coupling constants in $\mathcal{L}_{\text{eff}}^{\not{P}\not{T}}$,

$$\delta_B = \delta_B(\bar{\theta}) + \delta_B^{\text{qEDM}}(\delta_q) + \delta_B^{\text{qCEDM}}(\tilde{\delta}_q) + \delta_B^{\text{gCEDM}}(d_W) + \delta_B^{\text{4q}}(C_{ijkl}) \,. \qquad (1.51)$$

Since this set of operators is linearly independent, in principle, all different contributions can, be added up. There exist expressions for the EDM of the Λ evaluating the contributions of the θ term [88, 89, 82], the quark chromo-EDM (qCEDM) and four quark (4q) operators [90], and the quark EDM (qEDM) [91]. The latter uses the non-relativistic quark model to compute the EDM of the Λ in terms of the EDM of the constituent quarks which yields a null contributions from the u and d quarks, obtaining $\delta_\Lambda^{\text{qEDM}} = \delta_s$.

In contrast, no calculation of charmed baryon EDMs exists in the literature, although the dominance of the valence charm quark contributions might make this observable especially sensitive to the charm q(C)EDM. Nevertheless, the calculations of the EDM within the non-relativistic quark model are equivalent to those of the magnetic moment, from which we can infer that $\delta_{\Lambda_c^+}$ has a contribution from the charm-quark EDM of order $\delta_{\Lambda_c^+}^{\mathrm{qEDM}} = \delta_c$ [92]. Using the counting of Naive Dimensional Analysis of H. Georgi [93], we obtain the estimation to the overall $\delta_{\Lambda_c^+}$ also from the charm qCEDM, which holds also for the s-quark contribution in strange baryons,

$$\delta_{\Lambda_c^+} \approx \ \pm d_c \ \pm \ \frac{e}{4\pi} \tilde{d}_c \, . \tag{1.52}$$

The SM has very small contributions to the couplings in Equation (1.50), which happen at 3-loop level [94], while many BSM theories predict sizable contributions in different operators [86]. Any measurement of a non-zero EDM in the experiments planned for the next years would be a clear a sign of new physics.

EDM searches

The existence of non-zero EDM in different systems is related to different theories ranging from the nuclear scale to the TeV scale, as illustrated in Figure 1.6. As a result, an extensive experimental program is taking place worldwide to search for these non-zero EDMs. The systems that are putting the most stringent conditions in models of *CP* violation are those of the neutron, the diamagnetic atom ^{199}Hg and the electron. Bounds on the electron EDM are obtained by exploiting the strong electric field (~ 84 GV/cm) that the unpaired electron feels in the polar molecule ThO [56], achieving limits below $10^{-28}\, e\,\mathrm{cm}$. This technique requires theoretical input to infer the bound on the electron EDM. In contrast, the proposed experiment would measure directly the spin precession in baryons due to the intense electric field. So far, direct limits of baryon EDMs only exist for neutrons, which with $10^{-26}\, e\,\mathrm{cm}$ represents the EDM value closest to the SM prediction [95], and a rather loose bound on the Λ [62], $1.5 \times 10^{-16}\, e\,\mathrm{cm}$, which could be improved by two orders of magnitude by LHCb at the end Run 3 using pp collision data [71].

The proton EDM, in turn, has only been measured indirectly using atoms and molecules. A direct measurement of the proton EDM might be carried out at CERN with a future storage ring facility [96] together with new bounds of light nuclei such as D or He^3. The first direct proton EDM measurement is expected to increase the current bound by three orders of magnitude up to $\sim 10^{-29}\, e\,\mathrm{cm}$.

The measurement of the EDM for different systems will disentangle which mechanisms contribute and thereby put constraints on different theories [86]. Additionally, upper bounds on a broad range of systems are complementary to constrain the BSM parameters.

Indirect upper limits

Indirect bounds on the charm and beauty quark EDMs can be extracted from observables containing qEDM and qCEDM couplings combined with model and computational assumptions, including extrapolations to $q^2 = 0$.

In the case of the charm quark EDM, indirect upper limits have been obtained from the cross section $e^+e^- \to c\bar{c}$ [84], the branching ratio of $B \to X_s\gamma$ decays [77], the electron

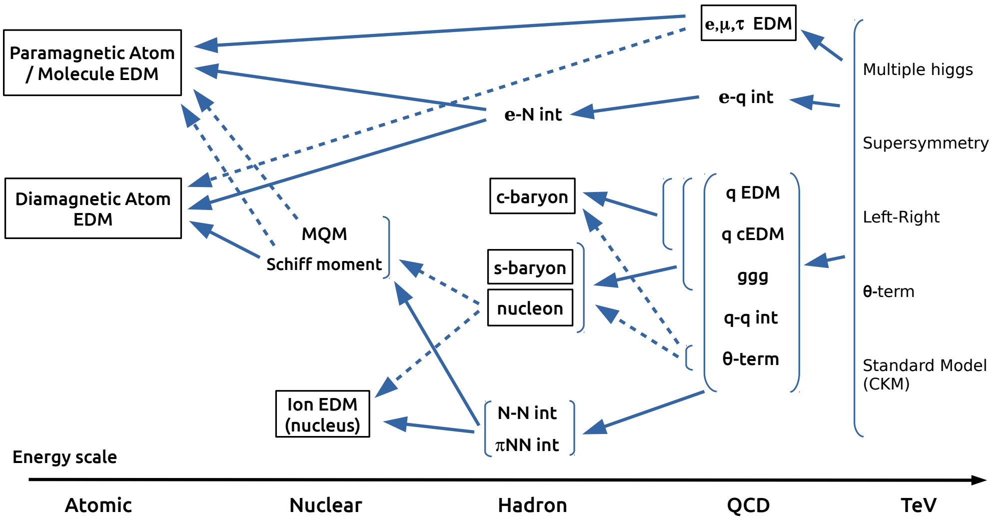

Figure 1.6: Contributions from every CP-violating term, going from fundamental theories (TeV scale) to the atomic regime. Dashed lines represent suppressed contributions. The terms at the "QCD scale" (meant as $\lesssim 1\,\text{GeV}$) grouped under a brace constitute the effective CP-odd Lagrangian in Equation (1.50). The boxed elements are the EDMs for which direct measurements can be done. This figure is based on [94] including the proposed observables: c-, b and s-baryon EDMs.

EDM [85] and the neutron EDM [77, 85], as illustrated in Figure 1.7. These limits, presented in Table 1.1, vary by several orders of magnitude, approximately from 10^{-17} to $10^{-15}\,e\,\text{cm}$, depending on the method used but also on the specific details of the calculation. From the strongest limit [77], the indirect upper bound on the Λ_c^+ baryon results in $\delta_{\Lambda_c^+} \lesssim 4.4 \times 10^{-17}\,e\,\text{cm}$. As discussed in Section 9.2, this indirect limit could be reached and improved by the direct measurements proposed here. Using the neutron EDM as input we see, however, that Reference [77] and [85] obtain different limits on d_c based on the same experimental bound on the neutron EDM, $|d_n| < 2.9 \times 10^{-26}\,e\,\text{cm}$. This difference arises from the longitudinal component of the W boson propagator, which are taken into account in [85], obtaining a much more conservative bound.

Similarly, indirect upper limits on the beauty quark EDM have been obtained from the cross section $e^+e^- \to b\bar{b}$ [84], the $Z \to b\bar{b}$ partial width [83], the electron EDM [85] and the neutron EDM [85, 97], as reported in Table 1.2. These limits vary by several orders of magnitude, from 10^{-17} to $10^{-12}\,e\,\text{cm}$. In the case of References [85, 97] the upper limits differ by more one order of magnitude despite they use the same input.

At LHC, constraints on the beauty [charm] qCEDM could be placed through the total cross sections $\sigma(pp \to b\bar{b}h)$ [$\sigma(pp \to hX)$] [76], reaching limits on the order of $|\tilde{d}_b| \lesssim 10^{-18}\,e\,\text{cm}$ [$|\tilde{d}_c| \lesssim 10^{-17}\,e\,\text{cm}$] [3]. These bounds are much weaker than those coming from the neutron EDM, also shown in Table 1.1 and 1.2. They could be improved by one order of magnitude by looking at the kinematic structure of $\sigma(pp \to b\bar{b}hX)$ events [98], in which the p_T of the Higgs boson is enhanced in the presence of a beauty CEDM.

---

[3] These values could be achieved with 14 TeV data and are dominated by systematic uncertainties.

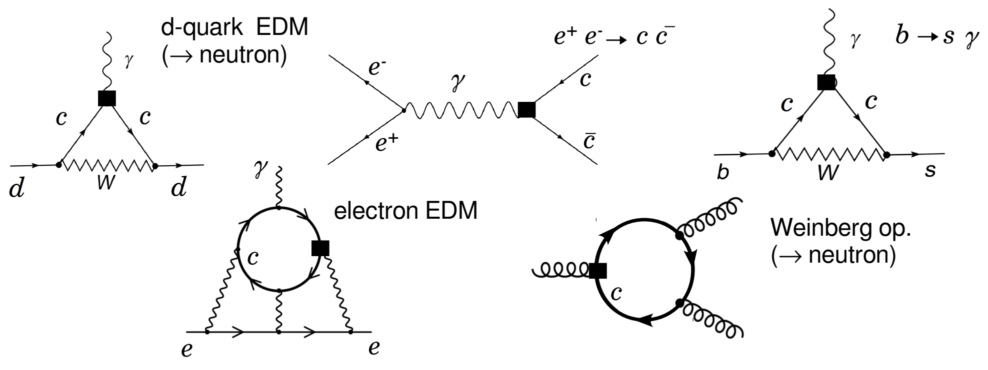

Figure 1.7: Examples of flavor-diagonal observables that can be used to set indirect bounds on the charm qEDM and qCEDM.

The strange Λ baryon is the only one for which a direct EDM limit exists and it was determined to be $1.5 \times 10^{-16}\, e\,\mathrm{cm}$ (95% C.L.) in a fixed-target experiment at Fermilab [62]. This bound is however much weaker than the indirect upper bounds based on the neutron EDM, which are predicted to be $\lesssim 4.4 \times 10^{-26}\, e\,\mathrm{cm}$ [82, 99, 88, 89]. The are no indirect bounds for baryons with two or three s valence quarks, although they are expected to differ by no more than approximately two orders of magnitude.

Potential to constrain BSM physics

As it will be discussed in Section 9.2, the sensitivity level that could be achieved by LHCb with this proposal would establish the most stringent constraint on the parameter d_c (charm quark EDM) and would lie close to the indirect constraints on d_b (beauty quark EDM). In this section we focus on the new and competitive constraints that can be put on specific BSM theories through this experiment. Indeed, it can be noted that the indirect bounds quoted in Table 1.1 and 1.2 are already being used to constrain BSM physics. For instance, the charm and beauty CEDM have been used to constrain CP-violating parameters in models of composite Higgs [101, 102, 103]. However, predictions for the charm EDM at the expected sensitivity level ($\sim 10^{-17} e\mathrm{cm}$) exist within different versions of supersymmetry, namely for the baryon-lepton minimal supersymmetric extension [104] and the low-energy SUSY model [105].

Other predictions for charm and beauty (C)EDM that are below the expected sensitivity may be found within the minimal supersymmetric extension [106, 107] ($d_c \sim 10^{-19}\, e\,\mathrm{cm}$ and $d_b \sim 10^{-20}\, e\,\mathrm{cm}$, respectively), extended color octet scalar [108] ($d_b, \tilde{d}_b \sim 10^{-21}\, e\,\mathrm{cm}$), effective CP-violating Yukawa couplings to quarks and gluons [79] ($\tilde{d}_c \sim 10^{-22}\, e\,\mathrm{cm}$, $\tilde{d}_b \sim 10^{-21}\, e\,\mathrm{cm}$) and radiative flavor SUSY [109] ($\tilde{d}_c \sim 10^{-29}\, e\,\mathrm{cm}$). In general, charm quark EDM upper limit is relevant for models that allow a non-negligible flavour violation in the up-quark sector, providing stronger constraints than from ΔA_{CP} measurements [77].

As it can be observed, predictions of different new physics models lie in a large range of orders of magnitude. Thus, both the presence or absence of an EDM signal in the proposed measurements would help to reveal the nature of the BSM theory.

Table 1.1: Indirect bounds on the charm quark EDM and chromo-EDM obtained from different experimental measurements. Ordered by year of publication.

Bound ($e\,\mathrm{cm}$)	Reference (year)	Measurement	Method
$\lvert d_c\rvert < 4.4\times10^{-17}$	[77] (2014)	neutron EDM	Considers threshold contributions of d_c into d_d. Neglects all other contributions to the d_n
$\lvert d_c\rvert < 3.4\times10^{-16}$	[77] (2014)	BR($B\to X_s\gamma$)	Considers contributions from d_c to the Wilson coefficient C_7
$\lvert d_c\rvert < 3\times10^{-16}$	[85] (2009)	electron EDM	Extracted from d_c threshold contribution to d_e through light-by-light scattering diagrams
$\lvert d_c\rvert < 1\times10^{-15}$	[85] (2009)	neutron EDM	Similar approach than ref. [77]. Evaluates contributions in two steps: c-quark → d-quark → neutron
$\lvert d_c\rvert < 5\times10^{-17}$	[84] (2009)	$e^+e^-\to c\bar{c}$	The total cross section (LEP) might be enhanced by the charm qEDM vertex $c\bar{c}\gamma$
$\lvert d_c\rvert < 8.9\times10^{-17}$	[83] (1994)	$\Gamma(Z\to c\bar{c})$	Measurement at the Z peak (LEP). Uses model dependent relationships to weight contributions from d_c and d_c^w
		chromo EDM	
$\lvert\tilde{d}_c\rvert < 1.0\times10^{-22}$	[77] (2014)	neutron EDM	Considers threshold contributions of d_c into the light quark EDMs $d_{u,d}$ and the Weinberg operator w
$\lvert\tilde{d}_c\rvert < 3\times10^{-14}$	[100] (2012)	$\psi'\to J/\psi\,\pi^+\pi^-$	The $\tilde{d}_c$ contributes to the static potential between c and $\bar{c}$ both in ψ' and J/ψ. It also affects the dynamical transition amplitudes

1.5.3 Magnetic dipole moments

Baryon magnetic moments are sensitive to non-perturbative QCD. Therefore their measurement can put non-perturbative QCD models to a stringent test, as well as improve our understanding of the internal structure of hadrons.

In this respect, baryons with a heavy quark Q are handled considering specific simplifications such as $m_Q\to\infty$ that introduce new symmetries involving the contributions of the subcomponents to the overall baryon spin. Magnetic moments of heavy baryons have been considered in many theoretical approaches, and there exists an extensive literature. Thus, contrary to the EDM case, for which there exists almost no theoretical work on the EDM of heavy baryons, there is a wide range of predictions for non-measured magnetic moments. All these models used to calculate the electromagnetic properties can only be tested through direct measurements and give access to test the possibility of an anomalous magnetic moment of the valence heavy quark. Table 1.3 and 1.4 summarize a number of predictions for the MDM of the $\mathit{\Lambda}_c^+$, $\mathit{\Xi}_c^+$, $\mathit{\Lambda}$, $\mathit{\Xi}^-$, $\mathit{\Omega}^-$, $\mathit{\Xi}_b^-$ and $\mathit{\Omega}_b^-$, extracted from [87, 110] and references therein. With a sensitivity at the order of $10^{-2}-10^{-1}\mu_N$, where μ_N is the nuclear magneton, we would be able to discriminate between many of these models.

The MDM of other systems such as leptons can be predicted by the SM with much higher accuracy, thanks to the perturbative nature of QED. This is the case of the muon $g-2$ where, in fact, the largest theoretical uncertainty comes from the hadronic contributions of mesons entering the loops [111]. The validity of the simplifications and the uncertainties of the low-energy QCD methods are thus the bottleneck to understand the electromagnetic properties of the SM particles.

Table 1.2: Indirect bounds on the beauty quark EDM and chromo-EDM obtained from different experimental measurements. Ordered by year of publication.

Bound ($e\,\mathrm{cm}$)	Reference (year)	Measurement	Method
$\|d_b\| < 7 \times 10^{-15}$	[85] (2009)	electron EDM	From the b-quark EDM threshold contribution to d_e through light-by-light scattering diagrams
$\|d_b\| < 2 \times 10^{-12}$	[85] (2009)	neutron EDM	Similar estimation but evaluating contributions in two steps: b-quark → up-quark → neutron
$\|d_b\| < 2 \times 10^{-17}$	[84] (2009)	$e^+e^- \to b\bar{b}$	The total cross section (LEP) might be enhanced by the charm qEDM vertex $b\bar{b}\gamma$
$\|d_b\| < 1.22 \times 10^{-13}$	[97] (2008)	neutron EDM	Similar estimation than [85]. But neglects longitudinal component in the W propagator, thus missing emerging divergences
$\|d_b\| < 8.9 \times 10^{-17}$	[83] (1994)	$\Gamma(Z \to b\bar{b})$	Measurement at the Z peak (LEP). Uses model dependent relationships to weight contributions from d_b and d_b^w
chromo EDM			
$\|\tilde{d}_b\| \lesssim 1.1 \times 10^{-21}$	[101] (2014)	neutron EDM	Numerical result based on the the contribution of the beauty CEDM into the Weinberg operator derived in [78]

Table 1.3: Magnetic dipole moment of c- and s-baryons (in units of μ_N) calculated in different approaches: non-relativistic quark model (NRQM), lattice QCD, QCD sum rules (QCDSR), QCD spectral sum rules (QSSR), light cone QCD sum rules (LCQSR), and the contributions of valence quarks, quark sea and their orbital angular momentum from SU(4) chiral constituent quark model (χCQM). Extracted from Reference [87] and references therein.

Baryon	Data	NRQM	Lattice QCD	QCDSR QSSR	LCQSR	Valence	Sea	Orbital	Total
$\mu(\Lambda_c^+)$	...	0.39	...	0.15 ± 0.05	0.40 ± 0.05	0.409	-0.019	0.0002	0.392
$\mu(\Xi_c^+)$	...	0.39	...	...	0.50 ± 0.05	0.41	-0.02	0.01	0.40
$\mu(\Lambda)$	-0.613 ± 0.004	-0.65	-0.50 ± 0.07	-0.56 ± 0.15	-0.7 ± 0.2	-0.59	0.02	-0.01	-0.58
$\mu(\Xi^-)$	-0.651 ± 0.003	-0.53	-0.51 ± 0.07	-0.64 ± 0.06	-0.7 ± 0.2	-0.59	0.03	0.06	-0.50
$\mu(\Omega^-)$	-2.02 ± 0.06	-1.94	-1.40 ± 0.10	-1.49 ± 0.45	-1.65 ± 0.35	-1.76	0.08	-0.03	-1.71

Table 1.4: Magnetic dipole moment of b-baryons (in units of μ_N) calculated in different approaches: effective quark mass scheme, shielded quark charge scheme, MIT bag model, MIT bag model with center-of-mass motion corrections, hypercentral model, relativistic three quark model and NRQM using AL1 potential and power-law potential model. Extracted from Reference [110] and references therein.

Baryon	Effective quark mass	Screened quark charge	MIT bag	MIT bag corrections	hypercentral	relativistic three quark	power-low potential
$\mu(\Xi_b^-)$	-0.062	-0.066	-0.063	-0.050	...	-0.06	...
$\mu(\Omega_b^-)$	-0.741	-0.863	-0.545	-0.79	-0.960	-0.82	-0.714

CHAPTER 2

LHC collider and LHCb detector

LHCb is one of the four major experiments operating at the Large Hadron Collider (LHC) at CERN, located near Geneva, at the border between France and Switzerland. In this chapter we will give a short description of the LHC collider, followed by an overview of the LHCb detector.

2.1 The Large Hadron Collider

LHC is a circular collider with a circumference of 26.7 km, lying between 45 m and 170 m below the surface and housed in the former LEP tunnel. The accelerator is designed to collide protons with an energy of 7 TeV per beam with an instantaneous luminosity of $10^{34}\,\mathrm{cm}^{-2}\,\mathrm{s}^{-1}$. Heavy-ion collisions (Pb-Pb) are also possible with an energy of 2.76 TeV per nucleon and a peak luminosity of $10^{27}\,\mathrm{cm}^{-2}\,\mathrm{s}^{-1}$. This energy will be reached after the restart of the LHC machine in 2021, following the second long shutdown. Until now, the LHC has collided protons at a centre-of-mass (CM) energy of $\sqrt{s} = 7$, 8 and $13\,\mathrm{TeV}$ in 2011, 2012 and 2015-2018, respectively. The schematic view with the underground structures is shown in Figure 2.1. Four main experiments operate at the LHC: ALICE, ATLAS, CMS, LHCb. Not only the locations of the four experiments are different but

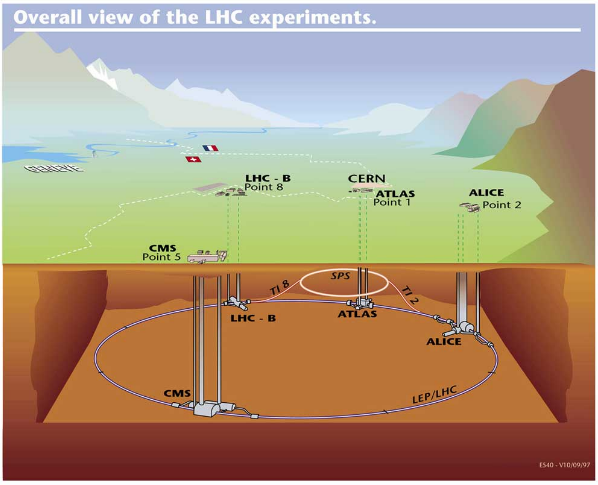

Figure 2.1: Schematic view of the LHC collider which is about 100 m underground. There are 4 access points to the main experiments (ALICE, ATLAS, CMS, LHCb).

also their scope: ATLAS and CMS are so called "General Purpose Detectors" for high transverse momentum physics; ALICE investigates the quark-gluon-plasma, a state of matter present in the early universe by studying heavy-ion collisions; LHCb is a dedicated b-physics experiment, focusing on CP-violating and rare decays of beauty and charm hadrons, but also performing analyses in the field of electroweak physics and spectroscopy.

To achieve the design energy of $7\,\mathrm{TeV}$, the bending magnets for protons have a field strength of 8.3 T. This requires the usage of superconducting magnets cooled with superfluid helium at 1.9K.

Radio Frequency (RF) cavities are used to accelerate the protons. These cavities operate at a frequency of $400\,\mathrm{MHz}$ and accelerate the protons using a longitudinally oscillating electric field. To achieve a constant acceleration over many turns of the protons, the frequency of the RF must be precisely tuned to the revolution frequency of the LHC. The RF system relies on superconducting technology to avoid losses of the electric field in the walls of the cavity.

The LHC is the last piece of a complicated chain of devices that produce and accelerate protons (and Pb atoms) until they finally collide at one of the four interaction points. Protons are extracted from ionized hydrogen atoms with an energy of $50\,\mathrm{keV}$ and guided to a linear accelerator (LINAC), where the energy is increased to $50\,\mathrm{MeV}$. They are then injected into a booster synchrotron which increases their energy to $1.4\,\mathrm{GeV}$ until they finally arrive at the Proton Synchrotron (PS). In this machine the protons are not only accelerated but also grouped into trains of bunches, a structure that is kept until the beams finally collide in the LHC. After leaving the PS, these bunch-trains are injected into the Super Proton Synchrotron (SPS), where they are further accelerated to the energy of $450\,\mathrm{GeV}$. They are transferred to the LHC via one of the two transfer lines. After filling both counter rotating beams with bunch-trains, the protons are accelerated while the magnetic field, in the bending dipoles, is simultaneously increased until the collision energy is reached. At the LHCb interaction point the beams are slightly defocused to reduce the instantaneous luminosity to $2 \times 10^{32}\,\mathrm{cm}^{-2}\,\mathrm{s}^{-1}$. Running at lower luminosity has some advantages: events are dominated by a single pp interaction per bunch crossing which are simpler to analyse than those with multiple primary pp interactions. Furthermore the occupancy in the detector remains low and radiation damage is reduced.

The excellent LHC performance allowed the LHCb experiment to collect more than 3 fb^{-1} of data during 2011-2012 data taking (Run 1) and 5.7 fb^{-1} during 2015-2018 (Run 2), with an efficiency of well over 90% (see Figure 2.2). The dataset collected in 2018 is not included in this thesis. This implies that an unprecedented large sample of D, B and heavy baryons has been collected, allowing the LHCb collaboration to perform world class precision measurements.

2.2 Beauty production at LHCb

The pp strong interactions can be analysed in terms of long- and short-distance contributions to the cross section.

The long distance interaction is non perturbative: protons see each other as point like particles without structure. The scattering is known as "soft", as the transferred momentum is low, the out-coming particles are therefore produced at small polar angles with respect to the beam axis. This process is not relevant for b-hadron production.

In short distance interactions the interacting particles are the partons of the incoming

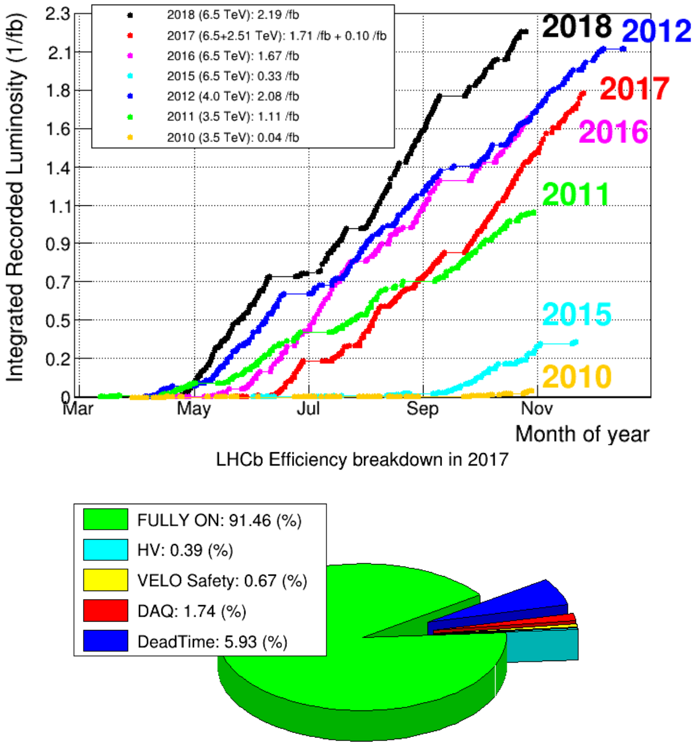

Figure 2.2: Above: Recorded luminosity by the LHCb experiment as a function of time. Below: pie chart showing the data taking efficiency of the LHCb detector (green) and various sources of inefficiency.

protons. In this case the interaction is described by perturbative QCD followed by a non perturbative hadronization into colourless hadrons. The transferred momentum is large, therefore the out-coming particles are produced with relatively large transverse momentum with respect to the beam axis. For leading-order (LO) contributions, the dominant processes are quark-antiquark annihilation ($q\bar{q} \rightarrow b\bar{b}$) and gluon-gluon fusion ($gg \rightarrow b\bar{b}$), commonly referred to as pair creation. The corresponding Feynman diagrams are shown in Figure 2.3. In the next-to-leading order (NLO), gluon-splitting and flavour-excitation come into play and are shown in Figure 2.4. The contribution of the leading-order processes with respect to the total b cross section decreases with increasing energy. In a pp collider at the CM energy of 7 TeV and 14 TeV the dominating process is flavour-excitation. The different contribution as implemented in the event generator PYTHIA 6.4 are shown in Figure 2.5. The cross section of $b\bar{b}$ pairs production increases almost linearly from 7 to 14 TeV.

Since the mass of b and $\bar{b}$ quark is low with respect to the energy involved in the pp collisions at the LHC, the pairs $b\bar{b}$ are created at high pseudorapidity. Furthermore there is a strong correlation between the b and the $\bar{b}$ which causes them both to end up in the

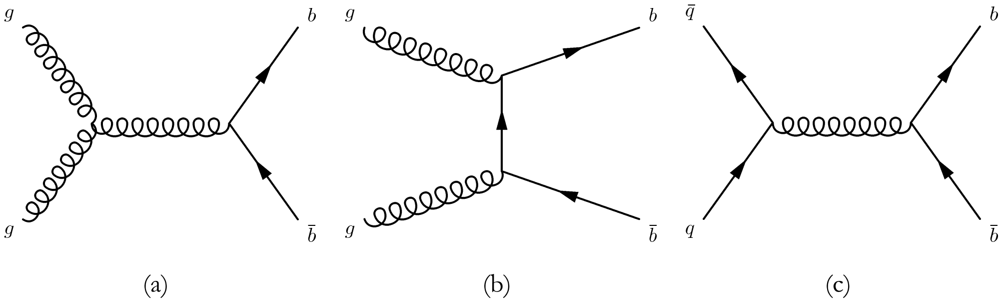

Figure 2.3: Feynman diagrams for leading order for $b\bar{b}$ production in pp collisions. (a) and (b) show gluon-gluon fusion processes while (c) shows quark-antiquark annihilation processes.

forward or backward direction. This is visualized in Figure 2.6 and played an important role in the design of the LHCb experiment.

The $b\bar{b}$ cross section has been measured in the forward region at the LHCb experiment in the pseudorapidity interval $2 < \eta < 6$ and is $75.3 \pm 5.4 \pm 13.0\,\mu\text{b}$ [113], where $\eta = -\ln\left(\tan\left(\frac{\theta}{2}\right)\right) \approx \frac{1}{2}\ln\left(\frac{|p|+p_L}{|p|-p_L}\right)$ (θ is the angle between the beam axis and a direction, $|p|$ is the momentum magnitude and p_L the transversal momentum of a particle).

In vacuum quarks do not exists as unconfined objects and can only be observed as bound states in the form of mesons or baryons. At some point the individual quarks must fragment into colourless bound objects. However the fragmentation fractions of quarks into bound states, *i.e.* the fraction of a quark to hadronize into a specific bound state, are difficult to predict theoretically as the fragmentation happens in the non-perturbative regime of QCD. They can however be measured experimentally *e.g.* by measuring the relative production of different b-hadron species [114]. The average results of the fragmentation fractions from different experiments are presented in Table 2.1. However it should be noted that fragmentation fractions can depend on quantities like the energy or the transverse momentum of the created hadron and so the quoted averages may therefore not be universally applicable.

Table 2.1: Fragmentation fractions for different hadrons containing b quark. For the first row, the B^0 and B^+ fraction are set equal and the number only applies for one type of B meson and not for both together. The numbers are taken from Reference [115].

Hadron species	Fraction
B^0 or B^+	0.406 ± 0.005
B_s^0	0.104 ± 0.006
b-baryon	0.084 ± 0.011

2.3 LHCb Detector

The LHCb detector [116, 117, 118] is a single arm spectrometer with a forward geometry as shown in Figure 2.7, covering angles from about $10\,\text{mrad}$ to approximately 300 (250) mrad in the horizontal (vertical) direction. The difference in the horizontal and vertical acceptance is justified by the fact that the horizontal plane is the bending plane for

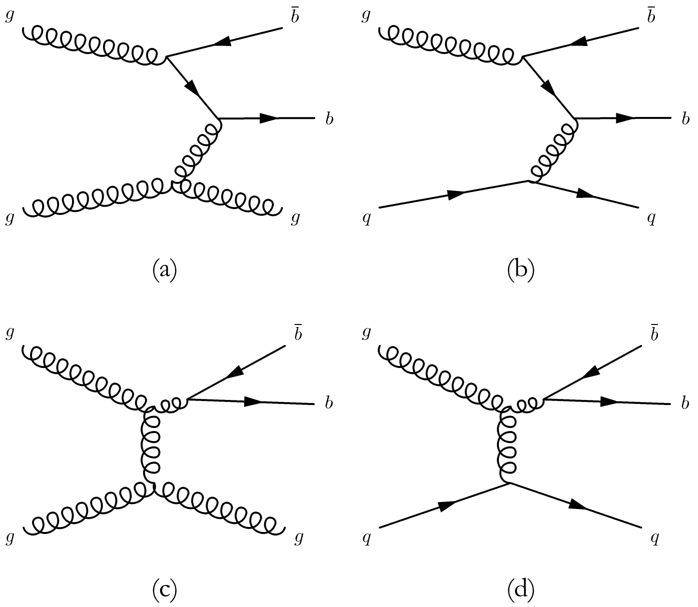

(a) (b)

(c) (d)

Figure 2.4: Feynman diagrams at next-to-leading order for $b\bar{b}$ production in pp collisions. (a) and (b) show flavour excitation processes while (c) and (d) show gluon splitting processes.

the charged particle deflected by the dipole magnetic field along the vertical axis. Its forward design originates from the fact that b and $\bar{b}$ quarks are produced in pairs and predominantly in the forward or backward direction (see Section 2.2). The fraction of b or $\bar{b}$ quark produced in a pp collision inside the LHCb acceptance is 27%. This geometry allows LHCb to reconstruct a large fraction of the produced particles containing a b or $\bar{b}$ quark while only covering a small solid angle.

The design luminosity of LHCb is $2 \times 10^{32}\,\mathrm{cm}^{-2}\,\mathrm{s}^{-1}$, two order of magnitude lower than the maximum capacity of the LHC. The maximum instantaneous luminosity in LHCb was $2 \times 10^{33}\,\mathrm{cm}^{-2}\,\mathrm{s}^{-1}$, in the 2017 data collection period. LHCb has decided against using the full luminosity provided by the LHC for several reasons. The forward region is dominated by a very high flux of particles which creates high occupancies in the detectors and induces radiation damage. Running at full luminosity would have put severe constraints on the choice of detector materials and segmentations to use. Moreover, separation of primary and secondary vertices is crucial for many analyses in LHCb, a task which is more difficult with large pile-up. Additionally, the ability to reconstruct all tracks in the event degrades with increasing number of interactions. The instantaneous luminosity for LHCb was therefore chosen as a compromise between all these parameters.

The LHCb detector can be grouped in three parts:

- **the track reconstruction system** for the measurement of the particle momentum;
- **the particle identification system** to identify different particle types;
- **the trigger system** selects the events of interest for the offline physics analysis.

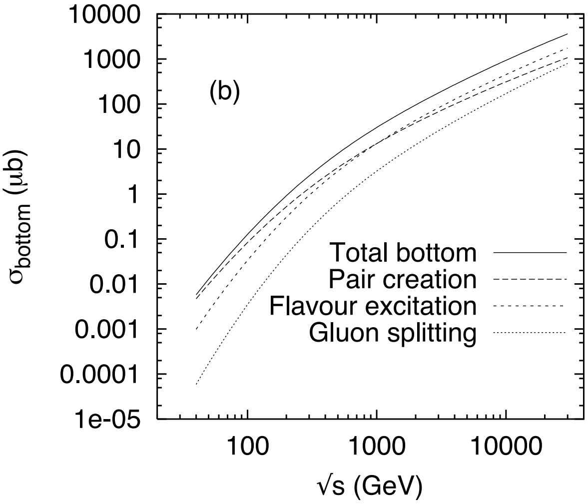

Figure 2.5: $b\bar{b}$ cross section at hadron colliders with different contribution due to pair creation, flavour excitation and gluon splitting. Figure taken from Reference [112].

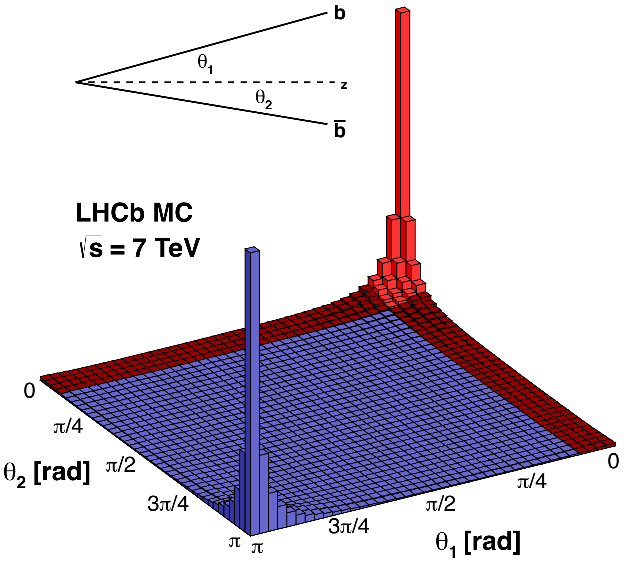

Figure 2.6: Distribution of $b\bar{b}$ quarks in simulated pp collisions at $\sqrt{s} = 7$ TeV, with θ being the angle between the quark and the beam axis. Red is the LHCb acceptance. The correlation between the two angles and related peak in the forward and backward direction is clearly visible.

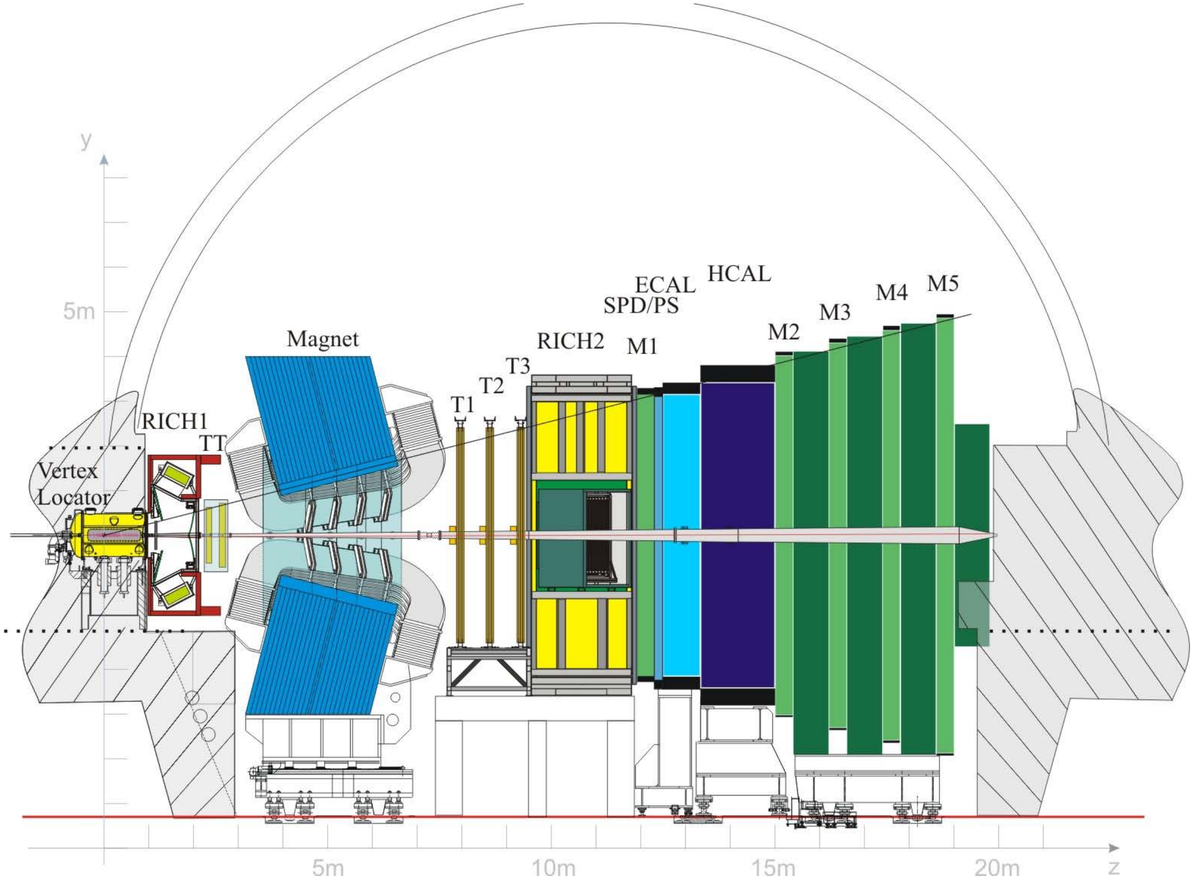

Figure 2.7: The LHCb detector. From left to right all the subdetectors are visible: Vertex Locator (VELO), Ring Imaging Cherenkov Detector 1 (RICH1), Tracker Turicensis (TT), Magnet, Tracking Stations (T1-T3), Ring Imaging Cherenkov Detector 2 (RICH2), Scintillating Pad/Preshower Detector (SPD/PS), Electromagnetic Calorimeter (ECAL), Hadronic Calorimeter (HCAL) and Muon Stations (M1-M5).

2.4 The LHCb tracking system

The tracking system is devoted to the identification of the interaction vertex, the reconstruction of the trajectories of charged particles in the dipole magnetic field and measurement of their momentum. The first task is accomplished by the Vertex Locator, which is also used for the track reconstruction, together with the Tracker Turicensis and the three tracking stations T1, T2 and T3. Finally, a warm dipole magnet generates the magnetic field.

2.4.1 The Vertex Locator

The Vertex Locator (VELO) [119] is the subdetector closest to the pp interactions. It is designed to precisely measure the position of the primary and secondary vertices, which is crucial to identify b (c)-hadrons with typical mean flight distance of about $1(0.3)\,\mathrm{cm}$ at LHCb. Due to high track multiplicity in LHC collisions, it is crucial to have a vertex locator with a micrometer precision in order to select signal events and reject most of the background.

The VELO is composed of 21 circular "stations" of silicon modules in a r-ϕ geometry installed along the beam line, as shown in Figure 2.8. Each station is divided into two halves; detectors modules are installed on the left and on the right side of the beam axis and a hole is left free in the middle for the proton beams that are not constant in shape when going from the injection state to the collision state. The modules therefore

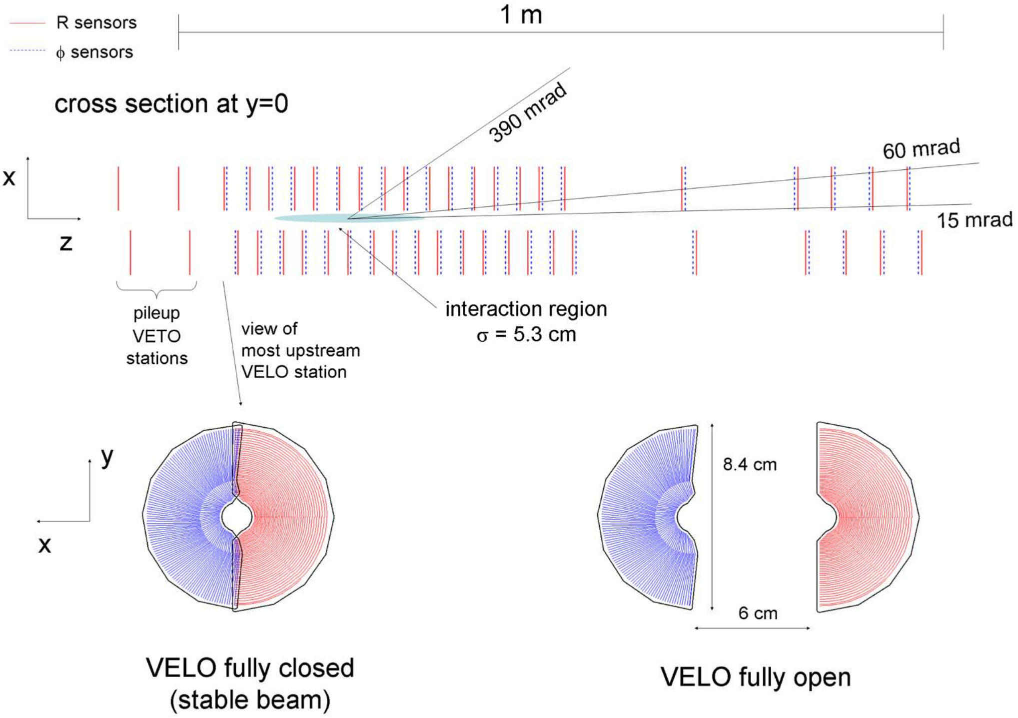

Figure 2.8: Top: top view of the VELO silicon sensors. Bottom: frontal view of the modules in the closed and open positions.

have to be retractable to avoid the danger of being damaged during beam injection. The open position places the two halves about 6 cm away from each other; when the LHC is in pp collision the halves are moved in until the sensors have a distance from the beam of only 8 mm. Each half is composed of two planes of 220 µm thick silicon microstrip sensors able to measure the distance from the beam and the azimuthal angle of hits, namely r and ϕ, generated by the ionizing particles that cross the VELO. The third coordinate z is simply measured knowing what modules give a signal for a particular particle hit. The structure of r-ϕ sensors is reported in Figure 2.9. The r sensors are divided into four parts per half, each one covering about 45°; the microstrips composing these parts are modelled in a semi-circular shape. The pitch for the strips closest to the beam is 40 µm, which increases linearly to 101.6 µm for the outermost strip. This design makes sure that strips closer to the interaction point get a larger weight for the impact parameter determination. The ϕ sensors are divided into two regions: the inner stops at a radius of 17.25 mm and has a pitch of 78.3 µm, the outer one starts at 17.25 mm and has a pitch of 39.3 µm. Inner and outer regions have different skew to the radial direction to improve pattern recognition: they are tilted by 20° and 10° respectively. Furthermore, to improve the track reconstruction, the longitudinally adjacent ϕ sensors have opposite skew to each other. The modules are installed in an aluminium walled box which is under vacuum.

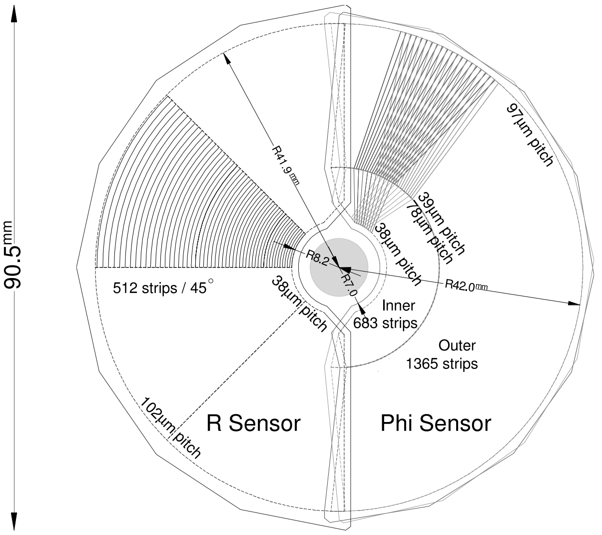

Figure 2.9: Geometry of the r (left) and ϕ (right) sensors of the silicon modules composing the VELO. For completeness in the right part strips of two adjacent ϕ modules are drawn to show their different orientation.

The performance of the VELO detector have been analysed using the data collected. The resolution in the X and Y coordinates ranges from 40 µm to 10 µm depending on the number of tracks fitted while the resolution on the Z coordinate ranges from 250 µm to 50 µm and the trend is shown in Figure 2.10.

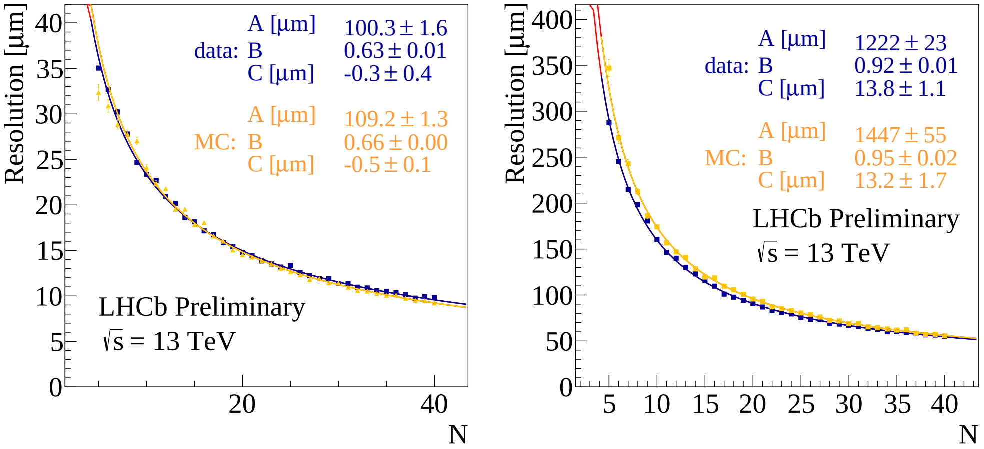

(a) (b)

Figure 2.10: Primary Vertex Resolution for X (a) and Z (b) axis in 2015 data/MC as a function of number of tracks associated to PV (N). The fitter function is described by $A/N^B + C$, where A, B and C are free parameters. The resolution along the Y axis is comparable to the resolution for the X axis.

2.4.2 The Tracker Turicensis

The Tracker Turicensis (TT) [120, 121] is located between RICH1 and the magnet. It is mainly used to improve momentum resolution for particle traversing the whole detector. It provides reference segments used to combine the tracks reconstructed in the tracking stations with those reconstructed in the VELO, and reconstructs flight paths of particles decaying after the VELO. It also improves the rejection of ghost tracks, which are tracks that do not belong to a real particle. An illustration of the setup is shown in Figure 2.11. It consists of four planes of silicon microstrip sensors with a pitch of 183 µm, strip length up to 37 cm and thickness of 500 µm. Each of the four planes covers a rectangular region of about 120 cm in height and about 150 cm in width. They are arranged in half modules, consisting of seven silicon sensors which are read out in sectors, containing four and three sensors (away from the beam pipe) or four, two and one sensors (close to the beam pipe). The different length of these read out sectors is due to the different flux of particles traversing the detector. The readout electronics are placed at the upper or lower edge of the half modules, lying outside the acceptance of LHCb. Two halves are joined together to span the full height of the TT. While the first and the last layer have sensors with strips running vertically, the second and third layer are tilted with and angle of +5° and -5° with respect to the vertical axis. The layers are divided into two stations: the first two planes and the last two planes, called TTa and TTb respectively. The two stations are separated by about 27 cm, while the layers inside TTa or TTb are divided by 36 mm. TTa has 30 half modules while TTb has 34, to cover the larger area spanned by the same solid angle at a larger value of z. The hit resolution is about 50 µm.

2.4.3 The tracking stations T1, T2 and T3

The three tracking stations T1, T2 and T3 are placed downstream of the magnet. They are divided in two main parts: the Inner Tracker (IT) [122] and Outer Tracker (OT) [123].

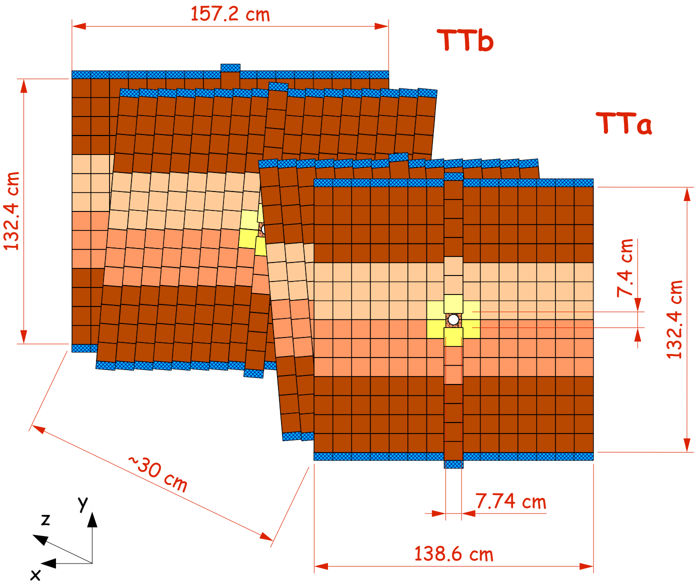

Figure 2.11: TT illustration. The first and the fourth stations have sensors parallel to the vertical plane, while the second and the third stations (called u-plane and v-plane) have sensors tilted respectively by +5° and -5°. The different colours correspond to different readout sectors, the blue region is the position of the readout electronics.

They are arranged as in Figure 2.12.

The IT forms the inner part closest to the beam pipe. As the particle flux is higher in these regions, silicon sensors were chosen as detecting devices. Each of the three stations comprise four detector boxes which are arranged around the beam pipe as in Figure 2.13. Each boxes houses four detector layers and each layer has a total number of seven modules. The first and last layer within a box run vertically, while the second and the third layer are tilted by +5° and -5°. The modules to the left and right of the beam pipe consist of two sensors, while the ones on top and bottom have only one sensor. The silicon sensors have a thickness of 320 μm for the one-sensor modules, 410 μm for the two-sensor modules. The strip pitch is 198 μm, which leads to a similar resolution as obtained in the TT. The total IT size is about 1.2 m in the bending plane and about 40 cm in the vertical plane.

The OT is built as an array of straw tube modules. The modules are arranged in three stations with four layers each, with the middle two layers in a station tilted by $\pm 5°$. Each plane is composed of two rows of tubes, arranged in a honeycomb structure, as shown in Figure 2.14. The module of each drift tube is filled with a gas mixture of $Ar/CF_4/CO_2$, which allows for a short drift time. The knowledge of the relation between the distance of closest approach of the particle to the anode and the drift time, which is the experimentally measured quantity, allows for a spatial resolution of about 200 μm for a single cell with a hit efficiency of more than 99%.

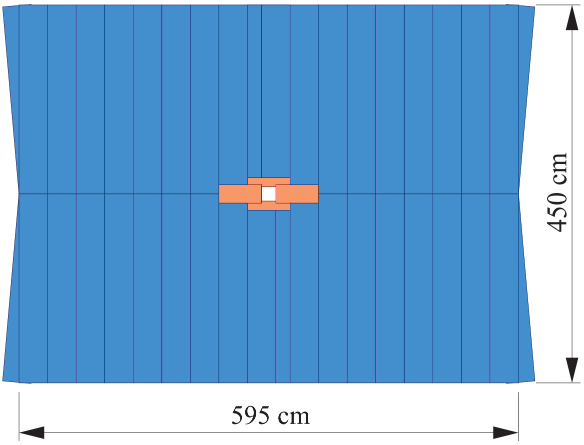

Figure 2.12: Sketch of one of the T stations with the OT in blue and the IT in orange.

2.4.4 The dipole magnet

The LHCb detector is provided with a warm (*i.e.* non superconducting) dipole magnet [124, 125, 126] with two aluminium coils inside an iron yoke placed between the TT and T stations. Its shape and field strength are illustrated in Figure 2.15. The magnet has an integrated field of $\int \vec{B}d\vec{l} = 4\,\mathrm{T\,m}$, where the main field component is along y axis with a maximum intensity of 1 T. Note that there is practically no field at the position of the VELO, while there is only a small field at the position of the TT and the T stations. The magnetic field polarity can be reversed, a procedure which is regularly undertaken during operation of the detector to minimize systematic effects.

In order to track the particles through the LHCb detector, a precise knowledge of the magnetic field map is crucial. The magnetic field was measured with Hall probes with a relative resolutions, whose results could then be compared to magnetic field simulations. The relative resolution on the magnetic field measurements was 3×10^{-4}. More information on this can be found in Reference [127].

2.4.5 Tracking algorithm and performances

We will now describe briefly how the tracking algorithm reconstructs the various track types, divided in five categories, as shown in Figure 2.16:

Long tracks
Particles generating hits in all tracking sub detectors.

VELO tracks
Particles generating hits only inside the VELO because they have been produced with a wide angle with respect to the beam pipe, escaping the geometrical acceptance of the detector before traversing the TT.

Upstream tracks
Particles with a very low momentum that are swept out by the magnetic field from the detector acceptance before they can reach T1. It is possible to measure the momentum of these particles thanks to the residual magnetic field present between

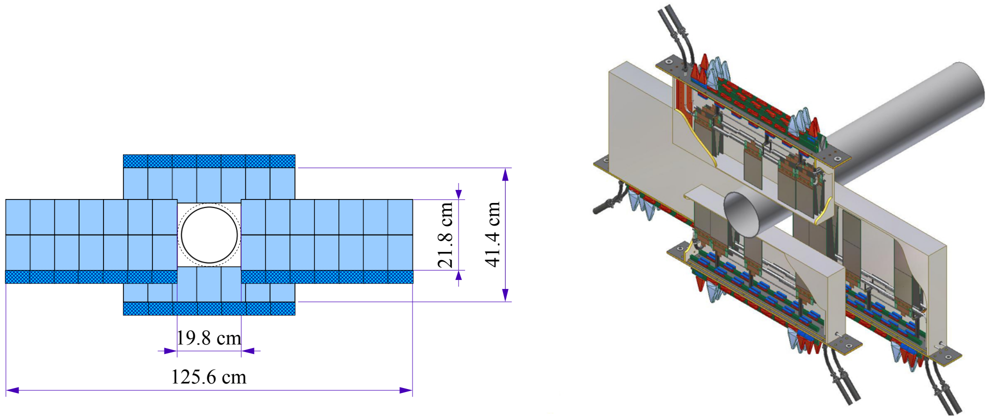

(a) (b)

Figure 2.13: Sketch of a layer in IT (a) with the light blue being the silicon sensors and the dark blue being the position of the readout electronics, the four boxes of an IT station (b) with its four layers of modules.

the VELO and the TT, even if the measurement is affected by a 20 % relative uncertainty.

Downstream tracks

Long lived neutral particles (*e.g.* K_S^0 or Λ) can decay between the VELO and the TT, producing charged particles that generate hits in the TT and in the three tracking stations.

T tracks

Track segments with hits in the tracking stations only are classified as T tracks.

Track finding and reconstruction algorithms are organized in different steps. The first starts with definition of segments in the various subdetectors. Inside the VELO, the segments are created matching all hits that lie on a straight line. In the tracking stations, a segment is created matching the hits contained in a section of the first and third stations, using the information given only by planes of vertically orientated microstrip sensors. Then, under the hypothesis of a parabolic trajectory, the algorithm calculates the position of the hit in the middle stations and searches for compatible hits. If a signal is found, it is added to the segment and it is used to better determine the parameters of the trajectory. Finally, the compatible hits coming from the tilted layers are also added, in order to have a 3-dimensional segment.

The reconstruction process is organized in a hierarchical way: the algorithm tries firstly to reconstruct long tracks and then it picks up unused segments to reconstruct downstream and upstream tracks. Long tracks are reconstructed with two algorithms used concurrently: the first extrapolates VELO segments to the tracking stations, adding to the track the compatible hits in the TT, the second matches VELO and tracking stations segments one to each other, extrapolating VELO segments in the forward direction and tracking stations segments in the backward direction. Downstream tracks are reconstructed starting from the T stations segments and then adding the compatible hits in the TT to those segments. Upstream tracks are obtained extrapolating VELO segments to the

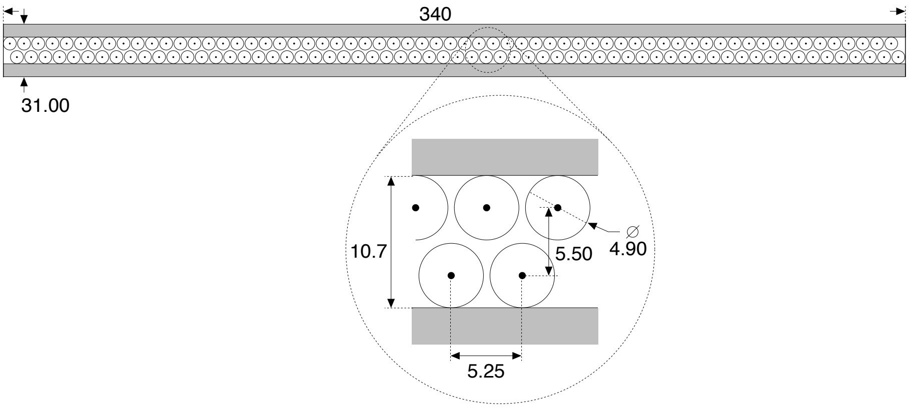

Figure 2.14: Cross section of a straw tube plane. The zoomed part shows the honeycomb structure of the two rows of tubes.

TT, adding compatible hits and requiring a non compatibility with any of the tracking station segments. Finally a clone killer compares the reconstructed tracks, two by two: if a pair of tracks shares more than a fixed percentage of hits, they are considered clones and the only one with the best χ^2 is stored.

2.5 The LHCb particle identification system

Most of the *CP* violation measurements of the LHCb physics program, and in particular those presented in this thesis, require the identification of charged particles. This task is accomplished by some dedicated sub detectors.

2.5.1 The Ring Imaging Cherenkov detectors

LHCb uses two Ring Imaging Cherenkov Detectors (RICH) [128] for particle identification. The structure of the two apparatus is shown in Figure 2.17. The working principle is based on the Cherenkov effect, namely particles traversing a medium with velocity v faster than the speed of light in this medium ($\frac{c}{n}$) will emit photons at an angle

$$\cos\theta_c = \frac{1}{n\beta}, \tag{2.1}$$

where n is the refraction index of the material and $\beta = \frac{v}{c}$. Knowing the refractive index of the material being traversed, this angle can be directly related to the speed of the particle. With the knowledge of the particle's momentum from the tracking system, then the mass and therefore the particle type can be determined.

The first Cherenkov detector, RICH1, is situated between the VELO and the TT and covers the full LHCb acceptance. It uses two kinds of radiators: the first is a $5\,\mathrm{cm}$ thick Aerogel layer with a $n = 1.03$ to provide separation for particles with a momentum of a few GeV/c; the second is a gaseous C_4F_{10} layer with $n = 1.0015$ which fills the remaining part of the detector and is employed to detect particles with higher momenta (up to $50\,\mathrm{GeV}/c$). The Cherenkov light is reflected via a spherical and a plane mirror into an array of Pixel Hybrid Photon Detectors (HPDs) at the top and bottom of the

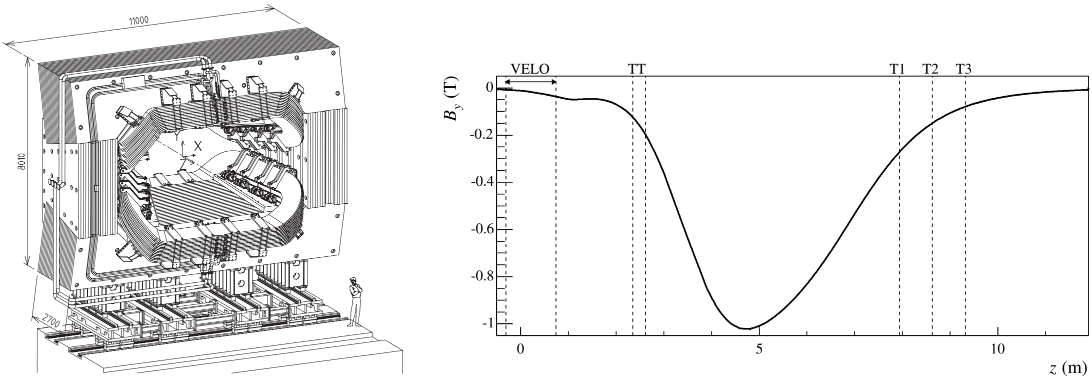

(a)

(b)

Figure 2.15: Technical drawing of the dipole magnet in LHCb (a) and strength of the y direction of the magnet field as a function of the z position (b).

RICH1 (outside the acceptance). These sensors provide a photon position measurement allowing the reconstruction of the "rings" created by the Cherenkov light. The radius of these rings is proportional to the Cherenkov angle. The photon detectors are sensitive to stray magnetic fields, hence they have to be embedded into a magnetic shield structure.

The second Cherenkov detector, RICH2 is located between T stations and the first muon station. It has a reduced angular acceptance from $15\,\mathrm{mrad}$ to $120\ (100)\,\mathrm{mrad}$ in the bending (non bending) plane. It uses CF_4 as a radiator, with $n = 1.0005$ and it is used for particle identification for high-momentum particles from about $15\,\mathrm{GeV}/c$ up to $100\,\mathrm{GeV}/c$. RICH2 has the HPDs and mirrors situated to the left and right of the beam pipe, incorporating a magnetic shield structure similar to the one in RICH1.

The Cherenkov angles for the three different radiators used in RICH1 and RICH2 are shown in Figure 2.18.

2.5.2 The calorimetry system

The calorimetry system [129] serves multiple purposes. On the one hand it is used to reconstruct photons and particularly π^0 with good precision, on the other hand it is part of the particle identification system providing information about the energy and position of photons, electrons and hadrons. Furthermore it is part of the hardware trigger, for fast decisions after the interaction.

The calorimetry system consist of three parts as represented in Figure 2.19: a scintillating pad/preshower detector (SPD/PS), an electromagnetic calorimeter (ECAL) and an hadronic calorimeter (HCAL). The SPD/PS and the ECAL follow the same substructure by dividing the active region in three parts, with a more coarse granulation away from the beam pipe. The HCAL is divided into two subparts. The segmentations are illustrated in Figure 2.20.

The SPD/PS consist of a $15\,\mathrm{mm}$ thick lead absorber, which is sandwiched by plates of scintillating pads. The pads are read out via wavelength shifting fibres guiding the light to photomultipliers. The SPD is used to discriminate between charged and neutral particle improving discrimination between photons and electrons, as the former ones produce light inside the scintillator layers while the latter do not. The lead absorber is

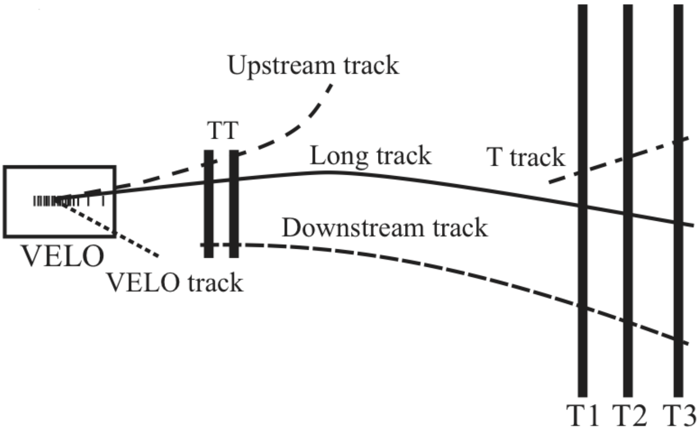

Figure 2.16: Illustration of the various track types.

used to start the showering, which can then be detected in the PS. It provides informations to improve the discrimination between pions and electrons, as they have different shower lengths. The SPD and PS pads have dimension of approximately $4 \times 4\,\mathrm{cm}^2$, $6 \times 6\,\mathrm{cm}^2$, $12 \times 12\,\mathrm{cm}^2$, depending on the region. The total material budget of the two sub detectors corresponds to about 2.5-3 X_0 (radiation length).

The structure of the ECAL is an alternating planes with absorbing layers made of lead (2 mm thick) and detecting layers made of scintillating material (4 mm thick, polystyrene). In total, there are 66 Pb and scintillating layers that form a stack of 42 cm length, which corresponds to 25 X_0. The read out of the scintillating tiles is similar to the one in the SPD/PS. The outer acceptance boundary of the ECAL matches the one from the tracking stations (300/250 mrad), the inner acceptance boundary (25 mrad) is limited by the radiation dose level close to the beam pipe.

The HCAL main task is to measure the energy of hadronic showers. This information is fundamental for the Level-0 trigger. The HCAL is built as a sampling device as well, made of layers of scintillators 4 mm thick separated by layers of iron 16 mm thick. The total material budget corresponds to 5.6 nuclear interaction lengths. Module sizes are bigger than for ECAL: $13 \times 13\,\mathrm{cm}^2$ for the inner ones and $26 \times 26\,\mathrm{cm}^2$ for the outer ones.

The calorimeter system performances have been evaluated from several test beams made before the start of the data taking [130]. Energy resolution are given by $\sigma(E)/E =$ 8-10$\%/\sqrt{E/\,\mathrm{GeV}} \oplus 0.9\%$ for ECAL and $\sigma(E)/E = 69\%/\sqrt{E/\,\mathrm{GeV}} \oplus 9\%$ for HCAL, where the two first terms are the resolution due to statistical fluctuations and the second terms are due to the read out. The ECAL calibration is obtained by reconstructing resonances decaying to two photons like $\pi^0 \to \gamma\gamma$ and $\eta \to \gamma\gamma$. Calibration of the HCAL can be realized by measuring the ratio E/p between the energy E as measured in the calorimeter for a hadron with momentum p, as measured by the tracking system.

2.5.3 Muon detectors

The muon system [131, 132, 133] consists of five stations: the first one (M1) is placed upstream of the calorimeters to avoid possible muon multiple scattering effects that could modify the particle trajectory, the other four stations (M2 to M5) are situated after the HCAL, and separated from each other with layers of 80 cm of iron, which serves as an

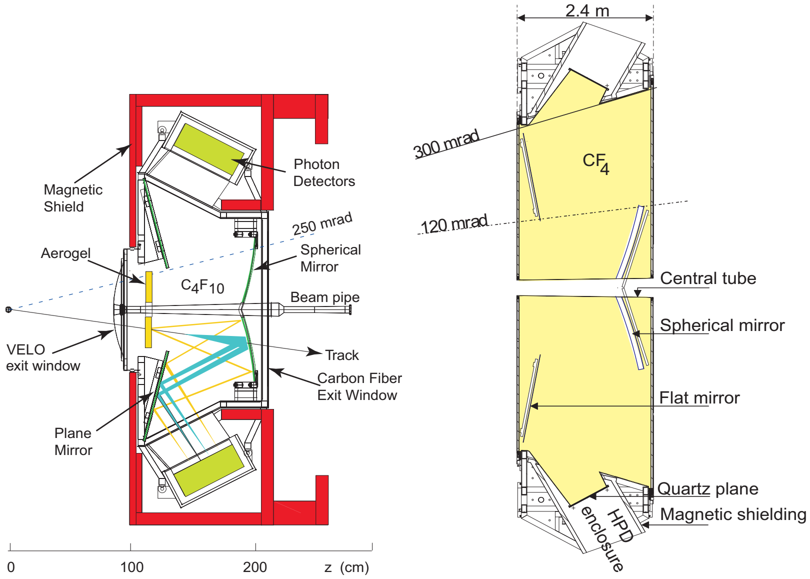

Figure 2.17: Left: schematic layout from a side view of the RICH1 detector. Right: schematic layout from a top view of the RICH2 detector.

absorber for all particles not being muons or neutrinos (see Figure 2.21). A muon needs to have a momentum of about 6 GeV/c to reach all muon stations. Similar to the calorimeters, the muon system uses different segmentations to cope with the varying particle flux over the full area: all stations are therefore divided into four regions (R1 to R4) with increasing distance from the beam pipe. The linear dimensions and their segmentation scale with factors of two from one region to another, as shown in Figure 2.22. The muon system covers an acceptance between 20 (16) mrad and 306 (258) mrad in the bending (non-bending) plane. It uses multi-wire proportional chambers (MWPC) for all stations, except in the innermost region of M1, where triple-GEM detectors are used due to the high particle flux and its demand for radiation hardness. MWPCs have four overlapped gaps, each one 5 mm thick and with a distance between wires of about 2 mm. In M1, the MWPCs only have two gaps to reduce the amount of material in front of the calorimeters. The triple-GEM detector consists of three gas electron multiplier foils sandwiched between anode and cathode planes.

2.6 The LHCb trigger

The production cross sections of $b\bar{b}$ and $c\bar{c}$ pairs are small compared with the inelastic pp cross section reported in Table 2.2. In addition, the capabilities to store data are limited by technological and cost constraints. A good trigger is necessary to accept the interesting events and reject most of the background events. The LHCb trigger [136] has been developed to work at the bunch crossing frequency of the LHC, in order to process the largest number of events. The only way to reach the desired performances is to divide the trigger into different levels, each processing the output of the previous.

The trigger system consists of two parts: L0, the first stage of the trigger implemented on hardware level, and the HLT, a two stage software trigger executed on event filter

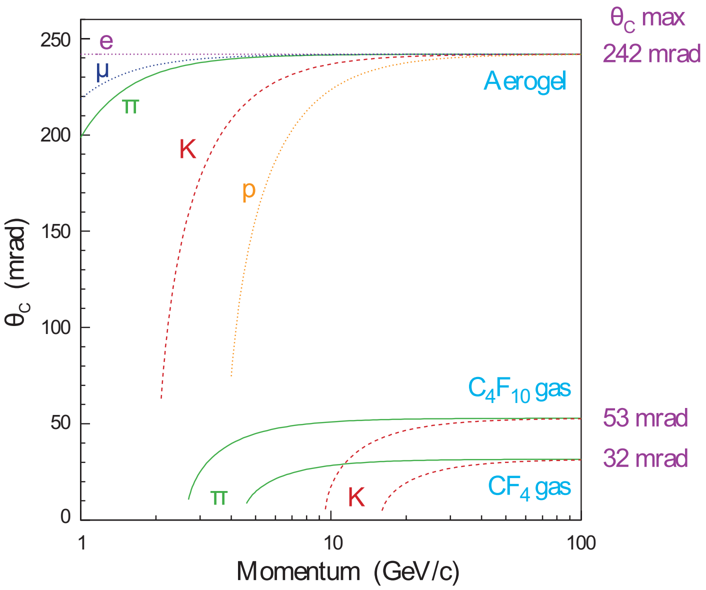

Figure 2.18: Cherenkov angle for the different radiators in different momentum regimes.

Table 2.2: Measured cross section at $\sqrt{s}$ = 7 TeV in the LHCb acceptance. Values taken from Reference [113, 134, 135]

Process	Value
pp inelastic	$55.0 \pm 2.4\,\text{mb}$
$pp \to c\bar{c}X$	$1.23 \pm 0.19\,\text{mb}$
$pp \to b\bar{b}X$	$75.3 \pm 14.0\,\mu\text{b}$

farms, to confirm the L0 decisions and to perform a (partial) event reconstruction for further data reduction.

2.6.1 Level-0 trigger

The Level-0 trigger (L0) is run synchronously with the LHC clock and reduces the rate of pp collisions to about 1.1 MHz, which is the maximum rate at which the full detector can be read out. The calorimeters (SPD,PS, ECAL, HCAL) are used to select particles with high transverse energy $E_T = E \cdot \sin\theta$ (photons, electrons, hadrons) and assign a particle hypothesis to them. The candidate with the highest E_T for every species is selected and triggers the event if the E_T is above a given threshold. Furthermore the SPD is used to provide an estimate for the charged particle multiplicity in the event. A cut on the SPD-multiplicity was set to reject too busy events which would take too much time to process and have a too high occupancy in the OT. The muon system performs a standalone reconstruction of muon tracks by forming straight tracks out of hits in all five stations, and calculates their transverse momentum under the assumption that the muon are originated at the interaction point. There is a single muon trigger and a dimuon trigger which have different thresholds for p_T and $\sum p_T$ respectively.

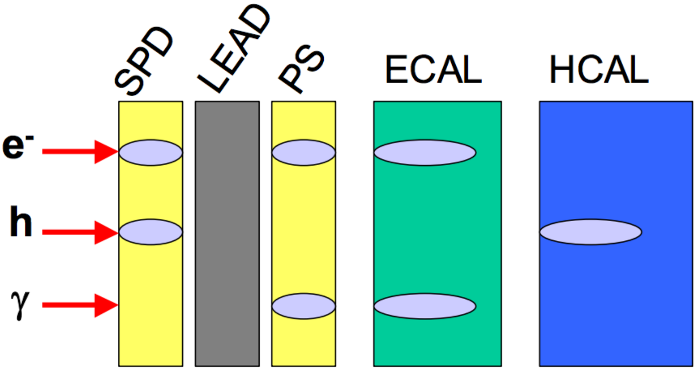

Figure 2.19: Signal deposited on the different parts of the calorimeter by an electron (e), a hadrons (h) and a photon (γ).

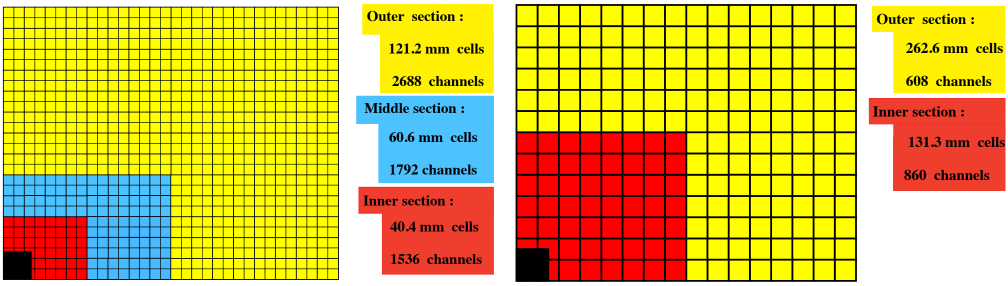

Figure 2.20: Layout of the SPD/PS/ECAL (left), showing the three segmentations, and layout of the HCAL (right) with only two segmentations. Note that only a quarter of the detectors is shown and the black region represents the beam pipe.

The efficiency of L0 strongly depends on the decay channel:

- for B decays to two muons, the L0 muon requirements are typically more than 90% efficient;
- the efficiency of the L0 hadron trigger for fully hadronic decay modes varies from $\sim 60\%$ for $B^0 \to h^+h^-$ decays to 20-30% for charm decays. Charm decays typically have lower efficiencies due to the lower mass of the charmed hadrons compared to a B hadron;
- the L0 photon/electron requirements are more than 80% efficient for radiative B decays, such as $B^0 \to K^{*0}\gamma$.

The L0 hadron and muon efficiencies are shown in Figure 2.23.

2.6.2 The high level trigger

The High Level Trigger (HLT) is subdivided in two software based stages, namely HLT1 and HLT2. The task of this trigger level is to reduce the input rate from the L0 trigger to a more manageable level of 3.5, 5 and 12.5 kHz for 2011, 2012 and Run 2 data taking periods, respectively. VELO reconstruction is fast enough to allow the full information on

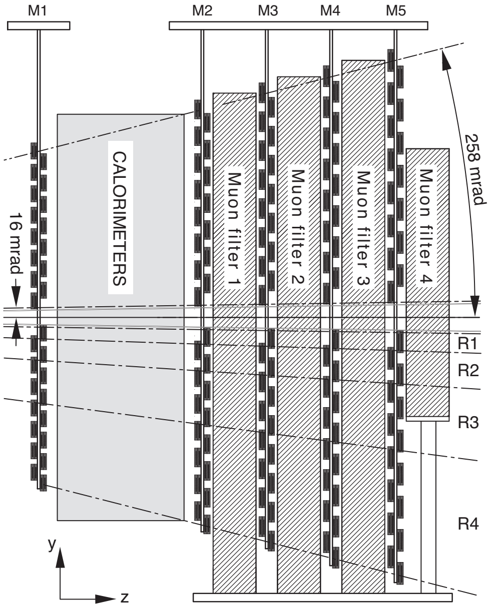

Figure 2.21: Side view of the five chambers of the muon system with the interleaved calorimeters and iron absorbers.

the primary vertex to be used by the HLT1 but the full reconstruction can be performed only for a limited number of tracks due to limited time available. This is the reason why the HLT has been divided in two sub-triggers.

HLT1 rejects events with an OT occupancy larger than 20% because it would take more than $\sim 25\,\mathrm{ms}$ to take a decision. After this first rough selection, it partially reconstructs the event around the object that triggered L0, while using information from different subdetectors. This task is for example accomplished by muon triggers which combine the information from the VELO with the one from the muon stations. Other triggers exists to confirm information from calorimeters. Additionally, a different type of HLT1 triggers exists, which does not rely on information from the L0 and are based on single track with high momentum, large impact parameter and good track quality. In total HLT1 has an output rate of approximately $50\,\mathrm{kHz}$. Figure 2.24 shows the efficiency of the HLT1 selection criteria as a function of p_T for both decays containing muons in the final state and purely hadronic decays.

The output rate of HLT1 is low enough to allow HLT2 to perform a reconstruction of the event which is was very close in Run 1 and has the same quality in Run 2 to the offline reconstruction. A great variety of trigger lines exist in HLT2, ranging from lines selecting prompt and detached muons to "topological lines" selecting n-body decays starting from two charged daughter tracks. The output rate of HLT2 was up to $3\,\mathrm{kHz}$.

The HLT2 efficiency for B decays with muons in the final state is above 90%, while for heavy flavour decays with hadrons in the final state is over 60%.

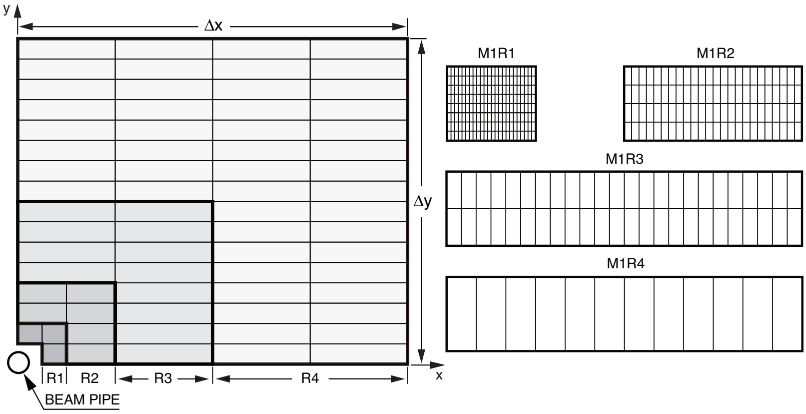

Figure 2.22: Front view of a quadrant of a muon station. Each rectangle represents one chamber.

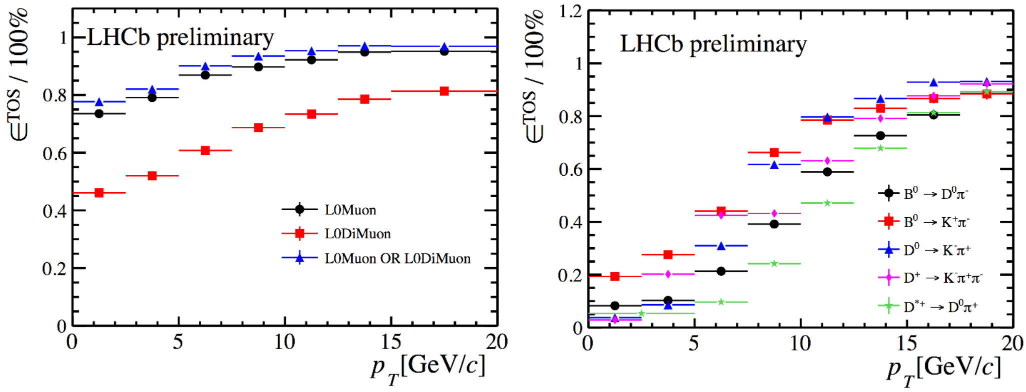

Figure 2.23: L0 efficiencies for data taken during 2012 of L0 muon requirements for $B^{\pm} \to J/\psi(\to \mu^+\mu^-)K^{\pm}$ (left) and L0 hadron requirements for several fully hadronic decay modes as a function of the parent p_T (right).

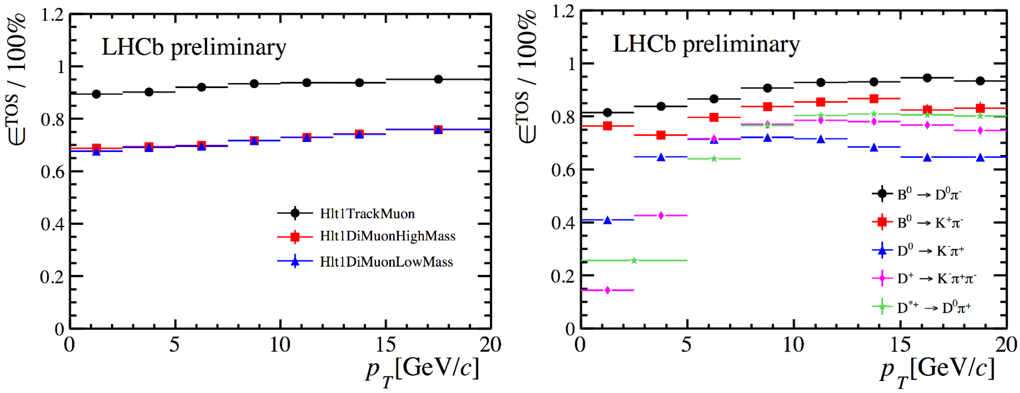

Figure 2.24: HLT1 efficiencies for data taken during 2012 for the HLT1 muon lines for $B^{\pm} \rightarrow J/\psi(\rightarrow \mu^+\mu^-)K^{\pm}$ (left) and the HLT1 lines selecting displaced tracks for several purely hadronic decays (right).

Part I

Measurement of CP violation in the angular distribution of $\Lambda_b^0 \to p\pi^-\pi^+\pi^-$ baryonic decay

CHAPTER 3

Selection

Using data from the LHCb experiment at the LHC, we made a search for CP-violating asymmetries in the decay angle distributions of Λ_b^0 baryons decaying to $p\pi^-\pi^+\pi^-$ final state. This analysis uses Run 1 and Run 2 data, corresponding to about 3.0 fb^{-1} and 3.7 fb^{-1} respectively, collected at centre-of-mass-energies of 7, 8 and 13 TeV in the 2011-2012 and 2015-2017 years. We update and extend the analysis of such decays that found first evidence for CPV in baryon decays in Run 1 data [38]. The sensitivity to CPV is improved according to an amplitude model that has been developed using the new data. Triple product asymmetries are evaluated and used to search for P-odd CPV effects.

Monte Carlo (MC) samples have been produced and used to study possible sources of background and characterize signal events.

The MC samples are divided into event types as reported in Table 3.1 and processed with identical selection requirements applied to data.

Table 3.1: MC samples and number of generated events. Events are produced with up/down magnet polarity in equal quantity.

Decay Mode	Yields (2011, 2012, Run 2)
$\Lambda_b^0 \to pK^-\pi^+\pi^-$	1046073, 2017682, 4137806
$\Lambda_b^0 \to p\pi^-\pi^+\pi^-$	1033876, 2025489, 4264938
$B^0 \to K^+\pi^-\pi^+\pi^-$	2048997, 4021486, 4605692

3.1 Trigger requirements

The events are required to pass through selected trigger lines, that ensure minimal bias from the trigger, see Table 3.2.

The `L0Hadron` trigger, used in both Run 1/2 data taking, selects events with the number of hits in the SPD less than 600 and with at least one cluster in the HCAL with transverse energy greater then $3.5\,\text{GeV}$. The `L0Global` trigger, used in both Run 1/2 data taking, is a logical OR of all L0 physics lines.

The `Hlt1TrackAllL0` trigger algorithm [137], used during Run 1 data taking, is divided into three steps. In the first step it applies cuts on global event variables in order to reduce the time used for the online reconstruction of the events. The requirements are: the number of hits in the OT (OTHits) less than 15000, the number of hits in the IT (ITHits) less than 3000 and the number of hits in the VELO (VeloHits) less than 10000. In the second step the algorithm performs the reconstruction of the primary vertices [138] and of the Velo Tracks using the following requirements:

Table 3.2: Trigger lines used in the analysis. We require each of the trigger level requirements and at least one of the trigger lines per each level to be flagged. The TOS (Trigger On Signal) indicates if the candidates fired the trigger, while TIS (Trigger Independent of Signal) if something else of the candidates fired the trigger.

Trigger Level	Trigger line	
	Run 1	Run 2
L0	Hadron TOS Global TIS	Hadron TOS Global TIS
HLT1	TrackALLL0 TOS	TrackOneTrackMVA TOS TrackTwoTrackMVA TOS
HLT2	Topo(2,3,4)Simple TOS Topo(2,3,4)BBDT TOS	Topo(2,3,4)Body TOS

- a difference between the expected and observed Velo hits less than 2;
- a number of hits in the Velo greater than 10;
- the minimum impact parameter with respect to all primary vertices of $100\,\mu\mathrm{m}$.

The Velo Tracks are then fully reconstructed using the entire LHCb tracking system. These tracks are selected requiring:

- a number of total hits in the tracking system greater than 17;
- a transverse momentum greater than $1.7\,\mathrm{GeV}/c$;
- a momentum greater than $10\,\mathrm{GeV}/c$.

The selected tracks are then fitted using a BiDirectional Kalman filter [139] and are required to have a χ^2 of the fit less than 2.5 and a χ^2 of the minimum impact parameter with respect to all the primary vertices greater than 16. The trigger algorithm selects events with at least one track satisfying the selection criteria described above.

The `Hlt2TopoSimple(BBDT)` trigger [137], used during Run 1 data taking, exploits the topological structure of B decays in a cut-based method using a multi-variate classifier. The principle of the topological triggers revolves around a corrected mass, which is used to trigger B decays using a subset of the final state particles. The corrected mass is defined as:

$$m_{corrected} = \sqrt{m^2 + |p'_{T\ missing}|^2} + |p'_{T\ missing}| \tag{3.1}$$

where $p'_{T\ missing}$ is the missing momentum transverse to the direction of flight of the B meson candidate calculated as the direction from the PV to the B candidate partially reconstructed vertex, and m is the invariant mass of the subset of the reconstructed particles in the final state of the B candidate. The cut-based topological triggers require that $m_{corrected}$ lies in the range $4 < m_{corrected} < 7\,\mathrm{GeV}/c^2$. Since this inclusive method is very robust against missing daughters particles, it can apply tight requirements on the selected tracks without penalty of efficiency [137]. These consist of $1.5\,\mathrm{GeV}/c$ on the hardest track p_T and the sum of the daughter p_T values be greater than $4\,\mathrm{GeV}/c$, $4.25\,\mathrm{GeV}/c$, $4.5\,\mathrm{GeV}/c$ for the 2-body, 3-body and 4-body lines, respectively. Also, in order to remove backgrounds from D decays, the $(n-1)$-body objects of the n-body topological trigger are required to have an invariant mass greater than $2.5\,\mathrm{GeV}/c^2$ or an $IP\ \chi^2$ with respect to the primary vertex (the difference in χ^2 when including or excluding the candidate from the primary vertex fit) greater than 16. Due to the relatively small difference between the masses of the final states with respect to the B hadron mass, the kaon mass is assigned to the tracks. The multi-variate classifier topological trigger is trained with a Boosted Decision Tree (BDT) [140] where the input variables are the corrected mass, information on the transverse momentum and $IP\ \chi^2$ of the track candidates and flight distance χ^2 (the significance of the separation between the primary and secondary vertex) of the B candidate.

The `Hlt1TrackOneTrackMVA` trigger [141], used during Run 2 data taking, searches for either one high transverse momentum ($p_T > 500\,\text{MeV}/c$) or high displacement track ($IP\ \chi^2 > 4$). A hyperbolic function in the plane defined by these two variables is used to define the interesting region to select the events. The `Hlt1TrackTwoTrackMVA` trigger [141], used during Run 2 data taking, searches for two tracks that form a displaced vertex. In this case a multivariate algorithm is used to select interesting events. It uses informations on the scalar sum of the transverse momentum of the two tracks, χ^2 of the vertex fit and flight distance χ^2.

The `Hlt2Topo(2,3,4)Body` trigger [141], used during Run 2 data taking, are designed to trigger efficiently on any B decay with at least two charged daughter tracks. It is designed to handle the possible omission of daughter particles, *i.e.* it is an inclusive trigger. It is a reoptimization of the `Hlt2TopoBBDT` trigger used during Run 1.

3.2 Preselection requirements

The preselection for $\Lambda_b^0 \to p\pi^-\pi^+\pi^-$ candidates is outlined in Table 3.3 and it is the same for Run 1 and Run 2 data taking. The decay chain of the Λ_b^0 candidate that satisfy the preselection is then fitted with the contraint that it comes from the primary vertex [142] to increase the resolution on the reconstructed invariant mass. In case multiple primary vertex are reconstructed, the primary vertex with the smallest impact parameter is choosen.

3.3 Resonance vetoes

The following charm resonances, reconstructed in the invariant mass of subsets of the Λ_b^0 daughters, are vetoed by requiring the reconstructed invariant mass to be more than 3σ away from the peaks, where σ is the resolution of the reconstructed invariant mass determined from a fit:

- c-quark long-lived particles Λ_c^+, D^0, D^+, D_s^+, including when the Λ_b^0 candidate is reconstructed under mis-ID hypothesis of K and π, *e.g.* assigning the K (π) mass to the p (K) track candidate;
- c-quark resonances poorly reconstructed (J/ψ) mainly due to the misidentification $\pi \to \mu$.

In order to further reduce cross-feed from B^0 decays, we veto also events with K^{*0} resonance reconstructed with the p candidate having the K mass hypothesis. No light-quark long-lived particles having a flight length $c\tau \approx \mathcal{O}(1\ \text{cm})$, such as Λ and K_s^0, are reconstructed. They are removed applying the cut $\chi^2_{\text{vtx}} < 20$ in the preselection stage. Strongly decaying resonances are part of the signal. The vetoed regions are listed in Table 3.4.

Table 3.3: Preselection criteria

	Description	Cut type
proton	Transverse momentum	$p_{\mathrm{T}} > 250\,\mathrm{MeV}/c$
	χ^2 difference between primary vertex fits when the track is added or excluded from the fit	$\chi^2_{\mathrm{IP}}(PV) > 16$
	χ^2 of the track fit divided by the number of degrees of freedom	$\chi^2_{track}/\mathrm{ndf} < 3$
	Output of a multivariate classifier that identifies ghost tracks, which are tracks that do not belong to real particles [143]	$\mathrm{Ghost.Prob.} < 0.4$
	Output of a multivariate classifier that identifies proton tracks [144, 145]	$\mathrm{ProbNNp} > 0.05$
	Momentum magnitude	$p > 1.5\,\mathrm{GeV}/c$
π		$p_{\mathrm{T}} > 250\,\mathrm{MeV}/c$ $\chi^2_{\mathrm{IP}}(PV) > 16$ $\chi^2/\mathrm{ndf} < 3$ $\mathrm{Ghost.Prob.} < 0.4$ $p > 1.5\,\mathrm{GeV}/c$
Daughters tracks combination (prior the vertex fit)	Invariant mass when the proton mass is assigned to one track and the pion mass to the others	$m(p\pi\pi\pi) < 6.405\,\mathrm{GeV}/c^2$
	Invariant mass when the proton mass is assigned to one track and the kaon mass to the others	$m(pKKK) > 5.195\,\mathrm{GeV}/c^2$
	Sum over the daughters of the transverse momentum	$\sum_{dau} p_{\mathrm{T}} > 3.5\,\mathrm{GeV}/c$
	Transverse momentum of the combination	$p_{\mathrm{T}} > 1.5\,\mathrm{GeV}/c$
	Significance of the distance between each pair of tracks	$\chi^2_{DOCA} < 20$
Λ_b^0	Vertex χ^2	$\chi^2_{\mathrm{vtx}} < 20$
	Significance of the separation between the primary and secondary vertex	$\chi^2_{VD}(PV) > 50$
	Difference between primary vertex fits when the daughters tracks are added or excluded from the fits	$\chi^2_{\mathrm{IP}}(PV) < 16$
	Cosine of the angle between the Λ_b^0 candidate momentum and the direction from the primary to the secondary vertex	$\cos(\mathrm{DIRA}) > 0.9999$

Table 3.4: List of vetoed resonances and the corresponding vetoed mass window. The misidentified particles are red. Fraction of rejected candidates for charm resonances veto is reported.

Resonance	Veto region [GeV/c^2]	Rejection fraction
$\Lambda_c^+ \to p\pi^+\pi^-_{slow}$	2.253-2.307	2.6%
$\Lambda_c^+ \to p\pi^+\pi^-_{fast}$	2.255-2.304	
$D^0 \to \pi^+\pi^-_{slow}$	1.826-1.881	2.6%
$D^0 \to \pi^+\pi^-_{fast}$	1.842-1.873	
$J/\psi \to \mu^+\mu^-$ $(\mu \to \pi^+, \pi^-_{fast})$	3.061-3.129	2.0%
$J/\psi \to \mu^+\mu^-$ $(\mu \to \pi^+, \pi^-_{slow})$	3.054-3.139	
$\Lambda_c^+ \to pK^-\pi^+$ $(K^- \to \pi^-_{fast})$	2.24-2.31	3.2%
$\Lambda_c^+ \to pK^-\pi^+$ $(K^- \to \pi^-_{slow})$	2.24-2.31	
$K^{*0}(892) \to K^+\pi^-_{fast}$ $(K^+ \to p)$	0.84-0.96	-
$K^{*0}(892) \to K^+\pi^-_{slow}$ $(K^+ \to p)$	0.84-0.96	-

3.4 Offline selection

The signal events are further selected using a MultiVariate Analysis (MVA) (based on the TMVA [146] toolkit) and particle identification criteria. A few kinematic variables are used to build the multivariate classifiers. We apply the selection with the multivariate classifiers and then optimize the p, π and K particle identification criteria on a control sample composed of vetoed resonances listed in Table 3.4. The ProbNNh ($h = p, \pi, K$) is the output of a multivariate classifier which uses kinematic variables and information from the PID detectors (RICH, CALO and MUON) to distinguish among particle types [144, 145]. From now on, we define the PID variables as a combination of different ProbNNh response, *i.e.* how much they are likely to be the correct mass hypothesis times not to be the wrong one:

- $\text{PID}_p = \text{ProbNN}p \cdot (1 - \text{ProbNN}K) \cdot (1 - \text{ProbNN}\pi) \cdot (1 - \text{ProbNN}\mu)$,
- $\text{PID}_\pi = \text{ProbNN}\pi \cdot (1 - \text{ProbNN}K) \cdot (1 - \text{ProbNN}p) \cdot (1 - \text{ProbNN}\mu)$,
- $\text{PID}_K = \text{ProbNN}K \cdot (1 - \text{ProbNN}p) \cdot (1 - \text{ProbNN}\pi) \cdot (1 - \text{ProbNN}\mu)$.

The key point is that the full offline selection is optimized on data without relying on Monte Carlo samples.

3.4.1 Boosted decision tree selection

We use the $\Lambda_b^0 \to pK^-\pi^+\pi^-$ signal sample, with higher signal yields but similar kinematics to the $\Lambda_b^0 \to p\pi^-\pi^+\pi^-$ signal sample, to train the classifier. With a random choice we divide the $\Lambda_b^0 \to pK^-\pi^+\pi^-$ signal sample into three statistically independent subsamples with equivalent statistics. We train the classifier on the first subsample, then test the response and choose the cut value of the classifier on the second sample and finally apply the selection to the third sample. This procedure, called k-fold or cross-validation method in the literature [147], is repeated iteratively changing the order of the subsamples and optimizing the classifier without introducing any bias.

We apply a preliminary cut of $\mathrm{PID}_h > 0.2$ on all final state tracks in order to be able to fit the spectra and extract the signal distributions directly from data using the *sPlot* technique [148]. This technique is applied to the fits shown in Figure 3.1 for the $\Lambda_b^0 \to pK^-\pi^+\pi^-$ decay, where also a peak due to $\Xi_b^0 \to pK^-\pi^+\pi^-$ appears, and it is used to extract the signal distributions for the BDT signal training sample. As background training sample for the classifier we use the events in the right sideband of the reconstructed $\Lambda_b^0 \to pK^-\pi^+\pi^-$ invariant mass, defined as $5.85\,\mathrm{GeV}/c^2 < m(pK^-\pi^+\pi^-) < 6.4\,\mathrm{GeV}/c^2$. In this region there are no peaking backgrounds and events are combinatoric background. For the fits described here, we use a simplified model where the Λ_b^0 (Ξ_b^0) signal is described as a sum of two Crystal ball functions, described in Section 4.1, with relative fractions and parameters describing the tails of the mass distribution fixed from Monte Carlo results. The quality of the fits is insured by the pulls because most of them lie within the interval $[-3, 3]$ and we checked they are Gaussian distributed. The combinatorial background is described by an exponential function, and the cross-feed background from $\Lambda_b^0 \to p\pi^-\pi^+\pi^-$ events where a π has been misidentified as a K, is described with a non-parametric distribution [149] from Monte Carlo simulations. An Argus function, described in Section 4.2.1, convoluted with a Gaussian function is used

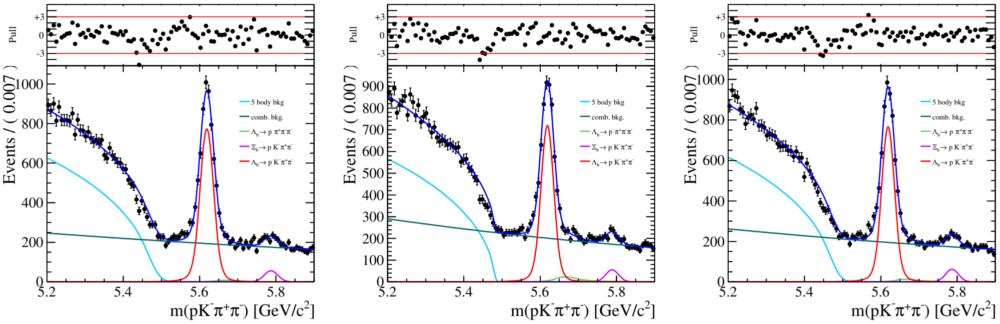

(a) Run 1 data taking

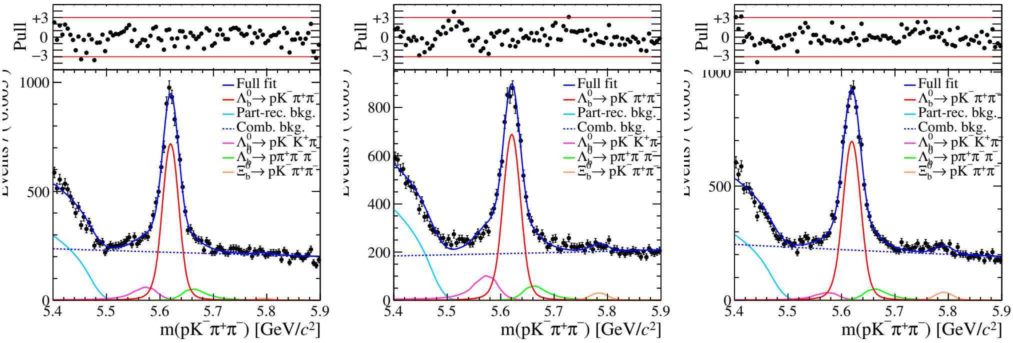

(b) 2016 data taking

Figure 3.1: Fit to the $\Lambda_b^0 \to pK^-\pi^+\pi^-$ control samples divided in three statistically independent samples after the preselection cuts and resonances veto. To perform easily the fit and remove most of the background an additional $\mathrm{PID}_h > 0.2$ cut is applied to all the four daughter tracks. In these fits the background from $B^0_{(s)}$ is removed by vetoing the relative mass windows once the proton candidate track is reconstructed using the kaon or pion mass hypothesis.

to describe the partially reconstructed background at low invariant mass. This background is not well modelled by the shape. Since it lies outside the signal window it does not have any impact on the extraction of the signal distributions. An additional veto is imposed on the $B^0_{(s)}$ masses to remove backgrounds $B^0_{(s)} \to h^+h^+h^-h^-$ where a misidentification $h^+ \to p$ occurred. It is crucial to remove this kind of misidentified events from the background training sample since it could mimic the signal kinematic distributions.

The distributions of the relevant variables for the classifier obtained with the procedure described above are shown in Figures 3.2 and 3.3 for Run 1 and Run 2 data taking periods, respectively, and described in Table 3.5. Since the centre of mass energy of the *pp* collissions changes considerably between Run 1 and Run 2 and some variables used as input clearly depend on the energy, we decided to use two different classifiers for the two different data taking periods. Their relevance in the classifier is shown in Table 3.6.

Table 3.5: Description of the discriminating variables used as input in the BDT.

Particle	Variable	Description
Λ_b^0	Lb_Cone_PTAsym_1	$\frac{p_{T\,\Lambda_b^0}-\sum p_\mathrm{T}}{p_{T\,\Lambda_b^0}+\sum p_\mathrm{T}}$, where $p_{T\,\Lambda_b^0}$ is the Λ_b^0 p_T and $\sum p_\mathrm{T}$ is the sum of all charged long tracks p_T in a cone around the Λ_b^0 candidate with a radius $R = \sqrt{(\Delta\phi)^2 + (\Delta\eta)^2} = 1$ (η = pseudorapidity, ϕ = azimuthal angle)
	Lb_LogIPChi2	$\log(\chi^2_{IP})$, χ^2_{IP} is the χ^2 difference between primary vertex fits when the Λ_b^0 candidate is added or excluded from the fit
	Lb_LogACosDIRA_OWNPV	$\log(\arccos(\mathrm{DIRA}))$, DIRA is the cosine of the direction angle, *i.e.* the angle between the particle momentum and the vector from the primary to the secondary vertex
	DTF_VCHI2NDOF	χ^2_vtx/ndf where is the χ^2 of the vertex fit
p	proton_pt	proton p_T
	proton_pz	proton p_z
$h^-h^+h^-$	Log_hm_IP_OWNPV	$\log(\mathrm{IP_{OWNPV}})$, $\mathrm{IP_{OWNPV}}$ is the impact parameter of the track with respect the primary vertex
	Log_hm2_IP_OWNPV	
	Log_hp_IP_OWNPV	

The ranking of the BDT input variables is derived by counting how often the variables are used to split decision tree nodes, and by weighting each split occurrence by the separation gain-squared it has achieved and by the number of events in the node [150].

Table 3.6: Ranking of the discriminating variables used as input in the BDT.

Variable	Relevance
proton_pt	1.953e-01
Lb_LogACosDIRA_OWNPV	1.813e-01
proton_pz	1.082e-01
Log_hm2_IP_OWNPV	1.054e-01
DTF_VCHI2NDOF	9.470e-02
Log_hp_IP_OWNPV	9.429e-02
Lb_Cone_PTAsym_1	8.401e-02
Log_hm_IP_OWNPV	7.922e-02
Lb_LogIPChi2	5.757e-02

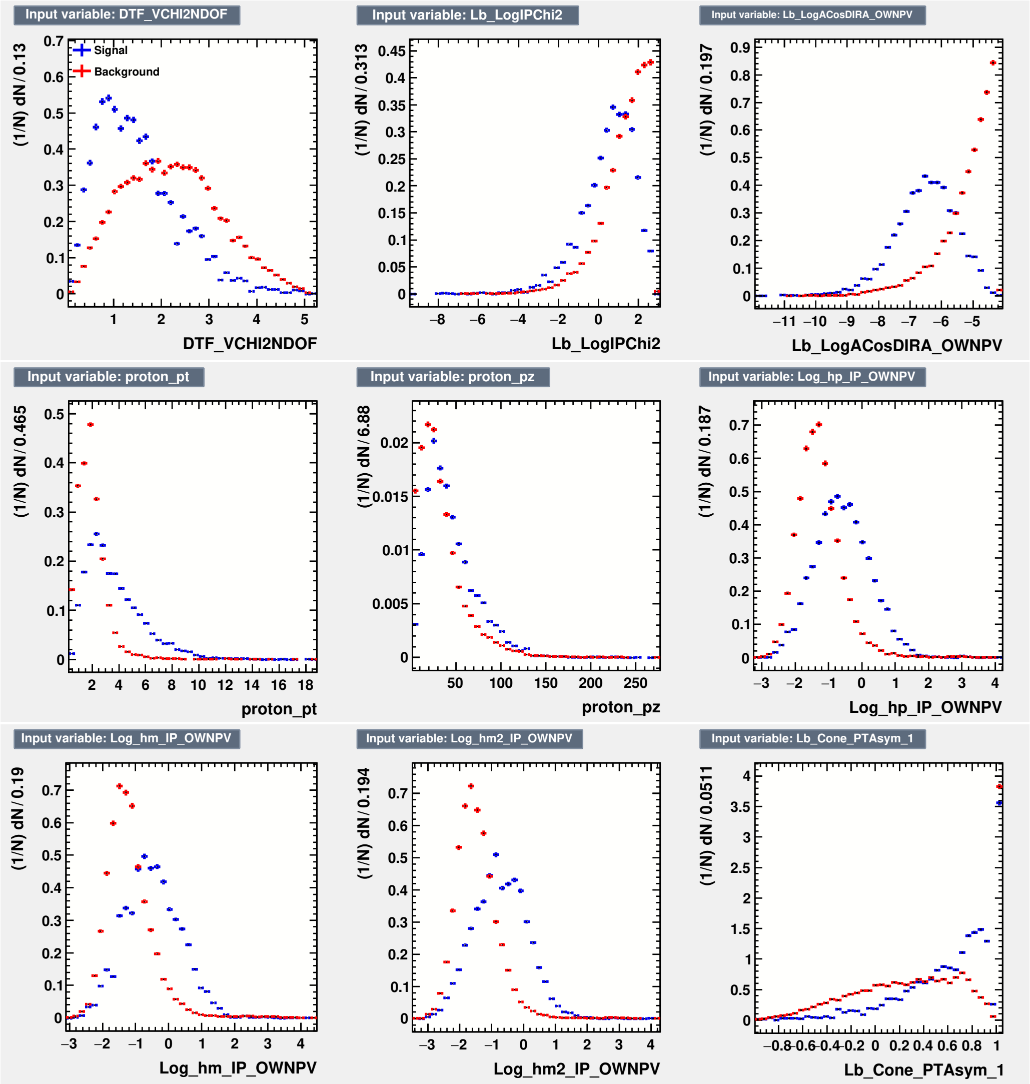

Figure 3.2: Discriminating variables described in Table 3.5 used as input to the BDT for Run 1 data taking period.

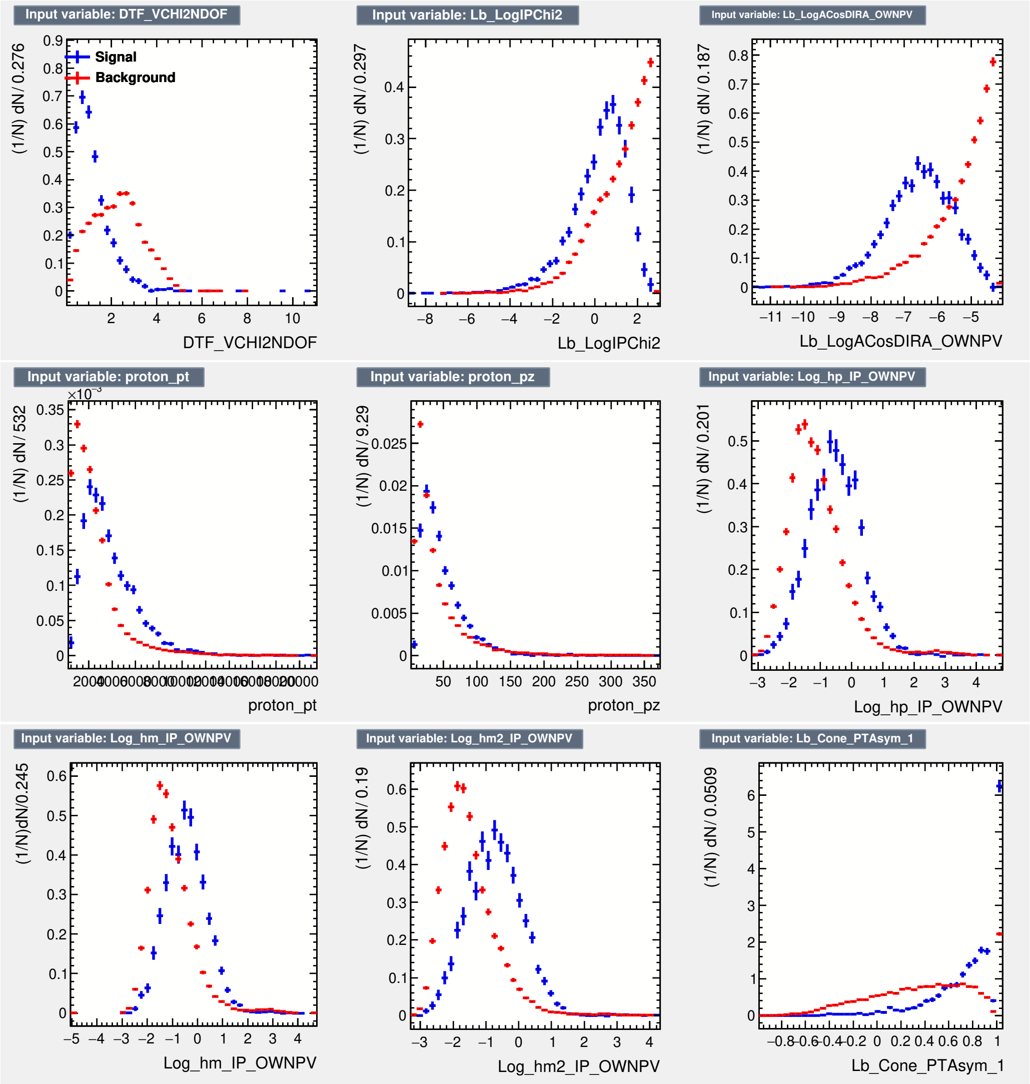

Figure 3.3: Discriminating variables described in Table 3.5 used as input to the BDT for Run 2 data taking period.

Different types of classifiers with various parameter configurations have been tested. The BDT with Adaptive Boost after de-correlation obtained the best performance, as shown in the ROC curve in Figure 3.4 (Left). We obtain a signal efficiency of 80/90% with 90/95% of background rejection. The BDT output on the training and testing samples are shown in Figure 3.4 (Right). No sign of overtraining was found. Correlation matrices of the input variables are shown in Figure 3.5.

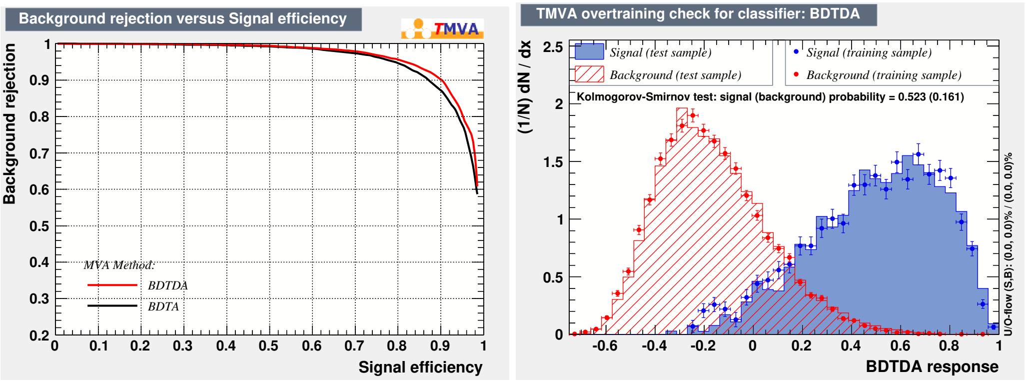

(a) Run 1 data taking

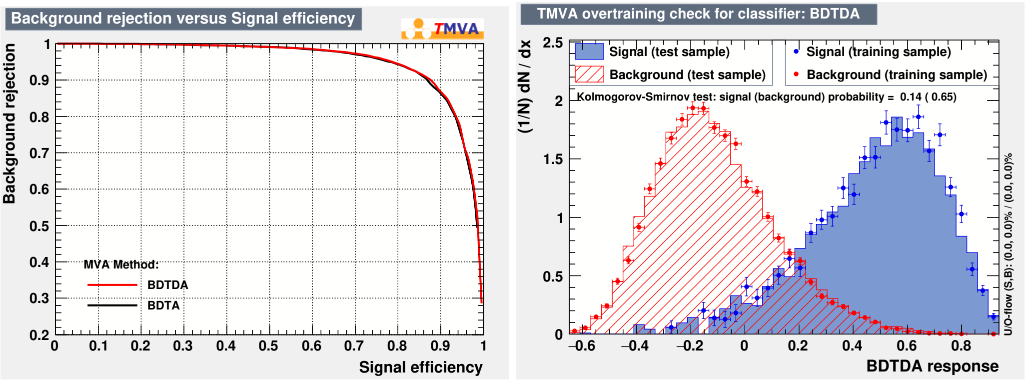

(b) Run 2 data taking

Figure 3.4: (Left) ROC curve for BDTDA (red line) and BDTA (black line) classifiers shows that BDTDA provides best performance in terms of signal efficiency and background rejection. (Right) BDTDA output for signal and background events. The Kolmogorov-Smirnov test does not show evidence of overtraining.

The applied cut on BDT output is chosen by optimising the significance $S/\sqrt{S+B}$. The significance, purity and efficiency dependence on different BDT cuts is shown in Figure 3.6. The signal (background) yield $S = \epsilon_S S_0$ ($B = \epsilon_B B_0$) is estimated using the yield S_0 (B_0) obtained before applying the BDT cut and the BDT efficiency ϵ_S (ϵ_B). S_0 and B_0 are determined from the fit to the invariant mass spectrum on data before applying BDT cuts and are calculated in the signal window [5.5-5.7] GeV/c^2. The data samples are selected with appropriate PID cuts, *e.g.* PID > 0.2, so that a signal peak is evident and a fit can be performed. The optimal cuts were found to be compatible among the 3 independent signal subsamples that we used for the classifier optimization

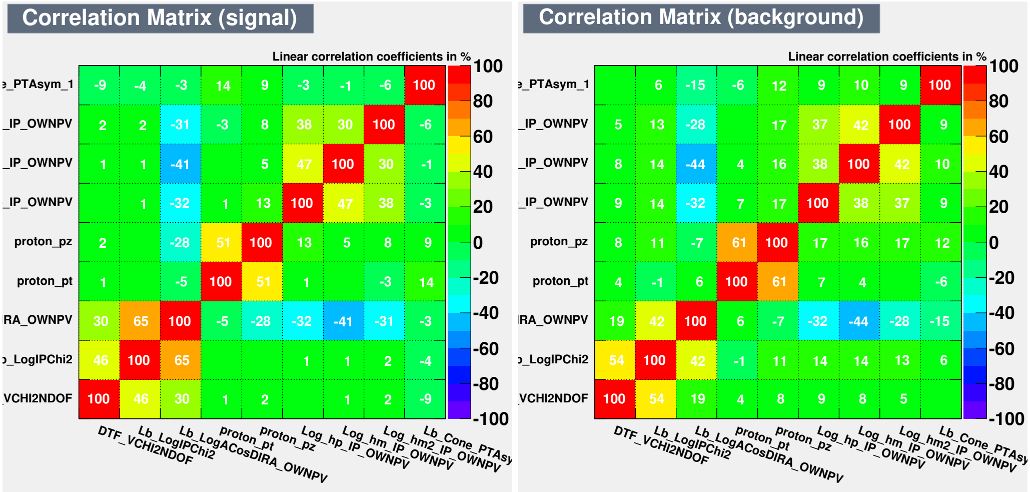

Correlation Matrix (signal)

	DTF_VCHI2NDOF	Lb_LogIPChi2	Lb_LogACosDIRA_OWNPV	proton_pt	proton_pz	Log_hp_IP_OWNPV	Log_hm_IP_OWNPV	Log_hm2_IP_OWNPV	Lb_Cone_PTAsy
e_PTAsym_1	-9	-4	-3	14	9	-3	-1	-6	100
_IP_OWNPV	2	2	-31	-3	8	38	30	100	-6
_IP_OWNPV	1	1	-41		5	47	100	30	-1
_IP_OWNPV		1	-32	1	13	100	47	38	-3
proton_pz	2		-28	51	100	13	5	8	9
proton_pt	1		-5	100	51	1		-3	14
RA_OWNPV	30	65	100	-5	-28	-32	-41	-31	-3
_LogIPChi2	46	100	65			1	1	2	-4
VCHI2NDOF	100	46	30	1	2		1	2	-9

Correlation Matrix (background)

	DTF_VCHI2NDOF	Lb_LogIPChi2	Lb_LogACosDIRA_OWNPV	proton_pt	proton_pz	Log_hp_IP_OWNPV	Log_hm_IP_OWNPV	Log_hm2_IP_OWNPV	Lb_Cone_PTAsy
e_PTAsym_1		6	-15	-6	12	9	10	9	100
_IP_OWNPV	5	13	-28		17	37	42	100	9
_IP_OWNPV	8	14	-44	4	16	38	100	42	10
_IP_OWNPV	9	14	-32	7	17	100	38	37	9
proton_pz	8	11	-7	61	100	17	16	17	12
proton_pt	4	-1	6	100	61	7	4		-6
RA_OWNPV	19	42	100	6	-7	-32	-44	-28	-15
_LogIPChi2	54	100	42	-1	11	14	14	13	6
VCHI2NDOF	100	54	19	4	8	9	8	5	

(a) Run 1 data taking

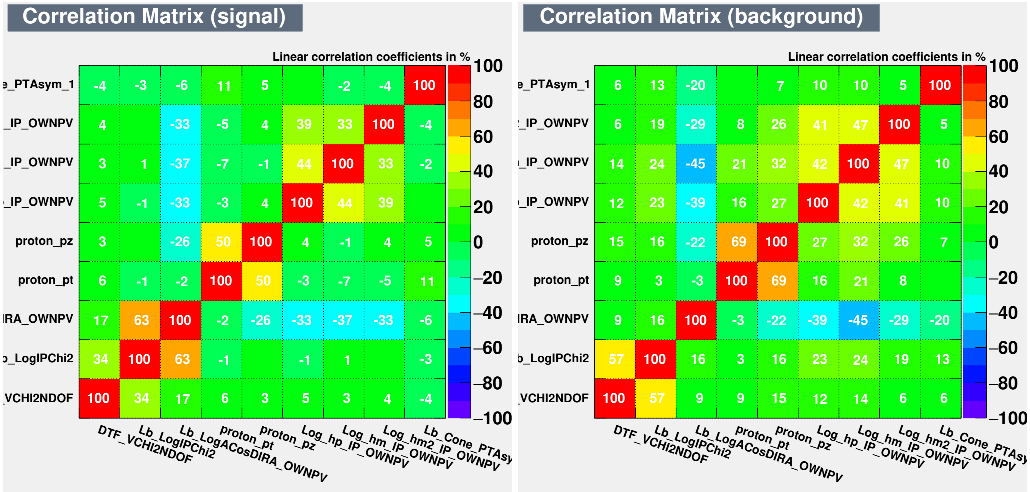

Correlation Matrix (signal)

	DTF_VCHI2NDOF	Lb_LogIPChi2	Lb_LogACosDIRA_OWNPV	proton_pt	proton_pz	Log_hp_IP_OWNPV	Log_hm_IP_OWNPV	Log_hm2_IP_OWNPV	Lb_Cone_PTAsy
e_PTAsym_1	-4	-3	-6	11	5		-2	-4	100
_IP_OWNPV	4		-33	-5	4	39	33	100	-4
_IP_OWNPV	3	1	-37	-7	-1	44	100	33	-2
_IP_OWNPV	5	-1	-33	-3	4	100	44	39	
proton_pz	3		-26	50	100	4	-1	4	5
proton_pt	6	-1	-2	100	50	-3	-7	-5	11
RA_OWNPV	17	63	100	-2	-26	-33	-37	-33	-6
_LogIPChi2	34	100	63	-1		-1	1		-3
VCHI2NDOF	100	34	17	6	3	5	3	4	-4

Correlation Matrix (background)

	DTF_VCHI2NDOF	Lb_LogIPChi2	Lb_LogACosDIRA_OWNPV	proton_pt	proton_pz	Log_hp_IP_OWNPV	Log_hm_IP_OWNPV	Log_hm2_IP_OWNPV	Lb_Cone_PTAsy
e_PTAsym_1	6	13	-20		7	10	10	5	100
_IP_OWNPV	6	19	-29	8	26	41	47	100	5
_IP_OWNPV	14	24	-45	21	32	42	100	47	10
_IP_OWNPV	12	23	-39	16	27	100	42	41	10
proton_pz	15	16	-22	69	100	27	32	26	7
proton_pt	9	3	-3	100	69	16	21	8	
RA_OWNPV	9	16	100	-3	-22	-39	-45	-29	-20
_LogIPChi2	57	100	16	3	16	23	24	19	13
VCHI2NDOF	100	57	9	9	15	12	14	6	6

(b) Run 2 data taking

Figure 3.5: Correlations among BDT variables for signal (Left) and background (Right) for different data taking periods.

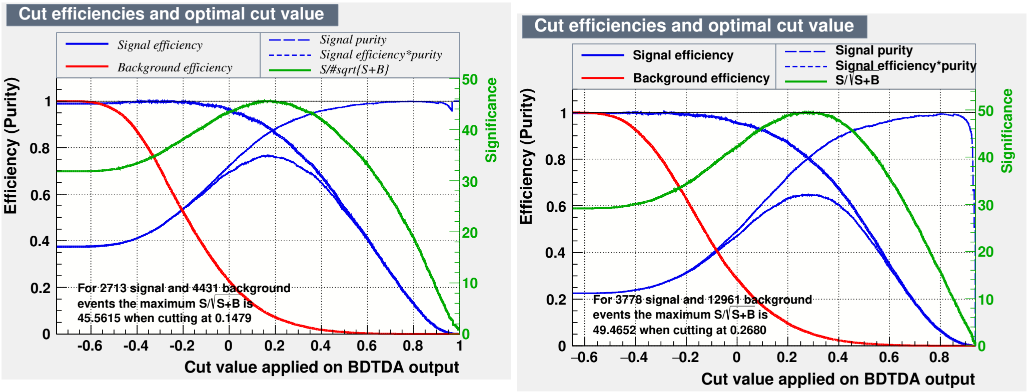

(a) Run 1 data taking

(b) Run 2 data taking

Figure 3.6: Significance, purity and efficiency dependence on the BDT cut applied for different data taking periods.

and therefore we applied the common cut $BDT_{output} > 0.1479$ ($BDT_{output} > 0.268$) on all Run 1 (Run 2) subsamples.

3.4.2 PID optimisation for charged tracks

We perform the PID optimization after the BDT selection to suppress the combinatorial background and cross-feed backgrounds $\Lambda_b^0 \rightarrow pK^-\pi^+\pi^-$ and $B^0 \rightarrow K^+\pi^-\pi^+\pi^-$ that are kinematically similar to signal $\Lambda_b^0 \rightarrow p\pi^-\pi^+\pi^-$ decays. We determine PID efficiencies for signal and backgrounds from the vetoed resonance sample $\Lambda_b^0 \rightarrow \Lambda_c^+(\rightarrow p\pi^+\pi^-)\pi^-$. The significance $\mathcal{S}$, and purity $\mathcal{P}$, are then calculated for the signal data samples:

$$\mathcal{S} = \frac{\varepsilon_S(\text{PID}) \cdot N_S}{\sqrt{\varepsilon_S(\text{PID}) \cdot N_S + \varepsilon_B(\text{PID}) N_B}}, \tag{3.2}$$

$$\mathcal{P} = \frac{\varepsilon_S(\text{PID}) \cdot N_S}{\varepsilon_S(\text{PID}) \cdot N_S + \varepsilon_B(\text{PID}) \cdot N_B}, \tag{3.3}$$

where $\varepsilon_S(\text{PID})$ ($\varepsilon_B(\text{PID})$) are the efficiencies for the signal (background) for different PID cuts and N_S (N_B) are the number of signal (background) events after BDT cut is applied and obtained from fit to the signal data sample. All these variables are calculated within Λ_b^0 mass window $[5.5, 5.7]$ GeV$/c^2$.

The dependence of signal significance and purity vs. PID cuts is shown in Figures 3.7 and 3.8 for Run 1 and Run 2 data taking periods, respectively. Our FoM is the significance $\mathcal{S}$ and we choose the cuts that maximize this quantity.

The final PID selections are $\text{PID}_p > 0.3$ and $\text{PID}_\pi > 0.4$.

3.5 $\Lambda_b^0 \rightarrow \Lambda_c^+(\rightarrow pK^-\pi^+)\pi^-$ control sample

The $\Lambda_b^0 \rightarrow \Lambda_c^+(\rightarrow pK^-\pi^+)\pi^-$ decay proceeds through $b \rightarrow c$ transition and subsequent $c \rightarrow s$ transitions for the Λ_c^+ decay. In the SM *CPV* is expected to be negligible and hence we use this decay mode for systematic uncertainty studies and to perform control checks.

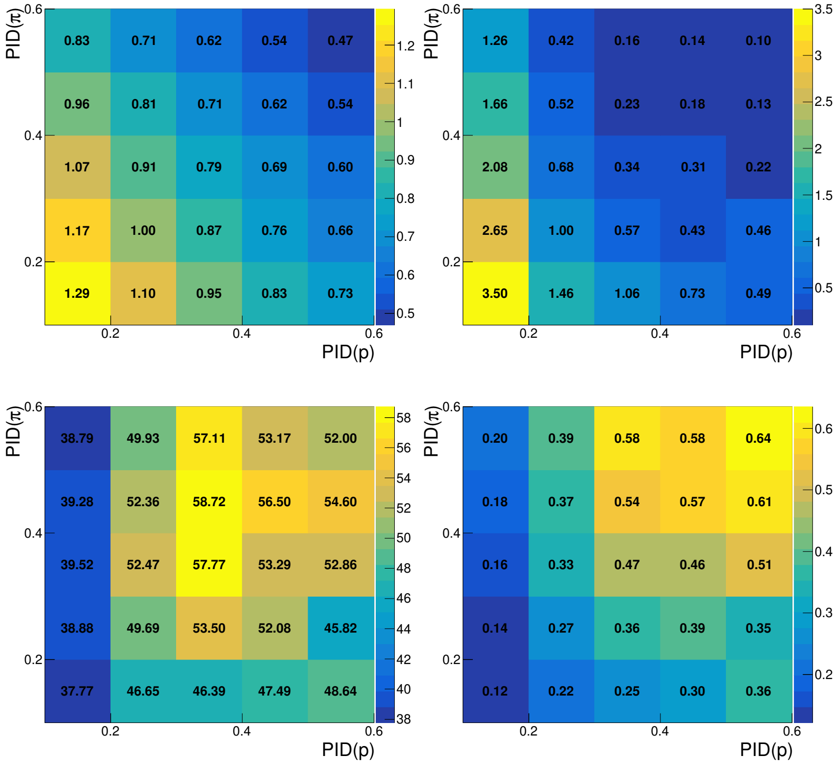

Figure 3.7: Signal efficiency (Top Left), background efficiency (Top Right), significance (Bottom Left) and purity (Bottom Right) for different PID cuts on p and π candidate tracks for Run 1 data taking period.

The kinematic distributions of protons and pions in $\Lambda_b^0 \to p\pi^-\pi^+\pi^-$ and $\Lambda_b^0 \to \Lambda_c^+(\to pK^-\pi^+)\pi^-$ samples are compared in Appendix A.1. The small differences are taken into account in Section 7.5.1 where we show the measured asymmetries do not depend on different final state kinematic distributions we obtain for different PID cuts. In Appendix A.2 we show the kinematic distributions of protons and pions in $\Lambda_b^0 \to \Lambda_c^+(\to pK^-\pi^+)\pi^-$ sample for different PID cuts.

To select the $\Lambda_b^0 \to \Lambda_c^+(\to pK^-\pi^+)\pi^-$ decays we applied some additional criteria listed in Table 3.7 with respect to the preselection stage: loose PID cuts and mass window selection around the Λ_c^+ mass. The reconstructed $m(pK^-\pi^+)$ mass after the preselection stage, used to select the Λ_c^+ candidates, is shown in Figure 3.9.

We define the triple product for the $\Lambda_b^0 \to \Lambda_c^+(\to pK^-\pi^+)\pi^-$ control sample using the Λ_c^+ daughter momenta in the Λ_b^0 rest frame, as $C_{\widehat{T}} \equiv \vec{p}_p \cdot (\vec{p}_{K^-} \times \vec{p}_{\pi^+})$ and analogously for $\overline{C}_{\widehat{T}} \equiv \vec{p}_{\overline{p}} \cdot (\vec{p}_{K^+} \times \vec{p}_{\pi^-})$.

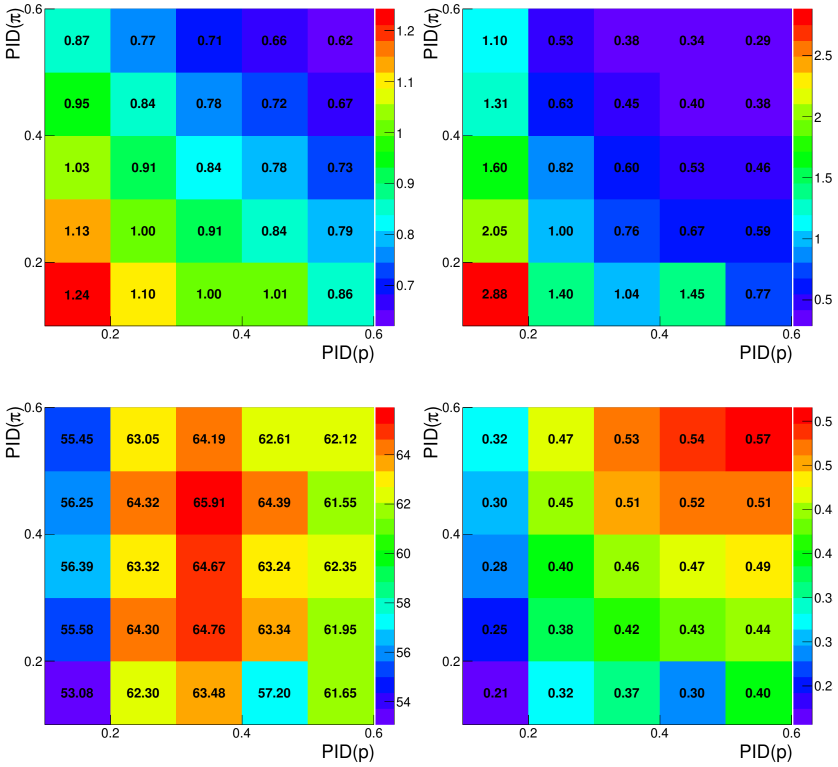

0.87	0.77	0.71	0.66	0.62
0.95	0.84	0.78	0.72	0.67
1.03	0.91	0.84	0.78	0.73
1.13	1.00	0.91	0.84	0.79
1.24	1.10	1.00	1.01	0.86

1.10	0.53	0.38	0.34	0.29
1.31	0.63	0.45	0.40	0.38
1.60	0.82	0.60	0.53	0.46
2.05	1.00	0.76	0.67	0.59
2.88	1.40	1.04	1.45	0.77

55.45	63.05	64.19	62.61	62.12
56.25	64.32	65.91	64.39	61.55
56.39	63.32	64.67	63.24	62.35
55.58	64.30	64.76	63.34	61.95
53.08	62.30	63.48	57.20	61.65

0.32	0.47	0.53	0.54	0.57
0.30	0.45	0.51	0.52	0.51
0.28	0.40	0.46	0.47	0.49
0.25	0.38	0.42	0.43	0.44
0.21	0.32	0.37	0.30	0.40

Figure 3.8: Signal efficiency (Top Left), background efficiency (Top Right), significance (Bottom Left) and purity (Bottom Right) for different PID cuts on p and π candidate tracks for Run 2 data taking period.

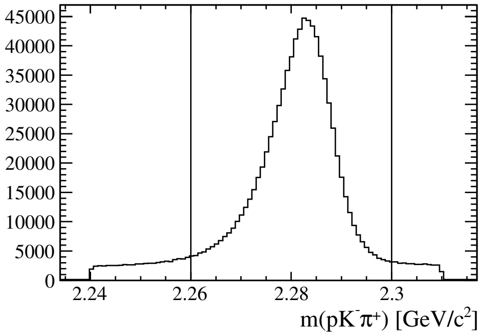

Figure 3.9: The reconstructed $pK^-\pi^+$ invariant mass after the preselection criteria have been applied. A clear peak is visible due to the contribution of $\Lambda_c^+ \to pK^-\pi^+$ decays. The vertical lines indicate the cuts applied on $m(pK^-\pi^+)$ to select the $\Lambda_b^0 \to \Lambda_c^+(\to pK^-\pi^+)\pi^-$ candidates for the control sample.

Table 3.7: Additional selection criteria with respect to the preselection for $\Lambda_b^0 \to \Lambda_c^+(\to pK^-\pi^+)\pi^-$ control sample.

variables	values
PID_p	> 0.05
PID_K	> 0.05
PID_π	> 0.05
Λ_c^+ signal region (MeV/c^2)	$m(pK^-\pi^+) \in [2260, 2300]$

CHAPTER 4

Fit Model

An unbinned extended maximum likelihood fit to the $m(p\pi^-\pi^+\pi^-)$ mass spectrum is performed using the signal and background shapes described in Section 4.1 and 4.2.

We define both the nominal and alternative shapes used in the nominal and the alternative fit, respectively. The latter is useful to estimate the systematic uncertainties due to the fit model in Section 7.3. The shapes are determined with the help of MC samples which are reweighted using data control samples to improve the description of the PID response. We use $D^{*+} \to D^0(\to K^-\pi^+)\pi^+$ control samples for π and K tracks and $\Lambda_c^+ \to pK^-\pi^+$ for p tracks. The reweighting procedure is performed in bins of pseudorapidity-momentum of the tracks and is deeply described in References [145, 151].

The likelihood $\mathcal{L}$ is defined as

$$\mathcal{L}\left(\vec{\theta}, N_{sig}, \vec{N}_{bkg}; \vec{m}\right) = \prod_{i=0}^{N} \underbrace{\frac{N_{sig}\mathcal{P}_{sig}\left(m_i;\vec{\theta}\right) + \sum_j N_{bkg_j}\mathcal{P}_{bkg_j}\left(m_i;\vec{\theta}\right)}{N_{sig}+\sum_j N_{bkg_j}}}_{\text{pdf mass model}}$$

$$\times \prod_{\omega \text{ constr.}} \underbrace{G\left(\omega;\varpi,\sigma_{\varpi}\right)}_{\text{Gaussian constraint}} \times \underbrace{P\left(N; N_{sig}+\sum_j N_{bkg_j}\right)}_{\text{extension}} \qquad (4.1)$$

and it depends on the parameters $\vec{\theta}$ of the signal (j-th background component) pdf $\mathcal{P}_{sig}$ ($\mathcal{P}_{bkg_j}$), number of signal (j-th background component) N_{sig} (N_{bkg_j}) given a dataset with N mass measurements $\vec{m}$. To keep into account external measurements ϖ with resolution σ_{ϖ} on the parameter ω that could either belong to $\vec{\theta}$ and $\vec{N}_{bkg}$, we apply Gaussian constraints multiplying the likelihood with a Gaussian function G with mean ϖ and sigma σ_{ϖ}. Finally we extend it to allow Poisson fluctuation on the total number of fitted events $N_{sig} + \sum_j N_{bkg_j}$ multiplying the likelihood with a Poisson distribution P with mean $N_{sig} + \sum_j N_{bkg_j}$.

We ensure the goodness of each fit to data (integrated and in bins of phase space) and MC showing the pulls on top of them. The vast majority of them lies within the interval [-3,3] and we check they are Gaussian distributed.

4.1 Signal shape

The invariant mass signal shape is determined by using $\Lambda_b^0 \to p\pi^-\pi^+\pi^-$ simulated MC decays and it is modeled by using the sum of two Crystal Ball (CB) functions [152] with the same peak and width parameters. In this way we are able to describe the Gaussian core of the distribution, along with the polynomial tail on the left and right hand side. The general form of the double CB signal shapes is

$$\mathcal{P}_{sig} = f \cdot \mathrm{CB}_1(x;\mu,\sigma,\alpha_1,n_1) + (1-f)\cdot \mathrm{CB}_2(x;\mu,\sigma,\alpha_2,n_2), \tag{4.2}$$

$$\mathrm{CB}(x;\mu,\sigma,\alpha,n) = N \cdot \begin{cases} \frac{(\frac{n}{|\alpha|})^n e^{-\frac{1}{2}\alpha^2}}{(\frac{n}{|\alpha|}-|\alpha|-\frac{x-\mu}{\sigma})^n}, & \text{for } x < -|\alpha| \\ e^{-\frac{1}{2}(\frac{x-\mu}{\sigma})^2}, & \text{for } x > -|\alpha| \end{cases} \tag{4.3}$$

where N is a normalisation factor. The signal candidates in the simulated sample are truth-matched by requiring that the four reconstructed daughters of the Λ_b^0 candidate are either directly produced from a Λ_b^0 decay or via strong intermediate resonances. Then they are reweighted using data control samples to improve the description of the PID response. The fitted shapes and pull distributions are shown in Figure 4.1 and the fit results are listed in Table 4.1. In the fit to data the peak μ and the σ of the signal distribution are free to vary for obtaining optimal fit results, while the tail parameters $\alpha_{1/2}, n_{1/2}$ and the relative fraction f_{CB_1} are fixed to values obtained from the nominal fit to MC signal events.

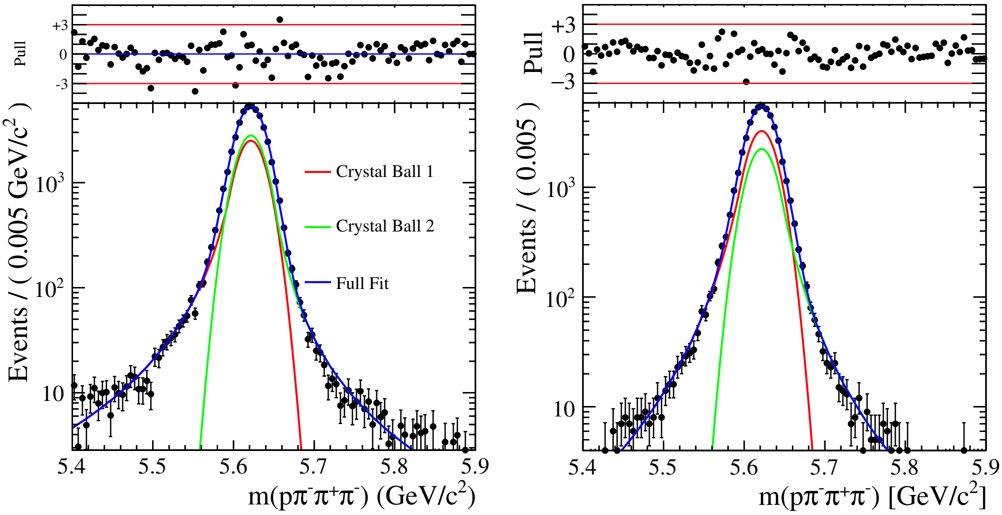

(a) Nominal Fit

(b) Alternative Fit

Figure 4.1: Double Crystal Ball model fit to signal MC $\Lambda_b^0 \to p\pi^-\pi^+\pi^-$ events for nominal and alternative fit.

4.2 Sources of background

Three main categories of background can be identified in this analysis:

- **Partially reconstructed decays**: it is localised in the region of low invariant mass. Part of these candidates are from $\Lambda_b^0 \to p\pi^+\pi^-\rho^-(\rho^- \to \pi^-\pi^0)$ and similar decays, in which the π^0 is not reconstructed. These candidates appear as a shoulder-like shape on the low-energy side of the mass distribution.

Table 4.1: Fit results to the invariant mass $m(p\pi^-\pi^+\pi^-)$ of the $\Lambda_b^0 \to p\pi^-\pi^+\pi^-$ Monte Carlo sample.

Variable	Nominal Value	Alternative Value
$\mu(\Lambda_b^0)(\mathrm{MeV}/c^2)$	5621.5 ± 0.1	5621.6 ± 0.1
$\sigma(\mathrm{MeV}/c^2)$	17.0 ± 0.1	17.2 ± 0.1
n_1	2.54 ± 0.19	3.86 ± 0.29
α_1	1.48 ± 0.13	1.47 ± 0.08
n_2	2.40 ± 0.18	3.68 ± 0.32
α_2	-1.85 ± 0.11	-1.51 ± 0.11
f_{CB_1}	0.48 ± 0.10	0.59 ± 0.07

- **Cross-feed background**: it is mainly due to 4-body Λ_b^0 and B^0 decays where one of the daughter particles has been misidentified and reconstructed with a wrong mass hypothesis. In particular it is due to $\Lambda_b^0 \to pK^-\pi^+\pi^-$ channels and $B^0 \to K^+\pi^-\pi^+\pi^-$ decays where a K is misidentified as a π or a p, respectively. This background can be reduced using adequate PID requirements and "ad hoc" resonance vetoes, *e.g.* veto $K^{*0}(892)$ resonance once reconstructing the decay with different mass hypothesis for proton candidate. This background is potentially dangerous since it is due to b-hadron decays that in principle can violate *CP* symmetry and also it has a distribution that is close to, and in some cases overlapping with, the signal shape, as can be seen in Figure 4.6. It can be considered as a peaking background source in the invariant mass spectrum.

- **Combinatorial background**: Mainly due to random combinations of charged tracks in the event. This source of background is reduced by requiring good quality tracks compatible with displaced vertices of Λ_b^0 hadrons.

4.2.1 Background fit model

The distribution of the **partially reconstructed background** can be empirically modelled by an Argus function convoluted with a Gaussian resolution function

$$\mathcal{P}_{Part.\ reco} = m\left(1-\left(\frac{m}{m_t}\right)^2\right)^{p_{Part.\ reco}} \cdot \exp\left(c_{Part.\ reco}\left(1-\left(\frac{m}{m_t}\right)^2\right)\right) \otimes G(0,\sigma), \tag{4.4}$$

where m is the mass, m_t is the threshold point, $c_{Part.\ reco}$ controls the low mass slope and $p_{Part.\ reco}$ the power. The functional shape is shown in Figure 4.2 with different values for the parameter $c_{Part.\ reco}$.

The threshold point is needed to describe the effect of the missing π^0 from the reconstructed Λ_b^0 decay. In the nominal fit, m_t is fixed to $\mu - m_{\pi^0}$ where μ is the peak of the signal distribution in Equation (4.2), σ is the mass resolution appearing in Equation (4.2) and $c_{Part.\ reco}$ and $p_{Part.\ reco}$ are allowed to vary.

The distributions of the **cross-feed backgrounds** are parametrised with kernel estimated probability density functions [153] by modelling the invariant mass distributions of $\Lambda_b^0 \to pK^-\pi^+\pi^-$ and $B^0 \to K^+\pi^-\pi^+\pi^-$ decays of MC samples under the wrong mass hypothesis for daughter particles, *e.g.* π mass and p mass for K daughter particles, respectively, as shown in Figure 4.3. The Monte Carlo is reweighted using data control samples to improve the description of the PID response. The potential systematic ef-

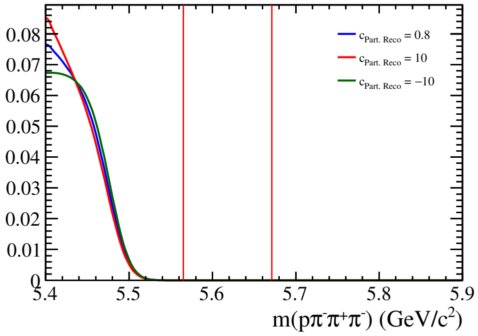

Figure 4.2: Argus function convoluted with a Gaussian resolution function defined in Equation (4.4) used to describe the partially reconstructed background. The blue shape represents the function fitted to data with the values of the parameters listed in Table 4.3, while for the others the $c_{Part.\ reco}$ value is changed accordingly to the legend. The signal region is delimited by the red lines placed at $\pm 3\sigma$, where σ is the experimental resolution of the signal peak.

fects in modelling the shapes from the MC is accounted for in the assigned systematic uncertainties discussed in Section 7.3. In the alternative model, the cross feed shapes are described with an unweighted MC, where the scale factors data/MC have not been applied. In Figure 4.4 it is shown the comparison between the nominal and alternative shapes used in the fit, along with the shapes smeared with a larger resolution in order to match the resolution measured on data. The smearing is performed with a Gaussian with resolution $\sigma = \sqrt{\sigma^2_{data} - \sigma^2_{MC}}$, where $\sigma_{data} = 17.7\,\mathrm{MeV}/c^2$ (from Table 4.3) and $\sigma_{MC} = 17.0\,\mathrm{MeV}/c^2$ (from Table 4.1). It is clear that this correction is negligibly small. The yields of cross-feed backgrounds from B^0, and other Λ_b^0 decays are estimated directly on data. Fits to the invariant mass spectrum obtained when assuming different mass hypothesis for final state particles are used to estimate the cross-feed background contributions, as shown in Figure 4.5. The spectra are fitted with a polynomial and a Gaussian to model the background and the signal respectively. In particular to estimate the contribution of the $B^0 \to K^+\pi^-\pi^+\pi^-$ ($\Lambda_b^0 \to pK^-\pi^+\pi^-$) decays the $\Lambda_b^0 \to p\pi^-\pi^+\pi^-$ candidates are reconstructed using the K mass hypothesis for the p (π) candidate. The estimates, listed in Table 4.2, are then applied as Gaussian constraints on cross-feed background yields in the nominal fit presented in Section 4.3.

Table 4.2: Estimates on the yields for the cross feeds present in $\Lambda_b^0 \to p\pi^-\pi^+\pi^-$ candidates. They are applied as Gaussian constraint in the nominal invariant mass fit of the $\Lambda_b^0 \to p\pi^-\pi^+\pi^-$ candidates.

Cross feed	Yield	Error
$\Lambda_b^0 \to pK^-\pi^+\pi^-$	5834	303
$B^0 \to K^-\pi^+\pi^-\pi^-$	2109	154

Finally, the distribution of the **combinatorial background** is modelled with an exponential function

$$\mathcal{P}_{comb} = A \exp\left(-\lambda_{comb} \cdot m\right). \tag{4.5}$$

with a shape parameter λ_{comb} that is left free to vary in the fit.

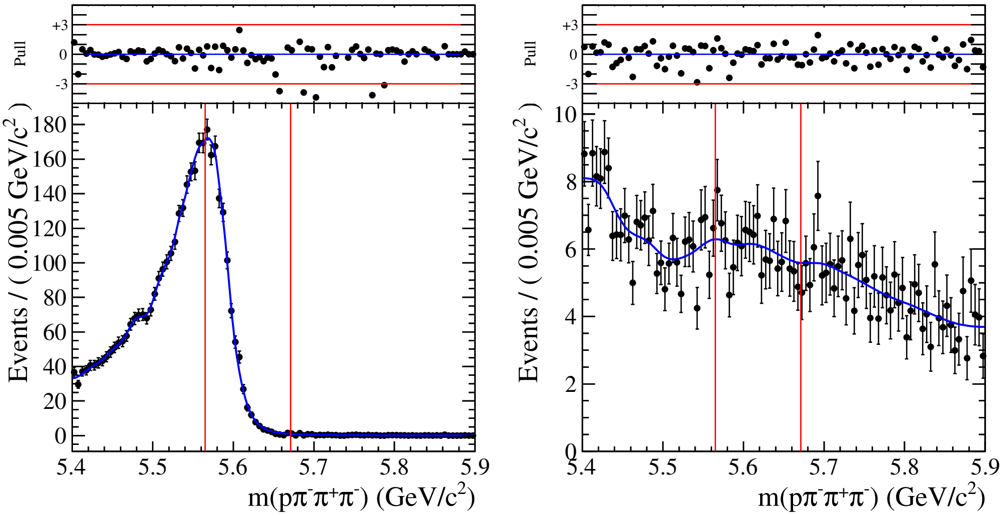

Figure 4.3: Parametrisation of the $m(p\pi^-\pi^+\pi^-)$ invariant mass for $\Lambda_b^0 \to pK^-\pi^+\pi^-$ (Left) and $B^0 \to K^+\pi^-\pi^+\pi^-$ (Right) decays under the wrong mass hypothesis for daughter particles, *e.g.* π mass and p mass for K daughter particles, respectively. The Monte Carlo has been reweighted using data control samples to match the response of the PID to data. These shapes are used in the nominal fit to describe the shapes of the cross feed backgrounds. The signal region is delimited by the red lines placed at $\pm 3\sigma$, where σ is the experimental resolution of the signal peak.

4.3 Fit to the invariant mass distribution $m(p\pi^-\pi^+\pi^-)$

We perform an unbinned maximum likelihood fit to the invariant mass distribution $m(p\pi^-\pi^+\pi^-)$ using the likelihood definition given in Equation (4.1) and the signal and background shapes described in Section 4.1 and 4.2. The results are listed in Table 4.3 and shown in Figure 4.6. The parameter $c_{Part.\ reco}$ has an higher error with respect to the fit to the control sample in Table 4.4. Indeed, as shown in Figure 4.2, this parameter describe the low mass shape of the partially reconstructed background, where the mass spectra of the control sample is further extended. However it does not affect the signal region and have no impact on the measured signal asymmetries.

4.4 Fit to the invariant mass distribution for $\Lambda_b^0 \to \Lambda_c^+(\to pK^-\pi^+)\pi^-$ control sample

Since the $\Lambda_b^0 \to \Lambda_c^+(\to pK^-\pi^+)\pi^-$ decay is governed by the $b \to c$ transition, *CPV* is expected to be negligible. We use this control sample to assess systematic uncertainty in Section 7.1.

We perform an unbinned extended maximum likelihood fit to the $\Lambda_c^+(pK^-\pi^+)\pi^-$ mass spectrum with the likelihood definition given in Equation (4.1).

The relative fraction $f_{\Lambda_b^0 \to \Lambda_c^+ K^-} = \frac{\mathcal{B}(\Lambda_b^0 \to \Lambda_c^+ K^-)}{\mathcal{B}(\Lambda_b^0 \to \Lambda_c^+ \pi^-)} \frac{\varepsilon^{PID}(\Lambda_b^0 \to \Lambda_c^+ \pi^-)}{\varepsilon^{PID}(\Lambda_b^0 \to \Lambda_c^+ K^-)}$ of the cross-feed background from $\Lambda_b^0 \to \Lambda_c^+ K^-$ with respect to the more abundant $\Lambda_b^0 \to \Lambda_c^+ \pi^-$, where $\mathcal{B}(X)$ and $\varepsilon^{PID}(X)$ are the branching fraction and the PID efficiency of the X mode, is estimated from the measured branching fractions, $(3.59 \pm 0.30) \times 10^{-4}$ and $(4.9 \pm 0.4) \times 10^{-3}$, and the PID efficiencies $(47.66 \pm 0.12)\%$ and $(92.73 \pm 0.05)\%$, respectively. The PID effi-

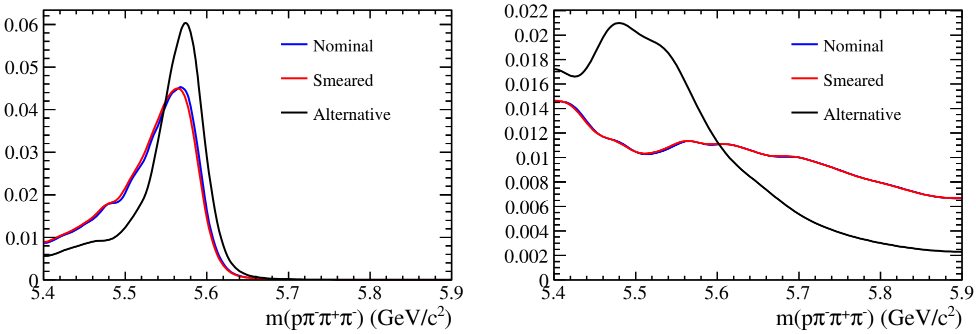

Figure 4.4: Comparison between cross feed shapes for $\Lambda_b^0 \to pK^-\pi^+\pi^-$ (Left) and $B^0 \to K^+\pi^-\pi^+\pi^-$ (Right) decay used in the nominal and alternative fit model, along with the shapes smeared with a resolution extracted from data.

Table 4.3: Fit results and parameters for the fit to data of $\Lambda_b^0 \to p\pi^-\pi^+\pi^-$ candidates. Signal model parameters are fixed in the fit from Monte Carlo results except for the peak μ and the σ value.

Variable	Value
Part. reco bkg	6931 ± 374
Comb. bkg	23766 ± 636
$B^0 \to K^+\pi^-\pi^+\pi^-$	2108 ± 154
$\Lambda_b^0 \to pK^-\pi^+\pi^-$	6407 ± 233
$\Lambda_b^0 \to p\pi^-\pi^+\pi^-$	27629 ± 210
$\mu(\Lambda_b^0)(\mathrm{MeV}/c^2)$	5618.1 ± 0.1
$\sigma(\mathrm{MeV}/c^2)$	17.7 ± 0.1
$c_{Part.\ reco}$	-6.4 ± 13.7
$p_{Part.\ reco}$	0.40 ± 0.20
$\lambda_{comb}(c^2/\mathrm{GeV})$	-4.40 ± 0.13
Λ_b^0 signal model	Value (fixed from MC)
n_1	2.54
α_1	1.48
n_2	2.40
α_2	-1.85
f_{CB_1}	0.48

ciencies are obtained from high statistics control samples. The obtained relative fraction $f_{\Lambda_b^0 \to \Lambda_c^+ K^-} = (3.77 \pm 0.44)\%$ has been Gaussian constrained in the fit. The shape is determined from $\Lambda_b^0 \to \Lambda_c^+(\to pK^-\pi^+)K^-$ MC sample reweighted to improve the description of the PID response and parametrised with a kernel estimated probability density function.

The partially reconstructed and combinatorial background are modelled with an Argus convolved with a Gaussian (the resolution is measured from data) and an exponential, respectively. The yields are left free to vary in the fit.

The invariant mass distribution is shown in Figure 4.7, and the results of the fit in Table 4.4.

Table 4.4: Fit results to the invariant mass distribution for the $\Lambda_b^0 \to \Lambda_c^+(\to pK^-\pi^+)\pi^-$ control sample.

Variable	Value
Part. reco bkg	115171 ± 1198
Comb. bkg	86292 ± 1440
$\Lambda_b^0 \to \Lambda_c^+(\to pK^-\pi^+)\pi^-$	425767 ± 1593
$f_{\Lambda_b^0 \to \Lambda_c^+(\to pK^-\pi^+)K^-}$	0.031 ± 0.003
$\mu(\mathrm{MeV}/c^2)$	5618.25 ± 0.04
$\sigma(\mathrm{MeV}/c^2)$	16.91 ± 0.04
$c_{Part.\ reco}$	-15.14 ± 0.91
$p_{Part.\ reco}$	0.09 ± 0.01
$\lambda(c^2/\mathrm{GeV})$	-6.13 ± 0.07
n_1	17.48 ± 1.65
α_1	1.02 ± 0.03
n_2	20.00 ± 0.52
α_2	-1.32 ± 0.03
f_{CB_1}	0.452 ± 0.029

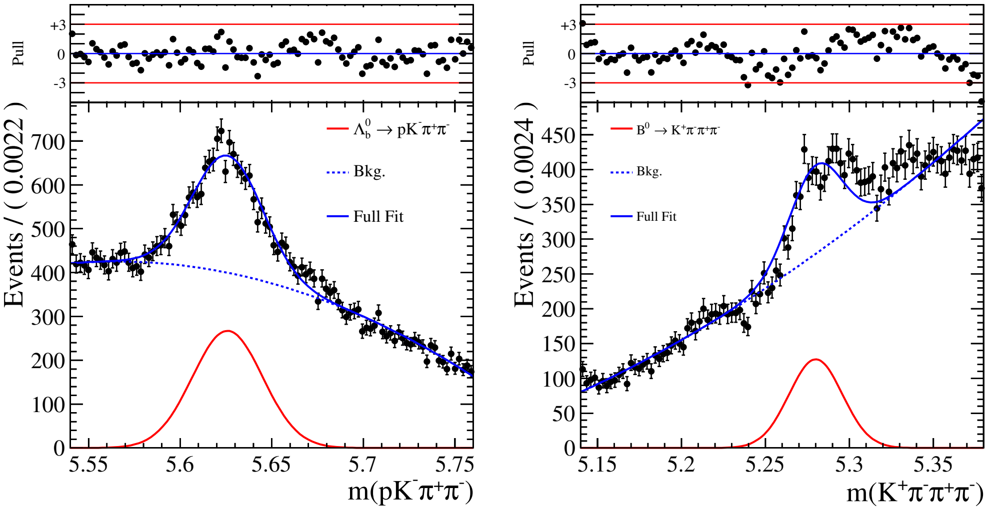

Figure 4.5: Fit to the invariant mass $m(pK^-\pi^+\pi^-)$ (Left) and $m(K^+\pi^-\pi^+\pi^-)$ (Right) for the $\Lambda_b^0 \to p\pi^-\pi^+\pi^-$ candidates reconstructed using the K mass hypothesis for the π and K candidates, respectively. The peaks correspond to the cross feeds and the estimate on the yield is used as Gaussian constraint in the nominal fit.

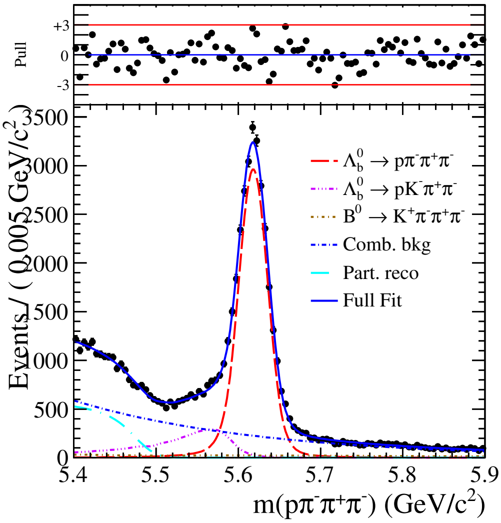

Figure 4.6: Fit to the reconstructed invariant mass distribution for $\Lambda_b^0 \to p\pi^-\pi^+\pi^-$ signal candidates using the combined Run 1 and Run 2 data samples. The fit result is overlaid, as described in the text.

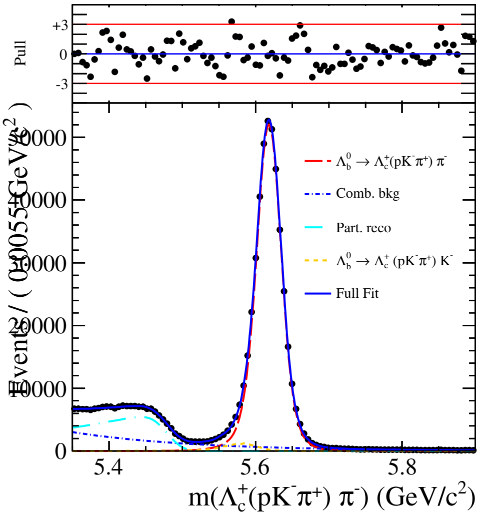

Figure 4.7: Fit to the reconstructed invariant mass of the $\Lambda_b^0 \to \Lambda_c^+(\to pK^-\pi^+)\pi^-$ control sample using the combined Run 1 and Run 2 data sample.

CHAPTER 5

Sensitivity studies for *CP* violation and optimisation of the analysis method

The default LHCb Monte Carlo cocktail for $\Lambda_b^0 \to p\pi^-\pi^+\pi^-$ does not describe well the dynamics since the decay model does not take into account several resonant contributions and the interference among amplitudes. We improved the decay model description in the MC in order to be sensitive to P-odd CPV effects based on the interference between P-odd and P-even amplitudes.

5.1 $\Lambda_b^0 \to p\pi^-\pi^+\pi^-$ decay model

The aim of this analysis is to search for P-odd CPV using a method based on triple-product asymmetries. Contrarily to P-even CPV effects generated by the interference of two generic amplitudes with different strong and weak phases, P-odd CPV effects could be present only in some particular decay topologies, such as two different interfering amplitudes with opposite parity, as pointed out in the literature [51]. We developed an amplitude model for the $\Lambda_b^0 \to p\pi^-\pi^+\pi^-$ decays in order to improve the description of the relevant resonant contribution and identify interesting regions where to search for P-odd CPV effects, or excluding non-interesting regions from the search. We developed the amplitude model using the helicity formalism, which is briefly explained in the following section.

5.1.1 Helicity formalism

The helicity formalism describes the decay of a mother into any number of daughters in the final state with sequential two-body decays proceeding via resonant contribution such that the full matrix element is obtained as a multiplication of the matrix element of each two-body decay. For each two-body decay $A \to BC$, a coordinate system is defined in the rest frame of A, with $\hat{z}$ being the direction of the quantization axis for its spin. We denote this coordinate system as $(x_0^{\{A\}}, y_0^{\{A\}}, z_0^{\{A\}})$, where the superscript "$\{A\}$" means "in the rest frame of A", while the subscript "0" means the initial coordinates. For the first particle in the decay chain (Λ_b^0), the choice of these coordinates is arbitrary. However, if a particle is known to be produced with a polarization along a direction, it's worth to define the initial reference frame with an axis along that particular direction in order to avoid dilution to the polarization sensitivity.

Once defined, these coordinates must be consistently used in the decay chain described by the matrix elements. For the subsequent decays, *e.g.* $B \to DE$, the choice of these coordinates is determined by the transformation from the A to the B rest frame, as discussed below. Helicity is defined as the projection of the spin of the particle onto the direction of its momentum. When the z axis coincides with the particle momentum, we denote its spin projection onto it (*i.e.* the m_z quantum number) as λ. To use the helicity formalism, the initial coordinate system must be rotated to align the z axis with the direction of the momentum of one of the daughter particles, *e.g.* the B.

A generalized rotation operator can be formulated in three-dimensional space, $\mathcal{R}(\alpha, \beta, \gamma)$, that uses Euler angles. Applying this operator results in the sequence of rotations: first by the angle α about the $\hat{z}_0$ axis, followed by the angle β about the rotated $\hat{y}_1$ axis and then finally by the angle γ about the rotated $\hat{z}_2$ axis. We use a subscript denoting the axes, to specify the rotations which have been already performed on the coordinates. The spin eigenstates of particle A in the $(x_0^{\{A\}}, y_0^{\{A\}}, z_0^{\{A\}})$ coordinate system, $|J_A, m_A\rangle$, can be expressed in the basis of its spin eigenstates in the rotated $(x_3^{\{A\}}, y_3^{\{A\}}, z_3^{\{A\}})$ coordinate system, $|J_A, m'_A\rangle$, with the help of Wigner's D-matrix,

$$|J_A, m_A\rangle = \sum_{m'_A} D^{J_A}_{m_A, m'_A}(\alpha, \beta, \gamma)|J_A, m'_A\rangle \tag{5.1}$$

where,

$$D^{J_A}_{m_A, m'_A}(\alpha, \beta, \gamma)^* = \langle J, m|\mathcal{R}(\alpha, \beta, \gamma)|J, m'\rangle^* = e^{im\alpha} d^J_{m,m'}(\beta) e^{im'\gamma}, \tag{5.2}$$

where the small-d Wigner's matrix contain known functions of β that depends on J, m, m'. To achieve the rotation of the original $z_0^{\{A\}}$ axis onto the B momentum $(\vec{p}_B^{\{A\}})$, it is sufficient to rotate by $\alpha = \phi_B^{\{A\}}$, $\beta = \theta_B^{\{A\}}$, where $\phi_B^{\{A\}}$, $\theta_B^{\{A\}}$ are the azimuthal and polar angles of the B momentum vector in the original coordinates *i.e.* $(x_0^{\{A\}}, y_0^{\{A\}}, z_0^{\{A\}})$. Since the third rotation is not necessary [154], we set $\gamma = 0$. The angle $\theta_B^{\{A\}}$ is usually called "the A helicity angle", thus to simplify the notation we will denote it as θ_A. For simplicity of notation, we will also denote $\phi_B^{\{A\}}$ as ϕ_B. These angles can be obtained from:

$$\begin{aligned}
\phi_B &= \operatorname{atan2}(p_{B\ y}^{\{A\}}, p_{B\ x}^{\{A\}}) \\
&= \operatorname{atan2}(\hat{y}_0^{\{A\}} \cdot \vec{p}_B^{\{A\}}, \hat{x}_0^{\{A\}} \cdot \vec{p}_B^{\{A\}}) \\
&= \operatorname{atan2}((\hat{z}_0^{\{A\}} \times \hat{x}_0^{\{A\}}) \cdot \vec{p}_B^{\{A\}}, \hat{x}_0^{\{A\}} \cdot \vec{p}_B^{\{A\}}) \\
\cos\theta_A &= \hat{z}_0^{\{A\}} \cdot \vec{p}_B^{\{A\}}
\end{aligned} \tag{5.3}$$

Angular momentum conservation implies, $m'_A = m'_B + m'_C = \lambda_B - \lambda_C$ ($m'_C = -\lambda_C$, since $\vec{p}_C^{\{A\}}$ points in the opposite direction to $\hat{z}_3^{\{A\}}$). Each two-body decay adds a multiplicative term to the full matrix element. Here, for example, the matrix element for the $A \to BC$ decay

$$\mathcal{M}^{A\to BC} = M_B(m_B) M_C(m_C) \sum_{\lambda_B, \lambda_C} \mathcal{H}^{A\to BC}_{\lambda_B, \lambda_C} D^{J_A}_{m_A, \lambda_B - \lambda_C}(\phi_B, \theta_A, 0)^*. \tag{5.4}$$

where M_X describe the mass shape of the broad resonance X and depends on the actual invariant mass of the X daughters m_X. These terms are not present if B and C are not broad resonances.

The helicity couplings $\mathcal{H}^{A\to BC}_{\lambda_B, \lambda_C}$ are complex numbers. Their products for subsequent decays have to be determined from the fit to data, and represent the decay dynamics. In strong decays parity is conserved and the number of independent helicity couplings is reduced using the relation,

$$\mathcal{H}^{A\to BC}_{-\lambda_B,-\lambda_C} = P_A P_B P_C (-1)^{J_B+J_C-J_A} \mathcal{H}^{A\to BC}_{\lambda_B,\lambda_C}, \tag{5.5}$$

where P stands for intrinsic parity of a particle. The sum in Equation (5.4) is over all possible helicity values of B and C particles constrained by $|\lambda_B| \leq J_B$, $|\lambda_C| \leq J_C$, $|\lambda_B - \lambda_C| \leq J_A$.

When dealing with the subsequent decay of the daughter, $B \to DE$, the four-vectors of all particles must be first boosted to the rest frame of B, along the $\vec{p}^{\{A\}}_B$ *i.e.* in the $\hat{z}^{\{A\}}_3$ direction. This transformation does not change vectors which are perpendicular to the boost direction. The transformed coordinates ($\hat{x}^{\{A\}}_3, \hat{y}^{\{A\}}_3, \hat{z}^{\{A\}}_3$) become the initial coordinate system for the quantization of the spin of B in its rest frame,

$$\begin{aligned} \hat{x}^{\{B\}}_0 &= \hat{x}^{\{A\}}_3, \\ \hat{y}^{\{B\}}_0 &= \hat{y}^{\{A\}}_3, \\ \hat{z}^{\{B\}}_0 &= \hat{z}^{\{A\}}_3. \end{aligned} \tag{5.6}$$

The processes of rotation and subsequent boosting can be repeated until the final state particles are reached. In practice, there are two equivalent ways to determine $\hat{z}^{\{B\}}_0$ direction. Using Equation (5.6) we can set it to the direction of B momentum in the A rest frame,

$$\hat{z}^{\{B\}}_0 = \hat{z}^{\{A\}}_3 = \hat{p}^{\{A\}}_B. \tag{5.7}$$

Alternatively, we can make use of the fact that B and C are back-to-back in the rest frame of A, $\hat{p}^{\{A\}}_C = -\hat{p}^{\{A\}}_B$. Since the momentum of C is antiparallel to the boost direction from the A to B rest frames, the C momentum in the B rest frame will be different, but it will still be antiparallel to this boost direction,

$$\hat{z}^{\{B\}}_0 = -\hat{p}^{\{B\}}_C. \tag{5.8}$$

To determine $\hat{x}^{\{B\}}_0$ from Equation (5.6), we need to find $\hat{x}^{\{A\}}_3$. After the first rotation by ϕ_B about $\hat{z}^{\{A\}}_0$, the $\hat{x}^{\{A\}}_1$ axis is along the component of $\vec{p}^{\{A\}}_B$ which is perpendicular to the $\hat{z}^{\{A\}}_0$ axis,

$$\begin{aligned} \vec{a}^{\{A\}}_{B\perp z_0} &\equiv (\vec{p}^{\{A\}}_B)_{\hat{z}^{\{A\}}_0} = \vec{p}^{\{A\}}_B - (\vec{p}^{\{A\}}_B)_{\parallel \hat{z}^{\{A\}}_0} \\ &= \vec{p}^{\{A\}}_B - (\vec{p}^{\{A\}}_B \cdot \hat{z}^{\{A\}}_0)\hat{z}^{\{A\}}_0 \\ \hat{x}^{\{A\}}_1 = \hat{a}^{\{A\}}_{B\perp z_0} &= \frac{\vec{a}^{\{A\}}_{B\perp z_0}}{|\vec{a}^{\{A\}}_{B\perp z_0}|} \end{aligned} \tag{5.9}$$

After the second rotation by θ_A about $\hat{y}^{\{A\}}_1$, $\hat{z}^{\{A\}}_2 \equiv \hat{z}^{\{A\}}_3 = \hat{p}^{\{A\}}_B$, and $\hat{x}^{\{A\}}_2 = \hat{x}^{\{A\}}_3$ (since $\gamma = 0$) is antiparallel to the component of the $\hat{z}^{\{A\}}_0$ vector that is perpendicular to the new z axis *i.e.* $\hat{p}^{\{A\}}_B$,

$$\begin{aligned} \vec{a}^{\{A\}}_{B\perp z_0} &\equiv (\hat{z}^{\{A\}}_0)_{\perp \vec{p}^{\{A\}}_B} = \hat{z}^{\{A\}}_0 - (\hat{z}^{\{A\}}_0 \cdot \hat{p}^{\{A\}}_B)\hat{p}^{\{A\}}_B \\ \hat{x}^{\{B\}}_0 = \hat{x}^{\{A\}}_3 &= -\hat{a}^{\{A\}}_{z_0\perp B} = -\frac{\vec{a}^{\{A\}}_{z_0\perp B}}{|\vec{a}^{\{A\}}_{z_0\perp B}|} \end{aligned} \tag{5.10}$$

then, $\hat{y}_0^{\{B\}} = \hat{z}_0^{\{B\}} \times \hat{x}_0^{\{B\}}$.

If C also decays, $C \to FG$, then the coordinates for the quantization of C spin in the C rest frame are initially defined by,

$$\begin{aligned} \hat{z}_0^{\{C\}} &= -\hat{z}_3^{\{A\}} = \vec{p}_C^{\{A\}} = -\hat{p}_B^{\{C\}} \\ \hat{x}^{\{C\}} &= \hat{x}_3^{\{A\}} = -\hat{a}_{z_0 \perp B}^{\{A\}} = +\hat{a}_{z_0 \perp C}^{\{A\}} \\ \hat{y}^{\{C\}} &= \hat{z}_0^{\{C\}} \times \hat{x}_0^{\{C\}} \end{aligned} \tag{5.11}$$

i.e. the z axis is reflected compared to the system used for the decay of particle B (it must point in the direction of C momentum in the A rest frame!), but the x axis is kept the same, since we chose particle B for the rotation used in Equation (5.4).

The full matrix elements of $A \to daughters$ for a certain decay chain where it is present the resonant contribution of B and C is given by the multiplication of each two-body decay matrix element in Equation (5.4)

$$\mathcal{M}^{A \to daughters} = \mathcal{M}^{A \to BC} \cdot \mathcal{M}^{B \to X_1} \cdot \mathcal{M}^{C \to X_2} \cdot \ldots \; . \tag{5.12}$$

The spin quantization axes depend on the different decay chain taken into account to perform the transformations. Consequently the helicity λ in Equation (5.4) depends on the decay chains. If we consider the helicity of the intermediate particles, this argument has no consequences after we sum (coherently) over all the available helicities because they belong to the same decay chain. However, the proton is a final state particle and we have to sum coherently matrix elements that belong to different decay chains. Therefore the proton helicity λ_p for a decay chain must be expressed in terms of the helicity λ'_p in the other decay chain as follows

$$|\lambda\rangle = \sum_{\lambda'} D^{J_p}_{\lambda,\lambda'}(\phi, \theta, 0)^* |\lambda'\rangle, \tag{5.13}$$

such that we are able to sum coherently the matrix elements of different decay chains $DC_1, DC_2, \ldots$ in Equation (5.12) as

$$\begin{aligned} \mathcal{M}_{\lambda_p}^{A \to pX} &= \mathcal{M}_{\lambda_p}^{DC_1} + \mathcal{M}_{\lambda_p}^{DC_2} + \ldots \\ &= \mathcal{M}_{\lambda_p}^{DC_1} + \sum_{\lambda'_p} D^{J_p}_{\lambda_p,\lambda'_p}(\phi_p, \theta_p, 0)^* \mathcal{M}_{\lambda'_p}^{DC_2} + \ldots \; . \end{aligned} \tag{5.14}$$

5.1.2 Resonant contributions to the decay model

The description of the decay amplitude over the 4-body phase space of $\Lambda_b^0 \to p\pi^-\pi^+\pi^-$ decay is quite complicated and we have to include many resonances in order to reproduce the Run 1 data distributions. The magnitude of the amplitudes is tuned to improve the description of the invariant mass distributions. However, since the angular distributions depend mostly on the phases of these couplings, our simplified model is not able to reproduce them. We include all the resonances, compatible with the subinvariant masses, that have a status of at least 3 stars over 4 in the PDG [155]. In the following, the resonant contribution of the model are listed:

- $\Lambda_b^0 \to (N^{+*} \to (\Delta^{++} \to p\pi^+)\pi^-)\pi^-$
  $N^{+*}(1520), N^{+*}(1535), N^{+*}(1650), N^{+*}(1675), N^{+*}(1680), N^{+*}(1700), N^{+*}(1710), N^{+*}(1720), N^{+*}(1875), N^{+*}(1900), N^{+*}(2190)$

- $\Lambda_b^0 \to (N^{+*} \to p(\rho \to \pi^+\pi^-))\pi^-$
  $N^{+*}(1720), N^{+*}(1875), N^{+*}(1900)$
- $\Lambda_b^0 \to (N^{+*} \to p(\sigma \to \pi^+\pi^-))\pi^-$
  $N^{+*}(1535), N^{+*}(1650), N^{+*}(1675), N^{+*}(1680), N^{+*}(1700), N^{+*}(1875), N^{+*}(1900)$
- $\Lambda_b^0 \to (a_1^- \to (\rho \to \pi^+\pi^-)\pi^-)p$
- non resonant $\Lambda_b^0 \to p\pi^-\pi^+\pi^-$.

All the resonances have already been discovered and their existence is undisputed [155].

The model has more than 80 helicity couplings which means more than 160 free real parameters. In principle a fit to data could determine these values. However a more refined description of the resonances shape is needed. The efficiency and detector resolution are not taken into account in the model. Figure 5.1 shows the comparison between the toy-model distributions and the invariant mass distributions obtained from Run 1 data using the *sPlot* technique. A reasonably good agreement is obtained, which helps to better understand the dynamics of the decay and determine the most relevant resonant contributions, fundamental to optimize the binning scheme and avoid to dilute the asymmetries. In Appendix A.3 the model is described with more details and the values for all the parameters are listed.

The most important contributions are $\Lambda_b^0 \to N^{*+}\pi^-$ and $\Lambda_b^0 \to pa_1^-$. Since they are located in different region of the phase space they almost do not interfere and can be easily separated with a cut $m(p\pi^+\pi^-_{slow}) < 2.8\,\text{GeV}/c^2$ (see Figure 5.1 Top Right).

5.2 Binning scheme for optimised sensitivity to *CP* violation

The goal is to optimize the binning scheme to enhance the violating effect of *CPV* and identify the relevant phase-space regions where it comes from. *P*-odd *CPV* effects are present only in particular decay topologies, for example where there is interference between two partial waves with opposite parity. We studied several angular distributions of different decay topologies and, according to Table 5.1, conclude that $\Lambda_b^0 \to pa_1^-$ can't produce *CPV* effects if

- Λ_b^0 is not polarized. According to LHCb [156], ATLAS [157], and CMS [158] results the Λ_b^0 polarization is small and compatible with zero. *P*-odd *CPV* effects, difference between *P*-violating effects in particle and antiparticle decays, could just be introduced by the *P*-odd terms. If the Λ_b^0 is unpolarized, most of the *P*-odd terms vanish and *P* violation remains encoded only in the last bunch of terms. However, here, no different behaviour is possible between particle and antiparticle because all the weak helicity amplitudes are squared and no CKM phases could appear in the angular distribution.
- the $\Lambda_b^0 \to (a_1^- \to (\rho^0 \to \pi^+\pi^-)\pi^-)p$ is the dominant amplitude and does not interfere with other amplitudes. This is confirmed by our model, where a_1^- decays mostly to $\rho^0\pi^-$, consistently with expectations [155].

We exclude this region from the *CPV* measurement to avoid dilution when measuring the triple product asymmetries. To exclude the $\Lambda_b^0 \to a_1^-p$ contribution from the measurement we apply a cut $m(p\pi^+\pi^-_{slow}) < 2.8\,\text{GeV}/c^2$ (see Figure 5.1 Top Right). It represents about 45% of all the signal. We use this vetoed sample for checking that the

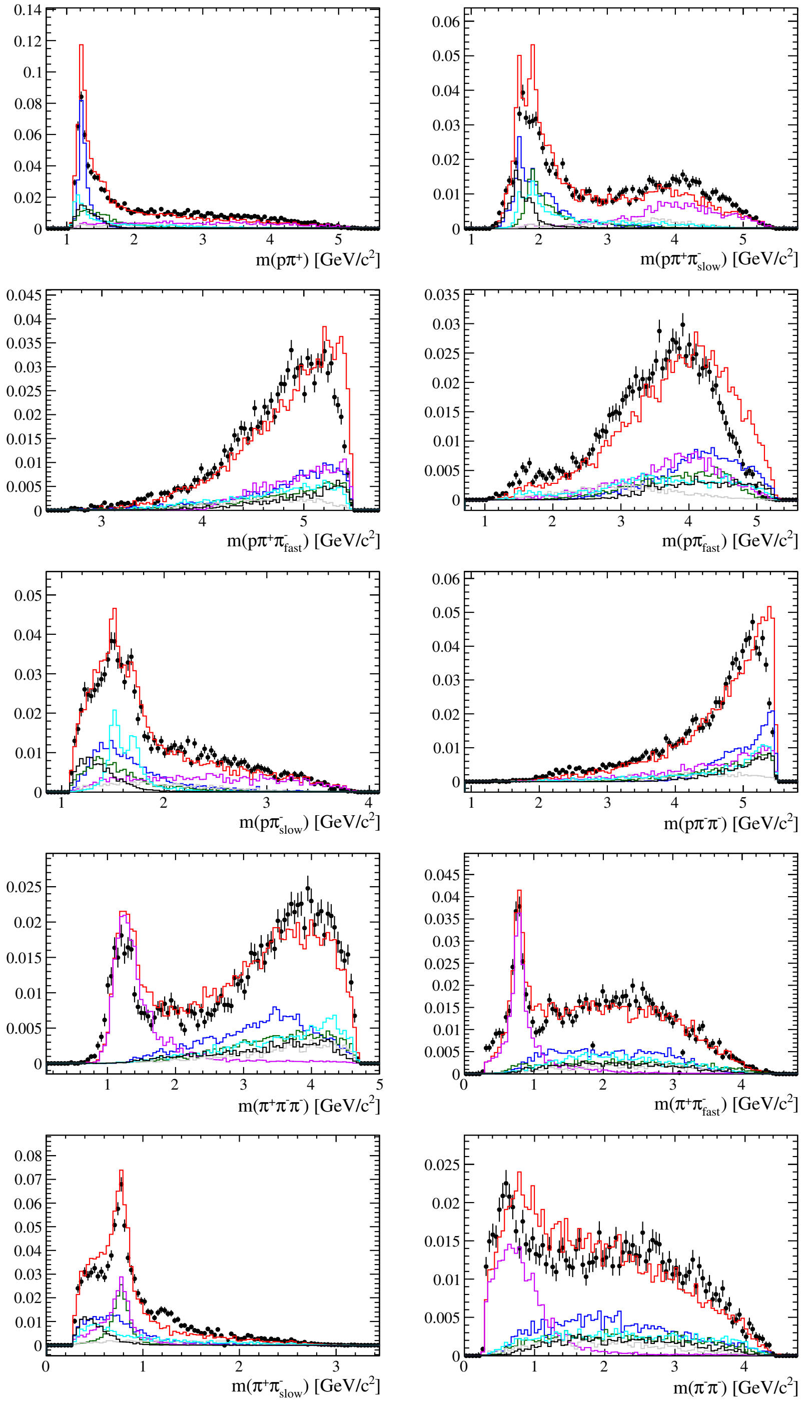

Figure 5.1: Invariant mass distributions for our amplitude model compared to Run 1 background subtracted data shown as black dot. The red histogram represents the decay model, in blu $\Lambda_b^0 \to (N^{+*} \to (\Delta^{++} \to p\pi^+)\pi^-)\pi^-$, in green $\Lambda_b^0 \to (N^{+*} \to p(\rho \to \pi^+\pi^-))\pi^-$, in black $\Lambda_b^0 \to (N^{+*} \to p(\sigma \to \pi^+\pi^-))\pi^-$, in purple $\Lambda_b^0 \to (a_1^- \to (\rho \to \pi^+\pi^-)\pi^-)p$, in grey the non resonant $\Lambda_b^0 \to p\pi^-\pi^+\pi^-$ contributions. The efficiency and detector resolution are not taken into account in the model.

measured asymmetries are compatible with no CPV in this region, but it will be not included in the calculation of the p-value for CPV.

Since the N^{*+} resonances have different spins, the decay $\Lambda_b^0 \to N^{*+}\pi^-$ proceeds through partial waves with opposite parities depending on the N^{*+} spin. For example, if N^{*+} has spin 1/2, the allowed partial waves are S and P, while if the spin is 3/2, P and D are allowed. Neglecting the higher partial waves contributions and assuming the two $N^{*+}_{1/2}$ and $N^{*+}_{3/2}$ resonances are close enough in mass, we have interference between S and P waves, the former due to $N^{*+}_{1/2}$ and the latter due to $N^{*+}_{3/2}$. This interference could introduce P-odd CPV effects. The last argument is just an example, confirmed by the angular distribution for the topology $\Lambda_b^0 \to (N^{+*} \to (\Delta^{++} \to p\pi^+)\pi^-)\pi^-$, shown in Table 5.2, where the two contributions from two general N^{*+} resonances with spin 1/2 ($N^{*+}_{1/2}$) and 3/2 ($N^{*+}_{3/2}$) are added coherently: it contains terms that are P-violating and if the P violation is different between particle and antiparticle then CPV occurs. The last four terms could introduce P-violating effects since they are proportional to $\sin\phi_p$ or $\sin 2\phi_p$ where the azimuthal angle ϕ_p is P-odd. Only the helicity amplitudes $A_\pm$ and $B_\pm$ refer to the weak decay $\Lambda_b^0 \to N^{+*}\pi^-$ and could contain a CKM phase. Then the CPV effects, difference between P-violating effects in particle and antiparticle decay, could just be encoded in the 8-th and 10-th angular term, where a CKM phase could appear.

We identify the interesting region where possible CPV effects could be present in the low mass $m(p\pi^+\pi^-_{slow})$ region, where several broad N^{*+} resonances interfere. Their contribution is indeed evident looking to both model, described in Section 5.1.2, and data in Figure 5.1 (Top Right). In this section we use a simpler decay model to study CPV effects and generate pseudoexperiments with three main resonant contributions:

1. $\Lambda_b^0 \to (N^{+*}_{1/2} \to (\Delta^{++} \to p\pi^+)\pi^-)\pi^-$;
2. $\Lambda_b^0 \to (N^{+*}_{3/2} \to (\Delta^{++} \to p\pi^+)\pi^-)\pi^-$;
3. $\Lambda_b^0 \to (a_1^- \to (\rho \to \pi^+\pi^-)\pi^-)p$.

This sample is used to test the sensitivity to CPV of the new binning scheme that will be introduced hereafter. In order to enhance the contribution of the CPV terms with respect to the CP conserving ones in the interference between two general N^{*+} resonances with 1/2 and 3/2 spins, we choose for the helicity amplitudes, defined in Table 5.2, the values shown in Table 5.3. The relations $b_{1/2/3+} = -b_{1/2/3-}$ are imposed by the P conservation in the strong decays $N^{*+}_{1/2,3/2} \to \Delta^{++}\pi^-$.

In Figure 5.2 we plot the asymmetry $a_{CP}^{\widehat{T}\text{-odd}}$, defined in Equation (1.47), versus the angle Φ (angle between the planes defined by the $p\pi^+$ and $\pi^-\pi^-$ systems) and Φ_p (azimuthal angle of the proton in the Δ^{++} rest frame). We are able to introduce CPV in region of phase space, although it integrates to zero over the phase space. CPV in N^{*+} resonances decay amplitudes is capable to reproduce, at least qualitatively, the asymmetry in $|\Phi|$ measured in Run 1. The sensitivity to CPV is increased using the Φ_p variable to divide the phase space because it is the angle directly related to the CPV amplitudes and to the specific decay N^{+*} topology. Instead we have dilution by dividing the phase space in $|\Phi|$ regions. However, we were able to reproduce $a_{CP}^{\widehat{T}\text{-odd}}$ different from 0 in $|\Phi|$, similarly to the effect that was measured in Run 1 data.

We define different binning schemes in order to improve the sensitivity to CPV:

- **scheme A**: the asymmetries are measured as a function of the angle $|\Phi|$, between

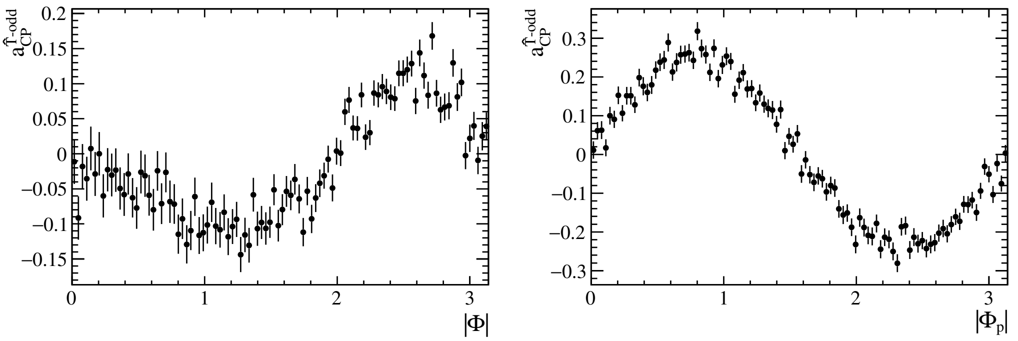

Figure 5.2: *CPV* asymmetries in regions of phase space are evident, while globally it integrates to 0. The sensitivity to *CPV* is is diluted in $|\Phi|$ (left plot) while it is increased in $|\Phi_p|$ (right plot).

the two decay planes defined by the $p\pi^-_{slow}$ and the $\pi^+\pi^-_{fast}$ tracks,

$$\Phi = \arccos\left(\hat{n}_{p\pi^-_{slow}} \cdot \hat{n}_{\pi^+\pi^-_{fast}}\right), \tag{5.15}$$

where $\hat{n}_{ab}$ is the normal to the plane defined by the particles a and b. The angle Φ is defined in the interval $(-\pi, \pi)$. We measure the asymmetries in 10 bins of $|\Phi|$ uniformly distributed in the interval $(0, \pi)$ for scheme A. This scheme has been used in the Run 1 analysis and could be subdivided into:

  - **scheme A1**: a cut $m(p\pi^+\pi^-_{slow}) > 2.8\,\text{GeV}/c^2$ to enhance the $\Lambda_b^0 \to pa_1^-(\to \rho\pi^-)$ contribution.
  - **scheme A2**: a cut $m(p\pi^+\pi^-_{slow}) < 2.8\,\text{GeV}/c^2$ to enhance the $\Lambda_b^0 \to N^*(\to \Delta^{++}\pi^-)\pi^-$ contribution.

- **scheme B**: this new binning scheme with respect to Run 1 analysis is designed to enhance the sensitivity to *CPV*. It improves the sensitivity to the interference of different N^* resonances with different spins in the topology $\Lambda_b^0 \to N^*(\to \Delta^{++}\pi^-)\pi^-$. It is defined In Table 5.4. This scheme could be subdivided into:
  - **scheme B1**: a cut $m(p\pi^+\pi^-_{slow}) > 2.8\,\text{GeV}/c^2$ is applied to enhance the $\Lambda_b^0 \to pa_1^-(\to \rho\pi^-)$ contribution.
  - **scheme B2**: a cut $m(p\pi^+\pi^-_{slow}) < 2.8\,\text{GeV}/c^2$ is applied to enhance the $\Lambda_b^0 \to N^*(\to \Delta^{++}\pi^-)\pi^-$ contribution.

We apply the binning schemes B1 and B2 to the pseudoexperiments to calculate the χ^2 with respect to the no *CPV* hypothesis. In Figure 5.3 the result is shown and compared with the binning scheme A used in Run 1. When the Run 1 binning scheme is used, we obtain a χ^2 different from 0 but far worse than the one obtained with the new binning schemes B1 and B2. When we exclude the $\Lambda_b^0 \to a_1^- p$ region, where we do not expect *CPV*, the sensitivity improves.

The new defined binning scheme is more sensitive to *CPV* effects in the $\Lambda_b^0 \to p\pi^-\pi^+\pi^-$ decay with respect to the analysis performed with Run 1 data [38] and it represents a big step forward. It demonstrates it is fundamental to understand the underlying dynamics of the $\Lambda_b^0 \to p\pi^-\pi^+\pi^-$ decay, with toys described in Section 5.1.2, to improve the sensitivity and avoid to dilute the asymmetry.

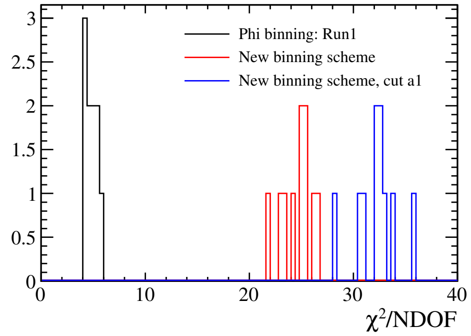

Figure 5.3: Calculated χ^2 using pseudoexperiments for no *CPV* hypothesis.

Table 5.1: Helicity amplitude decomposition for the $\Lambda_b^0 \to a_1^-(\rho^0\pi^-)p$ cascade. Only the helicity amplitudes denoted with capital letters refer to the weak decay $\Lambda_b^0 \to a_1^- p$ and could contain a *CKM* phase. The definition for the helicity amplitudes: $\mathcal{H}^{\Lambda_b^0\to a_1^- p}_{\lambda_{a_1^-}=0,\lambda_p=\pm1/2} = A_\pm$, $\mathcal{H}^{\Lambda_b^0\to a_1^- p}_{\lambda_{a_1^-}=\pm1,\lambda_p=\pm1/2} = B_\pm$, $\mathcal{H}^{a_1^-\to\rho^0\pi^-}_{\lambda_{a_1^-}=0,\lambda_{\pi^-}=0} = b_0$, $\mathcal{H}^{a_1^-\to\rho^0\pi^-}_{\lambda_{a_1^-}=\pm1,\lambda_{\pi^-}=0} = b_{1\pm}$, $\mathcal{H}^{\rho^0\to\pi^+\pi^-}_{\lambda_{\pi^+}=0,\lambda_{\pi^-}=0} = 1$.

Parity P	Coeff.	Helicity amplitudes	Pol.	Angular terms			
P-even	$+9/2$	$(\vert B_+\vert^2+\vert B_-\vert^2)\vert b_0\vert^2$			$\cos^2\theta_{\pi^+}$	$\sin^2\theta_{\rho^0}$	
	$+9/8$	$(\vert B_+\vert^2+\vert B_-\vert^2)(\vert b_{1+}\vert^2+\vert b_{1-}\vert^2)$			$\sin^2\theta_{\pi^+}$	$(1+\cos^2\theta_{\rho^0})$	
	$+9/4$	$(\vert B_+\vert^2-\vert B_-\vert^2)(\vert b_{1+}\vert^2-\vert b_{1-}\vert^2)$			$\sin^2\theta_{\pi^+}$	$\cos\theta_{\rho^0}$	
	$+9$	$(\vert A_+\vert^2+\vert A_-\vert^2)\vert b_0\vert^2$			$\cos^2\theta_{\pi^+}$	$\cos^2\theta_{\rho^0}$	
	$+9/4$	$(\vert A_+\vert^2+\vert A_-\vert^2)(\vert b_{1+}\vert^2+\vert b_{1-}\vert^2)$			$\sin^2\theta_{\pi^+}$	$\sin^2\theta_{\rho^0}$	
	$+9/4$	$(\vert B_+\vert^2-\vert B_-\vert^2)\Re((b_{1+}^*-b_{1-}^*)b_0)$			$\sin 2\theta_{\pi^+}$	$\sin\theta_{\rho^0}$	$\cos\phi_{\pi^+}$
	$-9/8$	$\big(2(\vert A_+\vert^2+\vert A_-\vert^2)-(\vert B_+\vert^2+\vert B_-\vert^2)\big)\,\Re((b_{1+}^*b_{1-})b_0)$			$\sin 2\theta_{\pi^+}$	$\sin 2\theta_{\rho^0}$	$\cos\phi_{\pi^+}$
	$+9/4$	$\big(2(\vert A_+\vert^2+\vert A_-\vert^2)-(\vert B_+\vert^2+\vert B_-\vert^2)\big)\,\Re(b_{1+}^*b_{1-})$			$\sin^2\theta_{\pi^+}$	$\sin^2\theta_{\rho^0}$	$\cos 2\phi_{\pi^+}$
P-even $\propto P_z$	$+9/4$	$(\vert B_+\vert^2+\vert B_-\vert^2)(\vert b_{1+}\vert^2-\vert b_{1-}\vert^2)$	P_z	$\cos\theta_{a_1^-}$	$\sin^2\theta_{\pi^+}$	$\cos\theta_{\rho^0}$	
	$+9/2$	$(\vert B_+\vert^2-\vert B_-\vert^2)\vert b_0\vert^2$	P_z	$\cos\theta_{a_1^-}$	$\cos^2\theta_{\pi^+}$	$\sin^2\theta_{\rho^0}$	
	$+9/8$	$(\vert B_+\vert^2-\vert B_-\vert^2)(\vert b_{1+}\vert^2+\vert b_{1-}\vert^2)$	P_z	$\cos\theta_{a_1^-}$	$\sin^2\theta_{\pi^+}$	$(1+\cos^2\theta_{\rho^0})$	
	-9	$(\vert A_+\vert^2-\vert A_-\vert^2)\vert b_0\vert^2$	P_z	$\cos\theta_{a_1^-}$	$\cos^2\theta_{\pi^+}$	$\cos^2\theta_{\rho^0}$	
	$-9/4$	$(\vert A_+\vert^2-\vert A_-\vert^2)(\vert b_{1+}\vert^2+\vert b_{1-}\vert^2)$	P_z	$\cos\theta_{a_1^-}$	$\sin^2\theta_{\pi^+}$	$\sin^2\theta_{\rho^0}$	
	$+9/4$	$(\vert B_+\vert^2+\vert B_-\vert^2)\Re((b_{1+}^*-b_{1-}^*)b_0)$	P_z	$\cos\theta_{a_1^-}$	$\sin 2\theta_{\pi^+}$	$\sin\theta_{\rho^0}$	$\cos\phi_{\pi^+}$
	$+9/8$	$\big(2(\vert A_+\vert^2-\vert A_-\vert^2)+(\vert B_+\vert^2-\vert B_-\vert^2)\big)\,\Re((b_{1+}^*+b_{1-}^*)b_0)$	P_z	$\cos\theta_{a_1^-}$	$\sin 2\theta_{\pi^+}$	$\sin 2\theta_{\rho^0}$	$\cos\phi_{\pi^+}$
	$-9/4$	$\big(2(\vert A_+\vert^2-\vert A_-\vert^2)+(\vert B_+\vert^2-\vert B_-\vert^2)\big)\,\Re(b_{1+}^*b_{1-})$	P_z	$\cos\theta_{a_1^-}$	$\sin^2\theta_{\pi^+}$	$\sin^2\theta_{\rho^0}$	$\cos 2\phi_{\pi^+}$
	$+9\sqrt{2}/2$	$\Re(A_+^*B_+-A_-^*B_-)\vert b_0\vert^2$	P_z	$\sin\theta_{a_1^-}$	$\cos^2\theta_{\pi^+}$	$\sin 2\theta_{\rho^0}$	$\cos\phi_{\rho^0}$
	$-9\sqrt{2}/8$	$(\vert b_{1+}\vert^2+\vert b_{1-}\vert^2)\Re(A_+^*B_+-A_-^*B_-)$	P_z	$\sin\theta_{a_1^-}$	$\sin^2\theta_{\pi^+}$	$\sin 2\theta_{\rho^0}$	$\cos\phi_{\rho^0}$
	$-9\sqrt{2}/4$	$(\vert b_{1+}\vert^2-\vert b_{1-}\vert^2)\Re(A_+^*B_++A_-^*B_-)$	P_z	$\sin\theta_{a_1^-}$	$\sin^2\theta_{\pi^+}$	$\sin\theta_{\rho^0}$	$\cos\phi_{\rho^0}$
	$+9\sqrt{2}/4$	$\Re((A_-^*B_--B_+^*A_+)b_{1+}^*b_{1-})$	P_z	$\sin\theta_{a_1^-}$	$\sin^2\theta_{\pi^+}$	$(1+\cos\theta_{\rho^0})\sin\theta_{\rho^0}$	$\cos(2\phi_{\pi^+}+\phi_{\rho^0})$
	$+9\sqrt{2}/4$	$\Re((A_+^*B_+-B_-^*A_-)b_{1+}^*b_{1-})$	P_z	$\sin\theta_{a_1^-}$	$\sin^2\theta_{\pi^+}$	$(1-\cos\theta_{\rho^0})\sin\theta_{\rho^0}$	$\cos(2\phi_{\pi^+}-\phi_{\rho^0})$
	$+9\sqrt{2}/4$	$\Re((B_+^*b_{1+}^*A_+-B_-^*b_{1-}^*A_-)b_0)$	P_z	$\sin\theta_{a_1^-}$	$\sin 2\theta_{\pi^+}$	$\cos\theta_{\rho^0}$	$\cos(\theta_{\pi^+}+\theta_{\rho^0})$
	$+9\sqrt{2}/4$	$\Re((A_+^*b_{1-}^*B_+-A_-^*b_{1+}^*B_-+B_+^*b_{1+}^*A_+-B_-^*b_{1-}^*A_-)b_0)$	P_z	$\sin\theta_{a_1^-}$	$\sin 2\theta_{\pi^+}$	$\cos^2\theta_{\rho^0}$	$\cos(\phi_{\pi^+}+\phi_{\rho^0})$
	$-9\sqrt{2}/4$	$\Re((A_+^*b_{1-}^*B_+-A_-^*b_{1+}^*B_-)b_0)$	P_z	$\sin\theta_{a_1^-}$	$\sin 2\theta_{\pi^+}$		$\cos(\phi_{\pi^+}+\phi_{\rho^0})$
	$-9\sqrt{2}/4$	$\Re((B_+^*b_{1-}^*A_+-B_-^*b_{1+}^*A_-)b_0)$	P_z	$\sin\theta_{a_1^-}$	$\sin 2\theta_{\pi^+}$	$\cos\theta_{\rho^0}$	$\cos(\phi_{\pi^+}-\phi_{\rho^0})$
	$+9\sqrt{2}/4$	$\Re((A_+^*b_{1+}^*B_+-A_-^*b_{1-}^*B_-+B_+^*b_{1-}^*A_+-B_-^*b_{1+}^*A_-)b_0)$	P_z	$\sin\theta_{a_1^-}$	$\sin 2\theta_{\pi^+}$	$\cos^2\theta_{\rho^0}$	$\cos(\phi_{\pi^+}-\phi_{\rho^0})$
	$-9\sqrt{2}/4$	$\Re((A_+^*b_{1+}^*B_+-A_-^*b_{1-}^*B_-)b_0)$	P_z	$\sin\theta_{a_1^-}$	$\sin 2\theta_{\pi^+}$		$\cos(\phi_{\pi^+}-\phi_{\rho^0})$
P-odd $\propto P_z$	$+9/4$	$(\vert B_+\vert^2+\vert B_-\vert^2)\Im((b_{1+}^*+b_{1-}*)b_0)$	P_z	$\cos\theta_{a_1^-}$	$\sin 2\theta_{\pi^+}$	$\sin\theta_{\rho^0}$	$\sin\phi_{\pi^+}$
	$+9/8$	$(2(\vert A_+\vert^2-\vert A_-\vert^2)+(\vert B_+\vert^2-\vert B_-\vert^2))\Im((b_{1+}^*-b_{1-}^*)b_0)$	P_z	$\cos\theta_{a_1^-}$	$\sin 2\theta_{\pi^+}$	$\sin 2\theta_{\rho^0}$	$\sin\phi_{\pi^+}$
	$-9/4$	$(2(\vert A_+\vert^2-\vert A_-\vert^2)+(\vert B_+\vert^2-\vert B_-\vert^2))\Im(b_{1+}^*b_{1-})$	P_z	$\cos\theta_{a_1^-}$	$\sin^2\theta_{\pi^+}$	$\sin^2\theta_{\rho^0}$	$\sin 2\phi_{\pi^+}$
	$-9\sqrt{2}/2$	$\Im(A_+^*B_++A_-^*B_-)\vert b_0\vert^2$	P_z	$\sin\theta_{a_1^-}$	$\cos^2\theta_{\pi^+}$	$\sin 2\theta_{\rho^0}$	$\sin\phi_{\rho^0}$
	$+9\sqrt{2}/8$	$(\vert b_{1+}\vert^2+\vert b_{1-}\vert^2)\Im(A_+^*B_++A_-^*B_-)$	P_z	$\sin\theta_{a_1^-}$	$\sin^2\theta_{\pi^+}$	$\sin 2\theta_{\rho^0}$	$\sin\phi_{\rho^0}$
	$+9\sqrt{2}/4$	$(\vert b_{1+}\vert^2-\vert b_{1-}\vert^2)\Im(A_+^*B_+-A_-^*B_-)$	P_z	$\sin\theta_{a_1^-}$	$\sin^2\theta_{\pi^+}$	$\sin\theta_{\rho^0}$	$\sin\phi_{\rho^0}$
	$+9\sqrt{2}/4$	$\Im((A_-^*B_--B_+^*A_+)b_{1+}^*b_{1-})$	P_z	$\sin\theta_{a_1^-}$	$\sin^2\theta_{\pi^+}$	$(1+\cos\theta_{\rho^0})\sin\theta_{\rho^0}$	$\sin(2\phi_{\pi^+}+\phi_{\rho^0})$
	$+9\sqrt{2}/4$	$\Im((A_+^*B_+-B_-^*A_-)b_{1+}^*b_{1-})$	P_z	$\sin\theta_{a_1^-}$	$\sin^2\theta_{\pi^+}$	$(1-\cos\theta_{\rho^0})\sin\theta_{\rho^0}$	$\sin(2\phi_{\pi^+}-\phi_{\rho^0})$
	$+9\sqrt{2}/4$	$\Im((B_+^*b_{1+}^*A_+-B_-^*b_{1-}^*A_-)b_0)$	P_z	$\sin\theta_{a_1^-}$	$\sin 2\theta_{\pi^+}$	$\cos\theta_{\rho^0}$	$\sin(\phi_{\pi^+}+\phi_{\rho^0})$
	$-9\sqrt{2}/4$	$\Im((A_+^*b_{1-}^*B_++A_-^*b_{1+}^*B_--B_+^*b_{1+}^*A_+-B_-^*b_{1-}^*A_-)b_0)$	P_z	$\sin\theta_{a_1^-}$	$\sin 2\theta_{\pi^+}$	$\cos^2\theta_{\rho^0}$	$\sin(\phi_{\pi^+}+\phi_{\rho^0})$
	$+9\sqrt{2}/4$	$\Im((A_+^*b_{1-}^*B_+-A_-^*b_{1+}^*B_-)b_0)$	P_z	$\sin\theta_{a_1^-}$	$\sin 2\theta_{\pi^+}$		$\sin(\phi_{\pi^+}+\phi_{\rho^0})$
	$+9\sqrt{2}/4$	$\Im((B_+^*b_{1-}^*A_++B_-^*b_{1+}^*A_-)b_0)$	P_z	$\sin\theta_{a_1^-}$	$\sin 2\theta_{\pi^+}$	$\cos\theta_{\rho^0}$	$\sin(\phi_{\pi^+}-\phi_{\rho^0})$
	$+9\sqrt{2}/4$	$\Im((A_+^*b_{1+}^*B_++A_-^*b_{1-}^*B_--B_+^*b_{1-}^*A_+-B_-^*b_{1+}^*A_-)b_0)$	P_z	$\sin\theta_{a_1^-}$	$\sin 2\theta_{\pi^+}$	$\cos^2\theta_{\rho^0}$	$\sin(\phi_{\pi^+}-\phi_{\rho^0})$
	$+9\sqrt{2}/4$	$\Im((A_+^*b_{1+}^*B_++A_-^*b_{1-}^*B_-)b_0)$	P_z	$\sin\theta_{a_1^-}$	$\sin 2\theta_{\pi^+}$		$\sin(\phi_{\pi^+}-\phi_{\rho^0})$
P-odd	$+9/4$	$(\vert B_+\vert^2-\vert B_-\vert^2)\Im((b_{1+}^*+b_{1-}^*)b_0)$			$\sin 2\theta_{\pi^+}$	$\sin\theta_{\rho^0}$	$\sin\phi_{\pi^+}$
	$-9/8$	$(2(\vert A_+\vert^2+\vert A_-\vert^2)-(\vert B_+\vert^2+\vert B_-\vert^2))\Im((b_{1+}^*-b_{1-}^*)b_0)$			$\sin 2\theta_{\pi^+}$	$\sin 2\theta_{\rho^0}$	$\sin\phi_{\pi^+}$
	$+9/4$	$(2(\vert A_+\vert^2+\vert A_-\vert^2)-(\vert B_+\vert^2+\vert B_-\vert^2))\Im(b_{1+}^*b_{1-})$			$\sin^2\theta_{\pi^+}$	$\sin^2\theta_{\rho^0}$	$\sin 2\phi_{\pi^+}$

Table 5.2: Helicity amplitude decomposition for the $\Lambda_b^0 \to (N^{+*} \to (\Delta^{++} \to p\pi^+)\pi^-)\pi^-$ cascade, with the Λ_b^0 polarization assumed vanishing and parity conservation in the decay of Δ^{++}. The definition for the helicity amplitudes: $\mathcal{H}^{\Lambda_b^0 \to N^{+*}(3/2)\pi^-}_{\lambda_{N^{+*}(3/2)}=\pm 1/2, \lambda_{\pi^-}=0} = A_\pm$, $\mathcal{H}^{\Lambda_b^0 \to N^{+*}(1/2)\pi^-}_{\lambda_{N^{+*}(1/2)}=\pm 1/2, \lambda_{\pi^-}=0} = B_\pm$, $\mathcal{H}^{N^{+*}(3/2) \to \Delta^{++}\pi^-}_{\lambda_{\Delta^{++}}=\pm 1/2, \lambda_{\pi^-}=0} = b_{1\pm}$, $\mathcal{H}^{N^{+*}(3/2) \to \Delta^{++}\pi^-}_{\lambda_{\Delta^{++}}=\pm 3/2, \lambda_{\pi^-}=0} = b_{2\pm}$, $\mathcal{H}^{N^{+*}(1/2) \to \Delta^{++}\pi^-}_{\lambda_{\Delta^{++}}=\pm 1/2, \lambda_{\pi^-}=0} = b_{3\pm}$, $\mathcal{H}^{\Delta^{++} \to p\pi^+}_{\lambda_p=+1/2, \lambda_{\pi^+}=0} + \mathcal{H}^{\Delta^{++} \to p\pi^+}_{\lambda_p=-1/2, \lambda_{\pi^+}=0} = 1$, $\mathcal{H}^{\Delta^{++} \to p\pi^+}_{\lambda_p=+1/2, \lambda_{\pi^+}=0} - \mathcal{H}^{\Delta^{++} \to p\pi^+}_{\lambda_p=-1/2, \lambda_{\pi^+}=0} = 0$.

Coeff.	Helicity amplitudes	Angular terms		
$\sqrt{2}$	$Re((A_+^* B_+ + A_-^* B_-)(b_{1+}^* b_{3+} + b_{1-}^* b_{3-}^*))$	$(1 + 3\cos^2\theta_p)$	$\cos\theta_{\Delta^{++}}$	
$1/2$	$(\lvert B_+\rvert^2 + \lvert B_-\rvert^2)(\lvert b_{3+}\rvert^2 + \lvert b_{3-}\rvert^2)$	$(1 + 3\cos^2\theta_p)$		
$9/4$	$(\lvert A_+\rvert^2 + \lvert A_-\rvert^2)(\lvert b_{2+}\rvert^2 + \lvert b_{2-}\rvert^2)$	$\sin^2\theta_p$	$\sin^2\theta_{\Delta^{++}}$	
$1/4$	$(\lvert A_+\rvert^2 + \lvert A_-\rvert^2)(\lvert b_{1+}\rvert^2 + \lvert b_{1-}\rvert^2)$	$(1 + 3\cos^2\theta_p)$	$(1 + 3\cos^2\theta_{\Delta^{++}})$	
$-3\sqrt{2}/2$	$Re((A_+^* B_+ + A_-^* B_-)(b_{2+}^* b_{3+} + b_{2-}^* b_{3-}))$	$\sin 2\theta_p$	$\sin\theta_{\Delta^{++}}$	$\cos\phi_p$
$-3/2$	$(\lvert A_+\rvert^2 + \lvert A_-\rvert^2)Re(b_{1+}^* b_{2+} + b_{1-}^* b_{2-})$	$\sin 2\theta_p$	$\sin 2\theta_{\Delta^{++}}$	$\cos\phi_p$
$3/2$	$(\lvert A_+\rvert^2 + \lvert A_-\rvert^2)Re(b_{1+}^* b_{2-} + b_{1-}^* b_{2+})$	$\sin^2\theta_p$	$\sin^2\theta_{\Delta^{++}}$	$\cos 2\phi_p$
$-3\sqrt{2}/4$	$Im((A_+^* B_+ - A_-^* B_-)(b_{2+}^* b_{3+} + b_{2-}^* b_{3-}))$	$\sin 2\theta_p$	$\sin 2\theta_{\Delta^{++}}$	$\sin\phi_p$
$-3/2$	$(\lvert A_+\rvert^2 - \lvert A_-\rvert^2)Im(b_{1+}^* b_{2+} + b_{1-}^* b_{2-})$	$\sin 2\theta_p$	$(1 - 3\cos^2\theta_{\Delta^{++}})\sin\theta_{\Delta^{++}}$	$\sin\phi_p$
$3\sqrt{2}/2$	$Im((A_+^* B_- - A_-^* B_-)(b_{2+}^* b_{3-} + b_{2-}^* b_{3+}))$	$\sin^2\theta_p$	$\sin^2\theta_{\Delta^{++}}$	$\sin 2\phi_p$
$-9/4$	$(\lvert A_+\rvert^2 - \lvert A_-\rvert^2)Im(b_{1+}^* b_{2-} + b_{1-}^* b_{2+})$	$\sin^2\theta_p$	$\sin\theta_{\Delta^{++}}\sin 2\theta_{\Delta^{++}}$	$\sin 2\phi_p$

Table 5.3: The specific choice of amplitudes used to include *CPV* in the MC sample for decays $\Lambda_b^0 \to (N_{1/2}^{+*} \to (\Delta^{++} \to p\pi^+)\pi^-)\pi^-$ and $\overline{\Lambda}_b^0 \to (N_{1/2}^{-*} \to (\Delta^{--} \to \overline{p}\pi^-)\pi^+)\pi^+$.

	A_+	A_-	B_+	B_-	$b_{1+}/-b_{1-}$	$b_{2+}/-b_{2-}$	$b_{2+}/-b_{2-}$
Λ_b^0	1	0	i	i	0	1	1
$\overline{\Lambda}_b^0$	1	0	i	$-i$	0	1	1

Table 5.4: Definition of the binning scheme B.

Bin number	Polar angles	Azimuthal angles
1	$\theta_p \in [0,\pi/4] \& \theta_{\Delta^{++}} \in [0,\pi/4]$ $\theta_p \in [\pi/2,3\pi/4] \& \theta_{\Delta^{++}} \in [\pi/2,3\pi/4]$	$\lvert\Phi_p\rvert \in [0,\pi/2]$
2	$\theta_p \in [0,\pi/4] \& \theta_{\Delta^{++}} \in [\pi/4,\pi/2]$ $\theta_p \in [\pi/2,3\pi/4] \& \theta_{\Delta^{++}} \in [3\pi/4,\pi]$	$\lvert\Phi_p\rvert \in [0,\pi/2]$
3	$\theta_p \in [0,\pi/4] \& \theta_{\Delta^{++}} \in [\pi/2,3\pi/4]$ $\theta_p \in [\pi/2,3\pi/4] \& \theta_{\Delta^{++}} \in [0,\pi/4]$	$\lvert\Phi_p\rvert \in [0,\pi/2]$
4	$\theta_p \in [0,\pi/4] \& \theta_{\Delta^{++}} \in [3\pi/4,\pi]$ $\theta_p \in [\pi/2,3\pi/4] \& \theta_{\Delta^{++}} \in [\pi/4,\pi/2]$	$\lvert\Phi_p\rvert \in [0,\pi/2]$
5	$\theta_p \in [\pi/4,\pi/2] \& \theta_{\Delta^{++}} \in [0,\pi/4]$ $\theta_p \in [3\pi/4,\pi] \& \theta_{\Delta^{++}} \in [\pi/2,3\pi/4]$	$\lvert\Phi_p\rvert \in [0,\pi/2]$
6	$\theta_p \in [\pi/4,\pi/2] \& \theta_{\Delta^{++}} \in [\pi/4,\pi/2]$ $\theta_p \in [3\pi/4,\pi] \& \theta_{\Delta^{++}} \in [3\pi/4,\pi]$	$\lvert\Phi_p\rvert \in [0,\pi/2]$
7	$\theta_p \in [\pi/4,\pi/2] \& \theta_{\Delta^{++}} \in [\pi/2,3\pi/4]$ $\theta_p \in [3\pi/4,\pi] \& \theta_{\Delta^{++}} \in [0,\pi/4]$	$\lvert\Phi_p\rvert \in [0,\pi/2]$
8	$\theta_p \in [\pi/4,\pi/2] \& \theta_{\Delta^{++}} \in [3\pi/4,\pi]$ $\theta_p \in [3\pi/4,\pi] \& \theta_{\Delta^{++}} \in [\pi/4,\pi/2]$	$\lvert\Phi_p\rvert \in [0,\pi/2]$
9	$\theta_p \in [0,\pi/4] \& \theta_{\Delta^{++}} \in [0,\pi/4]$ $\theta_p \in [\pi/2,3\pi/4] \& \theta_{\Delta^{++}} \in [\pi/2,3\pi/4]$	$\lvert\Phi_p\rvert \in [\pi/2,\pi]$
10	$\theta_p \in [0,\pi/4] \& \theta_{\Delta^{++}} \in [\pi/4,\pi/2]$ $\theta_p \in [\pi/2,3\pi/4] \& \theta_{\Delta^{++}} \in [3\pi/4,\pi]$	$\lvert\Phi_p\rvert \in [\pi/2,\pi]$
11	$\theta_p \in [0,\pi/4] \& \theta_{\Delta^{++}} \in [\pi/2,3\pi/4]$ $\theta_p \in [\pi/2,3\pi/4] \& \theta_{\Delta^{++}} \in [0,\pi/4]$	$\lvert\Phi_p\rvert \in [\pi/2,\pi]$
12	$\theta_p \in [0,\pi/4] \& \theta_{\Delta^{++}} \in [3\pi/4,\pi]$ $\theta_p \in [\pi/2,3\pi/4] \& \theta_{\Delta^{++}} \in [\pi/4,\pi/2]$	$\lvert\Phi_p\rvert \in [\pi/2,\pi]$
13	$\theta_p \in [\pi/4,\pi/2] \& \theta_{\Delta^{++}} \in [0,\pi/4]$ $\theta_p \in [3\pi/4,\pi] \& \theta_{\Delta^{++}} \in [\pi/2,3\pi/4]$	$\lvert\Phi_p\rvert \in [\pi/2,\pi]$
14	$\theta_p \in [\pi/4,\pi/2] \& \theta_{\Delta^{++}} \in [\pi/4,\pi/2]$ $\theta_p \in [3\pi/4,\pi] \& \theta_{\Delta^{++}} \in [3\pi/4,\pi]$	$\lvert\Phi_p\rvert \in [\pi/2,\pi]$
15	$\theta_p \in [\pi/4,\pi/2] \& \theta_{\Delta^{++}} \in [\pi/2,3\pi/4]$ $\theta_p \in [3\pi/4,\pi] \& \theta_{\Delta^{++}} \in [0,\pi/4]$	$\lvert\Phi_p\rvert \in [\pi/2,\pi]$
16	$\theta_p \in [\pi/4,\pi/2] \& \theta_{\Delta^{++}} \in [3\pi/4,\pi]$ $\theta_p \in [3\pi/4,\pi] \& \theta_{\Delta^{++}} \in [\pi/4,\pi/2]$	$\lvert\Phi_p\rvert \in [\pi/2,\pi]$

CHAPTER 6

Extraction of the asymmetries

The selected data sample is split into four subsamples according to the Λ_b^0 ($\overline{\Lambda}_b^0$) flavour and the sign of $C_{\widehat{T}}$ ($\overline{C}_{\widehat{T}}$). A simultaneous maximum likelihood fit to the $m(p\pi^-\pi^+\pi^-)$ distribution of the four subsamples is used to determine the number of signal and background events, and the asymmetries $A_{\widehat{T}}$ and $\overline{A}_{\widehat{T}}$. The fit model is described in Chapter 4, the shape parameters are common for all the 4 subsamples, while the yields of each component are estimated separately. The two asymmetries $A_{\widehat{T}}$ and $\overline{A}_{\widehat{T}}$ are included in the fit model as

$$\begin{aligned}
N_{\Lambda_b^0, C_{\widehat{T}}>0} &= \frac{1}{2} N_{\Lambda_b^0}(1 + A_{\widehat{T}}) \\
N_{\Lambda_b^0, C_{\widehat{T}}<0} &= \frac{1}{2} N_{\Lambda_b^0}(1 - A_{\widehat{T}}) \\
N_{\overline{\Lambda}_b^0, -\overline{C}_{\widehat{T}}>0} &= \frac{1}{2} N_{\overline{\Lambda}_b^0}(1 + \overline{A}_{\widehat{T}}) \\
N_{\overline{\Lambda}_b^0, -\overline{C}_{\widehat{T}}<0} &= \frac{1}{2} N_{\overline{\Lambda}_b^0}(1 - \overline{A}_{\widehat{T}}) \qquad (6.1)
\end{aligned}$$

following the definition of $A_{\widehat{T}}$, $\overline{A}_{\widehat{T}}$ in Equation (1.45). The *CP*-violating (P-violating) asymmetry $a_{CP}^{\widehat{T}\text{-odd}}$ ($a_{P}^{\widehat{T}\text{-odd}}$) is then calculated from $A_{\widehat{T}}$ and $\overline{A}_{\widehat{T}}$. Two different approaches are followed to search for CPV: a measurement integrated over phase space and measurements in different regions of phase space.

6.1 Search for *CP* violation integrated over phase space

A measurement integrated over phase space is performed. The results of this approach are obtained by fitting the full data sample and the results are shown in Figure 6.1 and Table 6.1.

The extracted asymmetries are listed in Table 6.2, where the uncertainties are statistical only. Negligible correlation ($< 0.1\%$) is found between $A_{\widehat{T}}$ and $\overline{A}_{\widehat{T}}$ asymmetries.

6.2 Search for localised *CP* violation in regions of the phase space

We perform measurements of triple-product asymmetries in bins of the phase space in order to improve the sensitivity to *CP* violation using the binning schemes defined in Section 5.2:

- **Scheme *A***: the fits for each bin are shown in Figures 6.2 and 6.3 and $a_{CP}^{\widehat{T}\text{-odd}}$ as a function of $|\Phi|$ is shown in Figure 6.4

Table 6.1: Results of the simultaneous fit to Run 1 and Run 2 data for the $\Lambda_b^0 \to p\pi^-\pi^+\pi^-$ sample.

Variable	Value
$\mu(\Lambda_b^0)(\mathrm{MeV}/c^2)$	5617.9 ± 0.1
$\sigma(\mathrm{MeV}/c^2)$	17.8 ± 0.1
$c_{Part.\ reco}$	-29.0 ± 19.5
$p_{Part.\ reco}$	0.74 ± 0.30
$\lambda_{comb}(c^2/\mathrm{GeV})$	-4.86 ± 0.10
$A_{\widehat{T}}(B^0 \to K^+\pi^-\pi^+\pi^-)(\%)$	7.7 ± 9.7
$\overline{A}_{\widehat{T}}(B^0 \to K^+\pi^-\pi^+\pi^-)(\%)$	-2.1 ± 9.7
$n_{\Lambda_b^0}(B^0 \to K^+\pi^-\pi^+\pi^-)$	1058 ± 106
$n_{\overline{\Lambda}_b^0}(B^0 \to K^+\pi^-\pi^+\pi^-)$	1054 ± 105
$A_{\widehat{T}}(\Lambda_b^0 \to pK^-\pi^+\pi^-)(\%)$	-0.3 ± 1.2
$\overline{A}_{\widehat{T}}(\Lambda_b^0 \to pK^-\pi^+\pi^-)(\%)$	-0.1 ± 1.2
$n_{\Lambda_b^0}(\Lambda_b^0 \to pK^-\pi^+\pi^-)$	2522 ± 31
$n_{\overline{\Lambda}_b^0}(\Lambda_b^0 \to pK^-\pi^+\pi^-)$	2510 ± 31
$A_{\widehat{T}}(Part.\ reco)(\%)$	1.7 ± 4.6
$\overline{A}_{\widehat{T}}(Part.\ reco)(\%)$	-0.4 ± 4.3
$n_{\Lambda_b^0}(Part.\ reco)$	2744 ± 182
$n_{\overline{\Lambda}_b^0}(Part.\ reco)$	2892 ± 179
$A_{\widehat{T}}(comb.)(\%)$	2.1 ± 1.8
$\overline{A}_{\widehat{T}}(comb.)(\%)$	2.4 ± 1.9
$n_{\Lambda_b^0}(comb.)$	13627 ± 292
$n_{\overline{\Lambda}_b^0}(comb.)$	12796 ± 289
$A_{\widehat{T}}(\Lambda_b^0 \to p\pi^-\pi^+\pi^-)(\%)$	-4.68 ± 0.99
$\overline{A}_{\widehat{T}}(\Lambda_b^0 \to p\pi^-\pi^+\pi^-)(\%)$	-3.29 ± 0.99
$n_{\Lambda_b^0}(\Lambda_b^0 \to p\pi^-\pi^+\pi^-)$	13790 ± 142
$n_{\overline{\Lambda}_b^0}(\Lambda_b^0 \to p\pi^-\pi^+\pi^-)$	13803 ± 142

  - **Scheme $\boldsymbol{A_1}$**: the fits for each bin are shown in Figures 6.5 and 6.6 and $a_{CP}^{\widehat{T}\text{-odd}}$ as a function of $|\Phi|$ is shown in Figure 6.9.
  - **Scheme $\boldsymbol{A_2}$**: the fits for each bin are shown in Figures 6.7 and 6.8 and $a_{CP}^{\widehat{T}\text{-odd}}$ as a function of $|\Phi|$ is shown in Figure 6.10

- **Scheme $\boldsymbol{B}$**:
  - **Scheme $\boldsymbol{B_1}$**: the fits for each bin are shown in Figures 6.11, 6.12 and 6.13 and $a_{CP}^{\widehat{T}\text{-odd}}$ as a function of the bins is shown in Figure 6.14.
  - **Scheme $\boldsymbol{B_2}$**: the fits for each bin are shown in Figures 6.15 6.16 and 6.17 and $a_{CP}^{\widehat{T}\text{-odd}}$ as a function of the bins is shown in Figure 6.18.

Table 6.2: Fit results for asymmetries integrated over phase space. For comparison we report the results for the dataset used in this thesis and for the Run 1 dataset already published [38]. With the additional statistics we improve a factor of 2 the sensitivity. The reported uncertainty is only statistical, however the systematic uncertainty is negligible.

Dataset	$A_{\widehat{T}}$ (%)	$\overline{A}_{\widehat{T}}$ (%)	$a_P^{\widehat{T}\text{-odd}}$ (%)	$a_{CP}^{\widehat{T}\text{-odd}}$ (%)
This thesis (2011-2017)	-4.68 ± 0.99	-3.29 ± 0.99	-3.98 ± 0.70	-0.70 ± 0.70
Run 1 (2011-2012)	-2.56 ± 2.05	-4.86 ± 2.05	-3.71 ± 1.45	1.15 ± 1.45

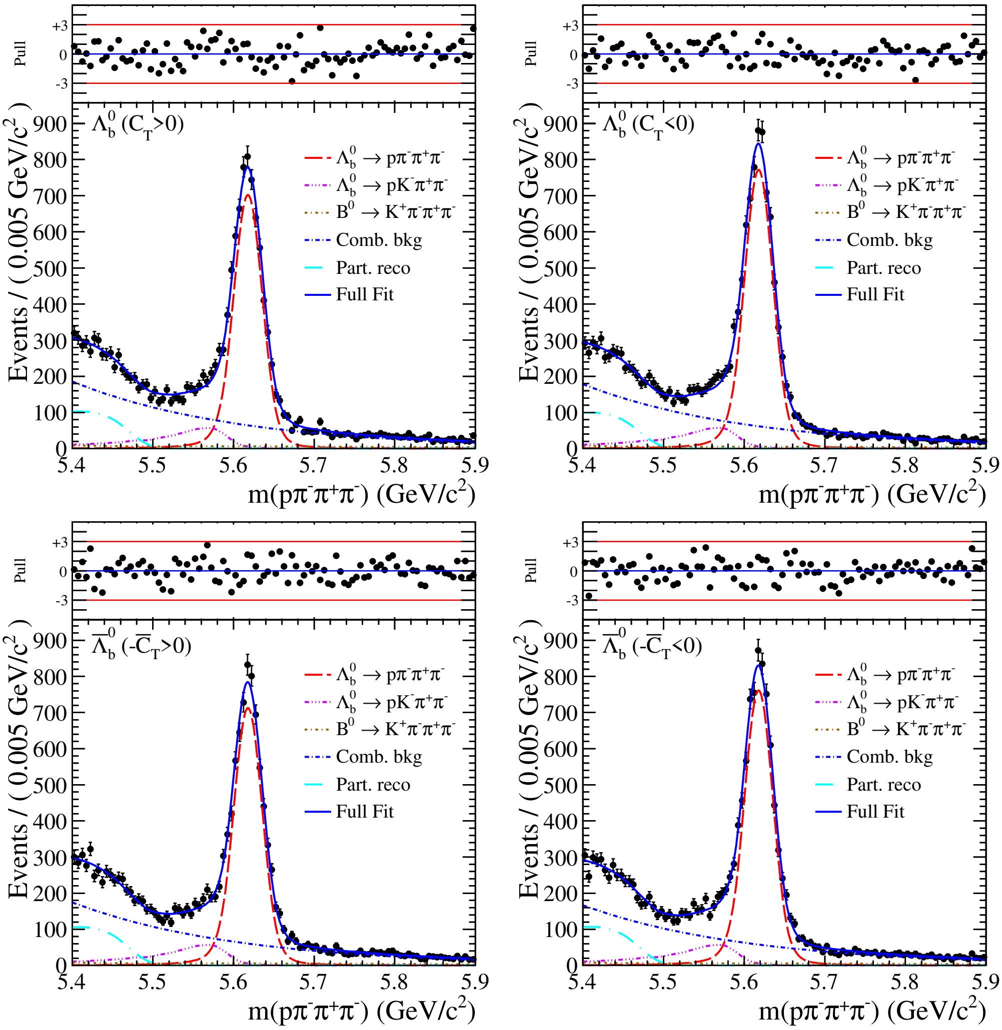

Figure 6.1: Fit projections on the $m(p\pi^-\pi^+\pi^-)$ distribution for the four different subsamples for $\Lambda_b^0 \rightarrow p\pi^-\pi^+\pi^-$ decay modes.

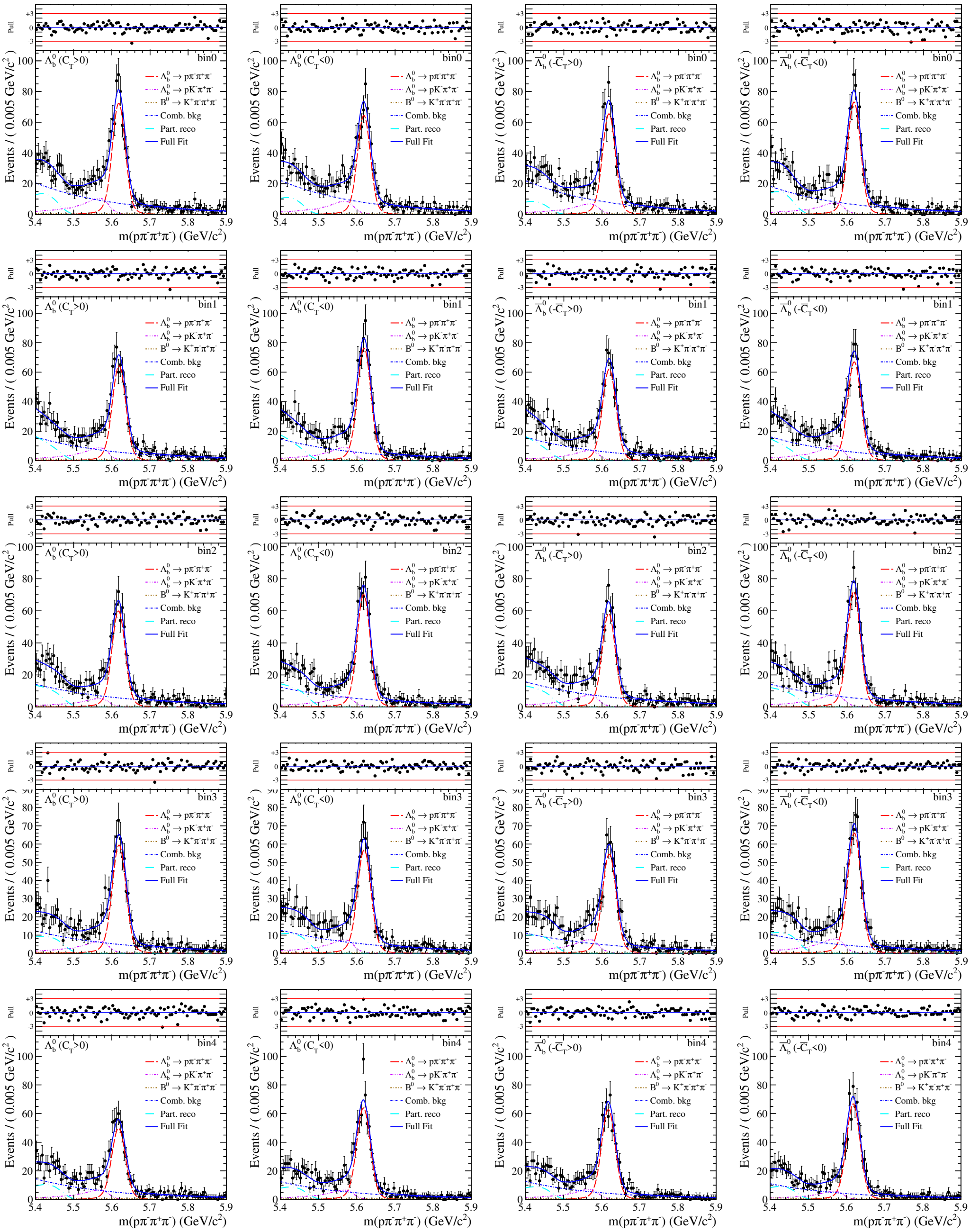

Figure 6.2: Projections of the simultaneous fit to the invariant mass $m(p\pi^-\pi^+\pi^-)$ distribution for the first 5 bin of the scheme A.

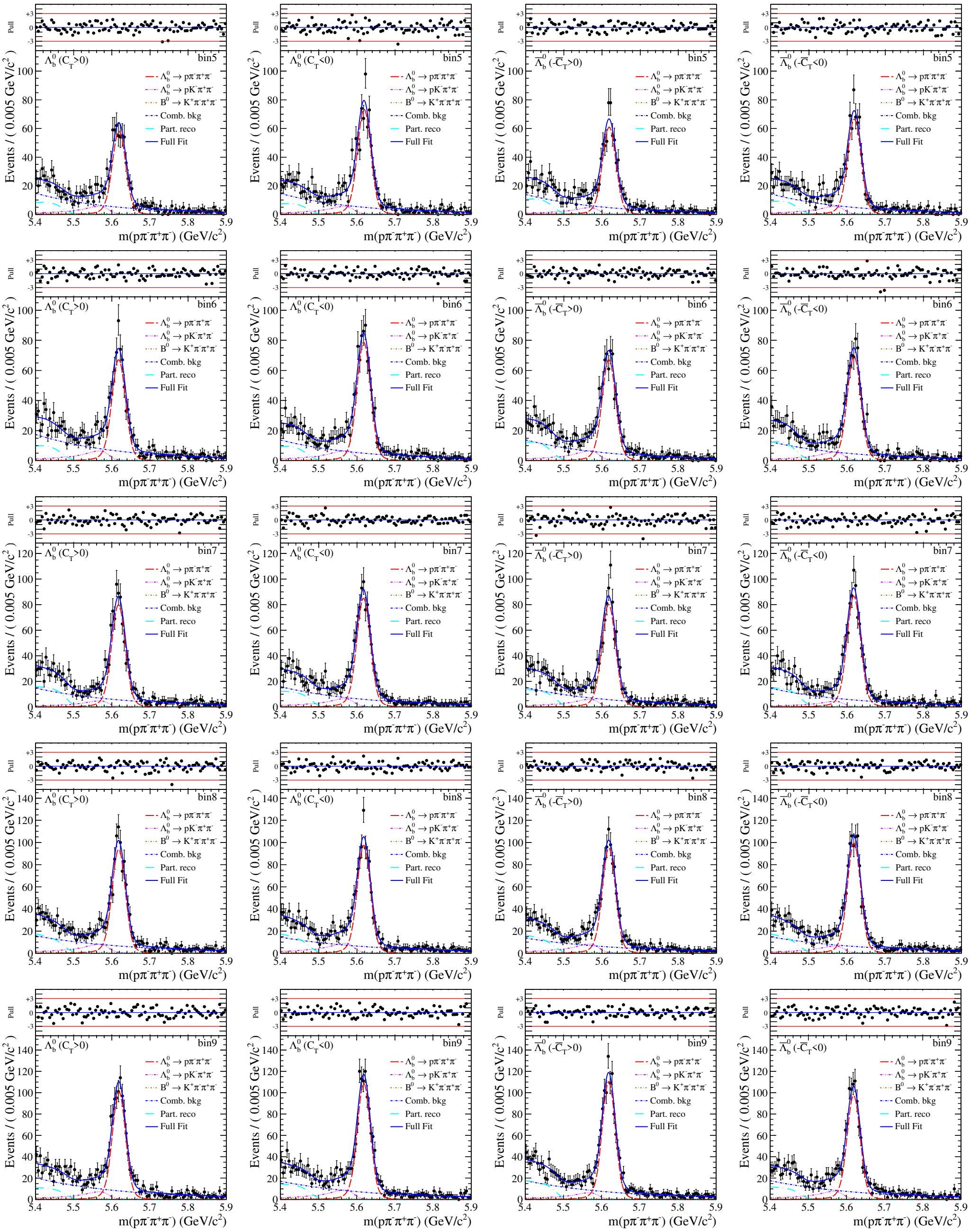

Figure 6.3: Projections of the simultaneous fit to the invariant mass $m(p\pi^-\pi^+\pi^-)$ distribution for the last 5 bin of the scheme A.

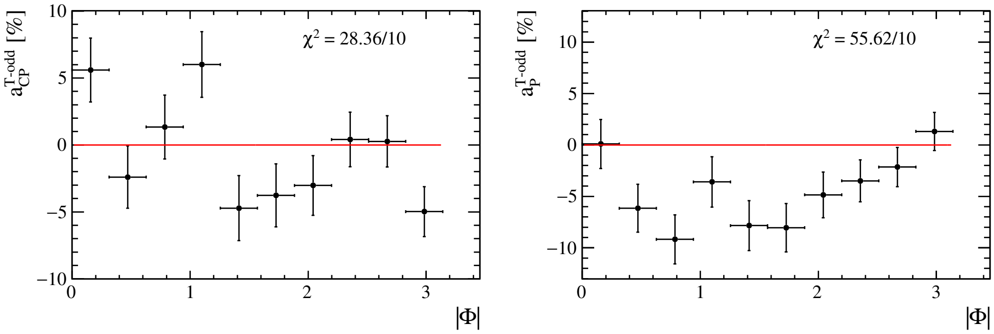

Figure 6.4: Asymmetries $a_{CP}^{\widehat{T}\text{-odd}}$ and $a_{P}^{\widehat{T}\text{-odd}}$ as a function of $|\Phi|$. The χ^2 is calculated with respect the no CPV and P violation hypotheses, represented by the two horizontal red line. Only statistical uncertainty is considered here.

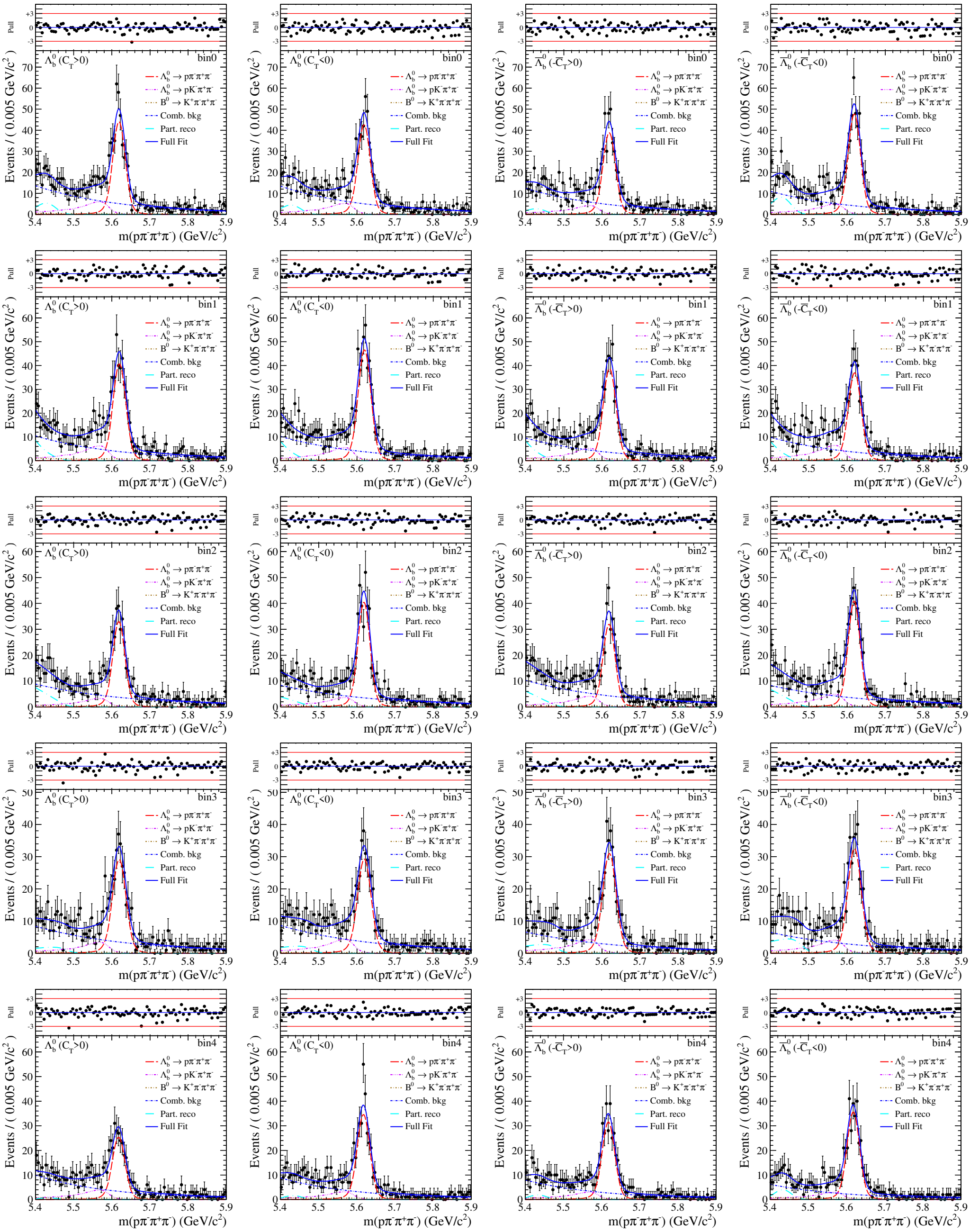

Figure 6.5: Projections of the simultaneous fit to the invariant mass $m(p\pi^-\pi^+\pi^-)$ distribution for the first 5 bin of the scheme A_1.

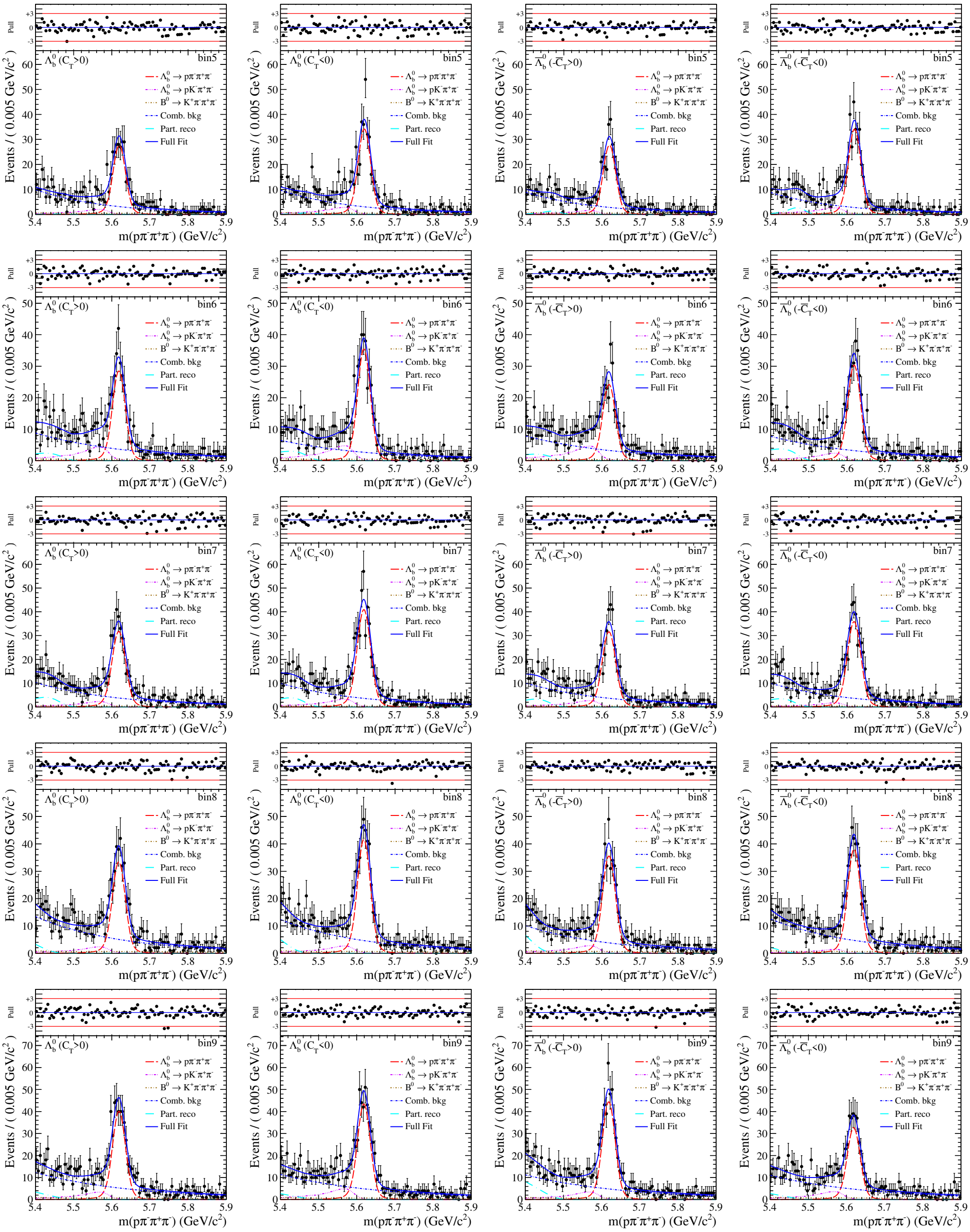

Figure 6.6: Projections of the simultaneous fit to the invariant mass $m(p\pi^-\pi^+\pi^-)$ distribution for the last 5 bin of the scheme A_1.

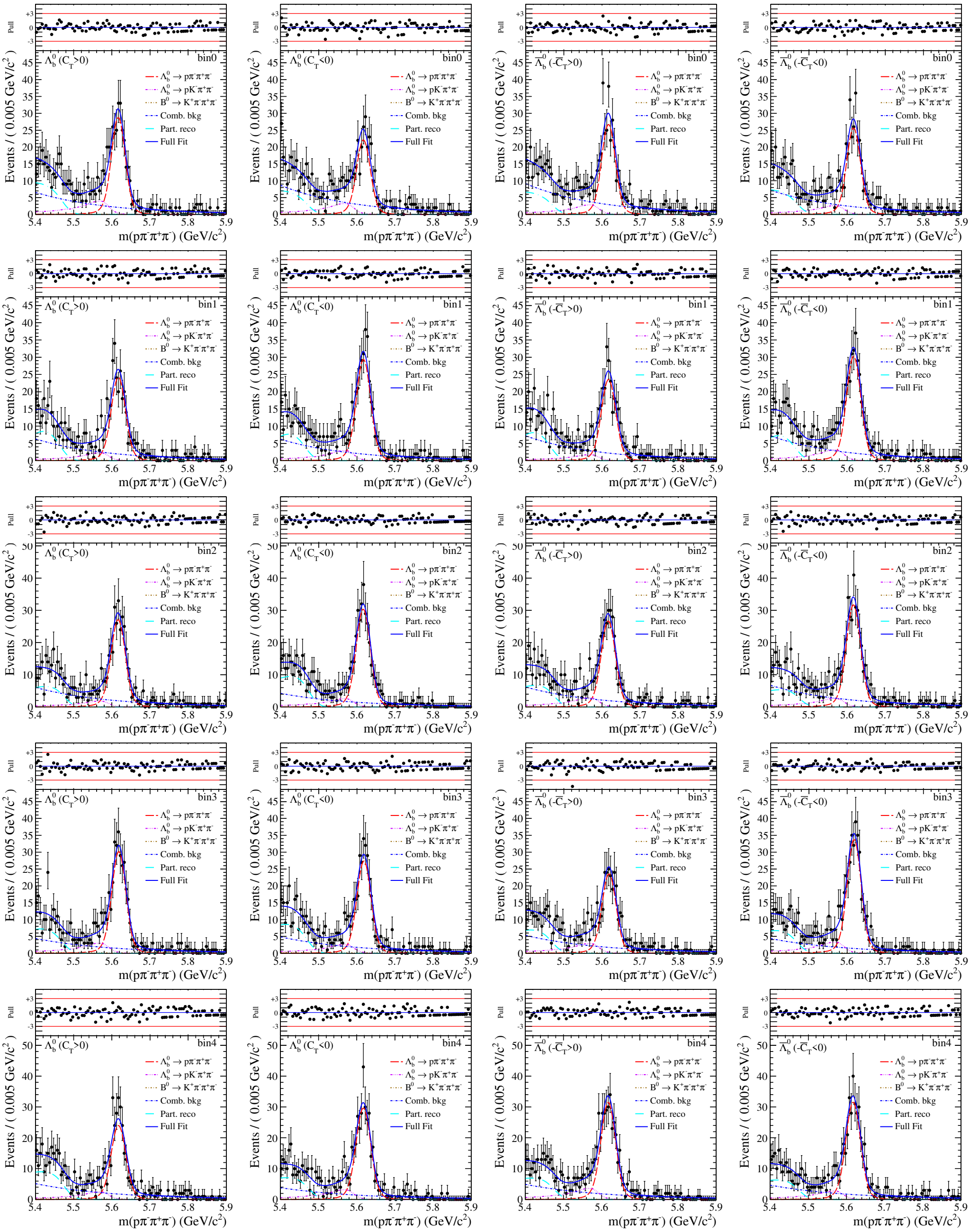

Figure 6.7: Projections of the simultaneous fit to the invariant mass $m(p\pi^-\pi^+\pi^-)$ distribution for the first 5 bin of the scheme A_2.

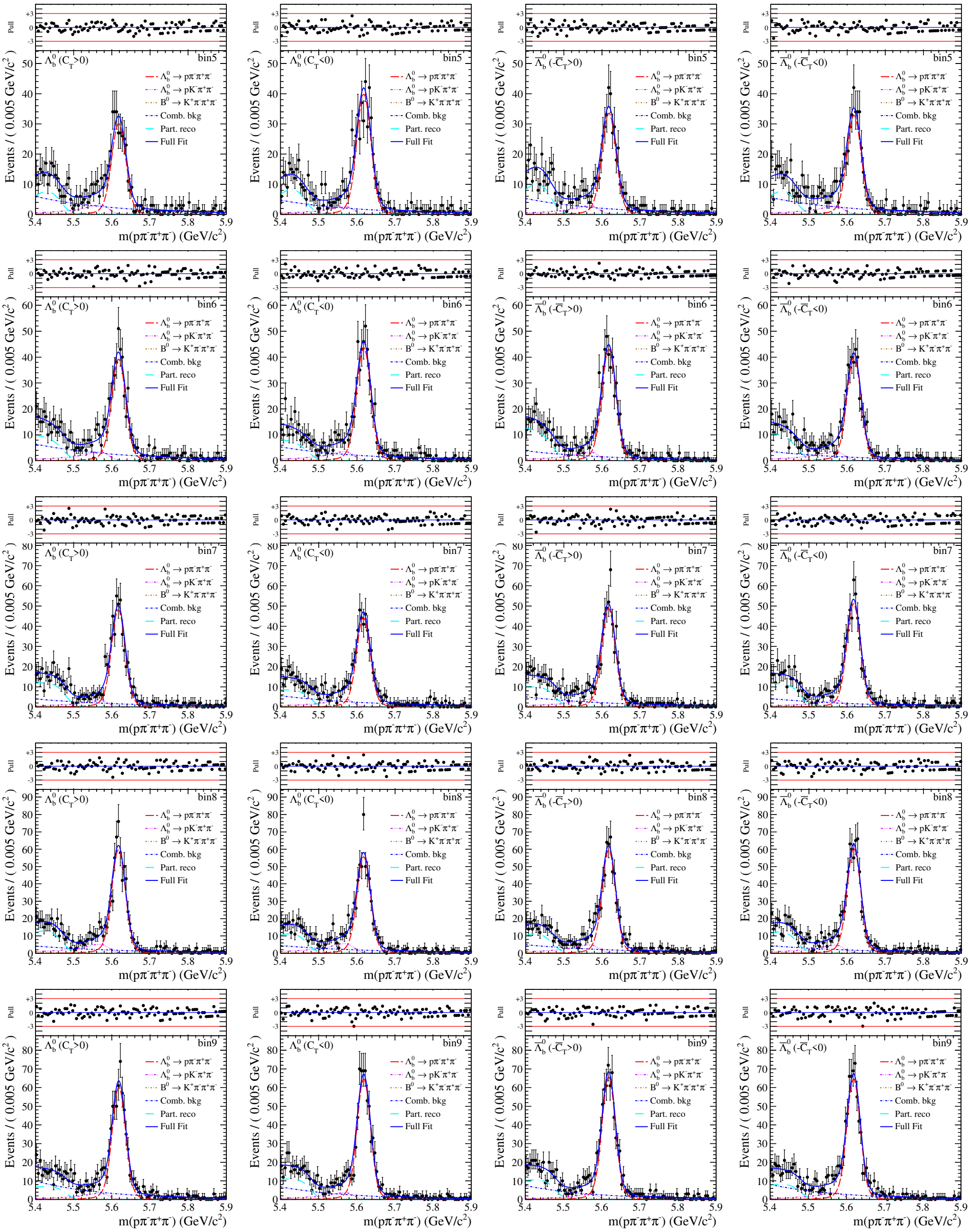

Figure 6.8: Projections of the simultaneous fit to the invariant mass $m(p\pi^-\pi^+\pi^-)$ distribution for the last 5 bin of the scheme A_2.

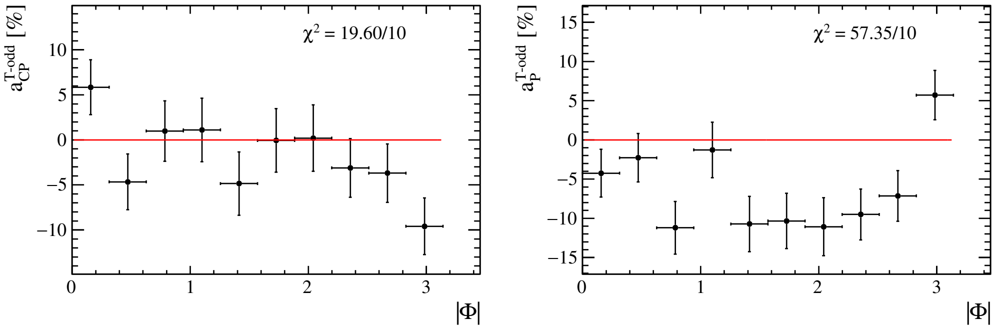

Figure 6.9: Asymmetries $a_{CP}^{\widehat{T}\text{-odd}}$ and $a_{P}^{\widehat{T}\text{-odd}}$ as a function of Φ for scheme A_1. The χ^2 is calculated with respect the no CPV and P violation hypotheses, represented by the two horizontal red line. Only statistical uncertainty is considered here.

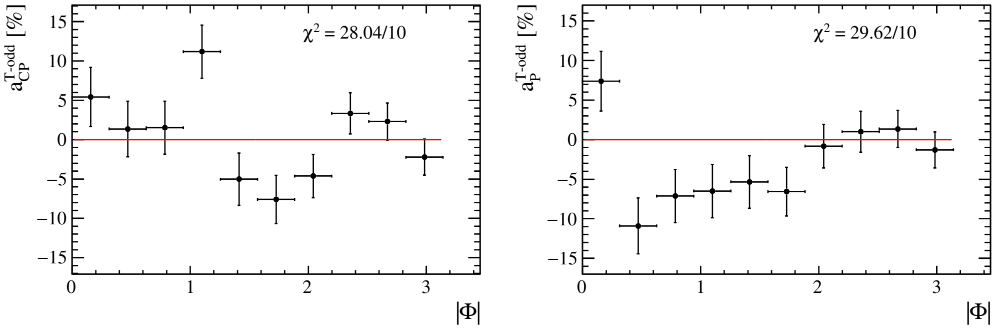

Figure 6.10: Asymmetries $a_{CP}^{\widehat{T}\text{-odd}}$ and $a_{P}^{\widehat{T}\text{-odd}}$ as a function of Φ for scheme A_2. The χ^2 is calculated with respect the no CPV and P violation hypotheses, represented by the two horizontal red line. Only statistical uncertainty is considered here.

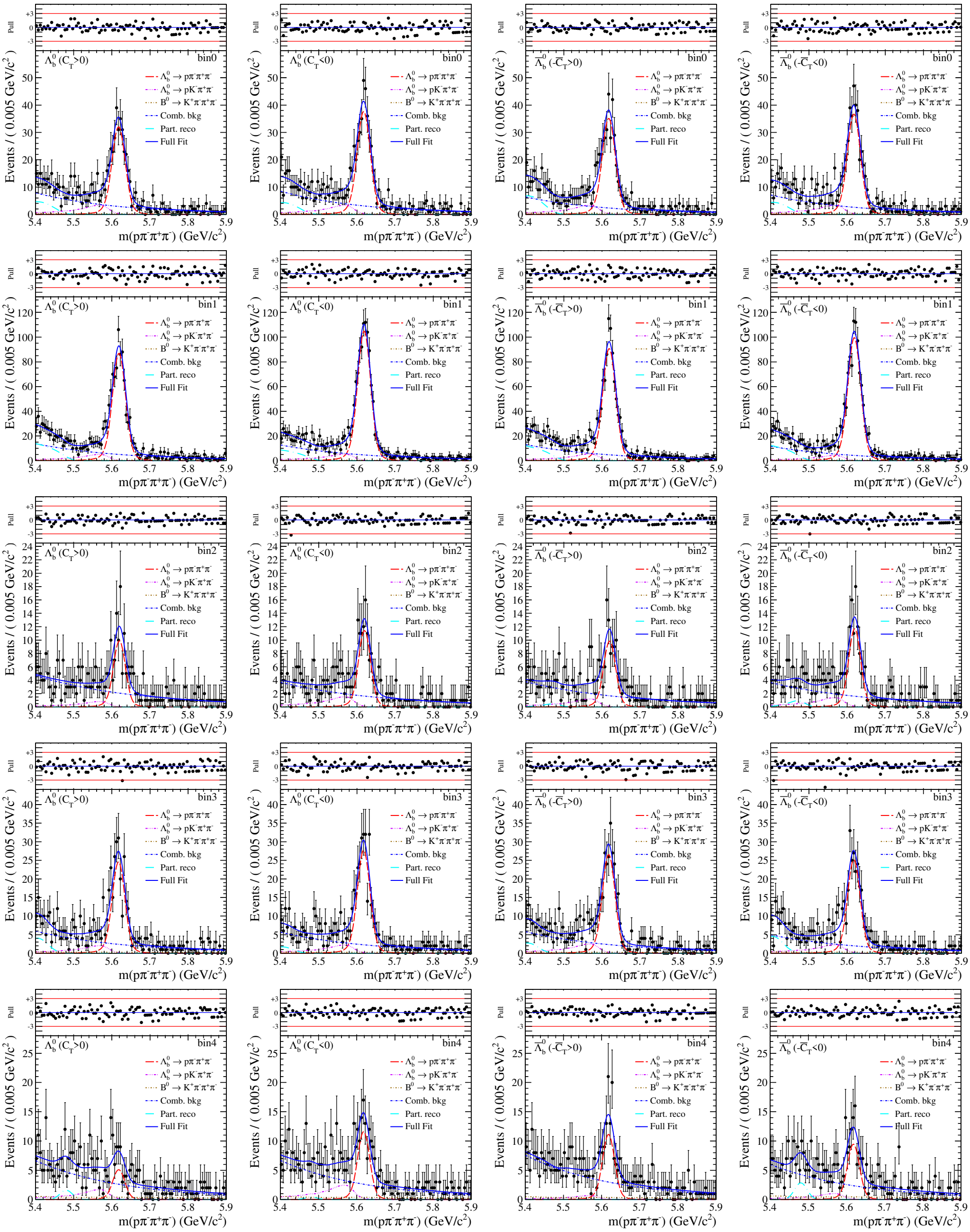

Figure 6.11: Projections of the simultaneous fit to the invariant mass $m(p\pi^-\pi^+\pi^-)$ distribution for the first 5 bin of the scheme B_1.

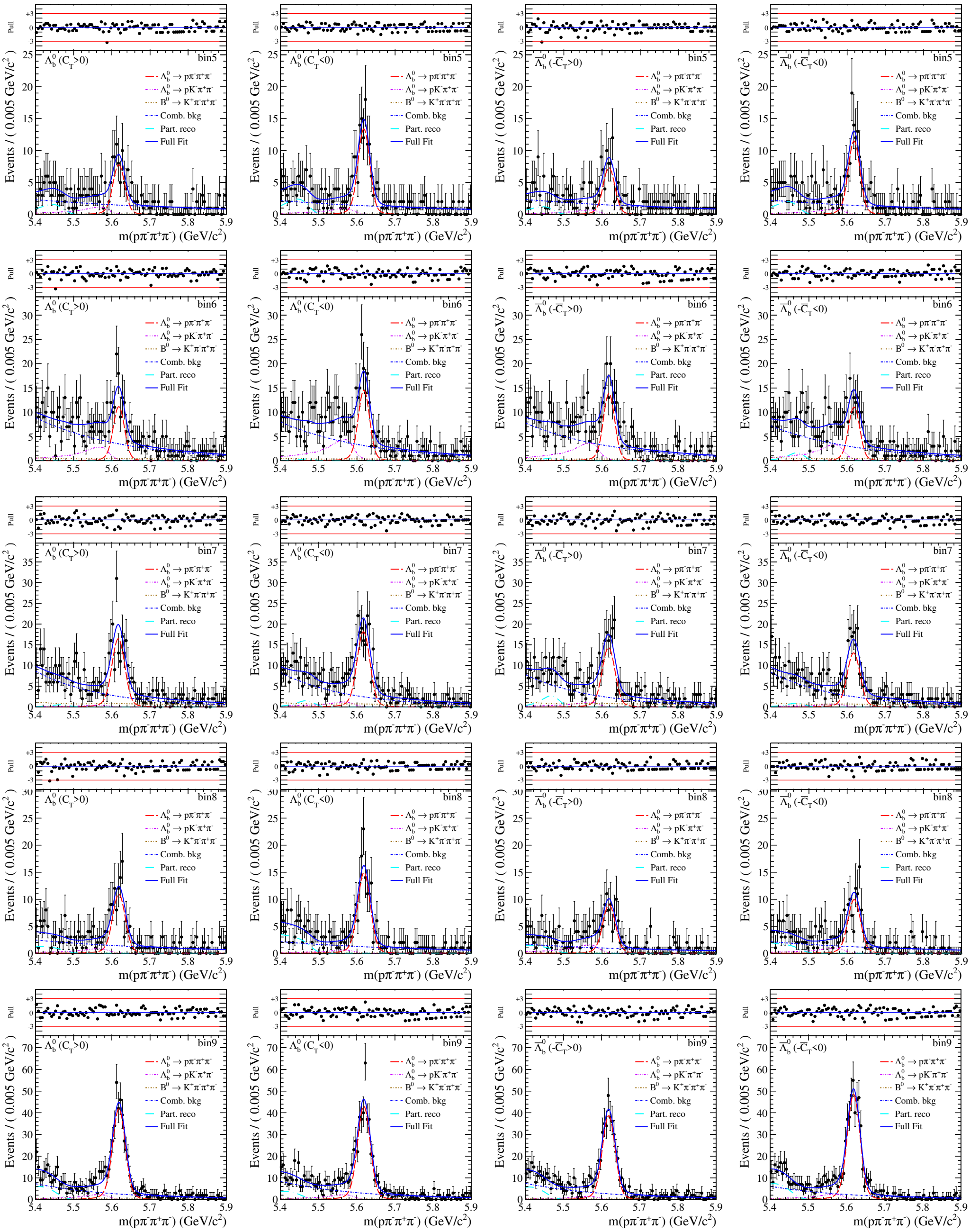

Figure 6.12: Projections of the simultaneous fit to the invariant mass $m(p\pi^-\pi^+\pi^-)$ distribution for the bins from 6 to 10 of the scheme B_1.

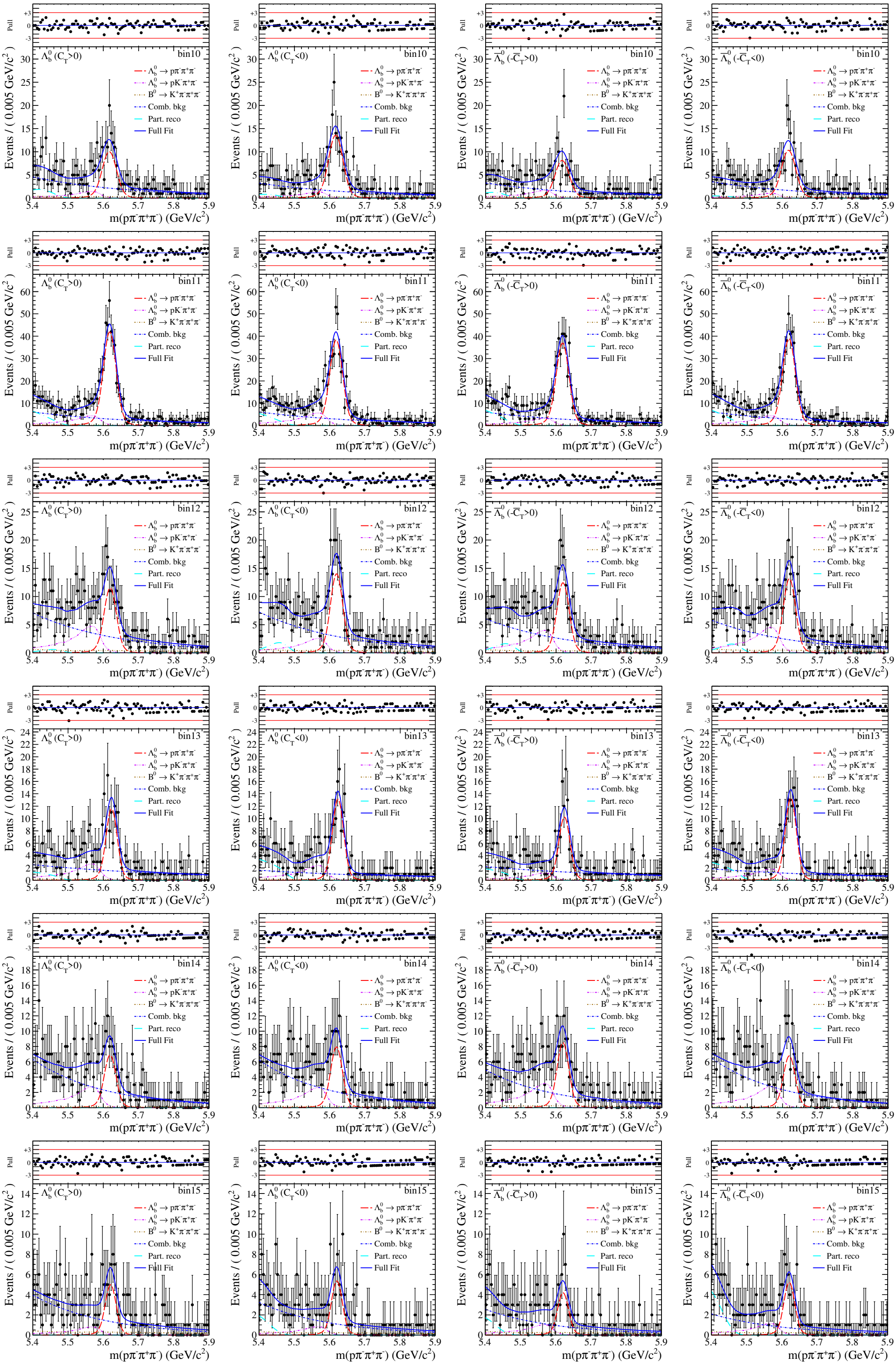

Figure 6.13: Projections of the simultaneous fit to the invariant mass $m(p\pi^-\pi^+\pi^-)$ distribution for the last 6 bins of the scheme B_1.

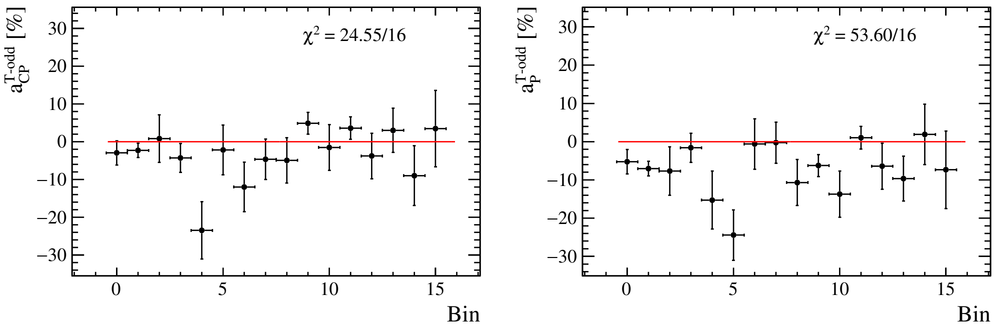

Figure 6.14: Asymmetries $a_{CP}^{\widehat{T}\text{-odd}}$ and $a_{P}^{\widehat{T}\text{-odd}}$ for each bin for scheme B_1. The χ^2 is calculated with respect the no CPV and P violation hypotheses, represented by the two horizontal red line. Only statistical uncertainty is considered here.

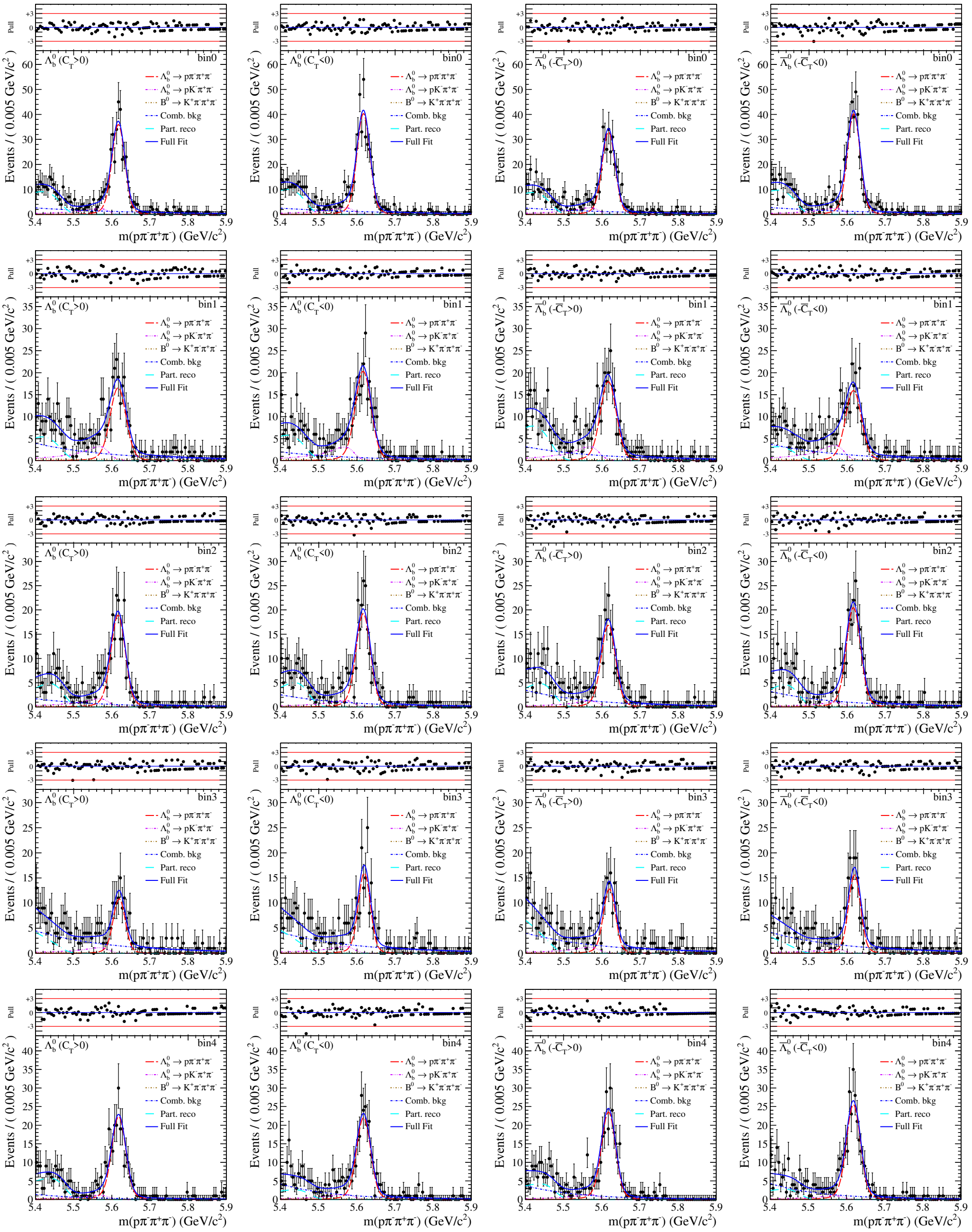

Figure 6.15: Projections of the simultaneous fit to the invariant mass $m(p\pi^-\pi^+\pi^-)$ distribution for the first 5 bin of the scheme B_2.

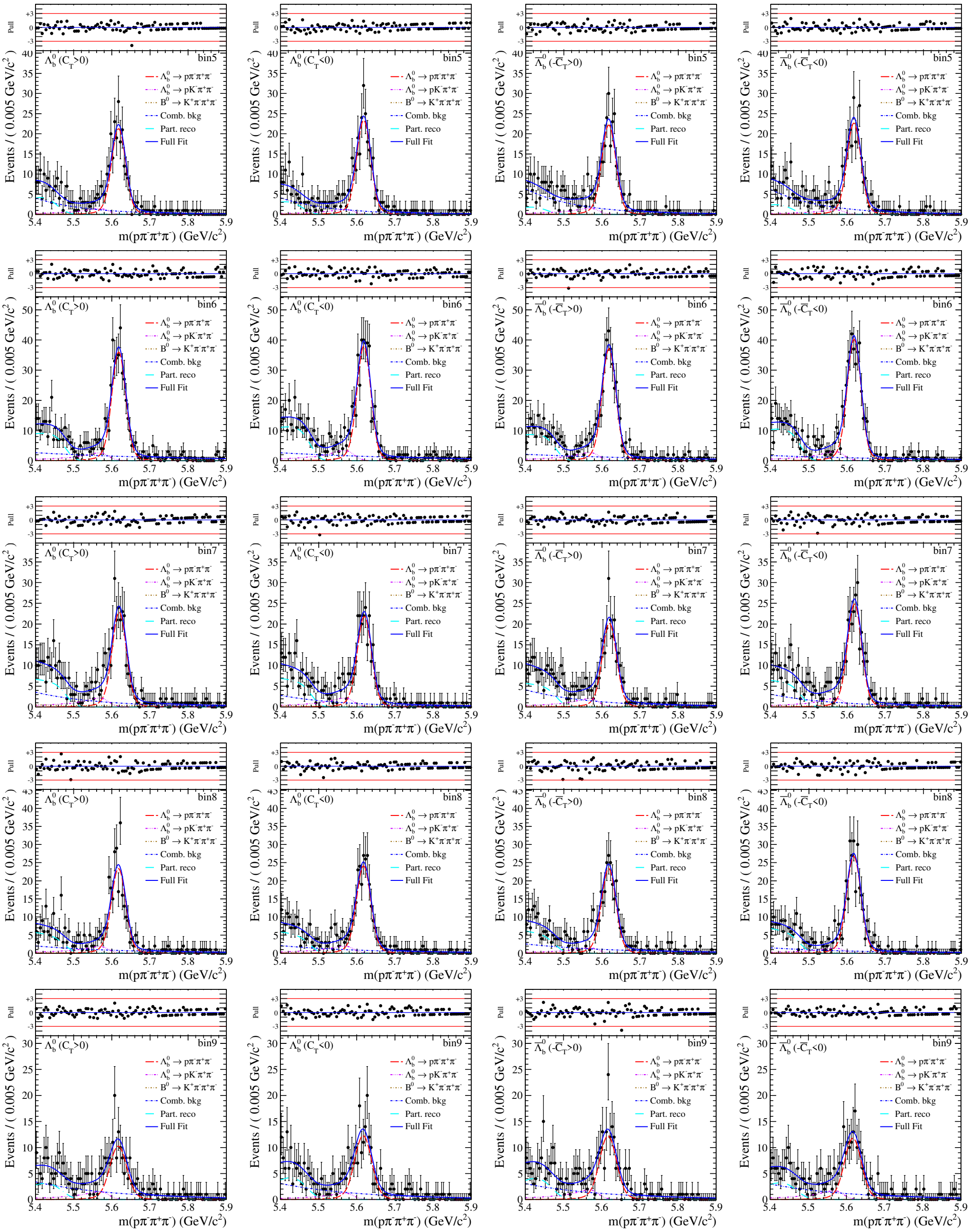

Figure 6.16: Projections of the simultaneous fit to the invariant mass $m(p\pi^-\pi^+\pi^-)$ distribution for the bins from 6 to 10 of the scheme B_2.

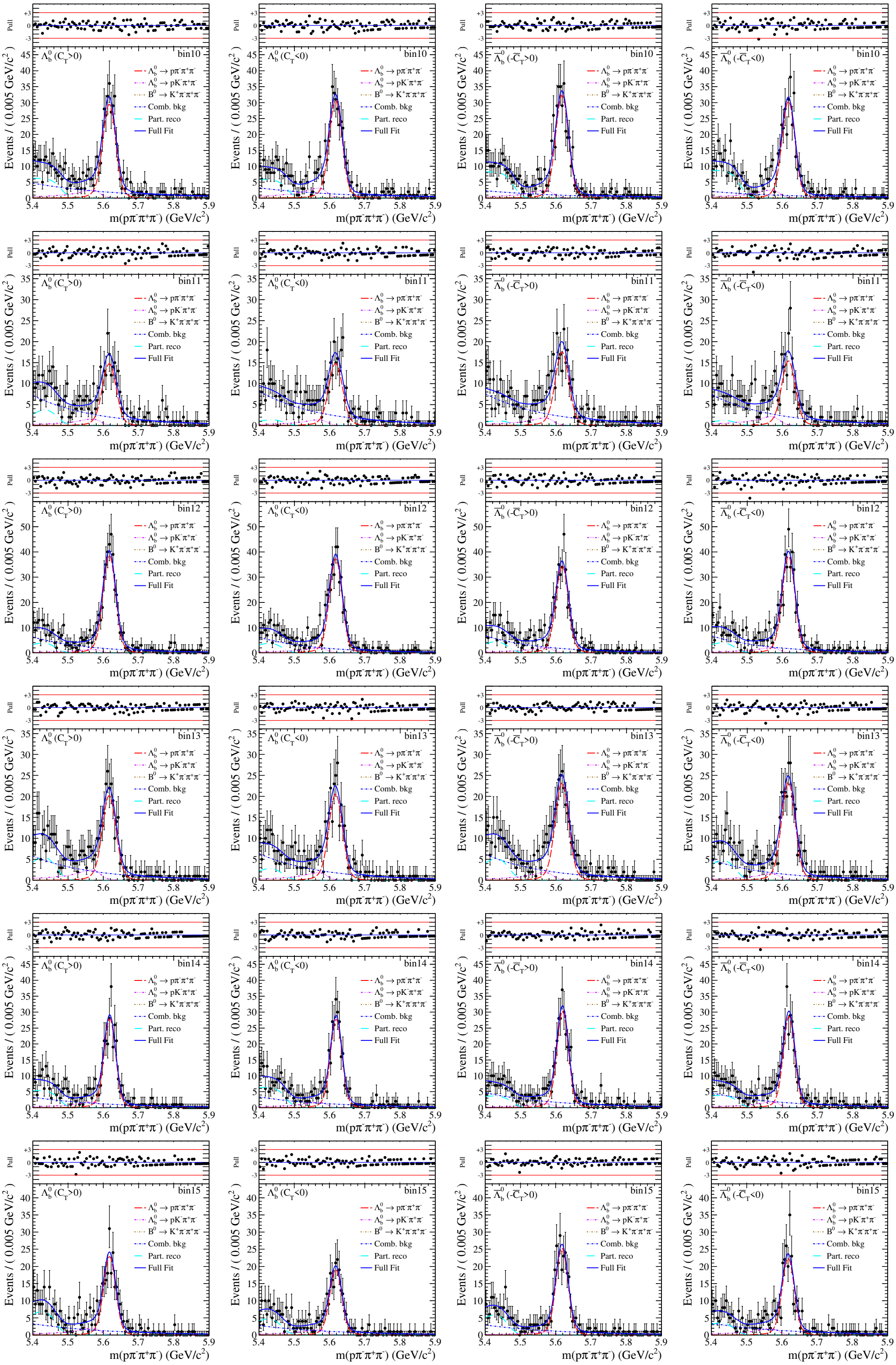

Figure 6.17: Projections of the simultaneous fit to the invariant mass $m(p\pi^-\pi^+\pi^-)$ distribution for the last 6 bins of the scheme B_2.

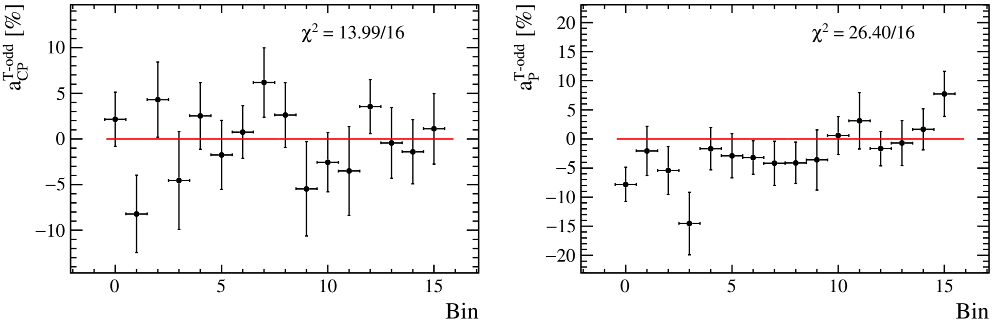

Figure 6.18: Asymmetries $a_{CP}^{\widehat{T}\text{-odd}}$ and $a_{P}^{\widehat{T}\text{-odd}}$ for each bin for scheme B_2. The χ^2 is calculated with respect the no CPV and P violation hypotheses, represented by the two horizontal red line. Only statistical uncertainty is considered here.

Chapter 7

Systematics uncertainties

A few sources of systematic uncertainties have been identified:

- experimental bias: possible bias introduced by the experimental reconstruction and analysis technique;
- detector resolution: the resolution on triple products $C_{\widehat{T}}$ and $\overline{C}_{\widehat{T}}$ could induce a migration of events between the categories $C_{\widehat{T}}\ \left(\overline{C}_{\widehat{T}}\right) > 0$ and $C_{\widehat{T}}\ \left(\overline{C}_{\widehat{T}}\right) < 0$
- fit model: due to the uncertainty on signal and background models.

We describe in the following the determination of the relevant systematic uncertainties.

7.1 Experimental bias

The selection criteria applied for the reconstruction of the decays $\Lambda_b^0 \to p\pi^-\pi^+\pi^-$ and the detector acceptance, in principle might introduce an experimental bias on the measurement of the $\widehat{T}$-odd variables $C_{\widehat{T}}$ and $\overline{C}_{\widehat{T}}$, hence on the $A_{\widehat{T}}$ and $\overline{A}_{\widehat{T}}$ observables and finally on $a_{CP}^{\widehat{T}\text{-odd}}$ and $a_{P}^{\widehat{T}\text{-odd}}$.

As a control sample, the Cabibbo-favoured $\Lambda_b^0 \to \Lambda_c^+(\to pK^-\pi^+)\pi^-$ decay has been selected as described in Section 3.5. In this case *CP*-violating effects are expected to be negligible. Any deviation from zero of the *CP*-violating asymmetry measured in this decay is considered as an experimental bias. We measure the $a_{CP}^{\widehat{T}\text{-odd}}(\Lambda_b^0 \to \Lambda_c^+(\to pK^-\pi^+)\pi^-) = (0.04 \pm 0.16)\%$ to be compatible with zero, where the uncertainty is statistical only. We measure also $A_{\widehat{T}}(\Lambda_b^0 \to \Lambda_c^+(\to pK^-\pi^+)\pi^-) = (-0.54 \pm 0.23)\%$ and $\overline{A}_{\widehat{T}}(\Lambda_b^0 \to \Lambda_c^+(\to pK^-\pi^+)\pi^-) = (-0.63 \pm 0.23)\%$. The fit is shown in Figure 7.1. We assign the statistical uncertainty on $a_{CP}^{\widehat{T}\text{-odd}}(\Lambda_b^0 \to \Lambda_c^+(\to pK^-\pi^+)\pi^-)$ as a systematic error $a_{CP}^{\widehat{T}\text{-odd}}$ for $\Lambda_b^0 \to p\pi^-\pi^+\pi^-$ decays due to a possible experimental bias. We measure $a_{CP}^{\widehat{T}\text{-odd}}$ in regions of phase space, as shown in Figure 7.2 in bins of $|\Phi|$ and in Figure 7.3 for the binning scheme defined in Table 5.4. In the latter no bias is observed and we conservatively assign the statistical uncertainty as systematic uncertainty in each bin. In order to take into account the high χ^2 observed in the binning in $|\Phi|$, we decide to assign the statistical uncertainty as systematic uncertainty in each bin enlarged by the factor 1.57 that represents the standard deviation of the quantity ${a_{CP}^{\widehat{T}\text{-odd}}}_i/\sigma_i$ from 0, where ${a_{CP}^{\widehat{T}\text{-odd}}}_i$ is the asymmetry measured in the bin i and σ_i is its uncertainty.

Since parity violation can introduce asymmetries in $A_{\widehat{T}}$, $\overline{A}_{\widehat{T}}$ and $a_{P}^{\widehat{T}\text{-odd}}$, we decide to estimate their systematic uncertainty as the statistical error propagated starting from $a_{CP}^{\widehat{T}\text{-odd}}$. The statistical error is the same for $A_{\widehat{T}}$ and $\overline{A}_{\widehat{T}}$ and no correlation is measured, then we conservatively estimate the systematic uncertainties on $A_{\widehat{T}}$ and $\overline{A}_{\widehat{T}}$ observable as error propagation $\sigma(A_T) = \sigma(\bar{A}_T) = \sqrt{2}\sigma(a_{CP}^{\widehat{T}\text{-odd}})_{\rm cs}$, where $\sigma(a_{CP}^{\widehat{T}\text{-odd}})_{\rm cs}$ is the statistical uncertainty of the CP-violating asymmetry measured on the control sample. The systematic uncertainty on $a_P^{\widehat{T}\text{-odd}}$ is estimated as $\sigma\left(a_P^{\widehat{T}\text{-odd}}\right) = \sigma\left(a_{CP}^{\widehat{T}\text{-odd}}\right)_{cs}$ The summary of the systematic uncertainties due to a possible experimental bias is reported in Table 7.1.

Table 7.1: Systematic uncertainties due to a possible experimental bias for integrated measurements and in bins of phase space.

Binning scheme	Bin	$\Delta A_{\widehat{T}}$ (%)	$\Delta \overline{A}_{\widehat{T}}$ (%)	$\Delta a_P^{\widehat{T}\text{-odd}}$ (%)	$\Delta a_{CP}^{\widehat{T}\text{-odd}}$ (%)
Integrated		± 0.23	± 0.23	± 0.16	± 0.16
A, A_1, A_2	0	± 1.25	± 1.25	± 0.89	± 0.89
	1	± 1.21	± 1.21	± 0.86	± 0.86
	2	± 1.16	± 1.16	± 0.82	± 0.82
	3	± 1.13	± 1.13	± 0.80	± 0.80
	4	± 1.14	± 1.14	± 0.81	± 0.81
	5	± 1.13	± 1.13	± 0.80	± 0.80
	6	± 1.17	± 1.17	± 0.83	± 0.83
	7	± 1.11	± 1.11	± 0.78	± 0.78
	8	± 1.03	± 1.03	± 0.73	± 0.73
	9	± 0.97	± 0.97	± 0.69	± 0.69
B_1, B_2	0	± 0.78	± 0.78	± 0.55	± 0.55
	1	± 0.86	± 0.86	± 0.61	± 0.61
	2	± 1.11	± 1.11	± 0.78	± 0.78
	3	± 1.66	± 1.66	± 1.17	± 1.17
	4	± 2.22	± 2.22	± 1.57	± 1.57
	5	± 2.61	± 2.61	± 1.85	± 1.85
	6	± 1.10	± 1.10	± 0.78	± 0.78
	7	± 0.91	± 0.91	± 0.64	± 0.64
	8	± 0.63	± 0.63	± 0.44	± 0.44
	9	± 0.69	± 0.69	± 0.49	± 0.49
	10	± 1.21	± 1.21	± 0.86	± 0.86
	11	± 1.09	± 1.09	± 0.77	± 0.77
	12	± 0.93	± 0.93	± 0.66	± 0.66
	13	± 1.19	± 1.19	± 0.84	± 0.84
	14	± 0.56	± 0.56	± 0.39	± 0.39
	15	± 0.74	± 0.74	± 0.52	± 0.52

7.2 Bias due to detector resolution on $C_{\widehat{T}}$

We aim to estimate the impact of the detector resolution on the $\widehat{T}$-odd observables and we assume that using Monte Carlo events is a reasonable approximation since it reproduces reasonably well momentum resolution for charged particle tracks. We apply the same selection on Monte Carlo as in data, but the PID requirements that are not well simulated. We reweight the Monte Carlo using data control sample. On Monte Carlo events we measured the residual distribution for signal truth matched events defined as $(C_{T,meas} - C_{T,true})$, where $C_{T,meas}$ is the reconstructed $C_{\widehat{T}}$ value, and $C_{T,true}$ is the true generated $C_{\widehat{T}}$ value. The residual distribution for $C_{\widehat{T}}$ is shown in Figure 7.4 and the mean is biased. The dependence of the detector resolution on $C_{\widehat{T}}$ as a function of the true generated $C_{T,true}$ value is shown in Figure 7.5. A small but sizeable bias at the per mill level in the reconstruction of $C_{\widehat{T}}$ as a function of $C_{T,true}$ is evident. The mean of the distribution is biased in different directions depending on the sign of $C_{T,true}$. However this bias doesn't affect our measurement because for $C_{T,true} > 0$ ($C_{T,true} < 0$) the $C_{T,meas}$ value is positively (negatively) biased and this helps us in improving the separation of the data sample depending on the sign of $C_{T,meas}$.

We evaluated the effect of the $C_{\widehat{T}}$ resolution on $A_{\widehat{T}}$, $\overline{A}_{\widehat{T}}$, $a_P^{\widehat{T}\text{-odd}}$ and $a_{CP}^{\widehat{T}\text{-odd}}$ observables using reweighted Monte Carlo signal events, as explained in Section 4.1, where neither P- nor CP-violating effects are simulated. We measured the $A_{\widehat{T}}$, $\overline{A}_{\widehat{T}}$, $a_P^{\widehat{T}\text{-odd}}$ and $a_{CP}^{\widehat{T}\text{-odd}}$ observables by counting the number of Λ_b^0 and $\overline{\Lambda}_b^0$ events with different values of $C_{\widehat{T}}$ and $\overline{C}_{\widehat{T}}$, using first the reconstructed values of $C_{\widehat{T}}$ and $\overline{C}_{\widehat{T}}$ (rec) and then the generated values (gen). Results are reported in Table 7.2. The systematic effect of detector resolution on $C_{\widehat{T}}$ is less than 1‰.

Table 7.2: Results for $A_{\widehat{T}}$, $\overline{A}_{\widehat{T}}$, $a_P^{\widehat{T}\text{-odd}}$ and $a_{CP}^{\widehat{T}\text{-odd}}$ observables on reweighted Monte Carlo signal events using $C_{\widehat{T}}$ and $\overline{C}_{\widehat{T}}$ generated values (gen) and reconstructed values (rec).

	$A_{\widehat{T}}$ (%)	$\overline{A}_{\widehat{T}}$ (%)	$a_P^{\widehat{T}\text{-odd}}$ (%)	$a_{CP}^{\widehat{T}\text{-odd}}$ (%)
gen	-0.05 ± 0.29	0.12 ± 0.30	0.04 ± 0.21	-0.07 ± 0.21
rec	-0.04 ± 0.29	0.13 ± 0.30	0.03 ± 0.21	-0.08 ± 0.21
syst. unc.	$\Delta A_{\widehat{T}}(\%)$ ± 0.01	$\Delta \overline{A}_{\widehat{T}}(\%)$ ± 0.01	$\Delta a_P^{\widehat{T}\text{-odd}}(\%)$ ± 0.01	$\Delta a_{CP}^{\widehat{T}\text{-odd}}(\%)$ ± 0.01

7.3 Fit model

We generate 1,000 Toy MonteCarlo pseudoexperiments with the fit parameters tuned to blind fit results to data using the alternative model. We perform a fit similar to the one performed on data with the nominal and alternative model, both described in Sections 4.1-4.2.1, and extract the asymmetry parameters values. The pull distributions, defined as pull$(A) = \frac{A_{rec} - A_{gen}}{\sigma_{A_{rec}}}$ where A_{rec} ($\sigma_{A_{rec}}$) is the value (error) of the reconstructed asymmetry returned from the fit with the nominal model and A_{gen} is the generated asymmetry, are shown in Figure 7.6. The difference of the asymmetries obtained fitting the nominal and alternative model to pseudoexperiments, defined as diff(A_{rec}), is shown in Figure 7.7. The pull distributions show the errors are correctly determined. A minimal bias is observed in P-odd asymmetries $A_{\widehat{T}}$, $\overline{A}_{\widehat{T}}$ and $a_P^{\widehat{T}\text{-odd}}$, while the asymmetry $a_{CP}^{\widehat{T}\text{-odd}}$ is much more robust for different model parametrizations. We apply the standard deviation σ of the diff(A_{rec}) distributions as systematic uncertainty due to the fit model. The systematic uncertainty for the asymmetries is summarized in Table 7.3.

Table 7.3: Systematic uncertainty on the asymmetries due to the fit model.

$\Delta A_{\widehat{T}}(\%)$	$\Delta \overline{A}_{\widehat{T}}(\%)$	$\Delta a_{P}^{\widehat{T}\text{-odd}}(\%)$	$\Delta a_{CP}^{\widehat{T}\text{-odd}}(\%)$
± 0.08	± 0.08	± 0.06	± 0.06

7.4 Summary of systematic uncertainties

In Table 7.4 we summarize the systematic uncertainties assigned to the measured asymmetries in the integrated sample and in bins of phase space.

7.5 Cross-checks

7.5.1 Particle identification requirements

The effects of particle identification criteria are tested by using the $\Lambda_b^0 \to \Lambda_c^+ (\to pK^-\pi^+)\pi^-$ control sample. The asymmetries are measured with four alternative identification criteria for the proton, kaon and pion, defined in Table 7.5, and the results are shown in Figure 7.8. The differences between the measured asymmetries ΔA are compatible with statistical fluctuations between different selection criteria when taking into account statistical correlations among them as shown in Table 7.6. The uncertainty $\sigma_{\Delta A}$ is calculated as $\sigma_{\Delta A} = \sqrt{\sigma_{A_i}^2 + \sigma_{A_0}^2 - 2\rho\sigma_{A_0}\sigma_{A_i}}$, where $\sigma_{A_{i(0)}}$ is the uncertainty on the asymmetry measured on the data sample with cut $i(0)$ while $\rho = \frac{N_i^{sig}}{N_0^{sig}}$ is the correlation between the two different data samples with signal events $N_{i(0)}^{sig}$.

7.5.2 Signal reconstruction efficiency on Monte Carlo events

The efficiency for positive and negative $C_{\widehat{T}}$ ($\overline{C}_{\widehat{T}}$) values for Λ_b^0 ($\overline{\Lambda}_b^0$) has already been checked directly on data on $\Lambda_b^0 \to \Lambda_c^+ (\to pK^-\pi^+)\pi^-$ control sample, where, as expected, we don't measure any *CPV* both integrated and in bins of the phase space. Any possible effect on the measured asymmetries of the dependence on the $C_{\widehat{T}}$ ($\overline{C}_{\widehat{T}}$) sign for the efficiency is included in the systematic uncertainty assigned in Section 7.1. In Figure 7.9 we check the efficiency on reweighted MC events. The efficiency for positive and negative $C_{\widehat{T}}$ ($\overline{C}_{\widehat{T}}$) values is defined as ε^+ ($\overline{\varepsilon}^+$) and ε^- ($\overline{\varepsilon}^-$) for Λ_b^0 ($\overline{\Lambda}_b^0$). The measured efficiencies are consistent between positive and negative $C_{\widehat{T}}$ ($\overline{C}_{\widehat{T}}$) values, *i.e.* they are compatible with $\varepsilon^+/\varepsilon^- = 1$ ($\overline{\varepsilon}^+/\overline{\varepsilon}^- = 1$) for Λ_b^0 ($\overline{\Lambda}_b^0$).

7.5.3 L0 trigger requirement

Since the asymmetry that arises from the reconstruction could be large for protons, we verify the stability of the result splitting the full data sample depending on different L0 trigger requirements. We divide the full data sample depending if the responsible for triggering the L0 are the final state candidates (TOS) or something else in the event (TIS). The result is shown in Figure 7.10 and doesn't show any dependence.

Table 7.4: Summary of systematic uncertainties assigned to the measured asymmetries in the integrated sample and in bins of the phase space. Where not specified, the systematic uncertainty is assigned to both integrated measurements and in bins of phase space.

Bias	Binning scheme	Bin	$\Delta A_{\widehat{T}}(\%)$	$\Delta \overline{A}_{\widehat{T}}(\%)$	$\Delta a_{CP}^{\widehat{T}\text{-odd}}(\%)$	$\Delta a_{CP}^{\widehat{T}\text{-odd}}(\%)$
Experimental Bias	Integrated		± 0.23	± 0.23	± 0.16	± 0.16
	A, A_1, A_2	0	± 1.25	± 1.25	± 0.89	± 0.89
		1	± 1.21	± 1.21	± 0.86	± 0.86
		2	± 1.16	± 1.16	± 0.82	± 0.82
		3	± 1.13	± 1.13	± 0.80	± 0.80
		4	± 1.14	± 1.14	± 0.81	± 0.81
		5	± 1.13	± 1.13	± 0.80	± 0.80
		6	± 1.17	± 1.17	± 0.83	± 0.83
		7	± 1.11	± 1.11	± 0.78	± 0.78
		8	± 1.03	± 1.03	± 0.73	± 0.73
		9	± 0.97	± 0.97	± 0.69	± 0.69
	B_1, B_2	0	± 0.78	± 0.78	± 0.55	± 0.55
		1	± 0.86	± 0.86	± 0.61	± 0.61
		2	± 1.11	± 1.11	± 0.78	± 0.78
		3	± 1.66	± 1.66	± 1.17	± 1.17
		4	± 2.22	± 2.22	± 1.57	± 1.57
		5	± 2.61	± 2.61	± 1.85	± 1.85
		6	± 1.10	± 1.10	± 0.78	± 0.78
		7	± 0.91	± 0.91	± 0.64	± 0.64
		8	± 0.63	± 0.63	± 0.44	± 0.44
		9	± 0.69	± 0.69	± 0.49	± 0.49
		10	± 1.21	± 1.21	± 0.86	± 0.86
		11	± 1.09	± 1.09	± 0.77	± 0.77
		12	± 0.93	± 0.93	± 0.66	± 0.66
		13	± 1.19	± 1.19	± 0.84	± 0.84
		14	± 0.56	± 0.56	± 0.39	± 0.39
		15	± 0.74	± 0.74	± 0.52	± 0.52
$C_{\widehat{T}}$ resolution			± 0.01	± 0.01	± 0.01	± 0.01
Fit Model			± 0.08	± 0.08	± 0.06	± 0.06

7.5.4 Magnet polarities

We check the stability of the results for different data taking conditions. The full dataset is splitted into the two magnet polarities and the asymmetries are measured in each data sample integrated and in bins of Φ, as shown in Figures 7.11-7.12 respectively. We found no evidence of any dependence of the asymmetries over the two magnet polarities.

Table 7.5: Definition of PID cuts for $\Lambda_b^0 \to \Lambda_c^+(\to pK^-\pi^+)\pi^-$ control sample for each bin.

PID cuts	Bins				
	0 (nominal)	1	2	3	4
PID$_p$	0.05	0.1	0.2	0.3	0.4
PID$_K$	0.05	0.1	0.2	0.3	0.4
PID$_\pi$	0.05	0.1	0.2	0.3	0.4
N_{sig}	214528	179386	124825	91160	70511

Table 7.6: Difference between the asymmetries measured with nominal and alternative PID cuts defined in Table 7.5 taking into account the correlations ρ among them. They are all compatible with statistical fluctuation.

Bin samples	$\Delta A_{\widehat{T}}(\%)$	$\Delta \overline{A}_{\widehat{T}}(\%)$	$\Delta a_{CP}^{\widehat{T}\text{-odd}}(\%)$	$\Delta a_{P}^{\widehat{T}\text{-odd}}(\%)$	$\rho(\%)$
(0,1)	0.180 ± 0.139	0.112 ± 0.141	0.034 ± 0.099	0.146 ± 0.099	83.80
(0,2)	0.009 ± 0.249	-0.237 ± 0.251	0.123 ± 0.177	-0.114 ± 0.177	58.41
(0,3)	0.174 ± 0.323	-0.059 ± 0.326	0.116 ± 0.230	0.058 ± 0.230	42.67
(0,4)	0.406 ± 0.381	0.051 ± 0.385	0.177 ± 0.271	0.228 ± 0.271	33.02

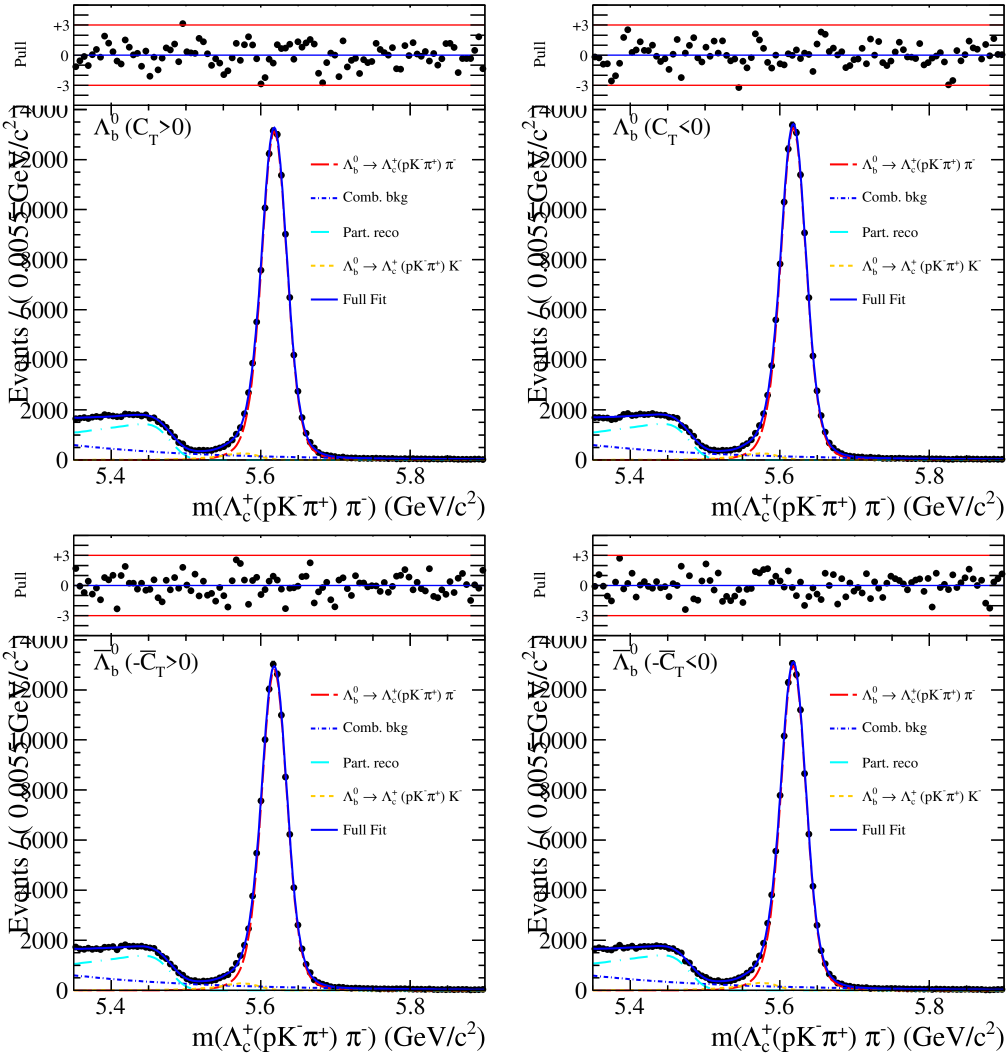

Figure 7.1: Fit projections of the simultaneous fit to the invariant m(Λ_c^+ ($pK^-\pi^+$)π^-) distribution for the four different subsamples of the control sample $\Lambda_b^0 \to \Lambda_c^+(\to pK^-\pi^+)\pi^-$.

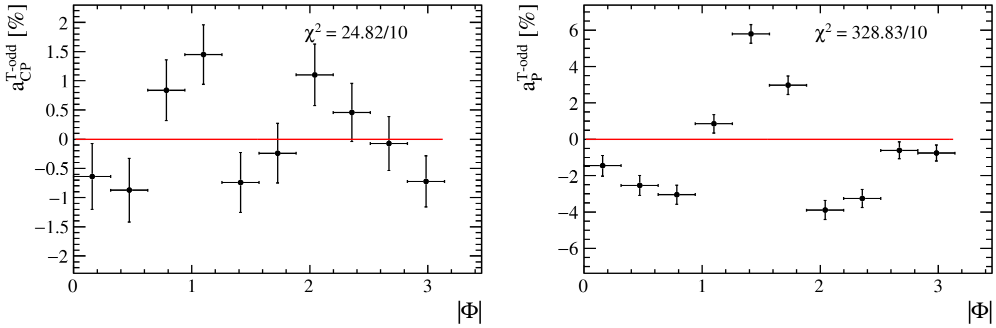

Figure 7.2: Asymmetries $a_{CP}^{\widehat{T}\text{-odd}}$ and $a_{P}^{\widehat{T}\text{-odd}}$ for the control sample $\Lambda_b^0 \to \Lambda_c^+(\to pK^-\pi^+)\pi^-$ in bins of $|\Phi|$. The χ^2 is calculated with respect to the no *CPV* and P violation hypotheses, represented by the two horizontal lines.

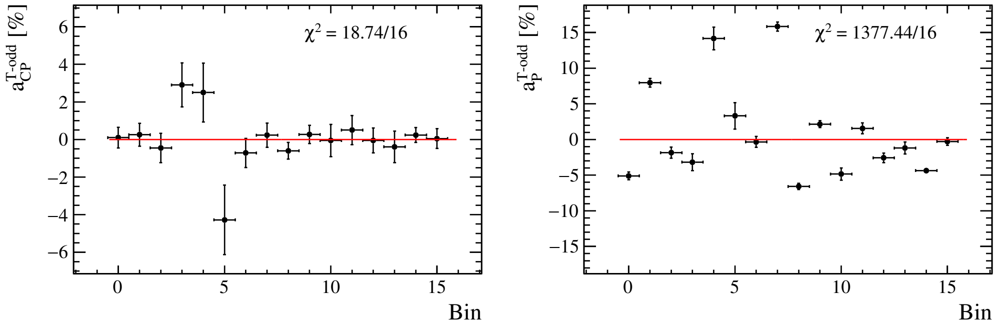

Figure 7.3: Asymmetries $a_{CP}^{\widehat{T}\text{-odd}}$ and $a_{P}^{\widehat{T}\text{-odd}}$ for the control sample $\Lambda_b^0 \to \Lambda_c^+(\to pK^-\pi^+)\pi^-$ with the new binning scheme. The χ^2 is calculated with respect to the no *CPV* and P violation hypotheses, represented by the two horizontal lines.

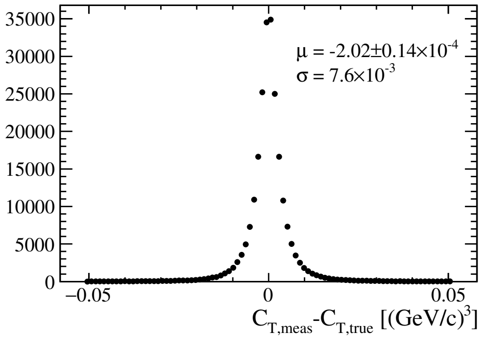

Figure 7.4: Residual distribution, $(C_{T,meas} - C_{T,true})$, for reweighted Monte Carlo $\Lambda_b^0 \to p\pi^-\pi^+\pi^-$ signal events.

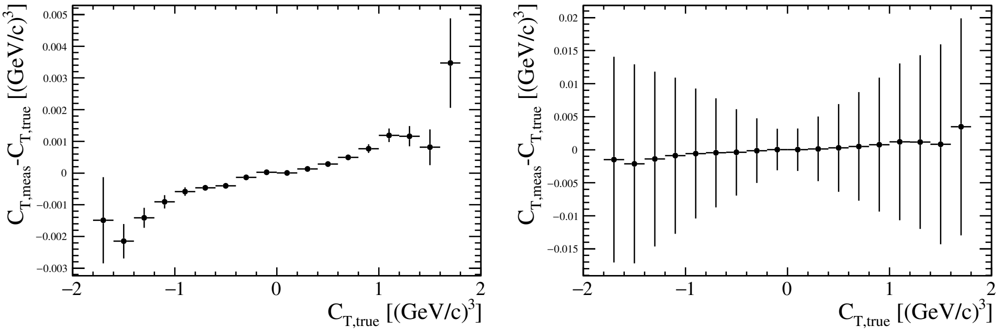

Figure 7.5: Residual distribution, $(C_{T,meas} - C_{T,true})$, as a function of $C_{T,true}$ for Monte Carlo signal events. The error bars correspond to the error on the mean (Left) and the standard deviation (Right) of the $C_{\widehat{T}}$ residual distribution in each bin.

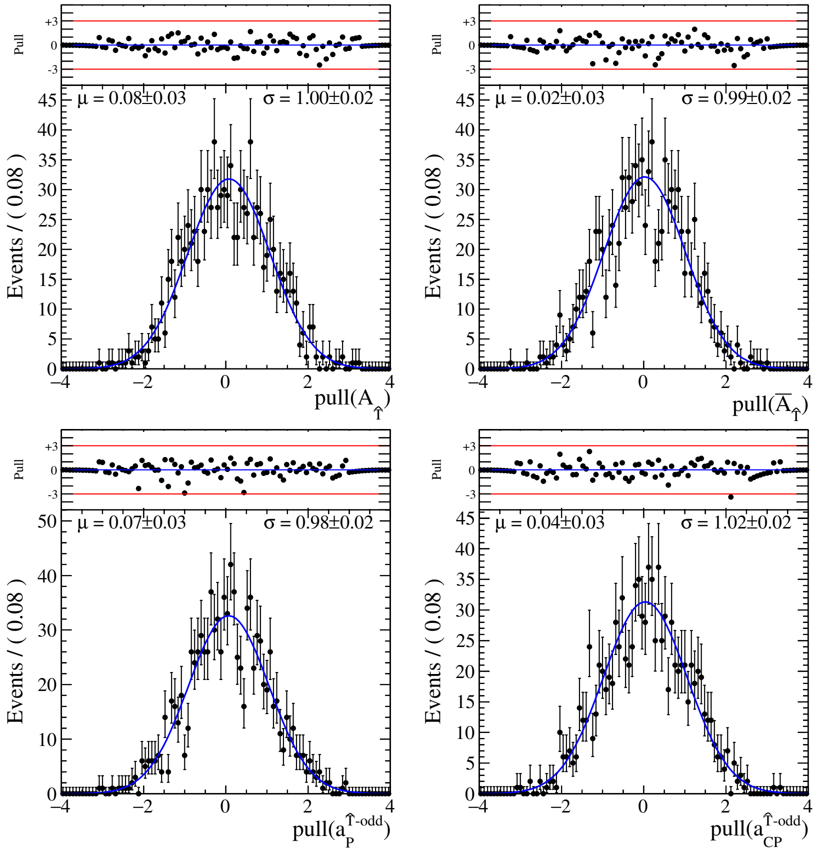

Figure 7.6: Pull distributions for the asymmetries.

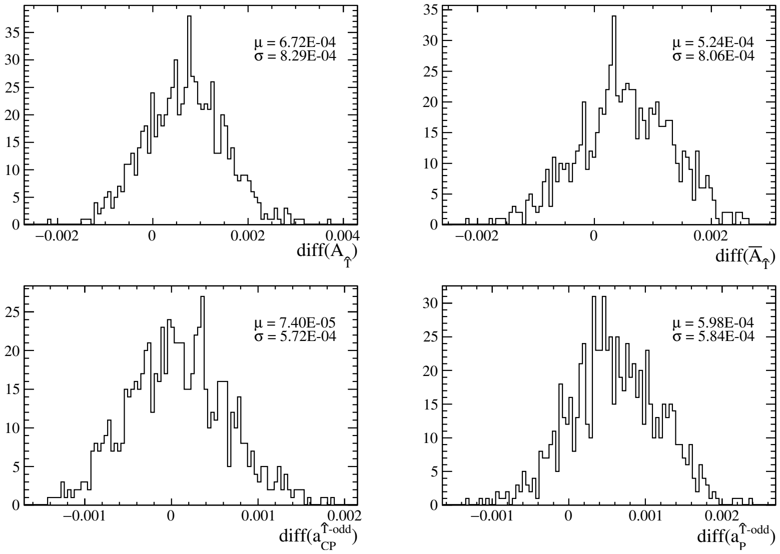

Figure 7.7: Difference between the results obtained fitting the pseudoexperiments with nominal and alternative models.

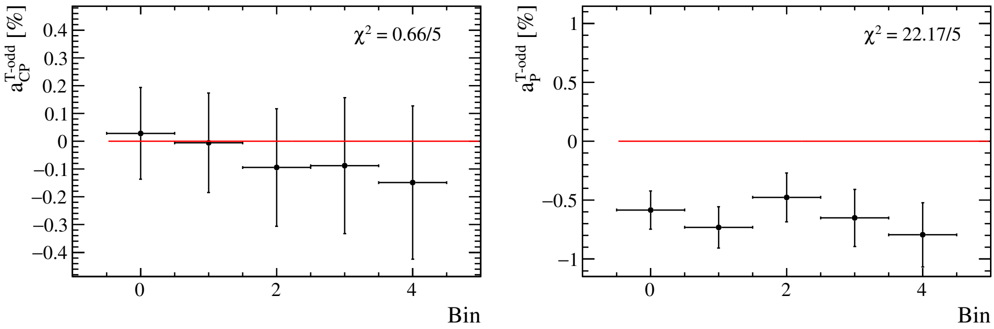

Figure 7.8: $a_{CP}^{\widehat{T}\text{-odd}}$ and $a_{P}^{\widehat{T}\text{-odd}}$ measured with different PID cuts for $\Lambda_b^0 \rightarrow \Lambda_c^+(\rightarrow pK^-\pi^+)\pi^-$ control sample. All the measurements are consistent with each other and doesn't show any dependence. The reported χ^2 takes into account the correlation among the bins and it is calculated with respect the no *CPV* and *P* violation hypotheses, represented by the two red horizontal lines.

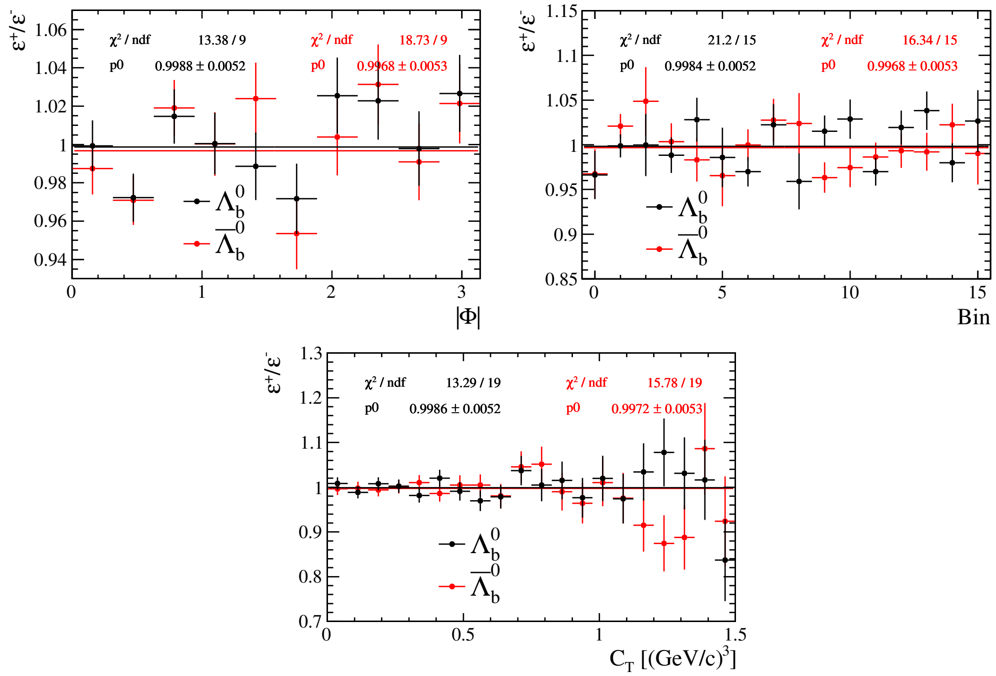

Figure 7.9: Ratio of the efficiencies for positive and negative $C_{\widehat{T}}$ ($\overline{C}_{\widehat{T}}$) values of Λ_b^0 ($\overline{\Lambda}_b^0$) on reweighted MC events for binning scheme A (Top Left), scheme B (Top Right) and in bins of $C_{\widehat{T}}$ ($\overline{C}_{\widehat{T}}$) (Bottom).

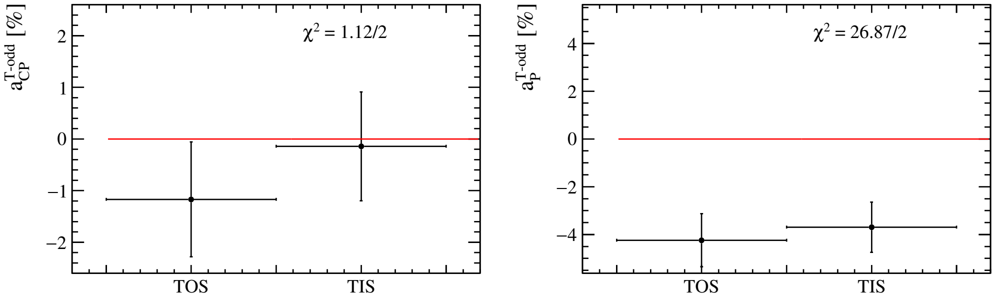

Figure 7.10: Stability of the results on data divided by L0 TIS and TOS requirements.

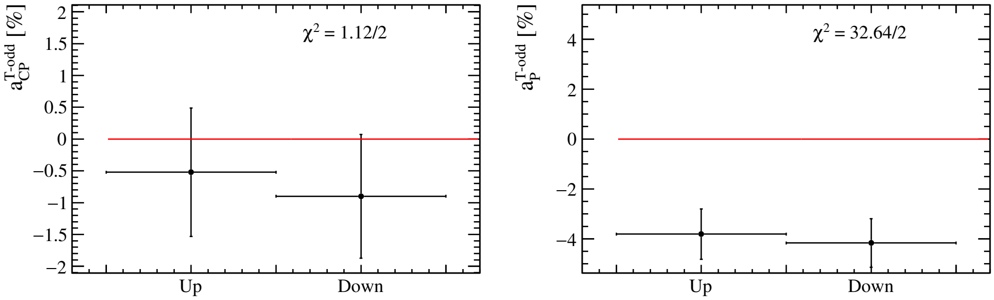

Figure 7.11: Stability of the result as a function of the magnet polarities.

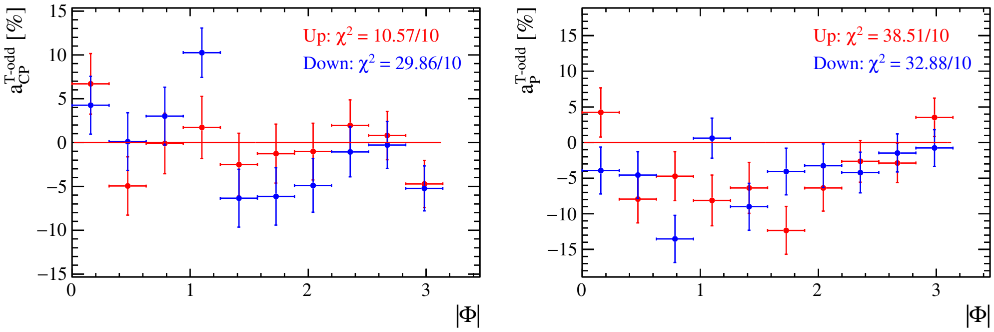

Figure 7.12: Measurements of the asymmetries in bins of Φ for different magnet polarities.

CHAPTER 8

Results

8.1 Measurement of the asymmetries integrated over the phase space

The asymmetries measured from the fit on the full dataset are listed in Table 8.1. We do not observe any deviation from the *CP* conserving hypothesis, while we observe a non-zero value for the $a_P^{\widehat{T}\text{-odd}}$ asymmetry. The effect, estimated with the profile likelihood ratio test, is at the level of 5.5σ and indicates the P violation is present integrated in the phase space in the $\Lambda_b^0 \to p\pi^-\pi^+\pi^-$ decay.

Table 8.1: Measurement of the asymmetries from the fit to the full dataset. The first uncertainty is statistical and the second systematic. For comparison we report the results for the dataset used in this thesis and for the Run 1 dataset already published [38].

Asymmetry	Dataset This thesis (2011-2017)	Run 1 (2011-2012)
$A_{\widehat{T}}$ (%)	$-4.68 \pm 0.99 \pm 0.24$	$-2.56 \pm 2.05 \pm 0.44$
$\overline{A}_{\widehat{T}}$ (%)	$-3.29 \pm 0.99 \pm 0.24$	$-4.86 \pm 2.05 \pm 0.44$
$a_P^{\widehat{T}\text{-odd}}$ (%)	$-3.98 \pm 0.70 \pm 0.17$	$-3.71 \pm 1.45 \pm 0.32$
$a_{CP}^{\widehat{T}\text{-odd}}$ (%)	$-0.70 \pm 0.70 \pm 0.17$	$1.15 \pm 1.45 \pm 0.32$

8.2 Measurement of the asymmetries in bins of the phase space

The asymmetries measured in $\Lambda_b^0 \to p\pi^-\pi^+\pi^-$ decays in region of the phase space dominated by the $\Lambda_b^0 \to N^{*+}\pi^-$ and $\Lambda_b^0 \to pa_1$ contributions in bins of the angle $|\Phi|$, defined in Equation (5.15) and in bins of the helicity angles (binning schemes A, A_1, A_2, B_1, B_2 defined in Section 6.2) are listed in Tables 8.2, 8.3, 8.4, 8.5 and 8.6, respectively. The result in each bin is reported with the first (second) error that represents the statistic (systematic) uncertainty. In the last row we calculate the weighted mean and its uncertainty over all the bins as

$$\sigma_{\overline{x}}^2 = (J^T C^{-1} J)^{-1} \tag{8.1}$$

$$\overline{x} = \sigma_{\overline{x}}^2 (J^T C^{-1} X) \tag{8.2}$$

where $\overline{x}$ is the mean and $\sigma_{\overline{x}}$ its error, X is the vector with all the measurements, J is a vector of ones with length as the number of bins, C is the covariance matrix calculated as the sum of the statistic and systematic covariance matrix. The systematic uncertainties

Table 8.2: Measured asymmetries in bins of the $|\Phi|$ angle (scheme A). The first (second) error represents the statistic (systematic) uncertainty. In the last row we calculate the weighted mean and its error over all the bins.

Bin	$A_{\widehat{T}}(\%)$	$\overline{A}_{\widehat{T}}(\%)$	$a_P^{\widehat{T}\text{-odd}}(\%)$	$a_{CP}^{\widehat{T}\text{-odd}}(\%)$
0	$5.7 \pm 3.4 \pm 1.3$	$-5.5 \pm 3.3 \pm 1.3$	$0.1 \pm 2.4 \pm 0.9$	$5.6 \pm 2.4 \pm 0.9$
1	$-8.6 \pm 3.2 \pm 1.2$	$-3.8 \pm 3.4 \pm 1.2$	$-6.2 \pm 2.3 \pm 0.9$	$-2.4 \pm 2.3 \pm 0.9$
2	$-7.8 \pm 3.4 \pm 1.2$	$-10.5 \pm 3.4 \pm 1.2$	$-9.2 \pm 2.4 \pm 0.8$	$1.3 \pm 2.4 \pm 0.8$
3	$2.4 \pm 3.5 \pm 1.1$	$-9.6 \pm 3.4 \pm 1.1$	$-3.6 \pm 2.4 \pm 0.8$	$6.0 \pm 2.4 \pm 0.8$
4	$-12.6 \pm 3.5 \pm 1.1$	$-3.1 \pm 3.3 \pm 1.1$	$-7.8 \pm 2.4 \pm 0.8$	$-4.7 \pm 2.4 \pm 0.8$
5	$-11.8 \pm 3.3 \pm 1.1$	$-4.3 \pm 3.3 \pm 1.1$	$-8.0 \pm 2.3 \pm 0.8$	$-3.8 \pm 2.3 \pm 0.8$
6	$-7.9 \pm 3.1 \pm 1.2$	$-1.8 \pm 3.2 \pm 1.2$	$-4.9 \pm 2.2 \pm 0.8$	$-3.0 \pm 2.2 \pm 0.8$
7	$-3.1 \pm 2.9 \pm 1.1$	$-3.9 \pm 2.9 \pm 1.1$	$-3.5 \pm 2.0 \pm 0.8$	$0.4 \pm 2.0 \pm 0.8$
8	$-1.9 \pm 2.7 \pm 1.0$	$-2.4 \pm 2.7 \pm 1.0$	$-2.2 \pm 1.9 \pm 0.7$	$0.3 \pm 1.9 \pm 0.7$
9	$-3.7 \pm 2.6 \pm 1.0$	$6.3 \pm 2.6 \pm 1.0$	$1.3 \pm 1.9 \pm 0.7$	$-5.0 \pm 1.9 \pm 0.7$
Mean	-4.8 ± 1.1	-3.2 ± 1.0	-4.0 ± 0.7	-0.8 ± 0.7

for the systematic covariance matrix are taken from Table 7.4 and assumed fully correlated but the "Experimental bias" which is assumed uncorrelated among the bins. In Figures 8.1 and 8.2 we show the measurements for $a_{CP}^{\widehat{T}\text{-odd}}$ and $a_P^{\widehat{T}\text{-odd}}$ for different binning schemes and in Figure 8.3 we show the comparison of the measured $a_{CP}^{\widehat{T}\text{-odd}}$ and $a_P^{\widehat{T}\text{-odd}}$ asymmetries in bins of $|\Phi|$ with the dataset used in this thesis and with the Run 1 dataset already published [38]. To test the *CP* and P conservation hypotheses we calculate the χ^2 for each binning scheme keeping into account systematic effects as

$$\chi^2 = X^T(C_{stat} + C_{syst})^{-1}X \tag{8.3}$$

where X is the vector of all the measurements in each bin and C_{stat} (C_{syst}) is the covariance matrix for the statistic (systematic) uncertainty. The χ^2 and p-value obtained for the *CP* and P conserving hypotheses for different binning schemes are listed in Table 8.7.

The considered binning schemes for searching for *CP* violation, chosen before the unblinding, are A_2 and B_2 where the contribution from N^* resonances is dominant. The observed p-values with respect to the *CP* conservation hypothesis correspond to statistical significances of 2.9σ and 0.5σ, respectively. Instead the observed p-value for the P symmetry hypothesis corresponds to a statistical significance of 5.1σ for binning scheme A. The p-values for the binning schemes A_1 and A_2 indicates that the P violation is concentrated in the a_1 region where the significance reaches the level of 5.5σ. This represents the first observation of P violation in region of the phase space in the $\Lambda_b^0 \to p\pi^-\pi^+\pi^-$ decay.

Table 8.3: Measured asymmetries in bins of the $|\Phi|$ angle in the region of the phase space dominated by the $\Lambda_b^0 \to p a_1$ contribution (scheme A_1). The first (second) error represents the statistic (systematic) uncertainty. In the last row we calculate the weighted mean and its error over all the bins.

Bin	$A_{\widehat{T}}(\%)$	$\overline{A}_{\widehat{T}}(\%)$	$a_P^{\widehat{T}\text{-odd}}(\%)$	$a_{CP}^{\widehat{T}\text{-odd}}(\%)$
0	$1.6 \pm 4.4 \pm 1.3$	$-10.1 \pm 4.2 \pm 1.3$	$-4.3 \pm 3.0 \pm 0.9$	$5.9 \pm 3.0 \pm 0.9$
1	$-6.9 \pm 4.2 \pm 1.2$	$2.4 \pm 4.5 \pm 1.2$	$-2.3 \pm 3.1 \pm 0.9$	$-4.7 \pm 3.1 \pm 0.9$
2	$-10.2 \pm 4.7 \pm 1.2$	$-12.2 \pm 4.8 \pm 1.2$	$-11.2 \pm 3.4 \pm 0.8$	$1.0 \pm 3.4 \pm 0.8$
3	$-0.2 \pm 5.2 \pm 1.1$	$-2.4 \pm 4.8 \pm 1.1$	$-1.3 \pm 3.5 \pm 0.8$	$1.1 \pm 3.5 \pm 0.8$
4	$-15.6 \pm 5.2 \pm 1.1$	$-5.9 \pm 4.7 \pm 1.1$	$-10.7 \pm 3.5 \pm 0.8$	$-4.9 \pm 3.5 \pm 0.8$
5	$-10.4 \pm 5.0 \pm 1.1$	$-10.3 \pm 5.0 \pm 1.1$	$-10.3 \pm 3.5 \pm 0.8$	$-0.1 \pm 3.5 \pm 0.8$
6	$-10.9 \pm 5.0 \pm 1.2$	$-11.3 \pm 5.5 \pm 1.2$	$-11.1 \pm 3.7 \pm 0.8$	$0.2 \pm 3.7 \pm 0.8$
7	$-12.6 \pm 4.5 \pm 1.1$	$-6.4 \pm 4.7 \pm 1.1$	$-9.5 \pm 3.2 \pm 0.8$	$-3.1 \pm 3.3 \pm 0.8$
8	$-10.8 \pm 4.6 \pm 1.0$	$-3.5 \pm 4.6 \pm 1.0$	$-7.1 \pm 3.2 \pm 0.7$	$-3.7 \pm 3.2 \pm 0.7$
9	$-3.9 \pm 4.4 \pm 1.0$	$15.3 \pm 4.5 \pm 1.0$	$5.7 \pm 3.1 \pm 0.7$	$-9.6 \pm 3.1 \pm 0.7$
Mean	-7.8 ± 1.5	-4.0 ± 1.5	-5.9 ± 1.1	-1.9 ± 1.1

Table 8.4: Measured asymmetries in bins of the $|\Phi|$ angle in the region of the phase space dominated by the $\Lambda_b^0 \to N^{*+}\pi^-$ contribution (scheme A_2). The first (second) error represents the statistic (systematic) uncertainty. In the last row we calculate the weighted mean and its error over all the bins.

Bin	$A_{\widehat{T}}(\%)$	$\overline{A}_{\widehat{T}}(\%)$	$a_P^{\widehat{T}\text{-odd}}(\%)$	$a_{CP}^{\widehat{T}\text{-odd}}(\%)$
0	$12.8 \pm 5.4 \pm 1.3$	$2.0 \pm 5.3 \pm 1.3$	$7.4 \pm 3.8 \pm 0.9$	$5.4 \pm 3.8 \pm 0.9$
1	$-9.5 \pm 5.0 \pm 1.2$	$-12.3 \pm 5.0 \pm 1.2$	$-10.9 \pm 3.5 \pm 0.9$	$1.4 \pm 3.5 \pm 0.9$
2	$-5.6 \pm 4.8 \pm 1.2$	$-8.6 \pm 4.8 \pm 1.2$	$-7.1 \pm 3.4 \pm 0.8$	$1.5 \pm 3.4 \pm 0.8$
3	$4.7 \pm 4.8 \pm 1.1$	$-17.7 \pm 4.8 \pm 1.1$	$-6.5 \pm 3.4 \pm 0.8$	$11.2 \pm 3.4 \pm 0.8$
4	$-10.4 \pm 4.8 \pm 1.1$	$-0.3 \pm 4.5 \pm 1.1$	$-5.3 \pm 3.3 \pm 0.8$	$-5.0 \pm 3.3 \pm 0.8$
5	$-14.2 \pm 4.3 \pm 1.1$	$1.0 \pm 4.4 \pm 1.1$	$-6.6 \pm 3.1 \pm 0.8$	$-7.6 \pm 3.1 \pm 0.8$
6	$-5.4 \pm 3.9 \pm 1.2$	$3.8 \pm 3.9 \pm 1.2$	$-0.8 \pm 2.8 \pm 0.8$	$-4.6 \pm 2.8 \pm 0.8$
7	$4.3 \pm 3.8 \pm 1.1$	$-2.3 \pm 3.6 \pm 1.1$	$1.0 \pm 2.6 \pm 0.8$	$3.3 \pm 2.6 \pm 0.8$
8	$3.7 \pm 3.3 \pm 1.0$	$-0.9 \pm 3.3 \pm 1.0$	$1.4 \pm 2.4 \pm 0.7$	$2.3 \pm 2.4 \pm 0.7$
9	$-3.5 \pm 3.3 \pm 1.0$	$0.9 \pm 3.2 \pm 1.0$	$-1.3 \pm 2.3 \pm 0.7$	$-2.2 \pm 2.3 \pm 0.7$
Mean	-2.2 ± 1.4	-2.5 ± 1.3	-2.3 ± 1.0	0.2 ± 1.0

Table 8.5: Measured asymmetries in bins of the helicity angles in the region of the phase space dominated by the $\Lambda_b^0 \to pa_1$ contribution (scheme B_1). The first (second) error represents the statistic (systematic) uncertainty. In the last row we calculate the weighted mean and its error over all the bins.

Bin	$A_{\widehat{T}}(\%)$	$\overline{A}_{\widehat{T}}(\%)$	$a_P^{\widehat{T}\text{-odd}}(\%)$	$a_{CP}^{\widehat{T}\text{-odd}}(\%)$
0	$-8.2 \pm 4.6 \pm 0.8$	$-2.3 \pm 4.5 \pm 0.8$	$-5.2 \pm 3.2 \pm 0.6$	$-3.0 \pm 3.2 \pm 0.6$
1	$-9.4 \pm 2.7 \pm 0.9$	$-4.7 \pm 2.7 \pm 0.9$	$-7.0 \pm 1.9 \pm 0.6$	$-2.3 \pm 1.9 \pm 0.6$
2	$-6.9 \pm 9.0 \pm 1.1$	$-8.5 \pm 8.8 \pm 1.1$	$-7.7 \pm 6.3 \pm 0.8$	$0.8 \pm 6.3 \pm 0.8$
3	$-5.9 \pm 5.4 \pm 1.7$	$2.7 \pm 5.4 \pm 1.7$	$-1.6 \pm 3.8 \pm 1.2$	$-4.3 \pm 3.8 \pm 1.2$
4	$-38.8 \pm 11.4 \pm 2.2$	$8.2 \pm 9.9 \pm 2.2$	$-15.3 \pm 7.6 \pm 1.6$	$-23.5 \pm 7.6 \pm 1.6$
5	$-26.6 \pm 8.9 \pm 2.6$	$-22.3 \pm 9.5 \pm 2.6$	$-24.4 \pm 6.6 \pm 1.8$	$-2.2 \pm 6.6 \pm 1.8$
6	$-12.6 \pm 9.2 \pm 1.1$	$11.4 \pm 9.2 \pm 1.1$	$-0.6 \pm 6.6 \pm 0.8$	$-12.0 \pm 6.6 \pm 0.8$
7	$-4.9 \pm 7.1 \pm 0.9$	$4.4 \pm 8.0 \pm 0.9$	$-0.3 \pm 5.4 \pm 0.6$	$-4.7 \pm 5.4 \pm 0.6$
8	$-15.6 \pm 7.6 \pm 0.6$	$-5.7 \pm 9.2 \pm 0.6$	$-10.7 \pm 6.0 \pm 0.4$	$-4.9 \pm 6.0 \pm 0.4$
9	$-1.4 \pm 4.1 \pm 0.7$	$-11.1 \pm 4.0 \pm 0.7$	$-6.3 \pm 2.9 \pm 0.5$	$4.9 \pm 2.9 \pm 0.5$
10	$-15.2 \pm 7.9 \pm 1.2$	$-12.2 \pm 9.1 \pm 1.2$	$-13.7 \pm 6.0 \pm 0.9$	$-1.5 \pm 6.1 \pm 0.9$
11	$4.6 \pm 4.2 \pm 1.1$	$-2.5 \pm 4.2 \pm 1.1$	$1.0 \pm 3.0 \pm 0.8$	$3.6 \pm 3.0 \pm 0.8$
12	$-10.2 \pm 8.5 \pm 0.9$	$-2.6 \pm 8.4 \pm 0.9$	$-6.4 \pm 6.0 \pm 0.7$	$-3.8 \pm 6.0 \pm 0.7$
13	$-6.7 \pm 8.3 \pm 1.2$	$-12.6 \pm 8.2 \pm 1.2$	$-9.6 \pm 5.8 \pm 0.8$	$3.0 \pm 5.9 \pm 0.8$
14	$-7.1 \pm 11.2 \pm 0.6$	$10.9 \pm 10.9 \pm 0.6$	$1.9 \pm 7.9 \pm 0.4$	$-9.0 \pm 7.9 \pm 0.4$
15	$-3.9 \pm 14.1 \pm 0.7$	$-10.8 \pm 14.1 \pm 0.7$	$-7.4 \pm 10.1 \pm 0.5$	$3.4 \pm 10.1 \pm 0.5$
Mean	-7.4 ± 1.5	-4.2 ± 1.5	-5.8 ± 1.1	-1.5 ± 1.1

Table 8.6: Measured asymmetries in bins of the helicity angles in the region of the phase space dominated by the $\Lambda_b^0 \to N^{*+}\pi^-$ contribution (scheme B_2). The first (second) error represents the statistic (systematic) uncertainty. In the last row we calculate the weighted mean and its error over all the bins.

Bin	$A_{\widehat{T}}(\%)$	$\overline{A}_{\widehat{T}}(\%)$	$a_P^{\widehat{T}\text{-odd}}(\%)$	$a_{CP}^{\widehat{T}\text{-odd}}(\%)$
0	$-5.7 \pm 4.1 \pm 0.8$	$-10.0 \pm 4.2 \pm 0.8$	$-7.8 \pm 3.0 \pm 0.6$	$2.2 \pm 3.0 \pm 0.6$
1	$-10.3 \pm 5.8 \pm 0.9$	$6.1 \pm 6.2 \pm 0.9$	$-2.1 \pm 4.2 \pm 0.6$	$-8.2 \pm 4.2 \pm 0.6$
2	$-1.1 \pm 5.7 \pm 1.1$	$-9.7 \pm 5.9 \pm 1.1$	$-5.4 \pm 4.1 \pm 0.8$	$4.3 \pm 4.1 \pm 0.8$
3	$-19.1 \pm 7.7 \pm 1.7$	$-10.0 \pm 7.4 \pm 1.7$	$-14.5 \pm 5.4 \pm 1.2$	$-4.5 \pm 5.4 \pm 1.2$
4	$0.8 \pm 5.2 \pm 2.2$	$-4.2 \pm 5.1 \pm 2.2$	$-1.7 \pm 3.6 \pm 1.6$	$2.5 \pm 3.6 \pm 1.6$
5	$-4.6 \pm 5.3 \pm 2.6$	$-1.2 \pm 5.3 \pm 2.6$	$-2.9 \pm 3.8 \pm 1.8$	$-1.7 \pm 3.8 \pm 1.8$
6	$-2.4 \pm 4.1 \pm 1.1$	$-4.0 \pm 4.0 \pm 1.1$	$-3.2 \pm 2.9 \pm 0.8$	$0.8 \pm 2.9 \pm 0.8$
7	$2.0 \pm 5.4 \pm 0.9$	$-10.3 \pm 5.3 \pm 0.9$	$-4.2 \pm 3.8 \pm 0.6$	$6.2 \pm 3.8 \pm 0.6$
8	$-1.5 \pm 5.1 \pm 0.6$	$-6.7 \pm 4.9 \pm 0.6$	$-4.1 \pm 3.5 \pm 0.4$	$2.6 \pm 3.6 \pm 0.4$
9	$-9.1 \pm 7.4 \pm 0.7$	$1.9 \pm 7.1 \pm 0.7$	$-3.6 \pm 5.2 \pm 0.5$	$-5.5 \pm 5.2 \pm 0.5$
10	$-2.0 \pm 4.7 \pm 1.2$	$3.1 \pm 4.5 \pm 1.2$	$0.6 \pm 3.2 \pm 0.9$	$-2.6 \pm 3.2 \pm 0.9$
11	$-0.4 \pm 7.0 \pm 1.1$	$6.6 \pm 6.6 \pm 1.1$	$3.1 \pm 4.8 \pm 0.8$	$-3.5 \pm 4.9 \pm 0.8$
12	$1.9 \pm 4.1 \pm 0.9$	$-5.2 \pm 4.2 \pm 0.9$	$-1.7 \pm 3.0 \pm 0.7$	$3.5 \pm 3.0 \pm 0.7$
13	$-1.1 \pm 5.7 \pm 1.2$	$-0.3 \pm 5.3 \pm 1.2$	$-0.7 \pm 3.9 \pm 0.8$	$-0.4 \pm 3.9 \pm 0.8$
14	$0.2 \pm 5.0 \pm 0.6$	$3.1 \pm 4.9 \pm 0.6$	$1.7 \pm 3.5 \pm 0.4$	$-1.4 \pm 3.5 \pm 0.4$
15	$8.9 \pm 5.7 \pm 0.7$	$6.6 \pm 5.3 \pm 0.7$	$7.7 \pm 3.9 \pm 0.5$	$1.1 \pm 3.9 \pm 0.5$
Mean	-2.0 ± 1.3	-2.6 ± 1.3	-2.3 ± 0.9	0.4 ± 0.9

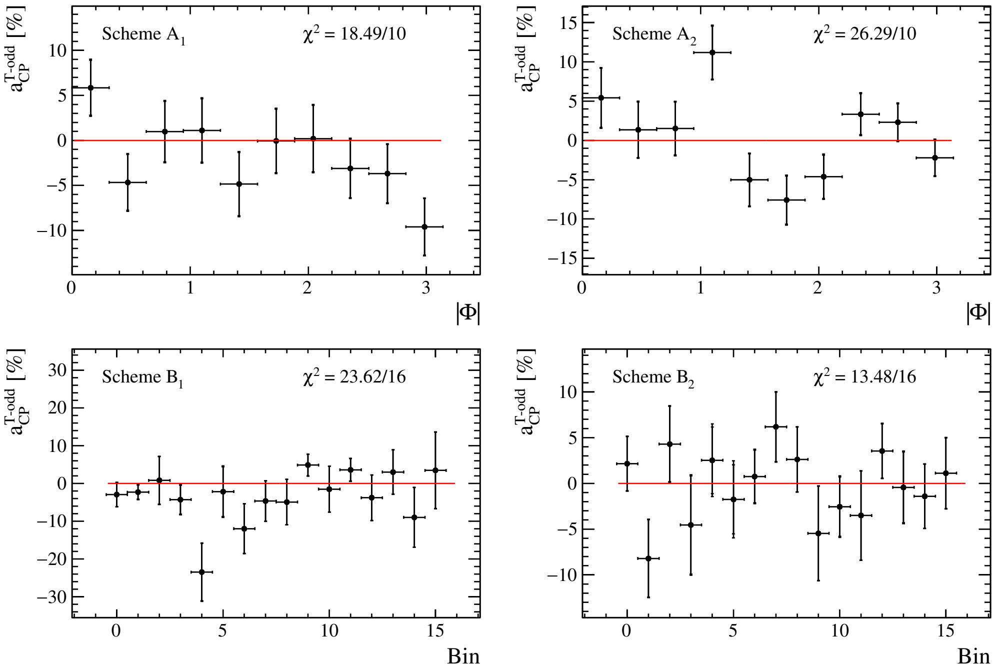

Figure 8.1: Measured $a_{CP}^{\widehat{T}\text{-odd}}$ asymmetry in bins of the angle $|\Phi|$ (helicity angles) for schemes A_1 and A_2 (B_1 and B_2) in the region where the $\Lambda_b^0 \to pa_1$ or $\Lambda_b^0 \to N^{*+}\pi^-$ contribution is dominant, respectively. The systematic uncertainty is represented by an additional error bar line but for most of the bins it is negligible and not visible. The χ^2 takes into account both the statistical and the systematic uncertainty.

Table 8.7: The χ^2 and p-value obtained for the *CP* and *P* conserving hypotheses for different binning schemes taking into account systematic effects.

Binning scheme	Dominant contribution	Hypotheses	χ^2/ndf	p-values	Significance
A (in $\|\Phi\|$)		*CP* conserving *P* conserving	25.20/10 49.38/10	0.50% 3.47×10^{-7}	2.8σ 5.1σ
A_1 (in $\|\Phi\|$)	$\Lambda_b^0 \to pa_1$	*CP* conserving *P* conserving	18.49/10 54.27/10	4.72% 4.32×10^{-8}	2.0σ 5.5σ
A_2 (in $\|\Phi\|$)	$\Lambda_b^0 \to N^{*+}\pi^-$	*CP* conserving *P* conserving	26.29/10 27.91/10	0.34% 1.87×10^{-3}	2.9σ 3.1σ
B_1 (helicity angles)	$\Lambda_b^0 \to pa_1$	*CP* conserving *P* conserving	23.62/16 50.59/16	9.81% 1.84×10^{-5}	1.7σ 4.3σ
B_2 (helicity angles)	$\Lambda_b^0 \to N^{*+}\pi^-$	*CP* conserving *P* conserving	13.48/16 25.34/16	63.72% 6.40%	0.5σ 1.9σ

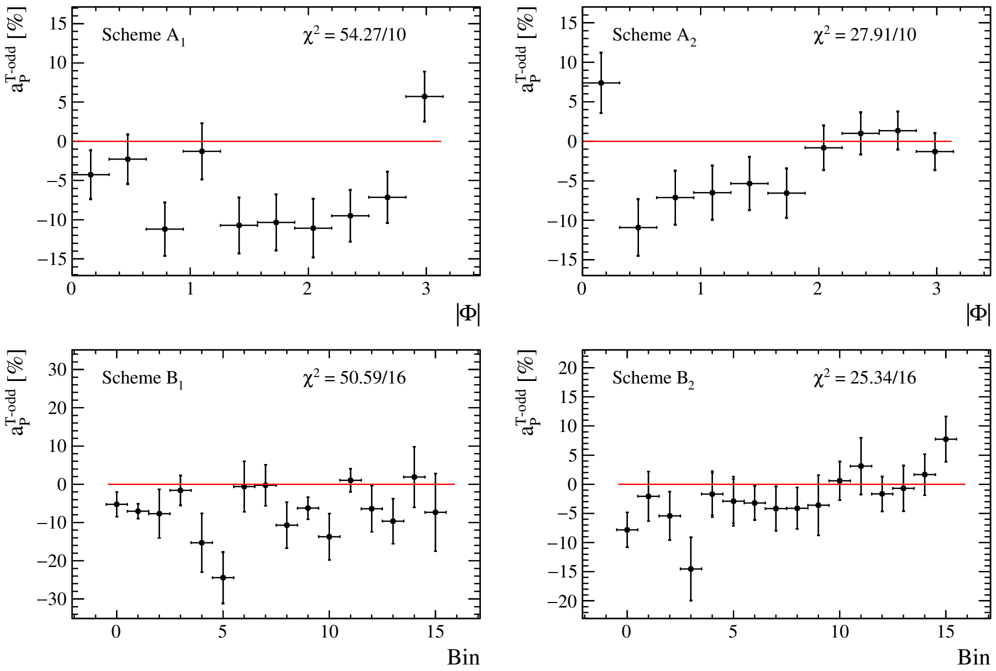

Figure 8.2: Measured $a_P^{\widehat{T}\text{-odd}}$ asymmetry in bins of the angle $|\Phi|$ (helicity angles) for schemes A_1 and A_2 (B_1 and B_2) in the region where the $\Lambda_b^0 \to p a_1$ or $\Lambda_b^0 \to N^{*+}\pi^-$ contribution is dominant, respectively. The systematic uncertainty is represented by an additional error bar line but for most of the bins it is negligible and not visible. The χ^2 takes into account both the statistical and the systematic uncertainty.

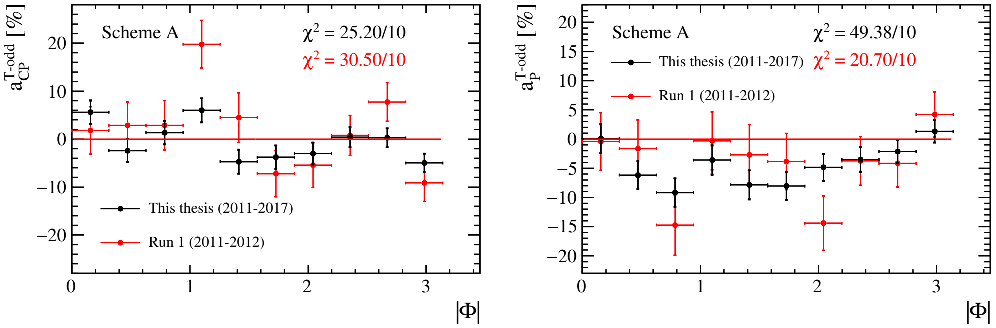

Figure 8.3: Comparison of the measured asymmetries $a_{CP}^{\widehat{T}\text{-odd}}$ and $a_P^{\widehat{T}\text{-odd}}$ in bins of the angle $|\Phi|$ with the dataset used in this thesis and with the Run 1 dataset already published [38]. The systematic uncertainty is represented by an additional error bar line but for most of the bins it is negligible and not visible. The χ^2 takes into account both the statistical and the systematic uncertainty.

Part II

Proposal for the search of heavy baryon EDM with bent crystal at LHCb

CHAPTER 9

Experiment concept and sensitivity

The magnetic and electric dipole moment of a spin-1/2 particle is given (in Gaussian units) by $\boldsymbol{\mu} = g\mu_B \mathbf{s}/2$ and $\boldsymbol{\delta} = d\mu_B \mathbf{s}/2$, respectively, where $\mathbf{s}$ is the spin-polarization vector[1] and $\mu_B = e\hbar/(2mc)$ is the particle magneton and m is its mass. The g and d dimensionless factors are referred to as the gyromagnetic and gyroelectric ratios, respectively. The interaction of magnetic and electric dipole moments with external electromagnetic fields causes the change of the particle spin direction. The experimental setup to measure this effect relies on three main elements:

- a source of polarized particles whose direction and polarization degree are known;
- an intense electromagnetic field able to induce a sizable spin precession angle during the lifetime of the particle;
- the detector to measure the final polarization vector by analysing the angular distribution of the particle decays.

The possibility to measure the MDM of short-lived charm baryons using channeling in bent crystals, in the momentum range of hundreds of GeV/c, is discussed in References [159, 160]. Its feasibility at LHC energies is studied in Reference [72] and offers clear advantages with respect to lower beam energies since the estimated number of produced charm baryons that are channeled into the crystal is proportional to $\gamma^{3/2}$, where γ is the Lorentz factor of the particles. The possibility to exploit the spin rotation in bent crystals to search for the EDM of charm baryons at LHC energies is discussed in Reference [71].

9.1 Experiment concept

Charm baryons produced by interaction of protons on a fixed target, *e.g.* a W target, are polarized perpendicularly to the production plane due to parity conservation in strong interactions [161]. The production plane xz, shown in (Left) Figure 9.1, is determined by the proton and the charm baryon momenta; the latter defines the z axis. The initial polarization vector $\mathbf{s}_0 = (0, s_0, 0)$ is perpendicular to the production plane, along the y axis. To induce spin rotation, the crystal is bent in the yz plane.

When a charged particle has an incident angle with respect to the crystallographic plane (or axis) that is smaller than the so-called Lindhard critical angle, then the successive collisions of the particle with the lattice atoms are correlated. In that case, one can consider the interaction of the charged particle with the atomic plane (string) rather than

---

[1] The spin-polarization vector is defined as $\mathbf{s} = 2\langle \mathbf{S} \rangle/\hbar$, where $\mathbf{S}$ is the spin operator.

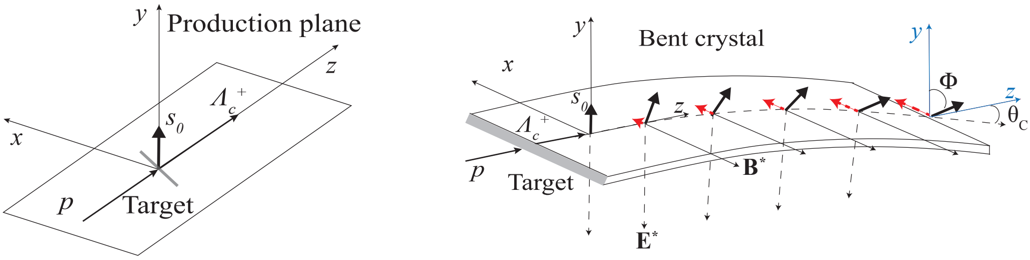

Figure 9.1: (Left) Production plane of the Λ_c^+ baryon defined by the proton and the Λ_c^+ momenta. The initial polarization vector $\mathbf{s}_0$ is perpendicular to the production plane, along the y axis, due to parity conservation in strong interactions. (Right) Deflection of the baryon trajectory and spin precession in the yz and xy plane induced by the MDM and the EDM, respectively. The red, dashed arrows indicate the s_x spin component proportional to the particle EDM, magnified for clarity purposes. Φ is the MDM precession angle and θ_C is the crystal bending angle.

the individual atoms [162]. The atomic plane (string) steers the particle away from the atoms, suppressing the encounters with small impact parameters. The angle by which the particle is reflected by the plane equals the incidence angle. Thus, if the particle is misaligned with respect to the atomic plane (strings) but moves at a small angle with respect to the crystallographic plane, the average potential well ($\approx$ harmonic) can trap the particle, which will oscillate in the plane transverse to its incident direction. If the crystal is bent along the incident direction, the channeled particles would move along the direction of the bent atomic planes, thus bending from the initial direction by the angle of the crystal bending. The crystal bending angle is defined as $\theta_C = L/\rho_0$, where L is the circular arc length of the crystal and ρ_0 the curvature radius.

The intense electric field between the crystal planes, $\mathbf{E}$, which deflects the charged particles transforms into a strong electromagnetic field $\mathbf{E}^* \approx \gamma\mathbf{E}$, $\mathbf{B}^* \approx -\gamma\boldsymbol{\beta} \times \mathbf{E}/c$ in the instantaneous rest frame of the particle and induces spin precession, as described in detail in Reference [163, 164] and illustrated in (Right) Figure 9.1. For a crystal bent in the y direction ,the precession angle Φ is defined as the angle between the polarization vector and the y axis, as shown in (Right) Figure 9.1. In the limit of large boost with Lorentz factor $\gamma \gg 1$, the precession angle in the yz plane induced by the MDM is [165]

$$\Phi \approx \frac{g-2}{2}\gamma\theta_C, \tag{9.1}$$

where g is the gyromagnetic factor.

In presence of a non-zero EDM, the spin precession is no longer confined to the yz plane, originating a s_x component proportional to the particle EDM represented by the red (dashed) arrows in (Right) Figure 9.1. The integration of the equation of motion in presence of EDM is published in Reference [71] and derived in Appendix B.2, as well as the approximations used to solve the equations analytically. It has been verified with simulations in Reference [166]. The polarization vector, after channeling through the crystal is

$$\mathbf{s} = \begin{cases} s_x \approx s_0 \dfrac{d}{g-2}(\cos\Phi - 1) \\ s_y \approx s_0 \cos\Phi \\ s_z \approx s_0 \sin\Phi \end{cases}, \tag{9.2}$$

where Φ is given by Equation (9.1). Therefore, as illustrated in Figure 9.2, the signature of the EDM is a polarization component perpendicular to the plane defined by the initial baryon momentum and polarization vector, otherwise not present, whereas the signature of the MDM is a rotation of the initial polarization vector parallel to that plane.

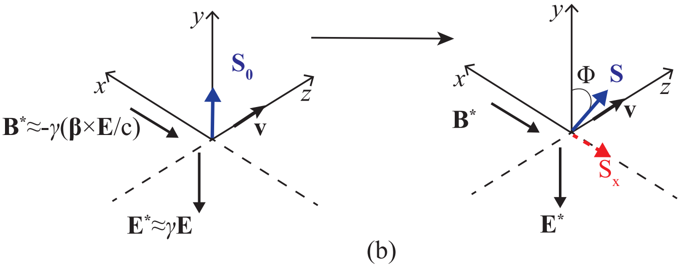

Figure 9.2: Spin precession in an electromagnetic field after time t for transversely polarized charm baryons. $\mathbf{s}_0$ ($\mathbf{s}$) represents the initial (final) polarization vector and $\mathbf{v}$ the particle velocity. The EDM signature is a spin component parallel to the magnetic field $\mathbf{B}^*$ (perpendicular to the particle motion and interplanar electric field) represented by a dashed red arrow. The MDM induces spin rotation of an angle Φ in the plane perpendicular to $\mathbf{B}^*$.

The polarization of channeled Λ_c^+ and Ξ_c^+ baryons, *i.e.* the final polarization, can be determined by studying the angular distribution of the final state particles. For Λ_c^+ decaying to two-body final states such as $f = pK^{*0}$, $\Delta^{++}K^-$, $\Lambda(1520)\pi^+$ and $\Lambda\pi^+$, the angular distribution is described by

$$\frac{dN}{d\Omega} \propto 1 + \alpha_f \mathbf{s}\cdot\hat{\mathbf{k}}\,, \tag{9.3}$$

where α_f is a parity-violating coefficient depending on the final state f, $\hat{\mathbf{k}} = (\sin\theta\cos\phi$, $\sin\theta\sin\phi, \cos\theta)$ the momentum direction of the final state baryon in its helicity frame, $\Omega = (\theta, \phi)$ the corresponding solid angle, and s the Λ_c^+ polarization vector.

The initial polarization s_0 would require in principle the measurement of the angular distribution for unchanneled particles. In practice, however, this will not be required since the measurement of the final polarization vector allows a simultaneous determination of g, d and s_0, as discussed in Appendix B.1.

The same method applies to other positively-charged baryons, like the strange long-lived $\overline{\Xi}^+$ and $\overline{\Omega}^+$ and beauty $\overline{\Xi}_b^+$ and $\overline{\Omega}_b^+$ anti-baryons. The main difference for the first two anti-baryons is the relatively long lifetime compared to the charm baryons. This has no effect on the spin rotation itself, as derived from Equation (9.1), although combined with the large boost will reduce the efficiency to contain the baryon decay inside the tracking volume. While the beauty anti-baryons have comparable lifetime compared to charm baryons (just 3-4 times higher), the main difference in this case is the lower production cross section that worsens the sensitivity on MDM and EDM.

9.2 Sensitivity reach

The number of B baryons produced with 7 TeV protons on a fixed target can be estimated as

$$N_B = \frac{Ft}{A}\sigma(pp\rightarrow BX)R_{\overline{q}/q}N_T, \tag{9.4}$$

where F is the proton rate, t the data-taking time, A the beam transverse area, N_T the number of target nucleons, and $\sigma(pp \to BX)$ is the cross-section for B production in pp interactions at $\sqrt{s} = 114.6\,\mathrm{GeV}$ center-of-mass energy and $R_{\overline{q}/q}$ is the antibaryon-to-baryon ratio for the case of antibaryon production. The number of target nucleons is $N_T = N_A \rho A T A_N R_{pT}/A_T$, where N_A is the Avogadro number, ρ (T) is the target density (thickness), and A_T (A_N) is the atomic mass (atomic mass number). The nuclear modification factor R_{pT} quantifies the difference between the proton-nucleus collisions and the proton-proton collisions, *i.e.* it is a correction needed to take into account the number of participant nucleons of the target which might differ from the total number of target nucleons (A_N) due to nuclear matter effects. For hard processes the cross section, in the absence of strong final-state modification, scales with A_N [167], thus we take $R_{pT} \approx 1$. The number of B particles channeled in the bent crystal and reconstructed in the LHCb detector is estimated as

$$N_B^{\mathrm{reco}} = N_B \mathcal{B}(B \to f) \varepsilon_{\mathrm{CH}} \varepsilon_{\mathrm{DF}}(B) \varepsilon_{\mathrm{det}}, \tag{9.5}$$

where $\varepsilon_{\mathrm{CH}}$ represents the channeling efficiency, $\varepsilon_{\mathrm{DF}}$ the decay flight length efficiency, *i.e.* the fraction of baryons that decay after the crystal length, $\varepsilon_{\mathrm{det}}$ the detector reconstruction efficiency. All these quantities and the corresponding estimated values are discussed below and summarised in Tables 9.1, 9.2 and 9.3.

Two possible configurations have been considered for the fixed-target and detector setup, referred to hereafter as S1 and S2. The former is based on the upgraded LHCb detector [168], which will become operational in 2021 and will run for the rest of the decade (LHC Run 3 and Run 4), whereas the latter is an hypothetical dedicated detector considered to function at even higher luminosities and providing an angular coverage to minimise the crystal bending angle. For the S1 scenario, a minimal crystal bending angle of about $14\,\mathrm{mrad}$ is required for channeled baryons to be deflected inside the detector fiducial volume. A beam intensity of $5 \times 10^8\,p/\mathrm{s}$ impinging the target, and an overall data taking efficiency of 50% is assumed. In this case in six weeks of dedicated detector operations, spanned over several years during the next decade, it would be possible to achieve a statistics of about 10^{15} protons on target (PoT). Accurate studies of the attainable proton flux are in progress [169], which has to be compliant with the LHC beam lifetime, machine operations and protection. An increase in proton fluxes, *e.g.* at High Luminosity LHC (HL-LHC) [170], combined with the design of a dedicated detector capable to afford the higher occupancy levels and longer data taking periods, could potentially offer the opportunity for S2 scenario to integrate $\sim 10^{17}$ PoT. Such detector could also extend the angular coverage at larger pseudorapidity to minimise the crystal bending angle.

9.2.1 Baryon and antibaryon production yields

The Λ_c^+ and Ξ_c^+ baryon cross sections can be estimated from the total charm production cross section measured by the PHENIX experiment in pp collisions at $\sqrt{s} = 200\,\mathrm{GeV}$ [172] rescaled to $\sqrt{s} = 114.6\,\mathrm{GeV}$, assuming a linear dependence on $\sqrt{s}$, and the corresponding fragmentation fractions. For the Λ_c^+ case the fragmentation fraction $f_{\Lambda_c^+} \approx 5.6\%$ is derived from [172], consistent with theoretical predictions [173]. The Λ_c^+ baryon branching fractions to $\Delta^{++}K^-$ and $\Lambda\pi^+$ final states are taken from Reference [171]. The Ξ_c^+ fragmentation fraction is estimated considering that all known c-hadron fractions, which amount to about 92%, leave room for the unknown Ξ_c^+, Ξ_c^0 and Ω_c^0 fractions [174, 175]. Assuming $f_{\Xi_c^+} \approx f_{\Xi_c^0} \gg f_{\Omega_c^0}$, we obtain $f_{\Xi_c^+} \approx 4\%$, which is used to rescale the Λ_c^+

Table 9.1: Definitions and estimated values for a tungsten (W) target with a silicon (Si) or germanium (Ge) bent crystal.

Definition	Quantity [unit]	Value
Avogadro number	N_A [atoms/mol]	6.022×10^{23}
Target density (W)	ρ [g/cm^3]	19.25
Target thickness	T [cm]	0.5
Atomic mass (W)	A_T [g/mol]	183.84
Atomic mass number (W)	A_N	183.84
Nuclear modification factor (W)	R_{pT}	≈ 1
	Si	
Crystal bending	θ_C [mrad]	14
Crystal length	L [cm]	7
Crystal radius	ρ_0 [m]	5
	Ge	
Crystal bending	θ_C [mrad]	15
Crystal length	L [cm]	5
Crystal radius	ρ_0 [m]	3.33

cross section by a factor $f_{\Xi_c^+}/f_{\Lambda_c^+} \approx 0.71$. The absolute $\Xi_c^+ \to \Delta^{++}K^-$ branching fraction is estimated from $\mathcal{B}(\Xi_c^+ \to pK^-\pi^+)$, measured relative to that of $\Xi_c^+ \to \Xi^-\pi^+\pi^+$, considering that all known decay modes sum to the total width and assuming that the relative resonant contribution to the $\Xi^-\pi^+\pi^+$ final state is the same in Ξ_c^+ and Λ_c^+ decays. No other quasi-two body Λ_c^+ or Ξ_c^+ decays to the final state $pK^-\pi^+$ are considered for this study. However, there are additional contributions, *e.g.* $\Lambda_c^+ \to \overline{K}^{*0}p$ and $\Lambda_c^+ \to \Lambda(1520)\pi^+$, with similar branching fractions [171, 176] that can be exploited to improve the sensitivity.

For $\overline{\Xi}_b^+$ and $\overline{\Omega}_b^+$ baryons produced from 7 TeV protons impinging on fixed target, the total beauty cross section can be estimated by rescaling the $pp \to b\bar{b}$ cross section measured at $\sqrt{s} = 7\,\text{TeV}$ [113]. As a working hypothesis the ratios $R_{\overline{q}/q}$ for bottom baryons are assumed to be ≈ 0.5, on the basis of the results for charm hadron production at lower energies [177, 178, 179]. Branching fractions for $\overline{\Xi}_b^+$ baryons are known for very few final states. Two suitable two-body decays, requiring a simple two-body angular analysis, are considered. Firstly, the $\overline{\Xi}_b^+ \to \overline{\Xi}^+ J/\psi$ decay, where the J/ψ and $\overline{\Xi}^+$ can be detected in the dimuon final state and as a positive track, respectively. This decay has been measured and its branching fraction times the $\overline{\Xi}_b^+$ fragmentation function is $\approx 6 \times 10^{-7}$ [171]. Secondly, the $\overline{\Xi}_b^+ \to \overline{\Xi}_c^0\pi^+$ decay, where the charm antibaryon can be reconstructed in the $\overline{\Xi}^+\pi^-\pi^+\pi^-$, $\overline{\Xi}^+\pi^-$ or $\overline{p}K^+K^+\pi^-$ final states. This decay has not been observed but its branching fraction can be estimated by comparing the efficiency corrected signal yields for $\Xi_b^- \to \Xi_c^0\pi^-$ and $\Lambda_b^0 \to \Lambda_c^+\pi^-$ decays [180]. The average fragmentation fraction $f_{\Lambda_b^0} \approx 7\%$ [181], the measured $\mathcal{B}(\Lambda_b^0 \to \Lambda_c^+\pi^-)$ [171], and the Ξ_c^0 branching ratios, estimated similarly to the previous Ξ_c^+ case, are used for this calculation. Summing together the contributions of the $\overline{\Xi}_b^+ \to \overline{\Xi}^+ J/\psi$ and the $\overline{\Xi}_b^+ \to \overline{\Xi}_c^0\pi^+$ decays, we obtain a global branching fraction times the fragmentation function as shown in Table 9.2. Similar decays can be considered for the $\overline{\Omega}_b^+$ baryon. In this case, the $\overline{\Omega}_b^+ \to \overline{\Omega}_c^0\pi^+$ and $\overline{\Omega}_c^0$ branching ratios are unknown, and we assume the latter to be the same as for Ξ_c^0 decays

Table 9.2: Production cross sections σ, initial polarizations $s_0$and antibaryon-to-baryon ratios $R_{\overline{q}/q}$ for pW collisions at $\sqrt{s} \approx 115\,\mathrm{GeV}$, along with the anomalous magnetic moment $g' = (g-2)/2$, decay channels, branching ratios $\mathcal{B}$ and decay asymmetry parameters α_f, for the different charm, beauty and strange charged baryons. For comparison purposes, the Λ_c^+ case has been considered in the $\Delta^{++}K^-$ and $\Lambda\pi^+$ final states. Other quantities like particle masses, spins and lifetimes are taken from Reference [171]. For $\overline{\Xi}_b^+$ and $\overline{\Omega}_b^+$ antibaryons, $\mathcal{B}$ includes the fragmentation fraction from $\overline{b}$ quarks, and σ is the total $pp \to b\overline{b}$ beauty cross section.

Particle	Λ_c^+		Ξ_c^+	$\overline{\Xi}_b^+$	$\overline{\Omega}_b^+$	$\overline{\Xi}^+$	$\overline{\Omega}^+$
Decay channel	$\Delta^{++}K^-$	$\Lambda\pi^+$	$\Delta^{++}K^-$	$\overline{\Xi}^+ J/\psi$ $\overline{\Xi}_c^0\pi^+$	$\overline{\Omega}^+ J/\psi$ $\overline{\Omega}_c^0\pi^+$	$\overline{\Lambda}\pi^+$	$\overline{\Lambda}K^+$
Cross section, σ [mb]	0.0182		0.0129	4.67×10^{-3}	4.67×10^{-3}	3.4	1.03
$\lvert s_0 \rvert$	0.6		0.6	0.6	0.6	0.5	0.2
g'	-0.3		-0.3	1.4	5.8	1.9	2.2
$\mathcal{B}$	1.09%	0.83%	0.31%	2.9×10^{-6}	8.3×10^{-7}	63.83%	43.32%
α_f	-0.67	-0.91	-0.67	0.91	0.91	0.458	-0.642
$R_{\overline{q}/q}$	1		1	0.5	0.5	0.8	0.9

and scale $f_{\overline{\Omega}_b^+}\mathcal{B}(\overline{\Omega}_b^+ \to \overline{\Omega}_c^0\pi^+)$ by ≈ 0.29, from the ratio between $f_{\Omega_b^-}\mathcal{B}(\Omega_b^- \to \Omega^- J/\psi)$ and $f_{\Xi_b^-}\mathcal{B}(\Xi_b^- \to \Xi^- J/\psi)$ [171].

For the $\overline{\Xi}^+$ and $\overline{\Omega}^+$ antibaryons, which contain two and three s valence antiquarks respectively, the cross sections are estimated by scaling the Λ production cross section using the universal strangeness suppression factor at high energies, $\lambda_s \approx 0.32$ [182]. In turn, the Λ production cross section is estimated from the inclusive $pp \to \Lambda X$ cross section measured at beam momenta of 158 GeV [183] and 405 GeV [184] ($\sqrt{s} \approx 17.2$ and 27.6 GeV, respectively). The ratios $R_{\overline{q}/q}$ are taken to be 0.8 and 0.9 for $\overline{\Xi}^+/\Xi^-$, $\overline{\Omega}^+/\Omega^-$, respectively, as inferred from Au+Au collisions at $\sqrt{s_{NN}} = 130\,\mathrm{GeV}$ [185]. All branching ratios are in this case known [171].

9.2.2 Efficiencies

The channeling efficiency $\varepsilon_{\mathrm{CH}}$ in Si and Ge crystals includes both the trapping efficiency ε_t and deflection efficiency ε_c, and has been estimated separately for each baryon type following the procedure described in Section 10.4. The trapping efficiency itself accounts for the angular and momentum divergence of the baryons produced in the target, and is evaluated from the fraction of baryons within the Lindhard angle and momentun $\gtrsim 800\,\mathrm{GeV}/c$. Crystal parameters, optimized for charm baryons, are taken to be common for all baryon species.

The decay flight efficiency $\varepsilon_{\mathrm{DF}}$ has two contributions: the survival efficiency, ε_s, which accounts for the fraction of channeled baryons decaying after the crystal, and the probability ε_l for long-lived baryons to decay within the VELO region, $\approx 80\,\mathrm{cm}$ downstream of the nominal pp collision point. When one of the baryon decay products is a long-lived Λ, ε_l also accommodates the probability of the Λ to decay before the large-area tracking system upstream the magnet, $\approx 2\,\mathrm{m}$ downstream of the collision point, assuming it takes on average half of the initial baryon momentum. For simplicity, the same requirements are applied for both S1 and S2 scenarios.

The detector efficiency $\varepsilon_{\mathrm{det}}$ can be estimated from the product of the geometrical, trigger and tracking efficiencies, the latter including combinatorics and selection efficiencies. The software-based trigger for the LHCb upgrade detector [186], our S1 scenario,

Table 9.3: Channeling, survival, decay flight and detector efficiencies, along with the average energy and squared transverse momentum of channeled baryons (before decay flight requirements), for a W target with a Si or Ge bent crystal in the S1 [S2] scenario. Note that $\varepsilon_{\mathrm{DF}}$ already includes ε_s. The sensitivity study based on pseudo-experiments makes use of the complete energy spectrum after channeling, from which $\overline{E}$ and $\overline{p_\perp^2}$ reported here are obtained. All estimates, except $\varepsilon_{\mathrm{det}}$ (see text), are obtained from samples of charm and strange baryons generated separately for each baryon type from 7 TeV proton beam collisions on protons at rest using PYTHIA. For beauty baryons, we scale the energy of other simulated baryons to obtain an average energy shift estimated assuming a linear dependence with the baryon mass difference.

Particle	Λ_c^+		Ξ_c^+	$\overline{\Xi}_b^+$	$\overline{\Omega}_b^+$	$\overline{\Xi}^+$	$\overline{\Omega}^+$
Decay channel	$\Delta^{++}K^-$	$\Lambda\pi^+$	$\Delta^{++}K^-$	$\overline{\Xi}^+ J/\psi$ $\overline{\Xi}_c^0\pi^+$	$\overline{\Omega}^+ J/\psi$ $\overline{\Omega}_c^0\pi^+$	$\overline{\Lambda}\pi^+$	$\overline{\Lambda}K^+$
				Si			
$\varepsilon_{\mathrm{CH}}$ [$\times 10^{-4}$]	1.24 [4.14]		1.04 [3.90]	2.09 [8.91]	2.11 [9.10]	1.75 [5.57]	1.44 [3.84]
$\overline{E}$ [TeV]	1.36 [2.70]		1.24 [2.40]	1.24 [2.44]	1.24 [2.48]	1.12 [1.54]	1.09 [1.33]
$\overline{p_\perp^2}$ [GeV^2/c^2]	1.22 [0.75]		1.09 [1.19]	1.55 [1.25]	1.49 [1.25]	0.20 [0.21]	0.34 [0.32]
ε_s [%]	9.9 [6.9]		31.7 [24.9]	46.3 [41.0]	45.1 [40.1]	99.8 [99.8]	99.5 [99.3]
$\varepsilon_{\mathrm{DF}}$ [%]	9.9 [6.9]	0.42 [0.16]	31.7 [24.7]	46.3 [39.5]	45.0 [38.7]	0.08 [0.05]	0.20 [0.15]
				Ge			
$\varepsilon_{\mathrm{CH}}$ [$\times 10^{-4}$]	2.32 [5.57]		2.06 [5.18]	3.92 [11.34]	3.98 [11.63]	3.18 [7.34]	2.57 [5.17]
$\overline{E}$ [TeV]	1.37 [2.26]		1.30 [2.07]	1.31 [2.16]	1.32 [2.18]	1.19 [1.51]	1.14 [1.30]
$\overline{p_\perp^2}$ [GeV^2/c^2]	1.16 [1.05]		1.47 [1.09]	1.51 [1.32]	1.52 [1.33]	0.22 [0.22]	0.35 [0.33]
ε_s [%]	20.0 [17.4]		44.9 [40.9]	59.0 [57.4]	57.9 [56.5]	99.9 [99.9]	99.7 [99.6]
$\varepsilon_{\mathrm{DF}}$ [%]	20.0 [17.4]	0.85 [0.52]	44.9 [40.7]	58.9 [56.0]	57.8 [55.2]	0.08 [0.06]	0.20 [0.16]
$\varepsilon_{\mathrm{det}}$ [%]	20	10	20	12	12	10	10

is expected to have efficiency for charm hadrons comparable to the current high level trigger [187], $\approx 80\%$, and similarly for other baryons. A specific trigger scheme for the fixed-target experiment based on the distinct signature of the signal events can enhance the trigger efficiency to $\approx 100\%$. The tracking efficiency is estimated to be 70% per track. We estimate the geometrical efficiency to be $\approx 50\%$. For decays to final states including Λ baryons we further apply a penalty factor $1/2$ to account for the additional inefficiencies to reconstruct highly displaced vertices. Note that the inefficiency due to the long lifetime of the Λ baryon is separately taken into account in $\varepsilon_{\mathrm{DF}}$, as discussed before.

9.2.3 Spin polarization of baryons

The asymmetry parameter of the $\Lambda_c^+ \to \Lambda\pi^+$ decay has been measured to be -0.91 ± 0.15 [171]. For other Λ_c^+ decays no measurements are available but an effective α_f parameter can be calculated from a Dalitz plot analysis of $\Lambda_c^+ \to pK^-\pi^+$ decays [176], *e.g.* $\alpha_{\Lambda_c^+\to\Delta^{++}K^-} = -0.67 \pm 0.30$ [71]. Eventually, a Dalitz plot analysis of $\Lambda_c^+ \to pK^-\pi^+$ decays would provide the ultimate sensitivity to dipole moments. For the $\Xi_c^+ \to \Delta^{++}K^-$ decay the asymmetry parameter is taken to be similar to the Λ_c^+ decay to the same final state, whereas for all beauty antibaryon decays it is assumed to be about the same as for the $\Lambda_c^+ \to \Lambda\pi^+$ decay. For the $\overline{\Xi}^+ \to \overline{\Lambda}\pi^+$ decay the asymmetry parameter is taken from [171]. The $\overline{\Omega}^+ \to \overline{\Lambda}\pi^+$ decay is predominantly parity-conserving and thus has a negligibly small asymmetry parameter [188]. The polarization can be determined in this case from the angular distribution of the antiproton from the $\overline{\Lambda}$ decay, as the $\overline{\Omega}^+$ polarization can be related to the polarization of its $\overline{\Lambda}$ child baryon such that $\mathrm{s}_{\overline{\Omega}^+} = \mathrm{s}_{\overline{\Lambda}}$ [189, 190].

The initial polarization of Λ_c^+ particles produced from the interaction of 7 TeV protons on a fixed target is unknown. However, a measurement from interaction of 230 GeV/c π^- on copper target yields $s_0 = -0.65^{+0.22}_{-0.18}$ for Λ_c^+ transverse momentum larger than 1.1 GeV/c [191]. Moreover, from data produced in the interactions of 500 GeV/c π^- on five thin target foils (one platinum, four diamond) [176], the polarization of the Λ_c^+ is measured as a function of the Λ_c^+ transverse momentum. The average polarization is about -0.1, reaching -0.7 for $p_\perp^2$ between about 1.24 and 5.2 GeV$^2/c^2$. Considering these measurements and the average transverse momentum of channeled Λ_c^+ baryons given in Table 9.3, we assume $|s_0| = 0.6$ for both Λ_c^+ and Ξ_c^+ baryons [160]. The same polarization is assumed for the $\overline{\Xi}_b^+$ and $\overline{\Omega}_b^+$ antibaryons. Similarly, the initial polarization of $\overline{\Xi}^+$ and $\overline{\Omega}^+$ antibaryons produced from the interaction of 7 TeV protons on fixed target is unknown. From proton production below the TeV region [189, 190, 192, 193, 194, 195], the $\overline{\Xi}^+$ are found to be polarized with the same sign and magnitude as the Ξ^-, increasing about linearly with momentum and reaching ≈ -0.2 at 250 GeV/c, whereas the Ω^- is consistent with no polarization. As a working hypothesis initial polarizations of $|s_0| = 0.5$ and 0.2 are assumed for $\overline{\Xi}^+$ and $\overline{\Omega}^+$, respectively, considering the large momentum of channeled antibaryons ≈ 1 TeV/c.

Theoretical predictions of $g-2$ for the Λ_c^+ and Ξ_c^+ baryons range between -0.64 and 0.22 [87, 160], thus a central value $g' = (g-2)/2 = -0.3$ is considered. For $\overline{\Xi}_b^+$ and $\overline{\Omega}_b^+$ antibaryons we take effective quark mass MDM calculations [110]. For all strange baryons under consideration there exist measurements [171].

9.2.4 Sensitivity on EDM and MDM

The main contribution to the statistical uncertainty on d and g, in the limit $\gamma \gg 1$, can be estimated as

$$\sigma_d \approx \frac{g-2}{\alpha_f s_0 (\cos\Phi - 1)} \frac{1}{\sqrt{N_B^{\rm reco}}}, \quad \sigma_g \approx \frac{2}{\alpha_f s_0 \gamma \theta_C} \frac{1}{\sqrt{N_B^{\rm reco}}}, \tag{9.6}$$

where $N_B^{\rm reco}$ is the number of channeled and reconstructed B baryons in Equation (9.5), and Φ ($\approx 2.5\,\text{rad}$ for the case of Λ_c^+) is the precession angle defined in Equation (9.1), which can be determined using the quantities reported in Tables 9.1, 9.2 and 9.3. The other terms are the ones defined in Section 9.1. These estimates assume negligibly small uncertainties on θ_C, γ and s_0, and they follow from the d and $g-2$ values that can be derived from Equation (9.2),

$$d \approx \frac{(g-2)A_x}{\alpha_f s_0 (\cos\Phi - 1)}, \quad g-2 \approx \frac{2}{\gamma\theta_C} \arccos\left(\frac{A_y}{\alpha_f s_0}\right) \approx \frac{2}{\gamma\theta_C} \arcsin\left(\frac{A_z}{\alpha_f s_0}\right), \tag{9.7}$$

where the quantity $A_{x,y,z} = \alpha_f s_{x,y,z}$ can be measured from a fit to the angular distribution of the decay products.

Another approach to assess the sensitivity is to generate pseudo-experiments using the angular distribution from Equation (9.3) and the dependence of the spin-polarization from Equations (9.1) and (9.2). A probability density function is then constructed to perform unbinned maximum likelihood fits to the pseudo-experiments with g and d factors left floated (fixing or floating s_0 does not affect the sensitivity on g nor d).

The two methods provide consistent results, although the former tends to underestimate the uncertainties by about a factor two compared to the latter. While the pseudo-experiments reproduce the energy dependence of the particles and their related sensitivity (γ enters in Equation (9.6)), the analytical formulas are useful to identify the main dependences.

Combining all parameters, measurements and estimates discussed above and summarized in Tables 9.2 and 9.3, we obtain the signal yields, normalized to the incident proton flux F, shown in (top) Figure 9.3. These rates procure the expected EDM and MDM sensitivities reported in (middle and bottom) Figure 9.3, for both Si and Ge crystals and the two considered experimental scenarios, S1 with 10^{15} PoT and S2 with 10^{17} PoT. Germanium crystals provide in all cases significantly better EDM (MDM) sensitivities, which are for S1 scenario of order 10^{-17}, 10^{-14} and 10^{-16} $e\,\mathrm{cm}$ (10^{-3}, 10^{-1} and 10^{-3} μ_N) for charm, beauty and strange baryons, respectively. Here $\mu_N = e\hbar/2m_pc$ is the nuclear magneton, and m_p the proton mass. Sensitivities for S2 scenario would improve by about one order of magnitude.

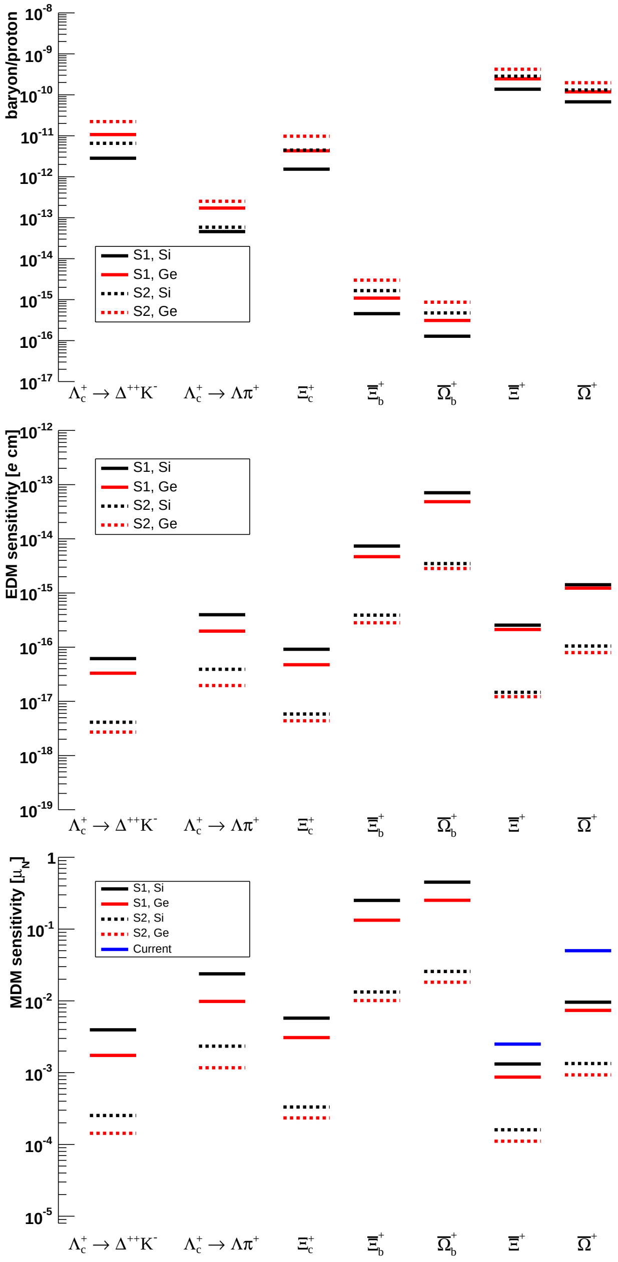

Figure 9.3: (Top) Estimated yields of channeled and reconstructed signal baryons per incident proton on target, and (middle) EDM and (bottom) MDM sensitivities, for Si and Ge with crystal parameters optimized for S1 and S2 scenarios. A total of 10^{15} and 10^{17} protons on target have been considered for S1 and S2 respectively. For comparison purposes, the Λ_c^+ case has been studied in the $\Delta^{++}K^-$ and $\Lambda\pi^+$ final states. Blue lines show the sensitivity of the current Ξ^- and Ω^- MDM measurements.

CHAPTER 10

Experimental setup

10.1 Proof of principle

The spin precession of particles in a bent crystal was first observed by the E761 collaboration that measured the MDM of the strange Σ^+ baryon in the decay of polarized $\Sigma^+ \to p\pi^0$ [75]. A Σ^+ beam with transversal polarization of about 12% and momentum of 375 GeV/c was produced by a 800 GeV/c proton beam impinging on a copper target. As illustrated in (Left) Figure 10.1, two bent silicon crystals of about $2.50 \times 0.04 \times 4.50\,\mathrm{cm}^3$ with approximately identical deflection angles of about $\pm 1.649\,\mathrm{mrad}$ were used. The beam was incident perpendicularly on the surface of the crystal and channeled along its $4.50\,\mathrm{cm}$ length. The average spin precession angle for down-bending and up-bending crystals was measured from an analysis of the angular distributions of decay protons in the Σ^+ rest frame, as shown in (Right) Figure 10.1, and found to be in agreement with the predicted value.

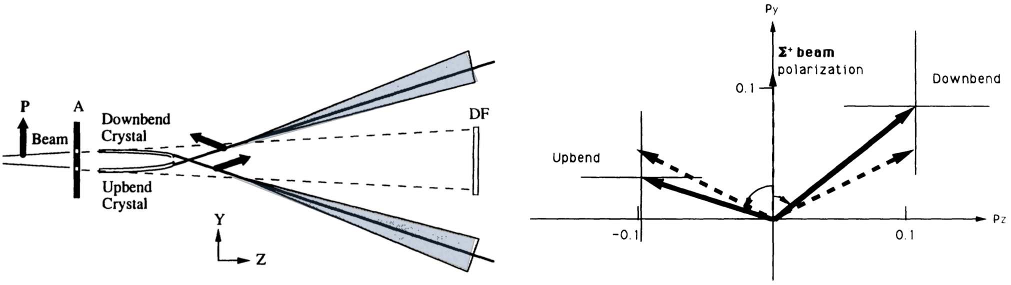

Figure 10.1: (Left) Sketch of the E761 experiment channeling apparatus. The arrows illustrate the opposite spin precession in the down-bending and up-bending crystals. Shaded areas depict the Σ^+ decay cone. The scintillation counters A and DF are part of the trigger system. In particular A rejects tracks that missed the crystal and DF rejects undeflected beam tracks. (Right) Measured polarizations and uncertainties (1σ statistical errors) after spins have been precessed by the two crystals. The dashed arrows show the expected precessions.

10.2 Experimental layout

The experimental layout is sketched in Figure 10.2 and consists of:

- **two crystal kickers for the deflection of 7 TeV protons from the beam halo.** The crystal kickers are positioned about $100\,\mathrm{m}$ upstream of the LHCb detector to deflect

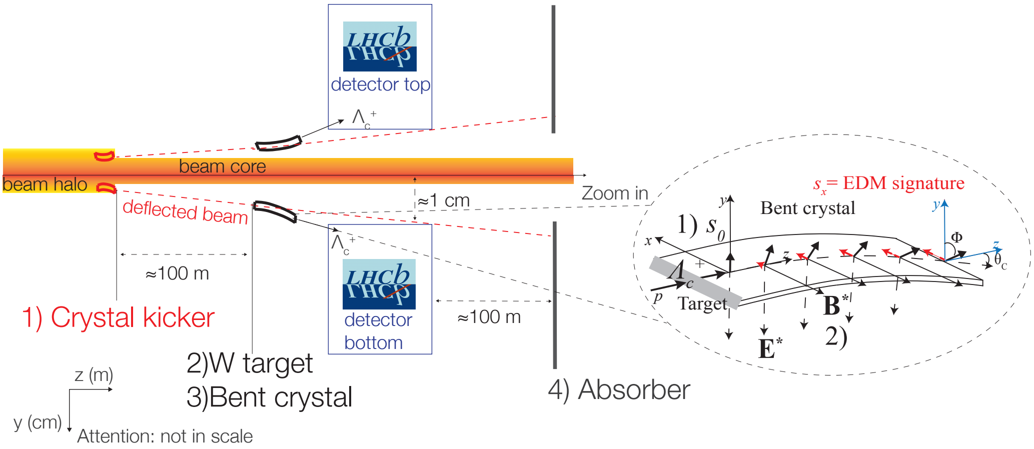

Figure 10.2: Conceptual layout of the fixed-target setup shown in side view with down- and up-bending crystals. The red, dashed line represents the trajectory of deflected protons that did not interact with the target and were not channeled by the crystal. The zoom in shows the spin precession in the down-bending crystal for channeled Λ_c^+ baryons.

the protons from the LHC beam halo at an angle of about $100\,\mu\text{rad}$, demonstrated to be feasible by the UA9 collaboration [196], without affecting the LHC beam lifetime. A beam with intensity up to 5×10^8 proton/s, to be directed on a fixed target, is attainable with this technique [197];

- **fixed-target** The fixed target has to be installed in front of the LHCb detector, possibly close to the VELO detector to obtain good vertex resolution. Two configurations have been considered for the target position, one at $z = -45\,\text{cm}$ inside of the VELO box, referred to hereafter as PI position, and a second one at $z = -116\,\text{cm}$, outside of the VELO vessel, referred to as PO. These two positions are illustrated in the upper part of Figure 10.3. We carried out the simulations for both, but finally the PO was choosen to minimize the impact on the VELO box. The target should be attached to the crystal to maximize the yield of short-lived charm baryons to be channeled.

- **up- and down-bending crystals** The use of up- and down-bending crystals induces opposite spin precession to channeled baryons and it is crucial to prove the robustness of the results and control systematic uncertainties.

  A small polar tilt angle θ_y^{tilt} of the crystal in the yz axis with respect to the incoming protons is required to avoid channeling of non-interacting protons. For tilt angles smaller than $200\,\mu\text{rad}$, the signal channeling efficiencies and the signal loss after background-removal cuts ($p_{\Lambda_c^+} > 800\,\text{GeV}/c$, see Section 11.2) are almost identical to the case of no tilt. Therefore, a crystal tilt θ_y^{tilt} around $25\,\mu\text{rad}$, much larger than the Lindhard critical angle of few μrad, would avoid channeling of incoming protons with no impact on the signal channeling efficiency.

- **Absorbers made of carbon-fibre composites positioned downstream of the LHCb detector to stop the deflected proton beam and background particles.** First results based on simulations of the layout are encouraging [169], and show that the proposed methods to control spill rates present strong synergy with ongoing studies of active loss controls for LHC collimation upgrades. The definition of the absorber system and its optimisation will be done in close connection with the LHC collimation team. Preliminary studies [169] show that it is possible to design and integrate such system in the present LHC layout and that a substantial reduction of the induced beam halo should be obtained to allow synergetic operation with the LHC.

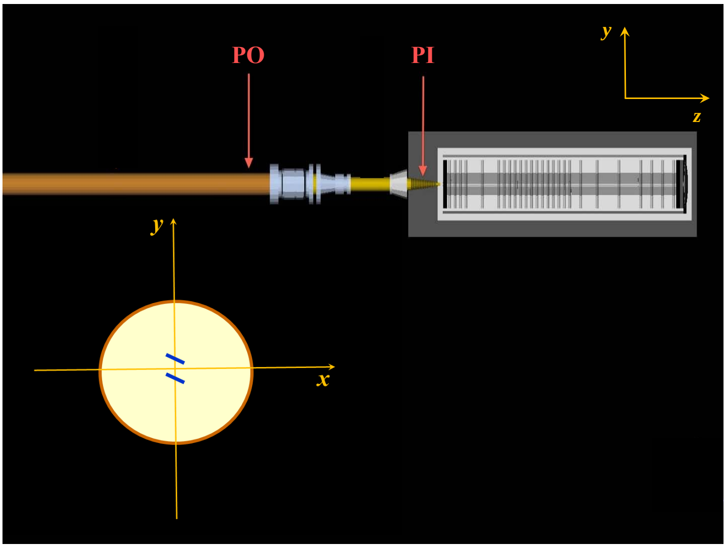

Figure 10.3: Sketch of the target and crystal setup position and rotation in the yz and xy planes. The baseline position, PO, is at $z = -116\,\mathrm{cm}$ upstream of nominal pp collisions, outside of the VELO tank, whereas PI corresponds to $z = -45\,\mathrm{cm}$, on the external wall of the VELO box, both at $x = 0$ and $y = 0.4\,\mathrm{cm}$ (beam vacuum internal radius is $2.5\,\mathrm{cm}$). The crystal bending axis is rotated 25° with respect to the detector y axis to avoid SciFi dead regions, maximizing reconstruction efficiency of the highly collimated baryon decays. A bending angle around 15 mrad is required for channeled particles to be within LHCb acceptance and have high reconstruction efficiency.

The construction of the fixed-target setup is based on few elements that already exist and were installed successfully in the LHC: bent crystals of high purity and high-accuracy rotational systems or "goniometers". Two types of bent crystals with different characteristics are required: the first crystal for the deflection of the protons from the beam halo is very similar to the one constructed at INFN Ferrara and used in the LHC test [198], of $4\,\mathrm{mm}$ length and bending angle of $\approx 100\,\mu\mathrm{rad}$; the second crystal should have larger bending angle $\theta_C \approx 15\,\mathrm{mrad}$, to induce spin precession to channeled baryons. Remotely controlled goniometers equipped with bent crystals will be used, similarly to the ones recently installed in the LHC. They were mounted on standard collimation supports using fast plug-in technology, which ensures fast handling of the object in the tunnel. The installation of the goniometers in the LHC takes about one week. They are based on a piezoelectric actuator and feature angular resolution of $0.1\,\mu\mathrm{rad}$ and linear resolution of $5\,\mu\mathrm{m}$, necessary to align the first bent crystal with respect to the beam halo, and position the bent crystal to intercept the deflected beam. All these devices are already in use at the LHC and are available on the market.

Prior to the installation in the LHC, the fixed-target setup should be tested at CERN North Area H8 proton beam line for a proof of principle. The optimal assembly and the efficiency of the setup will be studied, and the background and the data taking rates will be estimated. The tests will be based on 400 GeV protons with low divergence ($<$ 10 μrad).

The data taking for this program of measurements can be done with short dedicated runs to prove firstly the feasibility and with no others interfering collisions. This option has been studied using full LHCb simulations and are further discussed in Section 11.

10.3 Detector occupancies

The detector occupancy in fixed-target events is determined using the LHCb full simulation. Proton collision events with the W target and the Ge bent crystal are generated using EPOS [199], while nominal pp collision events are generated using PYTHIA [200, 201].

The average number of interactions per bunch crossing for nominal pp collisions is $\nu = 7.6$. This is determined as $\nu_{pp} = \mathcal{L}\sigma_{\rm tot}/f$, where the nominal value of the instantaneous luminosity for the LHCb upgrade is $\mathcal{L} = 2 \times 10^{33}\,{\rm cm}^{-2}\,{\rm s}^{-1}$, the total pp cross-section at $\sqrt{s} = 14$ TeV is $\sigma_{\rm tot} = 102.5\,{\rm mb}$, and the bunch collision frequency $f = 11245\,{\rm Hz} \times 2400 = 27\,{\rm MHz}$ is determined assuming 2400 bunches. The average number of interactions for fixed-target collisions is $\nu_{\rm W}$ and $\nu_{\rm Ge}$ for W target and bent crystal respectively. They are determined as:

$$\nu_{\rm W} = \frac{dN}{dt}\frac{1}{f} = F\, p_{\rm W}\frac{1}{f} = 0.181, \tag{10.1}$$

$$\nu_{\rm Ge} = \frac{dN}{dt}\frac{1}{f} = F\, p_{\rm Ge}\frac{1}{f} = 0.629, \tag{10.2}$$

where $p_{\rm W}$ ($p_{\rm Ge}$) is the probability of a proton to interact in the W target (Ge crystal), and $F = 10^8\,p/\,{\rm s}$ is the rate of impinging protons in the simulation. The probability of a proton to interact with the W target can be estimated as $p_{\rm W} = 1 - e^{-d_{\rm W}/\lambda_{\rm W}} = 0.049$, where $d_{\rm W} = 0.5\,{\rm cm}$ is the thickness of the W target and $\lambda_{\rm W} = 9.946\,{\rm cm}$ is the W nuclear interaction length. Analogously for the Ge crystal the probability is $p_{\rm Ge} = 1 - e^{-d_{\rm Ge}/\lambda_{\rm Ge}} = 0.170$, where $d = 5.0\,{\rm cm}$ is the thickness of the Ge crystal (see Section 10.4) and $\lambda_{\rm Ge} = 26.86\,{\rm cm}$ is the Ge nuclear interaction length. Due to the tilt of the Ge crystal, the channeled Λ_c^+ produced inside the crystal are those produced at an higher angle with a smaller momentum with respect to those produced inside the W target. A cut on the Λ_c^+ momentum will be able to distinguish between these two topologies.

For the studies of the detector occupancy in fixed-target collision events we produce two samples where the primary vertices (PVs) only occur in the W target (bent crystal) with the number of PVs described by a Poissonian distribution with mean $\nu_{\rm W}$ ($\nu_{\rm Ge}$). Then those samples are summed together to obtain the full occupancies reweighting the contribution for W target (bent crystal) to $1 - e^{-\nu_{\rm W}}$ $(1 - e^{-\nu_{\rm Ge}})$ to take into account the 0 PV case of the Poissonian distribution. In this study the flux $F = 10^8\,p/\,{\rm s}$ is equally divided by two targets ($5 \times 10^7\,p/\,{\rm s}$ each), one positioned at positive y while the other at negative y. The targets are placed at $x = 0$, $y = \pm(3, 4)\,{\rm mm}$, $z = (-450,\ -639.5,\ -1160,\ -1380)\,{\rm mm}$, in different positions to compare the results. We investigate also the possibility to change the beam pipe material before the VELO from aluminium (by default in the Upgrade) to beryllium. Figure 10.4 shows the occupancies produced by fixed target events compared to those produced by nominal pp collisions for VELO, SciFi and RICH detectors. The occupancies in the VELO decrease with the increase of the z

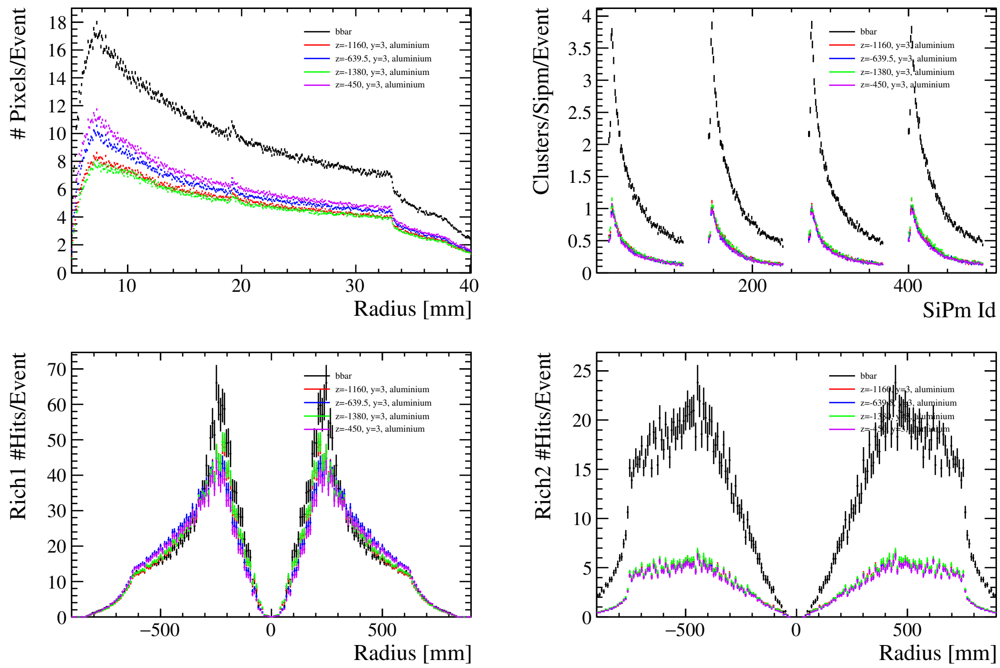

Figure 10.4: Hit radial distribution in VELO (Top/Left), clusters per silicon photomultiplier in SciFi (Top/Right), hit radial distribution in RICH1 (Bottom/Left) and RICH2 (Bottom/Right) for fixed-target events at different z positions compared to $b\bar{b}$ events in nominal pp collisions (black). The radial distance for RICH is calculated from point $(200, 0)\,\mathrm{mm}$ $[(-200, 0)\,\mathrm{mm}]$ in local coordinates for top [bottom] RICH1 panel and from $(400, 0)\,\mathrm{mm}$ $[(-400, 0)\,\mathrm{mm}]$ for left [right] RICH2 panel.

distance from the target. RICH1, RICH2 and SciFi do not show appreciable dependence on the distance. We demonstrate the impact of this change is negligible and no further study this possibility. The contributions to the occupancy from PVs generated in W target and Ge crystal are shown in Figure 10.5. Since the particles generated in W target have to traverse all the crystal generating lots of secondaries, this contribution is very important even if $\nu_{\mathrm{W}} \approx \nu_{\mathrm{Ge}}/4$. Figure 10.6 shows the occupancies varying the target distance from the beam axis and the material of the beam pipe. The occupancies do not show appreciable dependence on these parameters. All these distributions assume the trigger on $b\bar{b}$ events.

At the baseline PO position, for VELO, SciFi and RICH2 the occupancies at flux $F = 10^8\,p/\,\mathrm{s}$ are 3-4 times smaller than for $b\bar{b}$ events at nominal $\mathcal{L} = 2\times10^{33}\,\mathrm{cm}^{-2}\,\mathrm{s}^{-1}$ upgrade luminosity, whereas for RICH1 it is comparable.

10.4 Crystal parameters

Optimal crystal parameters (bending angle θ_C and length $L = \theta_C R$, with R the curvature radius) have been determined by simulating approximately 10^7 $\Lambda_c^+ \to pK^-\pi^+$ events, produced in a 7 TeV proton beam collision on protons at rest, using PYTHIA. Figure 10.7 shows some kinematic variables of the Λ_c^+ produced in the fixed-target setup. The opti-

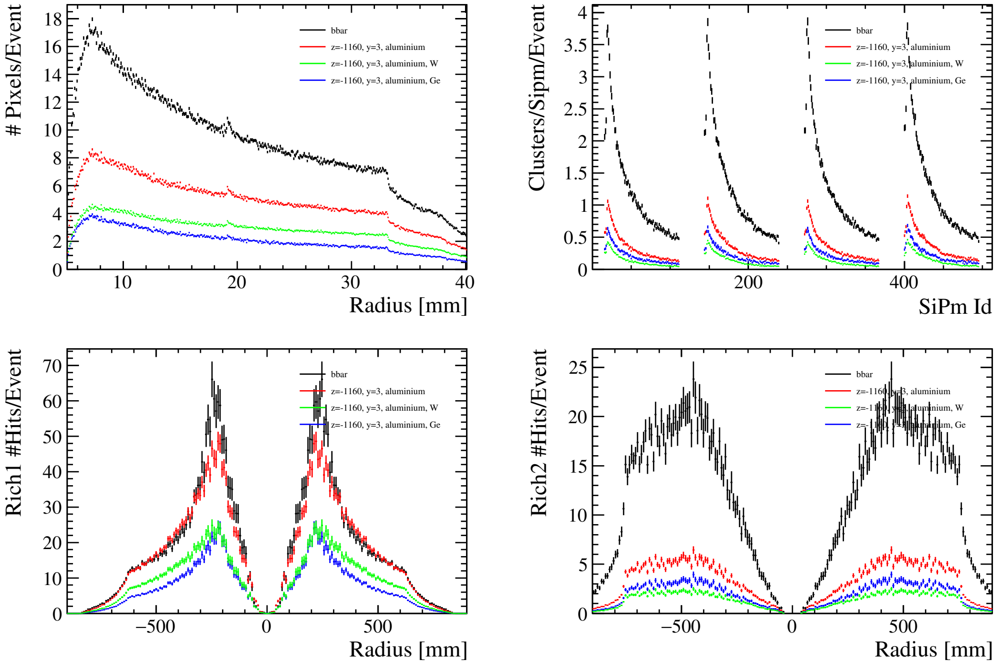

Figure 10.5: Hit radial distribution in VELO (Top/Left), clusters per silicon photomultiplier in SciFi (Top/Right), hit radial distribution in RICH1 (Bottom/Left) and RICH2 (Bottom/Right) for fixed-target events (red) compared to $b\bar{b}$ events in nominal pp collisions (black). It is also shown the contribution from events where the PV is in the W target (green) and in the Ge bent crystal (blue). The radial distance for RICH is calculated from point $(200, 0)\,\mathrm{mm}$ $[(-200, 0)\,\mathrm{mm}]$ in local coordinates for top [bottom] RICH1 panel and from $(400, 0)\,\mathrm{mm}$ $[(-400, 0)\,\mathrm{mm}]$ for left [right] RICH2 panel.

mization aims to identify the best values θ_C and L for the crystal in order to minimize the error on the EDM d and MDM g.

The Λ_c^+ channeling effects are simulated using a parameterisation based on current theoretical description and channeling measurements, as follows [162]:

- the polar angle θ_y of the generated Λ_c^+ must be below the Lindhard angle θ_L, *i.e.* $\theta_y \equiv \arctan \frac{p_y}{p_z} < \theta_L \equiv \sqrt{\frac{2U_0}{p}}$, where p, p_z and p_y denote total, longitudinal and y components (along crystal bending axis) of the Λ_c^+ momentum. $U_0 \equiv U(x_c)$ is the potential-well depth, where $x_c \approx d_p/2 - u_{\mathrm{T}}$ (in the harmonic potential approximation, $U \sim x^2$) is the critical transverse coordinate for the channeled particle, with d_p the interplanar spacing and u_{T} the thermal vibration rms amplitude;

- the critical radius, R_c, must be below the crystal radius R, *i.e.* $R_c \equiv \frac{pc}{U'(x_c)} < R$, where $U'(x)$ is the interplanar electric field;

- the length travelled by the Λ_c^+ particle must be larger than the crystal length L, *i.e.* $ct\gamma\beta > L$ where t is the time of life for a Λ_c^+ before the decay occurs;

- the dechanneling effects in the bent crystal can be estimated in the harmonic po-

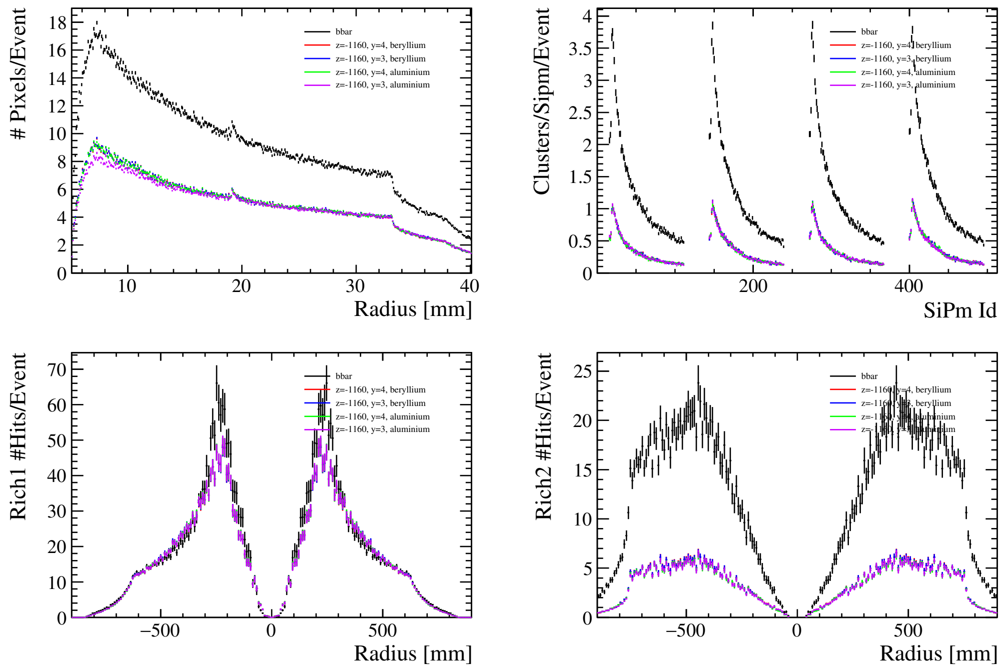

Figure 10.6: Hit radial distribution in VELO (Top/Left), clusters per silicon photomultiplier in SciFi (Top/Right), hit radial distribution in RICH1 (Bottom/Left) and RICH2 (Bottom/Right) for fixed-target events at different distance from beam axis (y position) and different material for the beam pipe before VELO, compared to $b\bar{b}$ events in nominal pp collisions (black). The radial distance for RICH is calculated from point $(200, 0)\,\mathrm{mm}$ $[(-200, 0)\,\mathrm{mm}]$ in local coordinates for top [bottom] RICH1 panel and from $(400, 0)\,\mathrm{mm}$ $[(-400, 0)\,\mathrm{mm}]$ for left [right] RICH2 panel.

tential approximation through a per-event weight w defined as [162]

$$\varepsilon_c(\theta_C, R) = \left(1 - \frac{R_c}{R}\right)^2 \exp\left(-\frac{\theta_C}{\theta_D \frac{R_c}{R}(1 - \frac{R_c}{R})^2}\right), \tag{10.3}$$

where $\theta_D = \frac{256}{9\pi} \frac{N Z a_{\mathrm{TF}} d_p^2}{\ln(2m_e c^2 \gamma / I) - 1}$ represents the ratio of the typical absorption length in a straight crystal to R_c, $N = N_A \frac{\rho}{A}$ is the number of atoms per unit volume, N_A the Avogadro number, A the atomic mass (g/mol), ρ the density, I the ionization potential, Z the atomic number and a_{TF} the screening distance, which characterises the screening effects of the potential of the atom charge distribution compared to the potential of the point-like charge. This weight is in fact the deflection efficiency of a bent crystal.

Values for all the material parameters introduced above are taken from Reference [162] and are listed in Table 10.1. The yields of channeled Λ_c^+ as a function of the crystal parameters are shown in Figure 10.8, for both Si and Ge crystals and are then multiplied by the reconstruction efficiency to determine the optimal values θ_C and L.

We perform a scan in θ_C from 10 to $20\,\mathrm{mrad}$ and in L from 1 to $20\,\mathrm{cm}$ to determine the minimal error on d and g separately. Since we have a momentum distribution for the channeled Λ_c^+ baryons, we generate and fit pseudo experiments using a

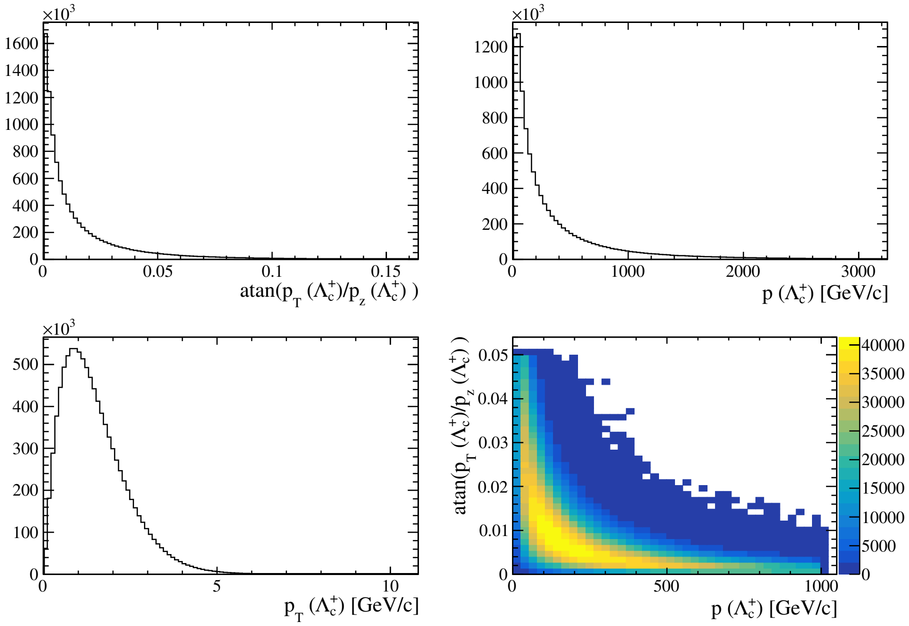

Figure 10.7: Kinematic distributions for Λ_c^+ produced in a fixed-target setup with a 7 TeV beam. The distribution are: (Top/Left) polar angle, (Top/Right) momentum, (Bottom/Left) transverse momentum, and (Bottom/Right) correlation between the polar angle and momentum.

Table 10.1: Material parameters used in the crystal optimization. See text for their definitions.

Material	d_p [Å]	a_{TF} [Å]	u_{T}[Å]	$U(x_c)$[eV]	$U'(x_c)$[GeV/cm]	I[eV]	ρ[g/cm^3]	A[g/mol]	Z
Si 110	1.92	0.194	0.075	16	5.7	173	2.329	28.0855	14
Ge 110	2.00	0.148	0.085	27	10	350	5.323	72.630	32
W 110	1.58	0.112	0.050	63	30	727	19.3	183.84	74

conditional probability density function constructed from the angular distribution from Equation (9.3) and the dependence of the spin-polarization from Equation (9.2) and (9.1), assuming $g' = (g-2)/2 = -0.64, -0.3, 0.22$ (range of variation of Λ_c^+ magnetic moment theoretical estimates, see Section 9.2.4), $d = 0$, $\alpha = -0.67$, $s_0 = 0.6$ and $m_{\Lambda_c^+} = 2286.43\,\mathrm{MeV}/c^2$. Figure 10.9 shows regions whose uncertainties on d (g) are increased by 20% (30%) with respect to the minimum, for Si and Ge at both PO and PI positions. The fact that g prefers higher L values is mainly due to the dependence $\sigma_g \propto 1/\gamma$, as given by Equation (9.6), which has a small impact on d but it is not neglibible in the case of g. The d contours do not depend on the generated g value, as expected according to Equation (9.6). There are wide minimum regions around $L = 7\,\mathrm{cm}$ and $\theta_C = 14\,\mathrm{mrad}$ for Si, and $L = 5\,\mathrm{cm}$ and $\theta_C = 15\,\mathrm{mrad}$ for Ge. These values are referred hereafter as reference optimal crystal parameters (optimal crystal, in short). The optimization with reconstruction efficiencies at 2 TeV does not affect the 20% regions for d, as the reconstruction efficiency is largely independent of the signal Λ_c^+ momentum, as discussed in Section 11.1 (Figure 11.9).

The average momentum of channeled Λ_c^+ as a function of the crystal parameters, as well as the momentum distributions for channeled particles at the reference optimal

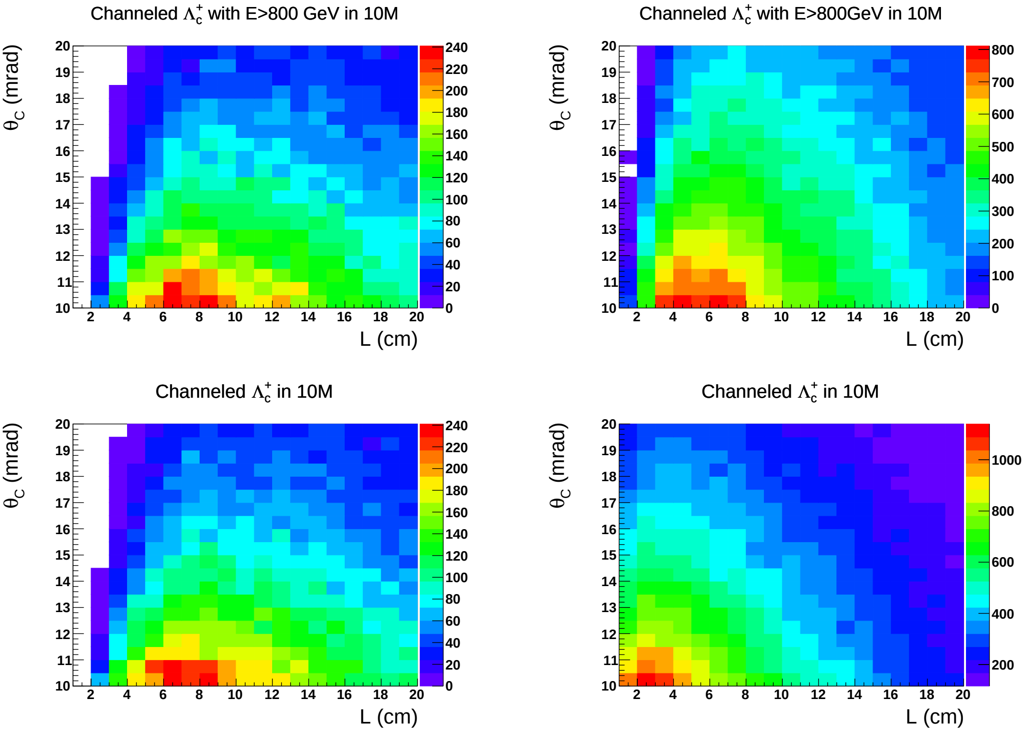

Figure 10.8: Number of Λ_c^+ channeled in 10M of Λ_c^+ generated as a function of the crystal parameters for Si (Left) and Ge (Right) crystals, with (Top) and without (Bottom) requiring $p > 800\,\mathrm{GeV}/c$. This channeling efficiency, which also accounts for the efficiency of the Λ_c^+ to decay after the crystal, *i.e.* $\varepsilon_{\mathrm{CH}}\varepsilon_{\mathrm{DF}}$, is independent of the target position.

configuration are shown in Figure 10.10, for both Si and Ge crystals. In the efficiency plot a requirement $p_{\Lambda_c^+} > 800\,\mathrm{GeV}/c$ is applied to experimentally reject the background as explained in Section 11.2.

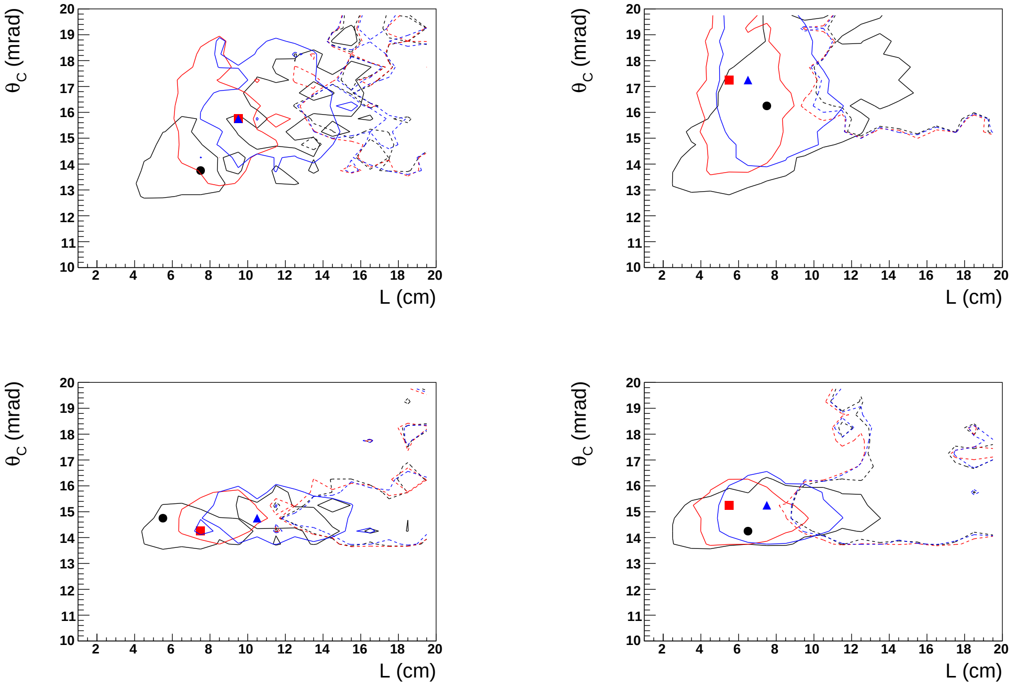

Figure 10.9: Regions of minimal uncertainty of d- and g-factors as a function of the crystal parameters L and θ_C, for Si (Left) and Ge (Right) at PO (Top) and PI (Bottom) positions. The coloured markers and continuous lines represent the minimum uncertainty and regions whose uncertainties on d are increased 20% with respect to the minimum, respectively. Dotted lines represent 30% uncertainty increase with respect to the minimum for the case of g. The different colours represent several assumptions for $g' = (g-2)/2$, ranging from -0.64 (black) to 0.22 (blue), with a central point around -0.3 (red).

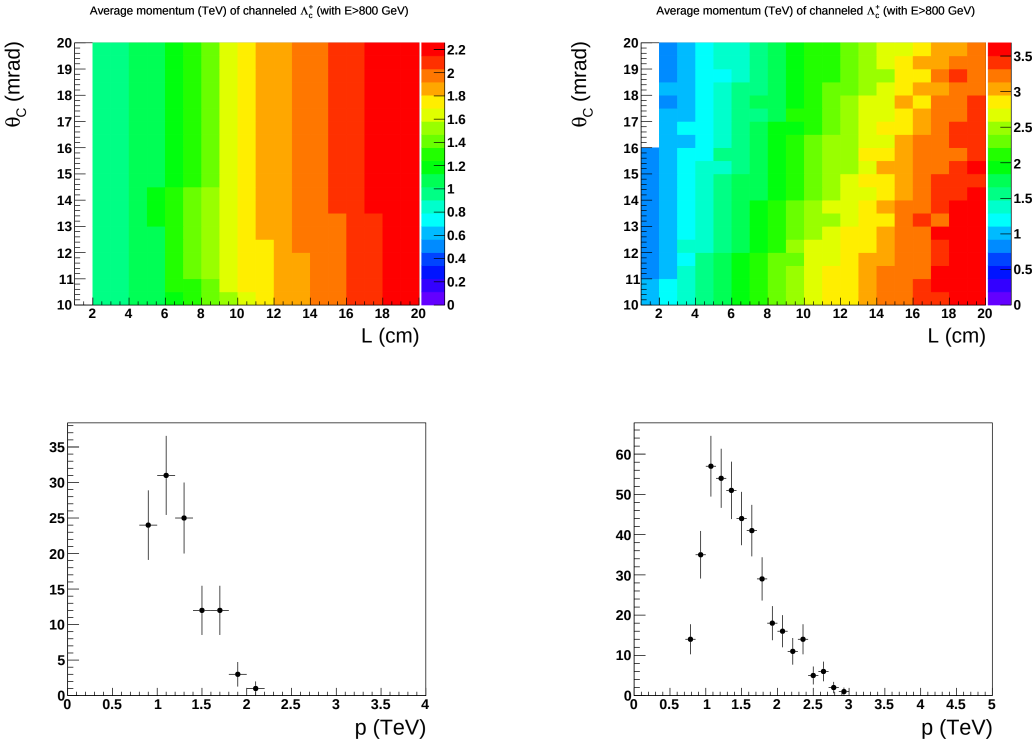

Figure 10.10: (Top) Average momentum (in TeV/c) of channeled Λ_c^+ baryons with $p > 800\,\mathrm{GeV}/c$ as a function of the crystal parameters for Si (Left) and Ge (Right) crystals. (Bottom) Momentum distribution for an optimal Si (Left) crystal with parameters $L = 7\,\mathrm{cm}$, $\theta_C = 14\,\mathrm{mrad}$ and an optimal Ge (Right) crystal with $L = 5\,\mathrm{cm}$, $\theta_C = 15\,\mathrm{mrad}$.

CHAPTER 11

Event reconstruction and identification

Particles from fixed-target collisions are produced in the very forward region. The polar angle distribution in the plane yz (θ_y), with respect to the impinging proton direction, versus the particle momentum is shown in Figure 11.1 for Λ_c^+ baryons. The signature of a typical Λ_c^+ event produced in the target and channeled inside the crystal is shown in Figure 11.2. The vast majority of the particles produced in the target do not enter the detector acceptance, remaining confined inside the beam pipe. The bent crystal is tilted of a small angle with respect to the incoming proton beam direction and rotated with respect to the y detector direction, as discussed in detail below. Particles entering the crystal with momenta parallel to the crystal atomic planes, within the Lindhard critical angle of few μrad, follow their orientation without hitting the atoms. The hard component of the momentum spectrum is channeled and bent inside the detector acceptance where they can be reconstructed.

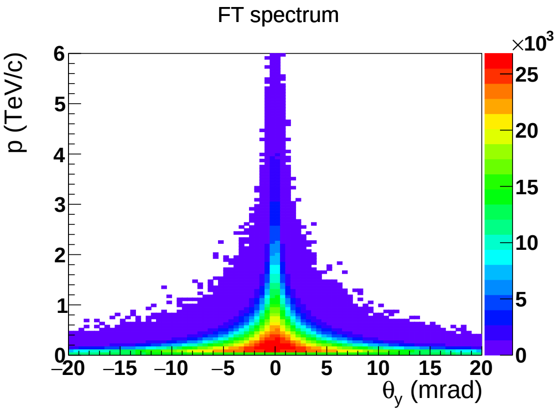

Figure 11.1: Distribution of polar angle θ_y vs momentum for Λ_c^+ baryons produced in the fixed target.

11.1 Acceptance, signal reconstruction and setup positioning

We study the Λ_c^+ reconstruction performance in fixed-target events using EPOS [199] to generate soft p (W+Ge) collisions and PYTHIA [200, 201] for hard interactions where the Λ_c^+ signal particles are produced.

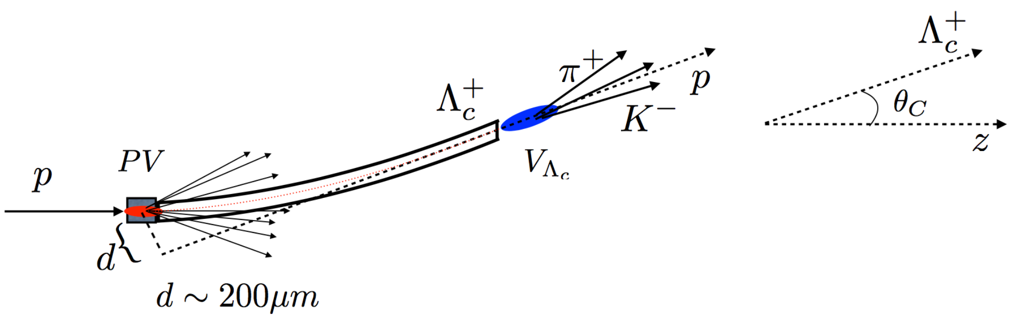

Figure 11.2: Sketch of a typical signal event: the Λ_c^+ baryon, produced in the W target at the primary vertex (PV) of the event, is channeled and bent at an angle θ_C determined by the curvature of the crystal. The Λ_c^+ decays outside of the crystal and the decay position ($V_{\Lambda_c^+}$) is determined by the vertex of the decay products reconstructed by the VELO detector.

We study the LHCb reconstructibility with particle decays in the TeV energy regime, simulating $\Lambda_c^+ \to pK^-\pi^+$ for different polar (θ_y) and azimuthal (ϕ) angles. Maximal reconstruction efficiency is found to be around $\phi = \frac{7}{10}\frac{\pi}{2} \approx 65°$. The drop in efficiency at $\pi/2$ and 0 is due to the not instrumented regions between the SciFi modules ($4\,\mathrm{mm}$ at $\phi = 90°$ and $2\,\mathrm{mm}$ at $0°$) [202] and the fact that the Λ_c^+ decay products are highly collimated. The optimal $\phi \approx 65°$ determines the $\approx 25°$ rotation of the crystal bending axis with respect to the detector y axis, as illustrated in the lower part of Figure 10.3 and in Figure 11.3. We are able to reconstruct Λ_c^+ events at $\theta_y = 12\,\mathrm{mrad}$ (or $\theta_x = 16\,\mathrm{mrad}$, the polar angle in the xz plane). However, a bending angle around $15\,\mathrm{mrad}$ (or $\theta_x = 19\,\mathrm{mrad}$) is required for channeled particles to get well inside detector acceptance and be reconstructed efficiently, with a total efficiency around 40%. These differences are due to the LHCb dipole magnet, which bends charged particles in the xz plane.

We choose to generate the Λ_c^+ baryons at polar angle $\theta_y = 15\,\mathrm{mrad}$ (crystal bending angle) and azimuthal angle $\phi = 0.7\frac{\pi}{2}, 0.7\frac{\pi}{2} + \pi$ in order to maximize reconstruction efficiencies. The W target is $0.5\,\mathrm{cm}$ thick and is positioned at $z = -1160\,\mathrm{mm}$. The Ge crystal is $5\,\mathrm{cm}$ long. Figure 11.3 shows a sketch of the target and crystal geometries implemented in the simulation, while a radiography of the device is shown in Figures 11.4 and 11.5. All the results reported below assume a dedicated run, *i.e.* pp collision events are not superimposed to the target fixed target collisions.

The kinematics of the channeled Λ_c^+ generated in this study is shown in Figure 11.6, where we require the flight distance of the baryon to be at least $5\,\mathrm{cm}$. For technical reasons it is not possible to generate different PV interactions pW and pGe in the same simulation. To be conservative we generate pW PVs with an average number of interactions $\nu_{\mathrm{W}} + \nu_{\mathrm{Ge}}$ and distribute those PVs in target and crystal according to the interaction probability of the two materials.

Figure 11.7 shows the $\Lambda_c^+ \to pK^-\pi^+$ reconstructed invariant mass and decay vertex resolutions for different incident proton fluxes, ranging from 10^8 to $10^9\,p$/s. Both the mass and decay vertex resolutions are independent of the proton flux. The resolutions on the PV reconstruction are shown in Figure 11.8, for events which have only one generated and one reconstructed PV generated in the target positioned at $z = -1160\,\mathrm{mm}$. We obtain resolutions around 0.06, 0.06 and $7\,\mathrm{mm}$ for the x, y, and z coordinates, respectively. The bias along positive z is due to tracks originated at secondary vertices which

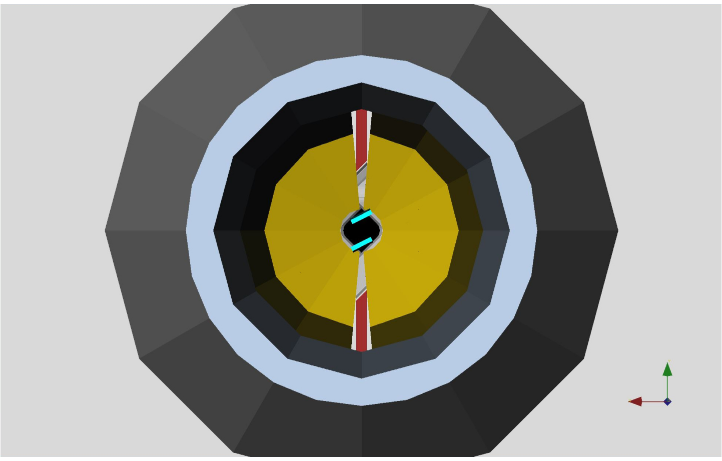

Figure 11.3: xy view of the target+crystal geometry (in azure). The yellow region at the center are the wake field suppressor elements, with the VELO modules visible downstream (grey and red elements).

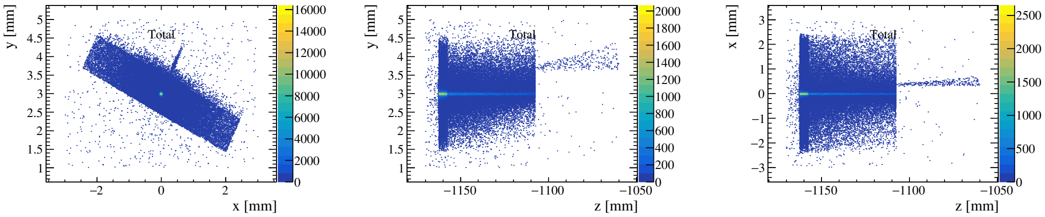

Figure 11.4: Radiography of the target and crystal geometries as integrated within the LHCb simulation, in the xy (Left), zy (Middle) and zx (Right) planes. The distributions show the origin vertex for stable charged particles in the simulation from different physics processes (Compton, δ rays, hadronic interactions and pair production). The presence of the Λ_c^+ decay vertex after the crystal is clearly visible.

cannot be resolved from the PVs.

Figure 11.9 shows the $\Lambda_c^+ \to pK^-\pi^+$ reconstruction efficiency as a function of the incoming proton flux and the Λ_c^+ momentum. It is observed that the reconstruction efficiency is stable with proton fluxes ranging from 10^8 to 10^9 p/s. There is an increase of reconstruction efficiency with momentum, which in practice can be considered almost constant for $p > 800\,\mathrm{GeV}/c$.

The probability that an extra positively-charged particle is channeled in the bent crystal, once the Λ_c^+ is channeled, has been evaluated using pW collisions simulated with the EPOS generator. About 3% of the events with a pW interaction have a charged particle that is channeled in the bent crystal. In this case, the separation between charged particles from signal Λ_c^+ events and extra channeled particles from pW interactions is performed by requiring the charged tracks to be originated from a common vertex (*i.e.* the Λ_c^+ decay vertex) and the reconstructed invariant mass to be peaked at the nominal Λ_c^+ mass.

Given the TeV momentum regime of signal baryons, their decay products are highly collimated so they might not be resolved in the VELO. Figure 11.10 shows the opening

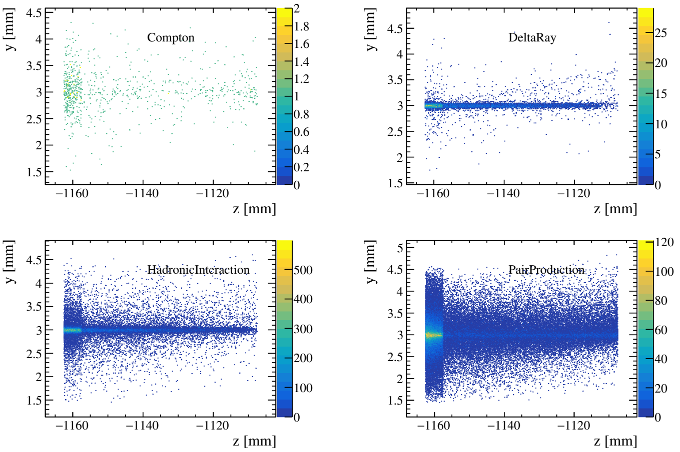

Figure 11.5: Radiography of the target and crystal geometries as integrated within the LHCb simulation, in the yz plane. The distributions show the origin vertex for stable charged particles in the simulation from Compton (Top/Left), δ rays (Top/Right), hadronic interactions (Bottom/Left) and pair production processes (Bottom/Right). The hadronic interactions are the dominating processes.

angle distribution for all pairs of tracks in signal Monte-Carlo $\Lambda_c^+ \to pK^-\pi^+$ decays. As expected, the average angular separation increases as the particles involved are lighter: $1.9\,\mathrm{mrad}$ for pK^-, $2.5\,\mathrm{mrad}$ for $p\pi^+$ and $2.7\,\mathrm{mrad}$ for π^+K^-. With the Λ_c^+ being produced at $z = -116\,\mathrm{cm}$ ($z = -45\,\mathrm{cm}$), this results in an average radial separation at the first VELO station, located at $z \approx -28.9\,\mathrm{cm}$, of about $r = 2\Delta z \tan\theta/2 \approx \Delta z\theta \approx 1.7\ (0.3)\,\mathrm{mm}$, well above the VELO pitch ($55 \times 55\,\mu\mathrm{m}^2$).

11.2 Signal identification and background rejection

The sketch of a typical Λ_c^+ signal event is shown in Figure 11.2. Signal events have a distinct signature which is characterized by particles with high momentum and fixed direction, determined by the crystal bending angle θ_C. This helps to distinguish signal from background events effectively.

These features as well as the separation of backgrounds from particle decays of similar kinematics and the requirements to have non-zero baryon polarization are discussed in the following.

11.2.1 Background from Λ_c^+ baryons

Among all Λ_c^+ particles produced in the fixed target setup (W target and bent crystal) only a tiny fraction ($\approx 10^{-5}$) are created in the W target and channeled through the whole crystal (signal events). The background from other Λ_c^+ baryons is composed by Λ_c^+ particles that:

- are created in the W target but are not channelled
- are channeled but decay inside the crystal
- are dechanneled

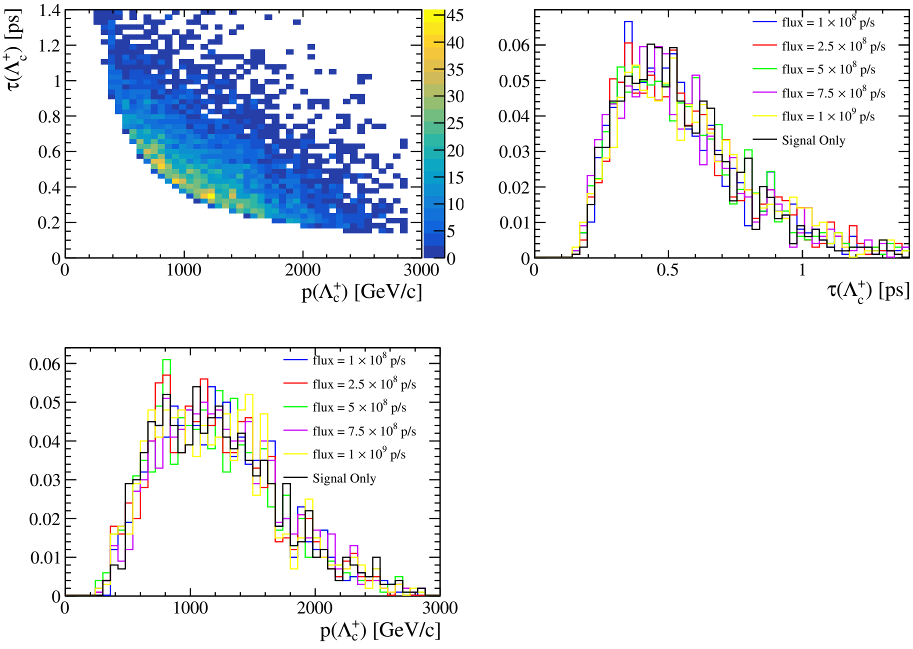

Figure 11.6: (Top/Left) Distribution of decay time versus momentum of the channeled Λ_c^+ generated for the study of signal reconstruction performance in full fixed-target events. (Top/Right) and (Bottom/Left) show the corresponding projections.

- are produced in the crystal and therefore do not see the electrical field of the whole crystal.

The Λ_c^+ particles that, being produced in the W target, are channeled but do not reach the end of the crystal (either because they decay or are dechanneled) acquire a bending angle θ_y smaller than θ_C, as it is shown in Figure 11.11 (Top). These background events can be rejected applying a selection on the outgoing Λ_c^+ angle requiring θ_y to be within $\pm 5\sigma_{\theta_y}$ around θ_C, given the good angular resolution $\sigma_{\theta_y} \approx 25\,\mu\text{rad}$. After this cut the full Λ_c^+ spectrum, shown in Figure 11.11 (Bottom/Left), still contain Λ_c^+ particles produced initially with large angle that, however, must have small momentum due to the correlation between θ_y and momentum shown in Figure 11.1. An additional cut $p_{\Lambda_c^+} > 800\,\text{GeV}/c$ leaves a sample of candidates, shown in (Bottom/Right) Figure 11.11, with only 4% of background events while retaining 81% of the signal.

Another type of background comes from Λ_c^+ particles produced in the crystal and channeled, reaching the end of the crystal with the same angle $\theta_y \approx \theta_C$ as signal events. These Λ_c^+ particles are produced with an initial polar angle parallel to the channel along the full crystal length ($\theta_y > (<) 0$ for upward (downward) bending crystal). These events, however, have typically lower momentum as shown in Figure 11.1, and the momentum cut rejects about 78% of these. The remaining events, which give a background/signal ratio of 19%, are those with smaller $|\theta_y|$ angle, which means that they are produced in the first part of the crystal and therefore have travelled through almost the whole crystal (signal-like events).

The latter background can be reduced using PV information to ensure that the parti-

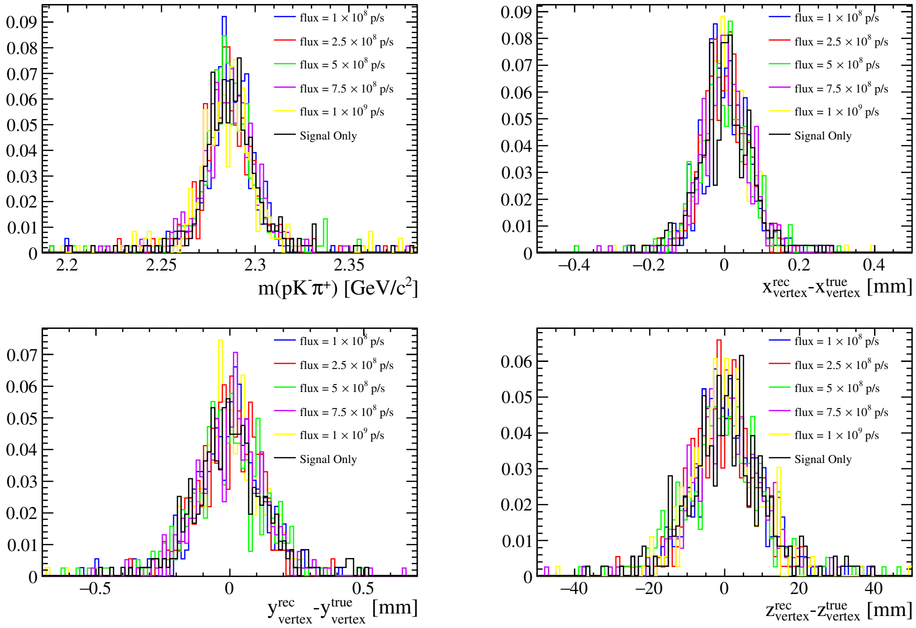

Figure 11.7: Reconstructed $\Lambda_c^+ \to pK^-\pi^+$ mass and decay vertex resolutions in full fixed-target events for different incident proton fluxes.

cles are produced in the target. With a resolution $\sigma_{z_{PV}} \approx 100\ \mu\mathrm{m}$, which would require additional tracking stations a few cm after the fixed target setup at $z \approx -1\,\mathrm{m}$, the background/signal ratio improves to 2%. More sophisticated vertexing techniques could be envisaged to fully exploit the primary and secondary vertex information available without instrumenting the fixed target setup.

11.2.2 Background from channeled charmed mesons

In order to distinguish Λ_c^+ signal events from other particles that are channeled and have similar kinematics, *e.g.* D^+ and D_s^+ mesons, we use the reconstructed invariant mass as a discriminating variable. Typical $\Lambda_c^+ \to pK^-\pi^+$ resolutions are about 20 MeV/c^2.

Channeled D^+ and D_s^+ mesons decaying to three hadrons may be easily misidentified as signal due to the poor hadron particle identification available at TeV/c momentum regime. The most important decay modes are $D^+ \to K^-\pi^+\pi^+$ and $D_s^+ \to K^+K^-\pi^+$ due to their high branching fractions. These can be separated from the signal by vetoing events whose reconstructed invariant mass with mass hypothesis interchanged peak at the charmed meson mass. Particle mass hypothesis is based on momentum hierarchy, as illustrated in Figure 11.12: the highest momentum track is assigned to be the proton, the second the K^- and the third the π^+.

In $D^+ \to K^-\pi^+\pi^+$ one pion can be reconstructed as a proton: as an example, removing events with $|m(\pi^+K^-\pi^+) - m(D^+)| < 55\,\mathrm{MeV}/c^2$ and requiring a signal region $|m(p^+K^-\pi^+) - m(D^+)| < 55\,\mathrm{MeV}/c^2$, a D^+ background efficiency of $\approx 1.6\%$ is expected, along with a signal efficiency of $\approx 70\%$. Figure 11.13 (Left) shows the expected background/signal ratio of $\approx 12\%$, obtained normalising the yields with c quark fragmentation functions and decay branching fractions.

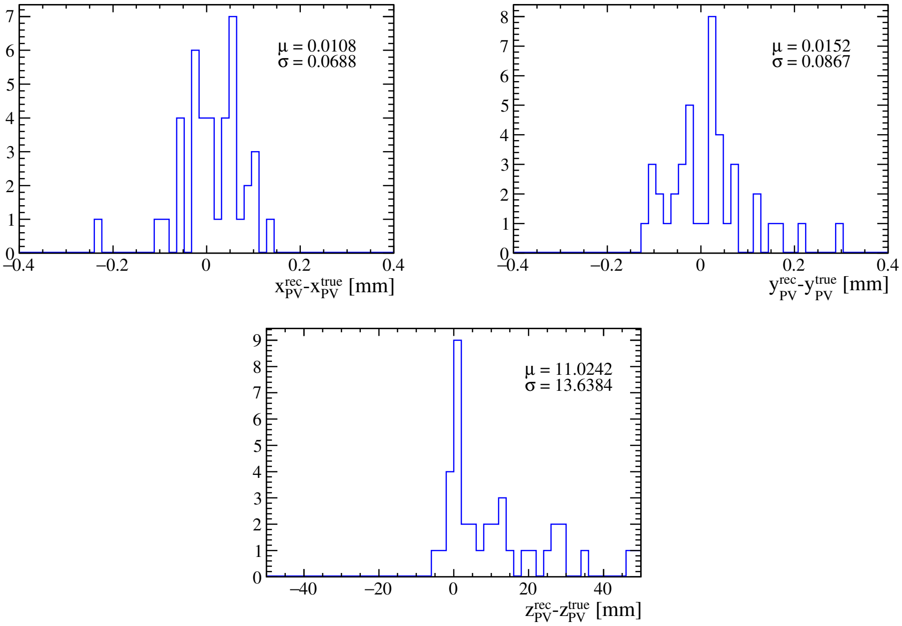

Figure 11.8: PV reconstruction resolution in full fixed-target simulated events. The bias along positive z is due to tracks originated at secondary vertices which cannot be disentagled from the PVs.

In $D_s^+ \to K^+K^-\pi^+$ decays the positive kaon can be misidentified either as a proton or as a pion, where in the latter case the pion is reconstructed as a proton. Requiring $|m(K^+K^-\pi^+) - m(D_s^+)| < 30\,\mathrm{MeV}/c^2$ and $|m(\pi^+K^-p) - m(D_s^+)| < 30\,\mathrm{MeV}/c^2$ in the same signal region as before, a D_s^+ background efficiency of $\approx 3.2\%$ is expected, along with a signal efficiency of $\approx 68\%$. (Right) Figure 11.13 shows the expected background/signal ratio of $\approx 5.2\%$.

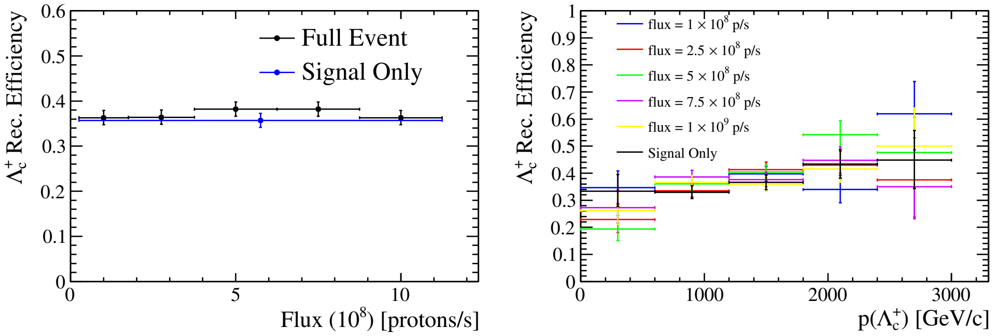

Figure 11.9: $\Lambda_c^+ \to pK^-\pi^+$ reconstruction efficiency as a function of (Left) the incoming proton flux and (Right) the Λ_c^+ momentum.

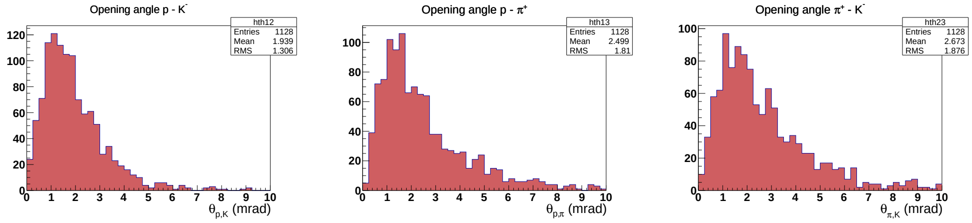

Figure 11.10: Opening angle between all pairs of tracks for signal $\Lambda_c^+ \to pK^-\pi^+$ decays: pK^- (Left), $p\pi^+$ (Center) and π^+K^- (Right).

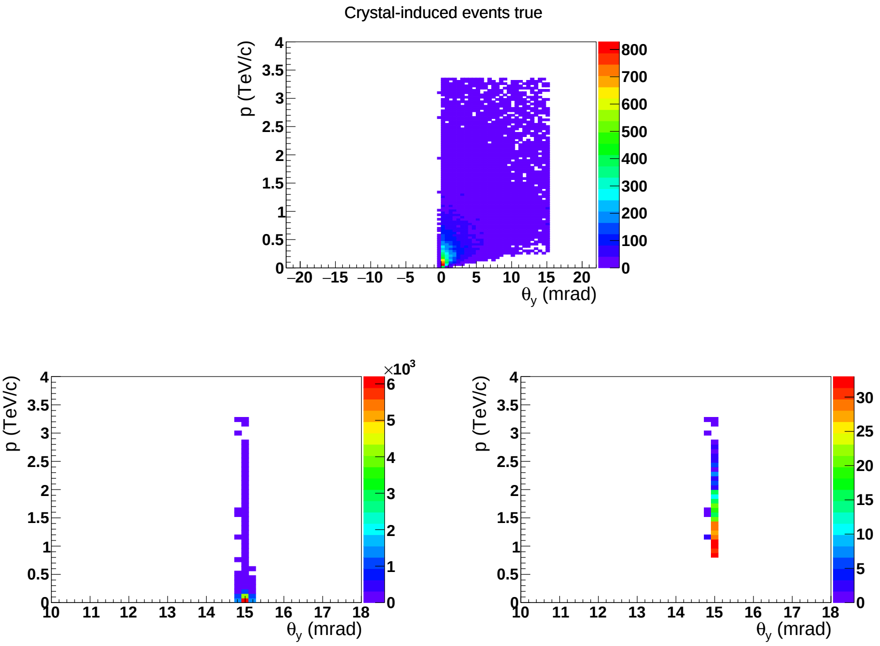

Figure 11.11: (Top) Momentum and polar angle θ_y of Λ_c^+ particles produced in the W target that do not reach the end of the crystal due to the decay or dechanneling processes. (Bottom/Left) Λ_c^+ events left after applying a cut on the polar angle $\theta_y \in |\theta_C \pm 5\sigma_\theta|$ and (Bottom/Right) on momentum $p_{\Lambda_c^+} > 800\,\mathrm{GeV}/c$.

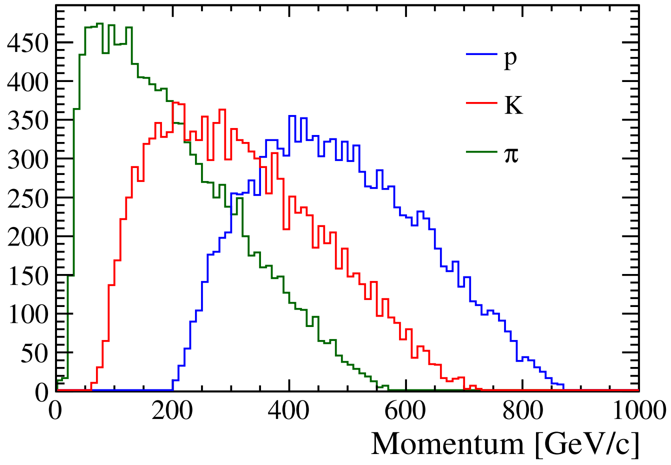

Figure 11.12: Momentum distribution for the p, K^- and π^+ from the Λ_c^+ decay. The particle mass association is based on momentum hierarchy: highest p, second K^- and then π^+.

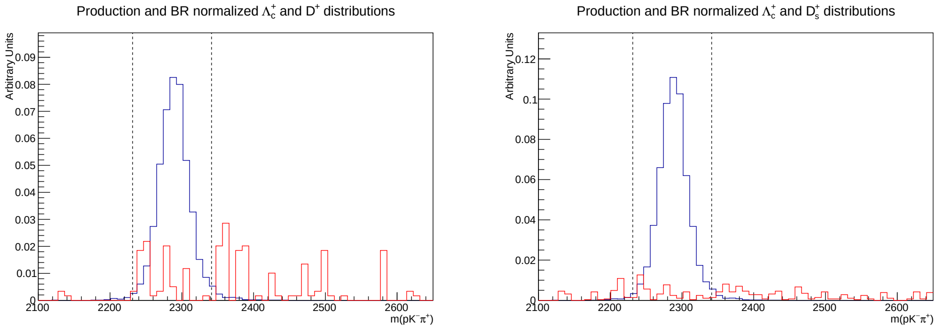

Production and BR normalized Λ_c^+ and D^+ distributions

Production and BR normalized Λ_c^+ and D_s^+ distributions

Figure 11.13: Mass distribution for 1 TeV (blue) signal $\Lambda_c^+ \to pK^-\pi^+$ events and (red) background charm meson decays, (Left) $D^+ \to \pi^+K^-\pi^+$ and (Right) $D_s^+ \to K^+K^-\pi^+$, passing the selection criteria and with particle mass hypotheses based on momentum hierarchy. Signal and background $m(pK^-\pi^+)$ distributions are normalized to each other according to the c-quark fragmentation functions and decay branching fractions. The vertical dashed lines indicate the chosen signal region.

CHAPTER 12

Results

We demonstrated the possibility to measure the EDM and MDM for strange, charm and beauty baryons with bent crystal. This would be the first measurement ever of these quantities for a charm and beauty baryon. Any sign of non-zero EDM, at the current experimental sensitivities, would represents BSM physics.

Baryons produced by interaction of protons on a fixed target are polarized and the intense electric field between the crystal planes induces a spin precession. MDM and EDM measurement are related to the precession angle. The polarization is measured via angular distribution of decay products. Solving the spin precession equation, we show the EDM signature is the appearance of a polarization component perpendicular to the plane defined by the initial baryon momentum and polarization vector, otherwise not present.

Combining all parameters, measurements and estimates discussed in this thesis we obtain the signal yields, normalized to the incident proton flux. These rates procure the expected EDM and MDM sensitivities, for both Si and Ge crystals, in the two considered experimental scenarios: at LHCb with 10^{15} PoT and in a dedicated experiment with 10^{17} PoT. Germanium crystals provide in all cases significantly better EDM (MDM) sensitivities, which are for LHCb scenario of order $10^{-17}, 10^{-14}$ and $10^{-16}\, e\,\mathrm{cm}$ ($10^{-3}, 10^{-1}$ and $10^{-3}\,\mu_N$) for charm, beauty and strange baryons, respectively. Here $\mu_N = e\hbar/2m_pc$ is the nuclear magneton, and m_p the proton mass. Sensitivities for the dedicated experiment scenario would improve by about one order of magnitude.

The experimental layout at LHCb consist of two crystal kickers for the deflection of $7\,\mathrm{TeV}$ protons from the beam halo, a fixed target installed in front of the LHCb detector and up- and down-bending crystals attached to the target. They deflect the signal particles inside the LHCb detector acceptance. Optimal bent crystal parameters are determined to be $7\,\mathrm{cm}$ ($5\,\mathrm{cm}$) length and $14\,\mathrm{mrad}$ ($15\,\mathrm{mrad}$) bending angle for Si (Ge), whereas for the dedicated experiment are found to be $12\,\mathrm{cm}$ ($7\,\mathrm{cm}$) and $7\,\mathrm{mrad}$ ($8\,\mathrm{mrad}$).

In this configuration, with a proton flux of $10^8\,p/\mathrm{s}$, the detector occupancy for fixed-target events is found to be well below than for pp collision events. We demonstrate the signal reconstruction efficiency does not depend on the incoming proton flux and it is feasible up to $10^9\,p/\mathrm{s}$.

The typical signature of signal events allows to isolate them from the background. They are characterized by particles with high momentum at a fixed direction, determined by the crystal bending angle. Moreover the optimal mass resolution of $\approx 20\,\mathrm{MeV}$ for Λ_c^+ at $1\,\mathrm{TeV}$ of energy helps to distinguish signal from backgrounds of particle decays with similar kinematics.

This proposal represents a unique program of measurements of EDM and MDM of charm, beauty and strange charged baryons at the LHC. The MDM measurements would provide important experimental anchor points for QCD calculations on the inner structure of baryons, while EDM measurements would extend the search for new physics at LHC improving the current indirect limits provided by the neutron EDM.

CHAPTER 13

Conclusions

In the **first part** of the thesis we present a search for CP and P violation using triple-product asymmetries in the $\Lambda_b^0 \to p\pi^-\pi^+\pi^-$ decay. Two different approaches have been followed to exploit the full potential of the data sample: a measurement integrated over phase space and measurements in bins of phase space. We perform a novel study of the dynamics of this decay developing an amplitude model and identifying the most important resonant contributions. Introducing CPV in the interference of N^{*+} resonances we are able to reproduce the pattern of the first hint of CPV observed at 3.3σ with Run 1 data. We identify the region where the $\Lambda_b^0 \to N^{*+}\pi^-$ contribution is dominant as the most promising to search for CPV and exclude the region $\Lambda_b^0 \to pa_1$ where no P-odd CPV is expected. We define a new binning scheme with respect to the previous analysis, based on the helicity angles, in order to improve the sensitivity to CPV and keep the binning scheme based on $|\Phi|$, *i.e.* the angle between the two decay planes defined by $p\pi^-_{slow}$ and $\pi^+\pi^-_{fast}$ tracks, where fast (slow) label indicates the most (less) energetic π^- in the Λ_b^0 frame. The region of the a_1 contribution is kept as a control check and doesn't show any significant deviation from the CP symmetry hypothesis. We measure a deviation from the CP conserving hypothesis with a statistical significance of 2.9σ in the N^{*+} resonances for the binning scheme based on $|\Phi|$. We found the first evidence of P violation in heavy b-baryon decays with a statistical significance of 5.5σ in bins of the phase space and 5.5σ integrated in phase space. The first hint of CPV, with a significance of 3.3σ, obtained with the analysis of Run 1 data is not still resolved. Additional data will be crucial to verify if this is a first hint of CPV in baryons or refuse it, if due to statistical fluctuation. Thanks to the increased signal yields, about a factor 4 with respect to Run 1, we reach a sensitivity at $\mathcal{O}(1\%)$ for the integrated measurement. The phenomenological amplitude model for the $\Lambda_b^0 \to p\pi^-\pi^+\pi^-$ decay that we have developed allowed to define a new binning scheme with potential improved sensitivity to P-odd CPV effects. We found clear structures due to the resonances in the phase space of the decay. This result suggest that a full amplitude analysis of this decay mode could unveil unexpected features and support searches for CPV in the resonant structure of the decay. The analysis is very promising for the LHCb Upgrade due to the low systematic uncertainties and the possibility of relying on a large control sample, *e.g.* the Cabibbo favoured $\Lambda_b^0 \to \Lambda_c^+(\to pK^-\pi^+)\pi^-$, for their estimate. LHCb experiment allows unprecedented measurements in the heavy baryon sector offering the possibility to search and eventually find CPV in this sector.

In the **second part** of the thesis a unique opportunity to measure the EDM and MDM of charm, beauty and strange charged baryons at LHC has been discussed. Electric and magnetic dipole moments of short-lived baryons are powerful probes for physics within and beyond the SM. However, EDM and MDM for charm and beauty baryons have not been accessible to date. The EDM is sensitive to flavour diagonal CPV contributions that are predicted to be minuscule in the SM. The idea is to use heavy baryons produced by the interaction of protons with a fixed target positioned in front of the LHCb detector and channeled in a bent crystal. The EDM and MDM are measured from the spin precession that is induced by the intense electric field between crystal atomic planes. We developed a detailed simulation and demonstrated the feasibility of this proposal solving the equation of motion of the spin precession, calculating the expected sensitivity, determining the optimal parameters of the crystal, the occupancies of the detector and verifying the ability of the LHCb detector to reconstruct the signal with a good resolution and isolate it from the dangerous backgrounds. Optimal bent crystal parameters are determined to be $7\,\mathrm{cm}$ ($5\,\mathrm{cm}$) length and $14\,\mathrm{mrad}$ ($15\,\mathrm{mrad}$) bending angle for Si (Ge). For proton flux of $\sim 10^8 p/\mathrm{s}$ the occupancy for these fixed-target events is 2-4 times lower than the expected occupancy from pp collision in the LHCb Upgrade allowing a good performance for the signal reconstruction that reaches $20\,\mathrm{MeV}/c^2$ of mass resolution for Λ_c^+ particles with $\mathcal{O}(\mathrm{TeV})$ energy. LHCb can reach a sensitivity of $\sim 10^{-17}\,e\,\mathrm{cm}$ on charm EDM, better than the indirect constraint from the neutron EDM and useful to discriminate between new physics models. The sensitivity on the MDM will be at the level of $\sim 10^{-2}\mu_N$, where μ_N is the nuclear magneton, and would provide important experimental anchor points for QCD calculations. Those searches will extend the new physics discovery potential of the LHC.

Appendices

APPENDIX A

Part I

A.1 Kinematic distributions comparison of $\Lambda_b^0 \to \Lambda_c^+(\to pK^-\pi^+)\pi^-$ control sample and $\Lambda_b^0 \to p\pi^-\pi^+\pi^-$ data

In Figures A.1-A.2-A.3A.4 we compare the kinematic distributions of protons and pions between $\Lambda_b^0 \to p\pi^-\pi^+\pi^-$ and $\Lambda_b^0 \to \Lambda_c^+(\to pK^-\pi^+)\pi^-$ samples integrated in phase space and in bins of Φ (scheme A defined in Section 5.2), where the angle Φ is defined in Equation (5.15). The $\Lambda_b^0 \to p\pi^-\pi^+\pi^-$ data distributions are background subtracted with the *sPlot* technique where the model fitted to data to calculate the *sWeights* is described in Chapter 4. The $\Lambda_b^0 \to \Lambda_c^+(\to pK^-\pi^+)\pi^-$ control sample distributions are obtained selecting the Λ_b^0 reconstructed invariant mass to be within $\pm 2\sigma$ (σ is the resolution obtained from the fit to data in Table 4.4) where the background contribution is negligible.

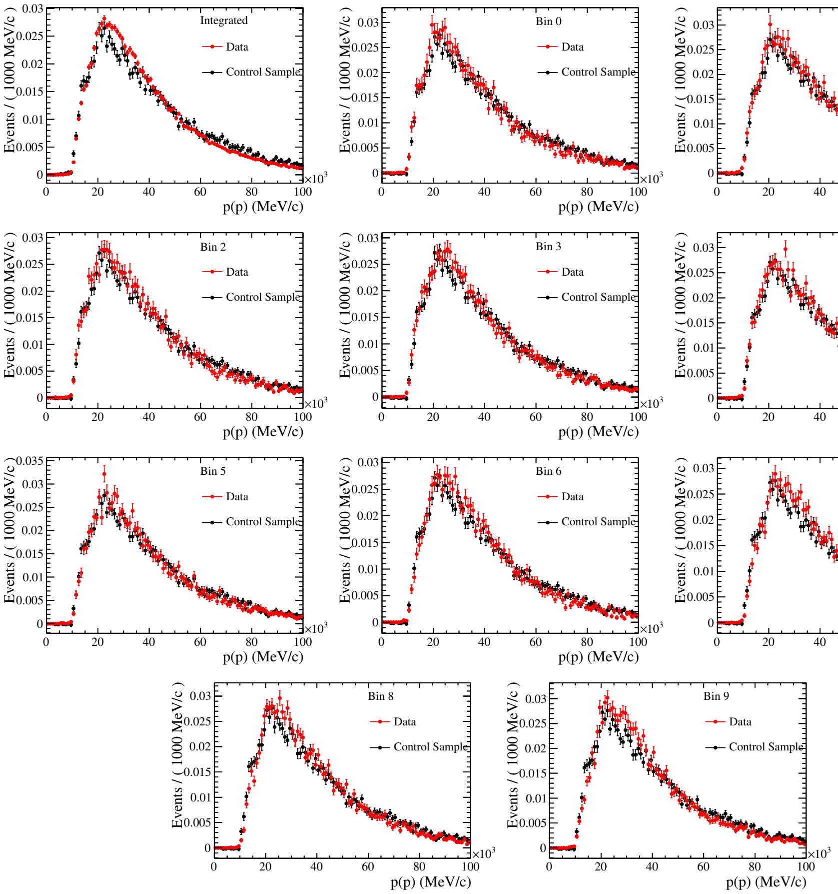

Figure A.1: Proton momentum distributions of $\Lambda_b^0 \to \Lambda_c^+(\to pK^-\pi^+)\pi^-$ control sample and $\Lambda_b^0 \to p\pi^-\pi^+\pi^-$ data integrated in phase space and in bins of Φ.

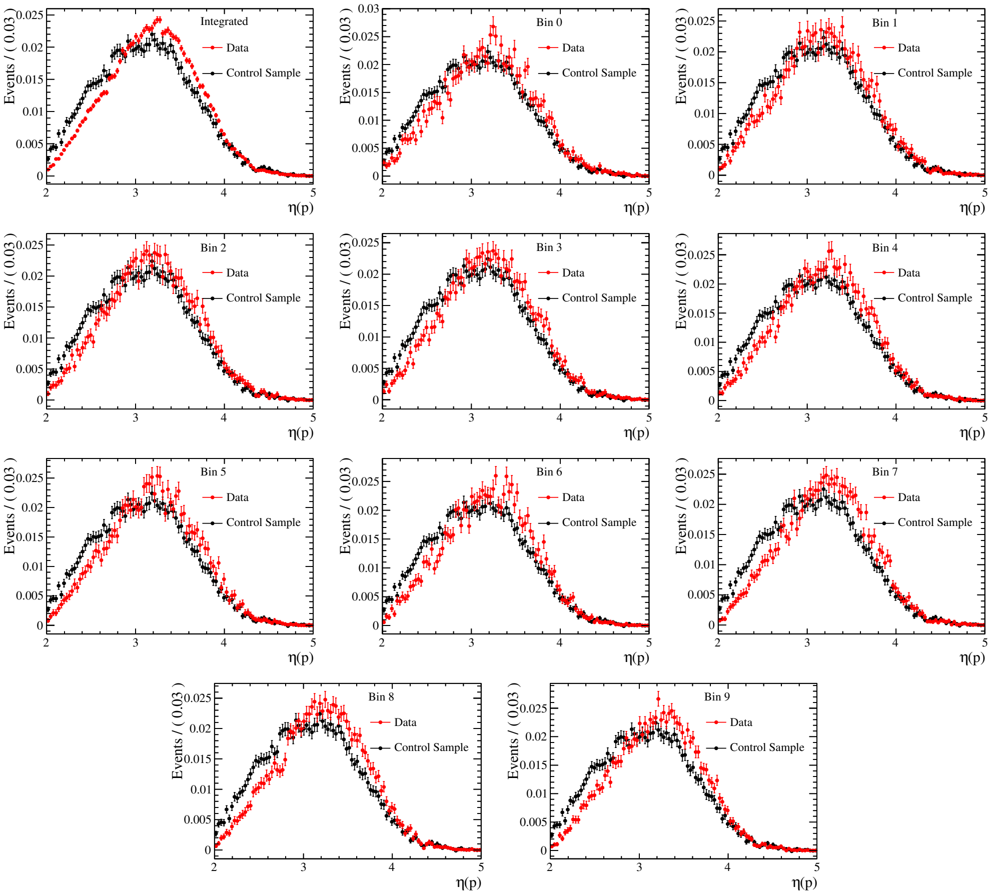

Figure A.2: Proton pseudorapidity distributions of $\Lambda_b^0 \to \Lambda_c^+(\to pK^-\pi^+)\pi^-$ control sample and $\Lambda_b^0 \to p\pi^-\pi^+\pi^-$ data integrated in phase space and in bins of Φ.

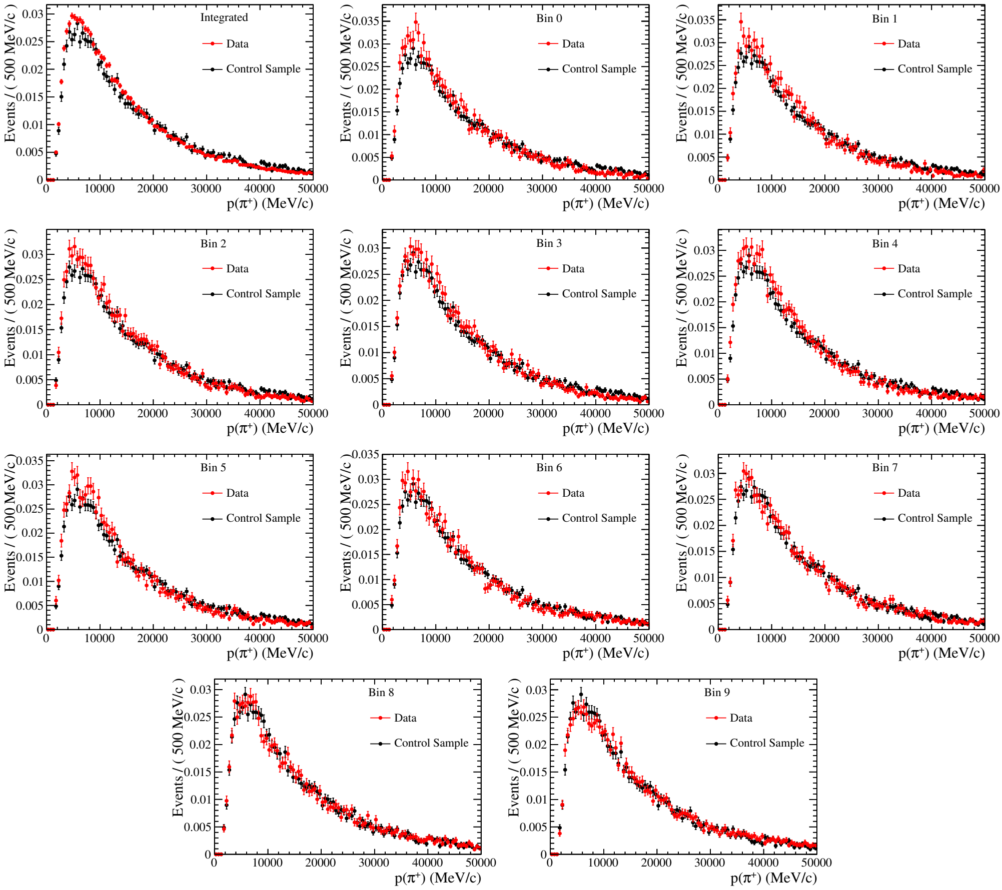

Figure A.3: Pion momentum distributions of $\Lambda_b^0 \to \Lambda_c^+(\to pK^-\pi^+)\pi^-$ control sample and $\Lambda_b^0 \to p\pi^-\pi^+\pi^-$ data integrated in phase space and in bins of Φ.

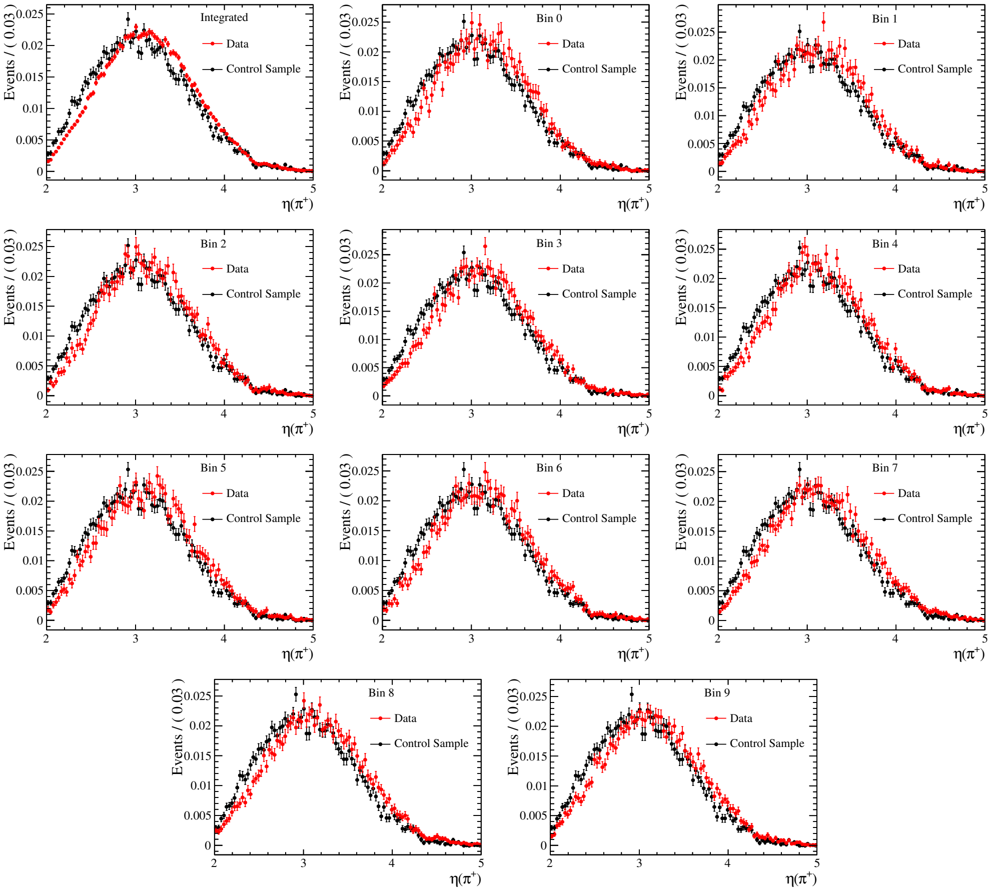

Figure A.4: Pion pseudorapidity distributions of $\Lambda_b^0 \to \Lambda_c^+(\to pK^-\pi^+)\pi^-$ control sample and $\Lambda_b^0 \to p\pi^-\pi^+\pi^-$ data integrated in phase space and in bins of Φ.

A.2 Kinematic distributions of $\Lambda_b^0 \to \Lambda_c^+(\to pK^-\pi^+)\pi^-$ control sample

In Figure A.5 we show the momentum and pseudorapidity distributions of protons and pions in $\Lambda_b^0 \to \Lambda_c^+(\to pK^-\pi^+)\pi^-$ control sample for different PID cuts defined in Table 7.5.

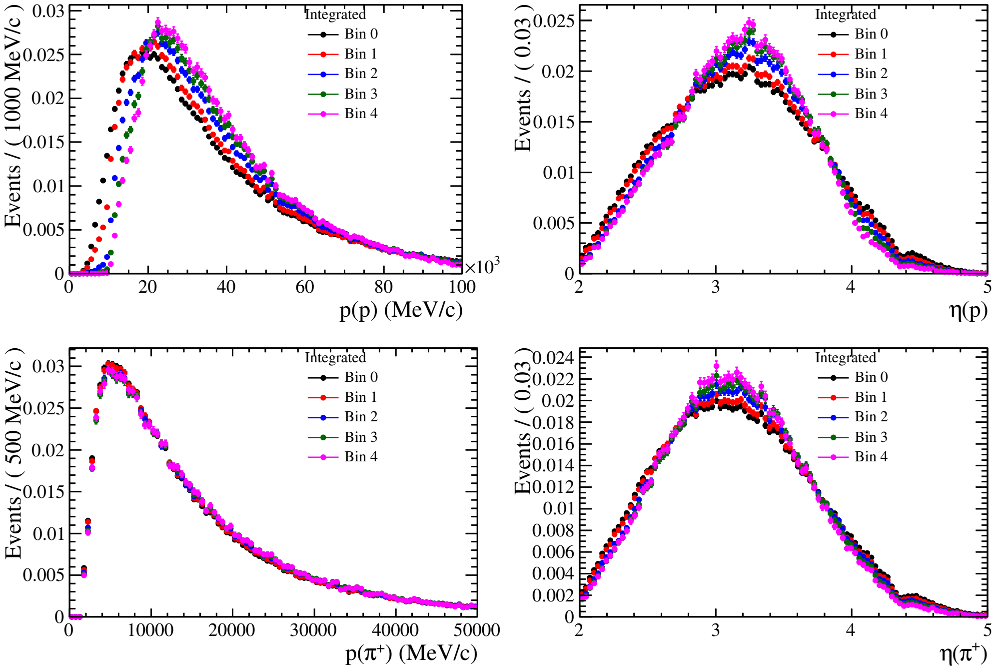

Figure A.5: Kinematic distributions for protons and pions in $\Lambda_b^0 \to \Lambda_c^+(\to pK^-\pi^+)\pi^-$ control sample for different PID cut.

A.3 Amplitude model description

Here we give some further information on how the amplitude model is developed. We use the helicity formalism described in Section 5.1.1.

All the resonances are parametrized with relativistic Breit-Wigner line shapes of the form

$$f_{BW}(M^2) = \frac{F_{\Lambda_b^0}(M, L_{\Lambda_b^0})}{m_r^2 - M^2 - m_r\Gamma(M)} \tag{A.1}$$

with the mass-dependent width $\Gamma(M, L_r)$ given by

$$\Gamma(M) = \Gamma_0 \left(\frac{p(M)}{p_0}\right)^{2L_r+1} \frac{m_r}{M} F_r^2(M, L_r), \tag{A.2}$$

and the Blatt-Weisskopf form factors for the resonance $F_r(M, L_r)$ and Λ_b^0 $F_{\Lambda_b^0}(M, L_{\Lambda_b^0})$. The form factors F_r and $F_{\Lambda_b^0}$ are parametrised as

$$F_{r,\Lambda_b^0}(M, L) = \begin{cases} 1 & L = 0 \\ \sqrt{\frac{1+z^2(M)}{1+Z_0^2}} & L = 1 \\ \sqrt{\frac{9+3z^2(M)+z^4(M)}{9+3z_0^2+z_0^4}} & L = 2 \\ \sqrt{\frac{225+45z^2(M)+6z^4(M)+z^6(M)}{225+45z_0^2+6z_0^4+z_0^6}} & L = 3 \end{cases} \tag{A.3}$$

where $z(M) = p(M)d$, $z_0 = p_0 d$, d is the radial parameter ($5.0\mathrm{GeV}^{-1}$ for Λ_b^0 and $1.5\mathrm{GeV}^{-1}$ for resonances), $p(M)$ is the momentum of two-body decay with the resonance mass equal to M, and p_0 is the momentum for resonance mass equal to its nominal mass. Mass-dependent width and form factors depend on the angular momentum of the two-body decay. For the weak decay of Λ_b^0 we take the minimum possible angular momentum equal to $L_{\Lambda_b^0} = J - 1/2$ (where J is the spin of the resonance), while for the strong decay of the intermediate resonance, the angular momentum L_r is uniquely identified by the parity of the resonance, $P = (-1)^{L_r+1}$, and conservation of angular momentum $L_r = J \pm 1/2$. We know that some of resonances, especially a_1, have different shape than the Breit-Wigner, however this model is not used to fit the data but just to give some hint what are the main resonant contributions.

The values for the helicity amplitudes $\mathcal{H}^{A\to BC}_{\lambda_B,\lambda_C}$ in Equation (5.4) are listed in Tables A.1 and A.2.

Table A.1: Values for helicity amplitudes for the different contributions to the model. Not all the amplitudes are listed for strong decays: we use the parity conservation to derive them with Equation (5.5).

Decay	Values		
	$\mathcal{H}_{1/2,0}$	$\mathcal{H}_{-1/2,0}$	
$\mathit{\Lambda}_b^0 \to N^{*+}(1520)\pi^-$	$0.2 + 0.2i$	$0.2 + 0.2i$	
$\mathit{\Lambda}_b^0 \to N^{*+}(1535)\pi^-$	$0.2 + 0.2i$	$0.2 + 0.2i$	
$\mathit{\Lambda}_b^0 \to N^{*+}(1650)\pi^-$	$0.2 + 0.2i$	$0.2 + 0.2i$	
$\mathit{\Lambda}_b^0 \to N^{*+}(1675)\pi^-$	$0.2 + 0.2i$	$0.2 + 0.2i$	
$\mathit{\Lambda}_b^0 \to N^{*+}(1680)\pi^-$	$0.1 + 0.1i$	$0.1 + 0.1i$	
$\mathit{\Lambda}_b^0 \to N^{*+}(1700)\pi^-$	$0.1 + 0.1i$	$0.1 + 0.1i$	
$\mathit{\Lambda}_b^0 \to N^{*+}(1710)\pi^-$	$0.15 + 0.15i$	$0.15 + 0.15i$	
$\mathit{\Lambda}_b^0 \to N^{*+}(1720)\pi^-$	$0.15 + 0.15i$	$0.15 + 0.15i$	
$\mathit{\Lambda}_b^0 \to N^{*+}(1875)\pi^-$	$0.2 + 0.2i$	$0.2 + 0.2i$	
$\mathit{\Lambda}_b^0 \to N^{*+}(1900)\pi^-$	$0.2 + 0.2i$	$0.2 + 0.2i$	
$\mathit{\Lambda}_b^0 \to N^{*+}(2190)\pi^-$	$0.9 + 0.9i$	$0.9 + 0.9i$	
	$\mathcal{H}_{1/2,0}$	$\mathcal{H}_{3/2,0}$	
$N^{*+}(1520) \to \Delta^{++}\pi^-$	$1 + i$	$1 + i$	
$N^{*+}(1535) \to \Delta^{++}\pi^-$	$0.47 + 0.47i$	/	
$N^{*+}(1650) \to \Delta^{++}\pi^-$	$0.8 + 0.8i$	/	
$N^{*+}(1675) \to \Delta^{++}\pi^-$	$0.8 + 0.8i$	$0.8 + 0.8i$	
$N^{*+}(1680) \to \Delta^{++}\pi^-$	$0.8 + 0.8i$	$0.8 + 0.8i$	
$N^{*+}(1700) \to \Delta^{++}\pi^-$	$1.3 + 1.3i$	$1.3 + 1.3i$	
$N^{*+}(1710) \to \Delta^{++}\pi^-$	$1 + i$	/	
$N^{*+}(1720) \to \Delta^{++}\pi^-$	$1.3 + 1.3i$	$1.3 + 1.3i$	
$N^{*+}(1875) \to \Delta^{++}\pi^-$	$0.8 + 0.8i$	$0.8 + 0.8i$	
$N^{*+}(1900) \to \Delta^{++}\pi^-$	$1.05 + 1.05i$	$1.05 + 1.05i$	
$N^{*+}(2190) \to \Delta^{++}\pi^-$	$1 + i$	$1 + 1i$	
	$\mathcal{H}_{1/2,0}$		
$\Delta^{++} \to p\pi^+$	$1 + i$		
	$\mathcal{H}_{1/2,1}$	$\mathcal{H}_{1/2,0}$	$\mathcal{H}_{1/2,-1}$
$N^{*+}(1720) \to p\rho$	1.3	1.3	1.3
$N^{*+}(1875) \to p\rho$	$0.8 + 0.8i$	$0.8 + 0.8i$	$0.8 + 0.8i$
$N^{*+}(1900) \to p\rho$	$0.2 + 0.2i$	$0.2 + 0.2i$	$0.2 + 0.2i$
	$\mathcal{H}_{1/2,0}$		
$N^{*+}(1535) \to p\sigma$	$0.375 + 0.375i$		
$N^{*+}(1650) \to p\sigma$	$0.375 + 0.375i$		
$N^{*+}(1675) \to p\sigma$	$0.3 + 0.3i$		
$N^{*+}(1680) \to p\sigma$	$0.75 + 0.75i$		
$N^{*+}(1700) \to p\sigma$	$0.08 + 0.08i$		
$N^{*+}(1875) \to p\sigma$	$0.6 + 0.6i$		
$N^{*+}(1900) \to p\sigma$	$0.075 + 0.075i$		

Table A.2: Values for helicity amplitudes for the different contributions to the model. Not all the amplitudes are listed for strong decays: we use the parity conservation to derive them with Equation (5.5).

Decay	Values			
	$\mathcal{H}_{0,0}$			
$\rho \to \pi^+\pi^-$	$1+i$			
$\sigma \to \pi^+\pi^-$	$1+i$			
	$\mathcal{H}_{1/2,0}$	$\mathcal{H}_{3/2,0}$		
$N^{*+}(1700) \to N^{*0}(1520)\pi^+$	$4+4i$	$4+4i$		
$N^{*+}(1900) \to N^{*0}(1700)\pi^+$	$3+3i$			
	$\mathcal{H}_{1/2,0}$			
$N^{*0}(1520) \to p\pi^-$	$1+i$			
$N^{*0}(1700) \to p\pi^-$	$1+i$			
	$\mathcal{H}_{1/2,1}$	$\mathcal{H}_{1/2,0}$	$\mathcal{H}_{-1/2,0}$	$\mathcal{H}_{-1/2,-1}$
$\Lambda_b^0 \to p a_1^-$	$0.18+0.18i$	$0.18+0.18i$	$0.18+0.18i$	$0.18+0.18i$
	$\mathcal{H}_{1,0}$	$\mathcal{H}_{0,0}$		
$a_1^- \to \rho\pi^-$	$0.8+0.8i$	$0.8+0.8i$		

A.4 Fit Model validation in each bin

We validate the fit model in each bin of the phase space generating pseudo experiments and fitting them with the same model. The pull distribution of the asymmetries are shown in Figures A.6-A.7, A.8-A.9, A.10-A.11, A.12-A.13-A.14 and A.15-A.16-A.17 for binning scheme A, A_1, A_2, B_1 and B_2 respectively. No sign of bias is observed, while the uncertainty is correctly estimated from fit.

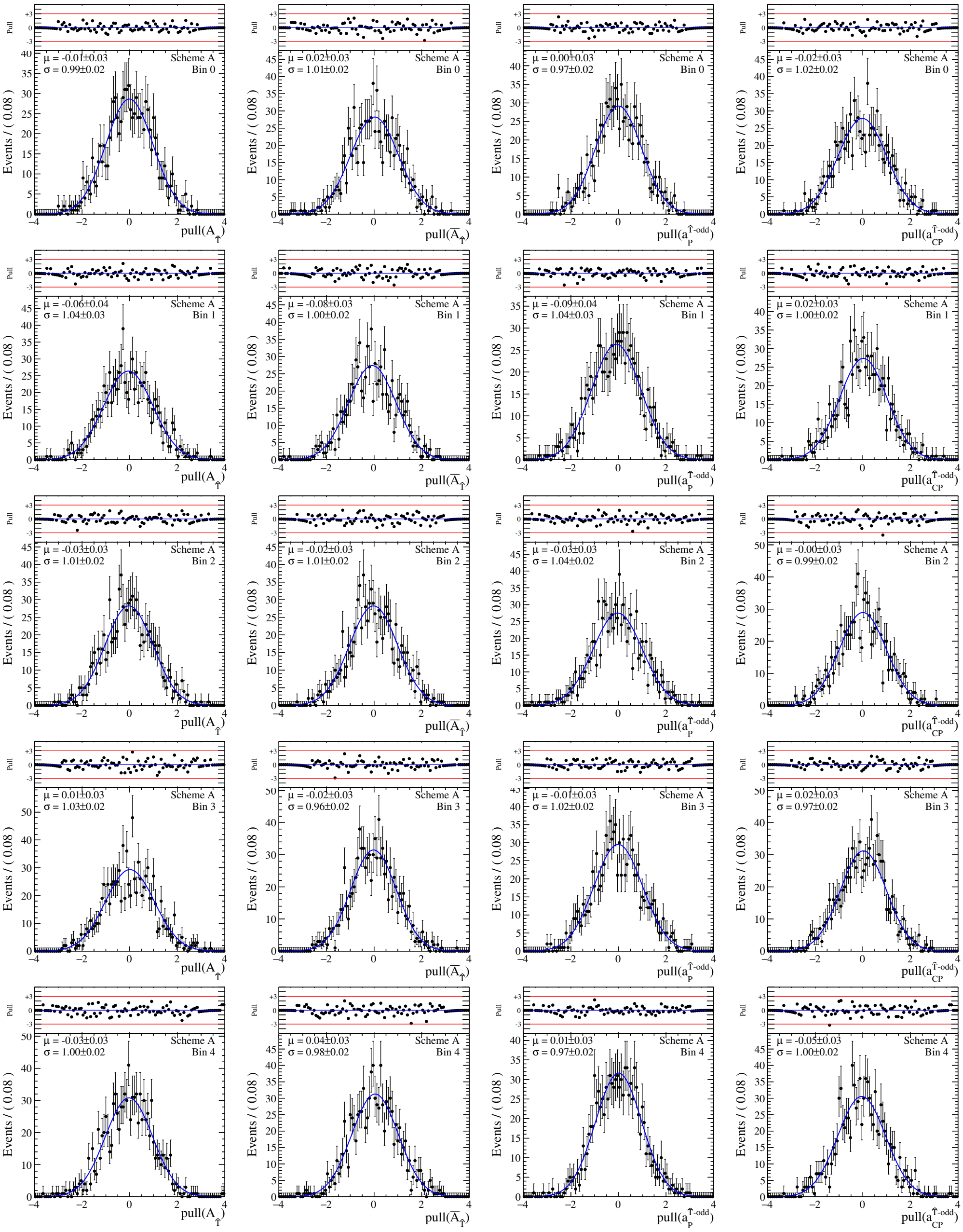

Figure A.6: Pull distributions for asymmetries in A binning scheme for bins from 0 to 4.

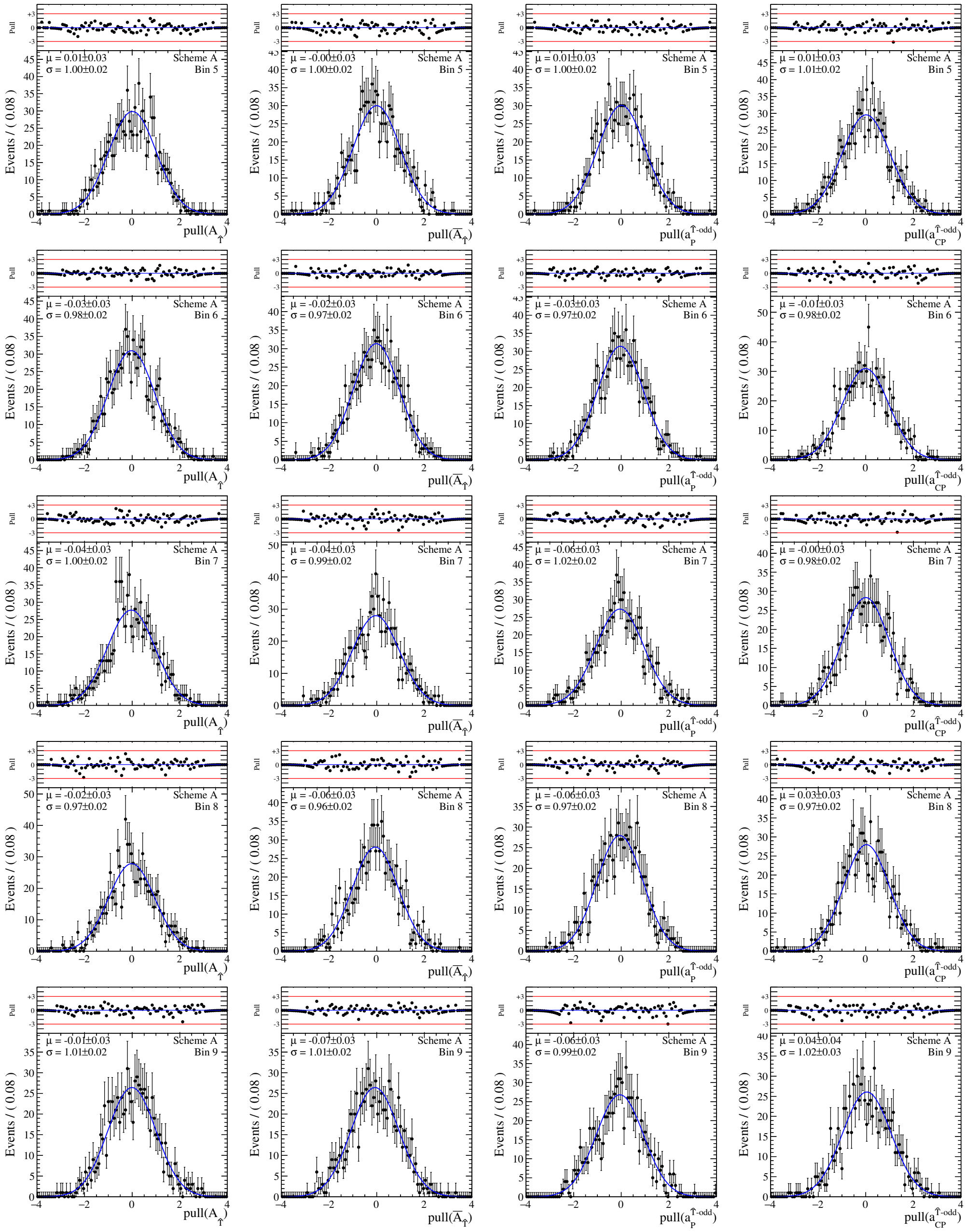

Figure A.7: Pull distributions for asymmetries in A binning scheme for bins from 5 to 9.

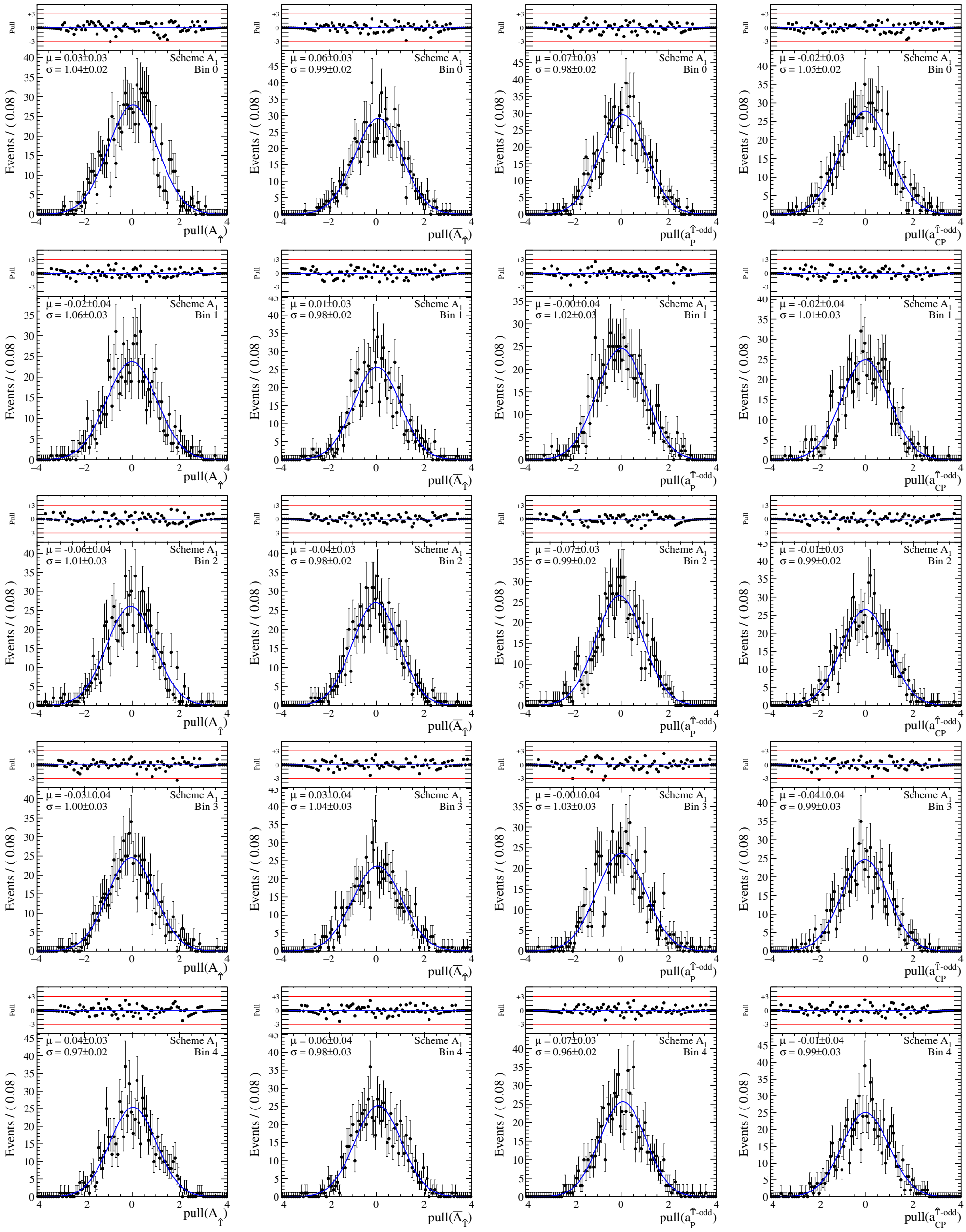

Figure A.8: Pull distributions for asymmetries in A_1 binning scheme for bins from 0 to 4.

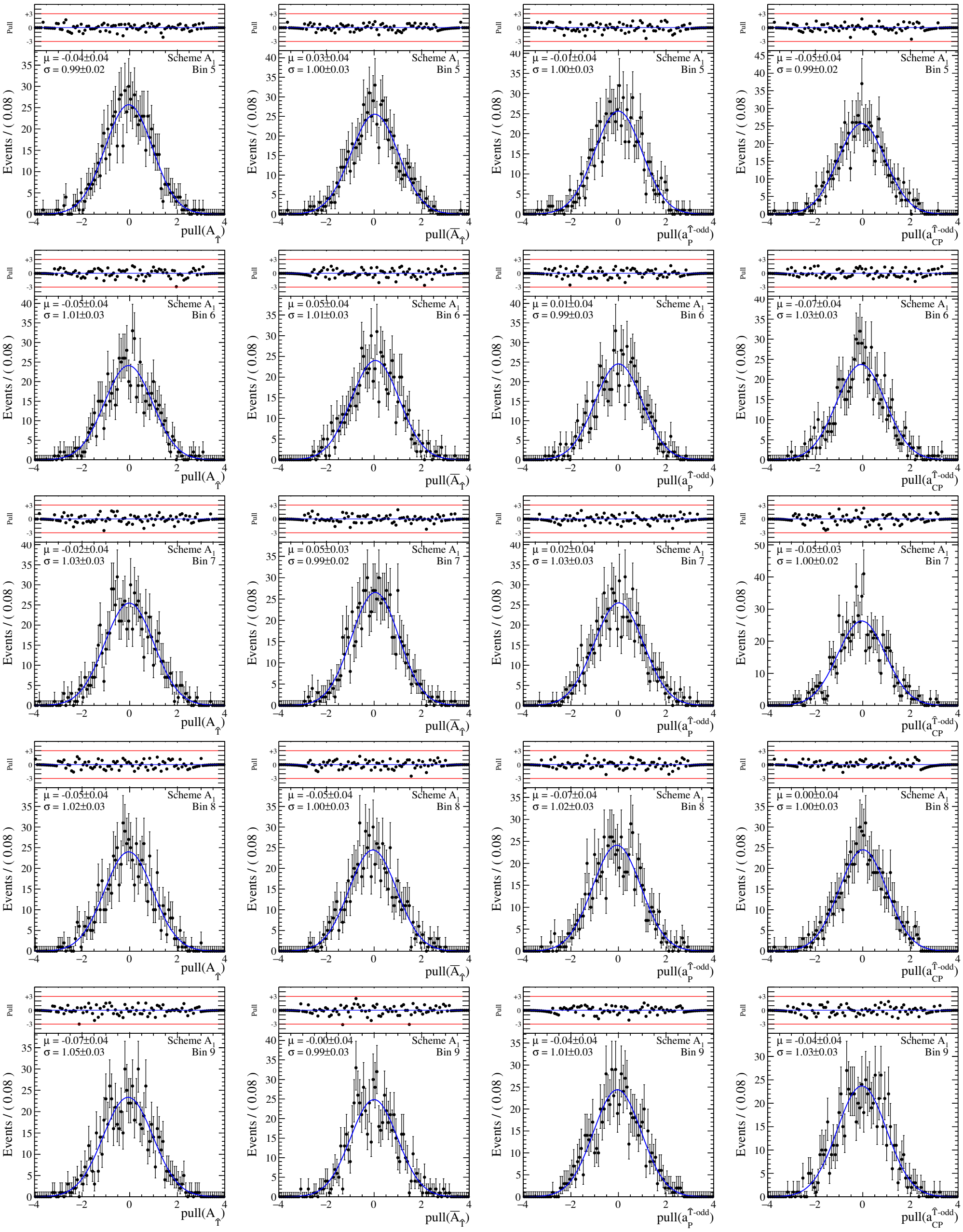

Figure A.9: Pull distributions for asymmetries in A_1 binning scheme for bins from 5 to 9.

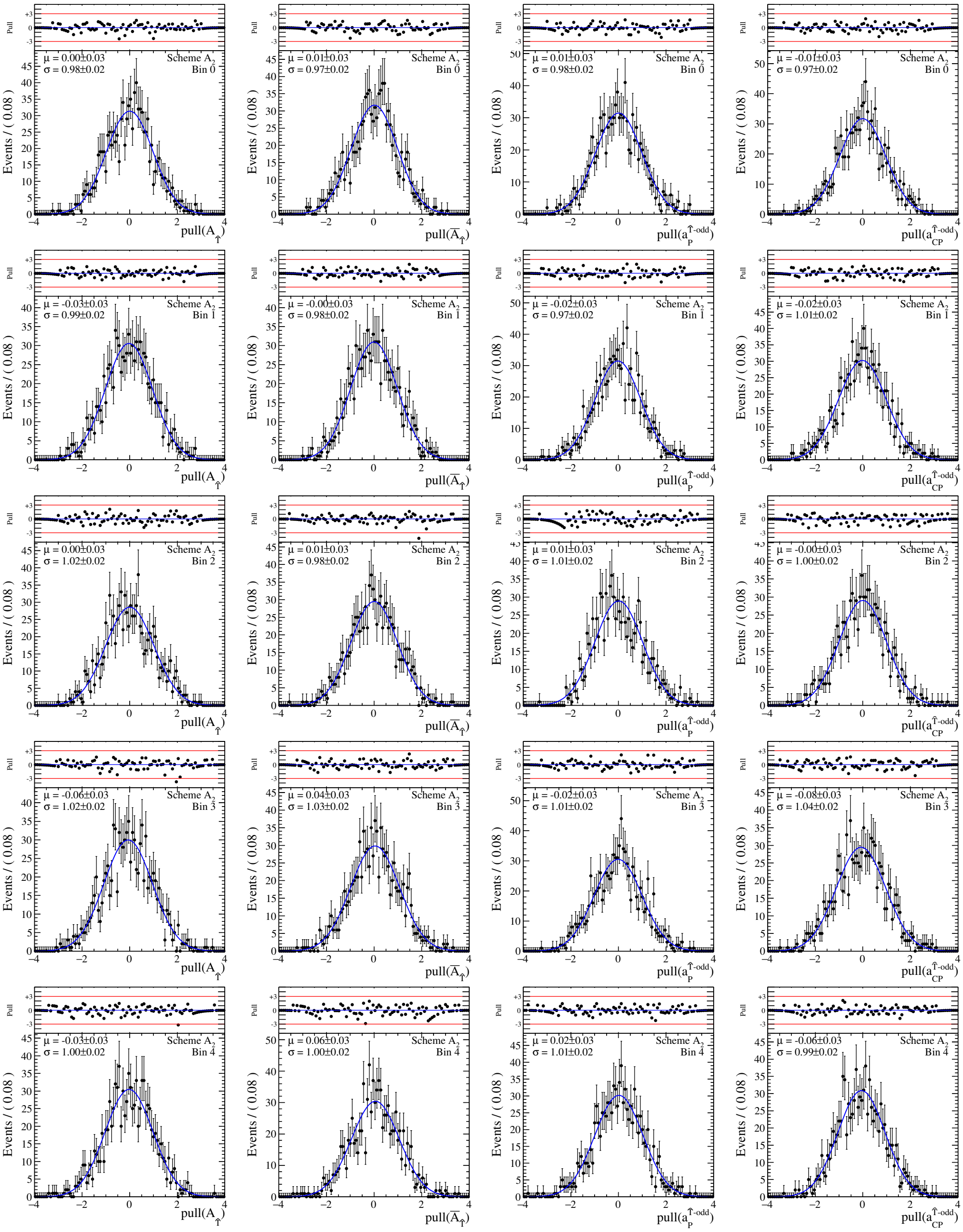

Figure A.10: Pull distributions for asymmetries in A_2 binning scheme for bins from 0 to 4.

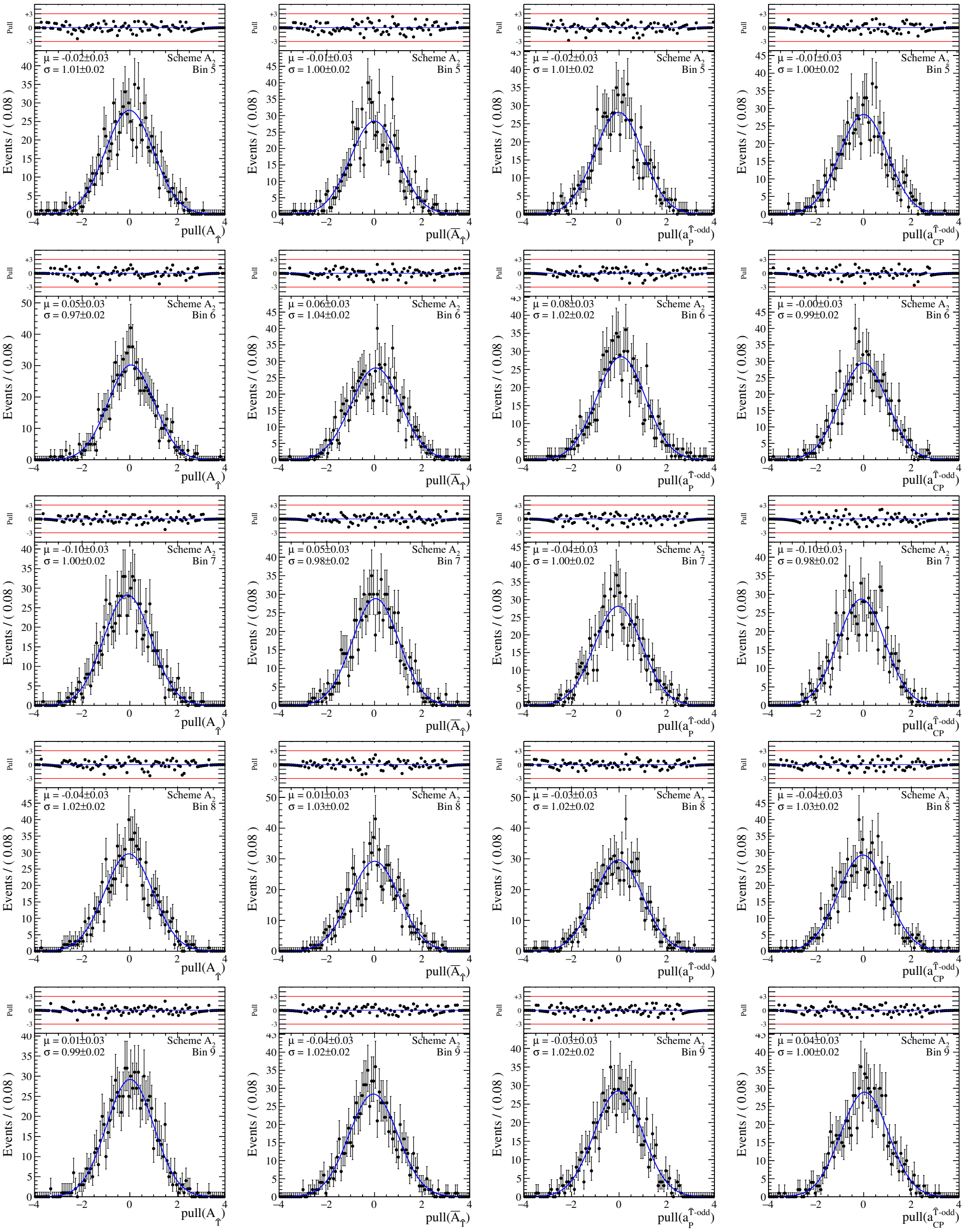

Figure A.11: Pull distributions for asymmetries in A_2 binning scheme for bins from 5 to 9.

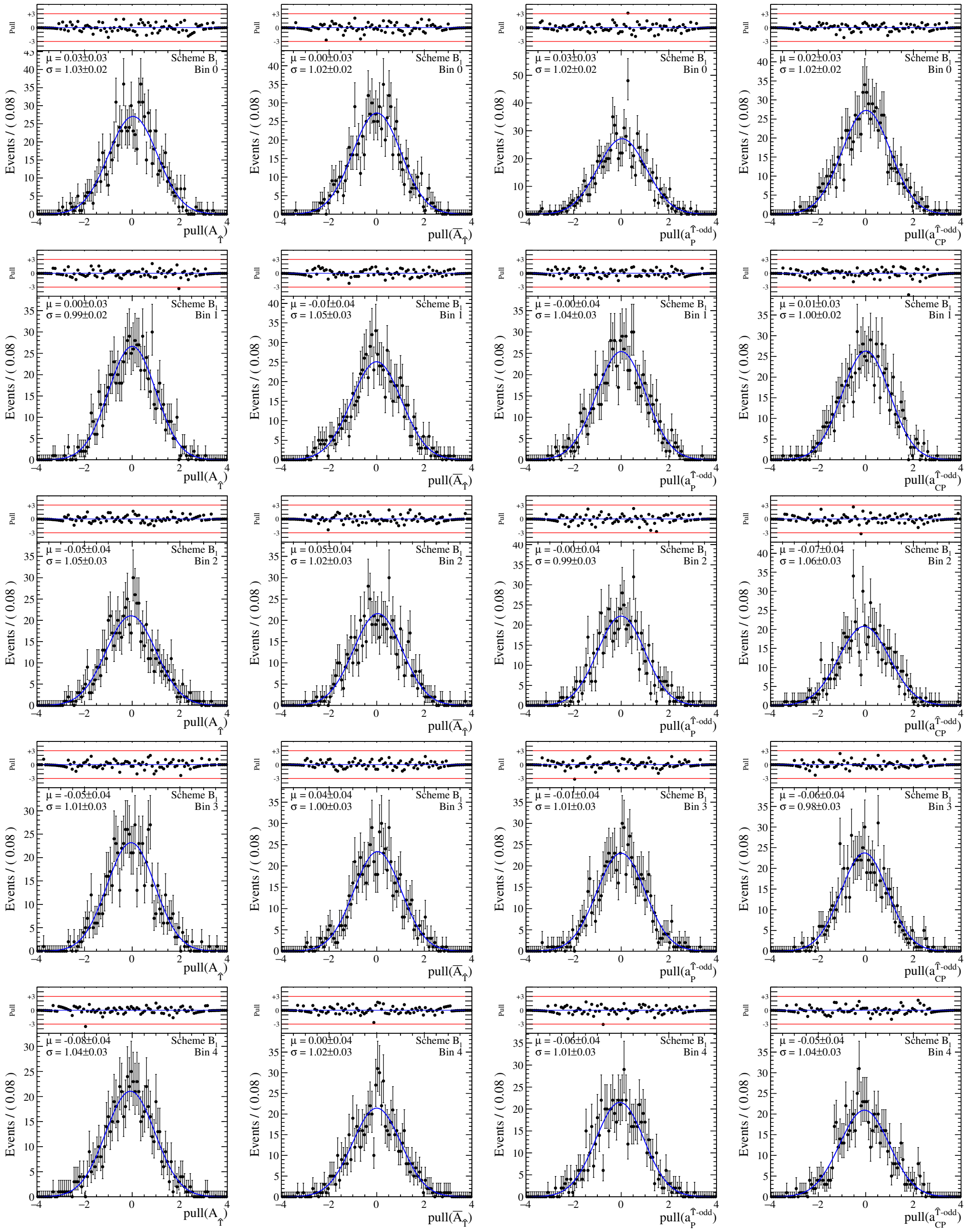

Figure A.12: Pull distributions for asymmetries in B_1 binning scheme for bins from 0 to 4.

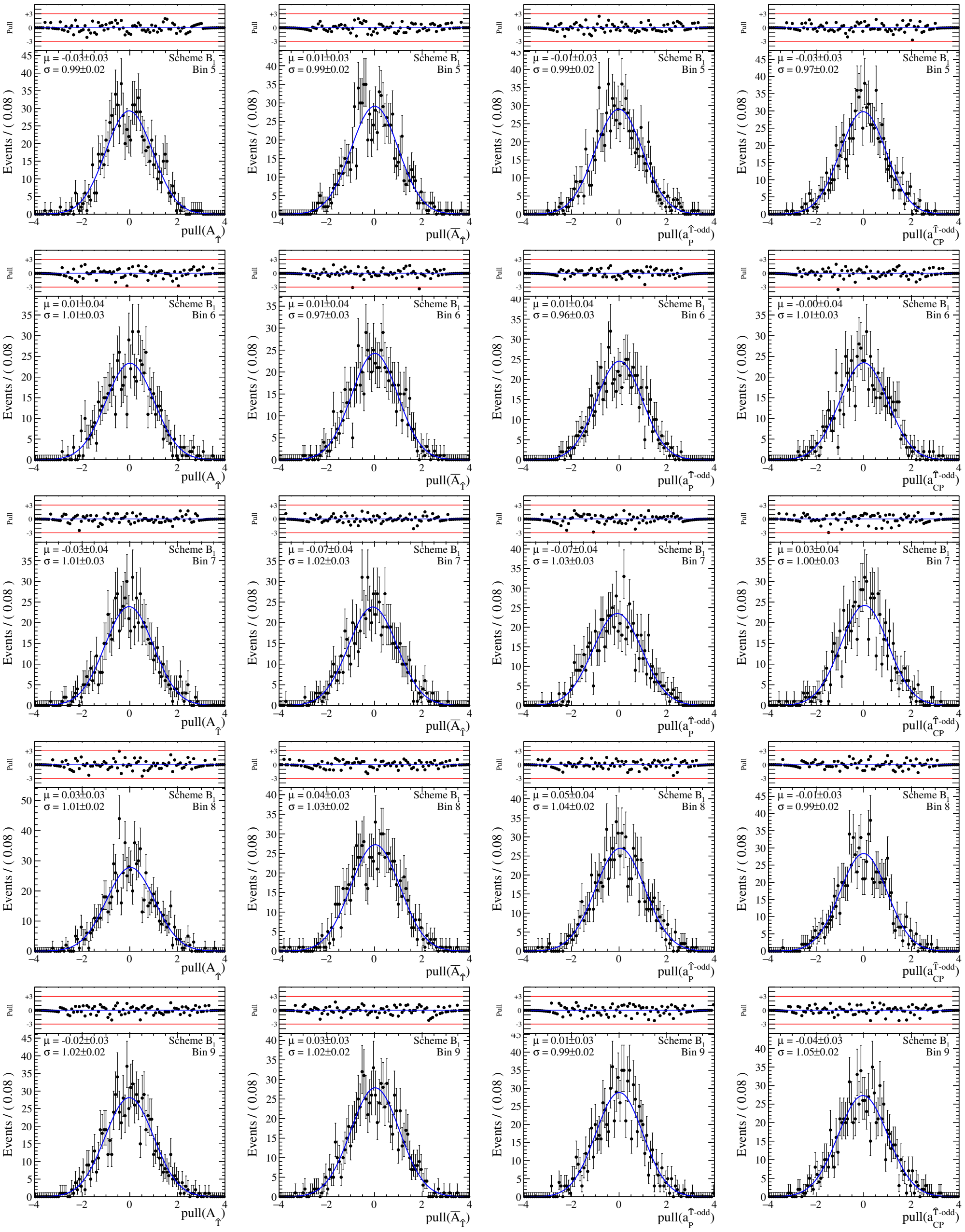

Figure A.13: Pull distributions for asymmetries in B_1 binning scheme for bins from 5 to 9.

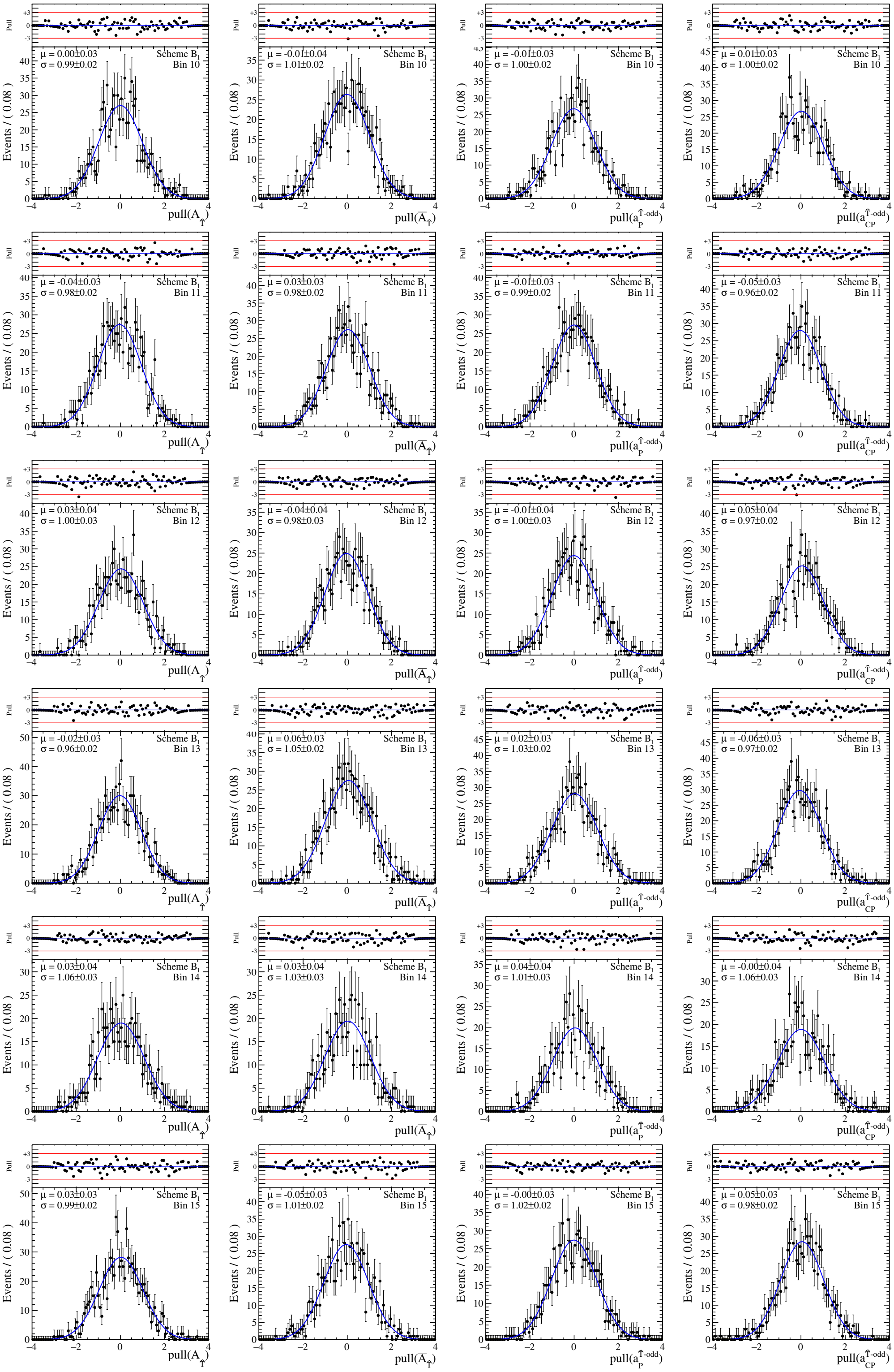

Figure A.14: Pull distributions for asymmetries in B_1 binning scheme for bins from 10 to 15.

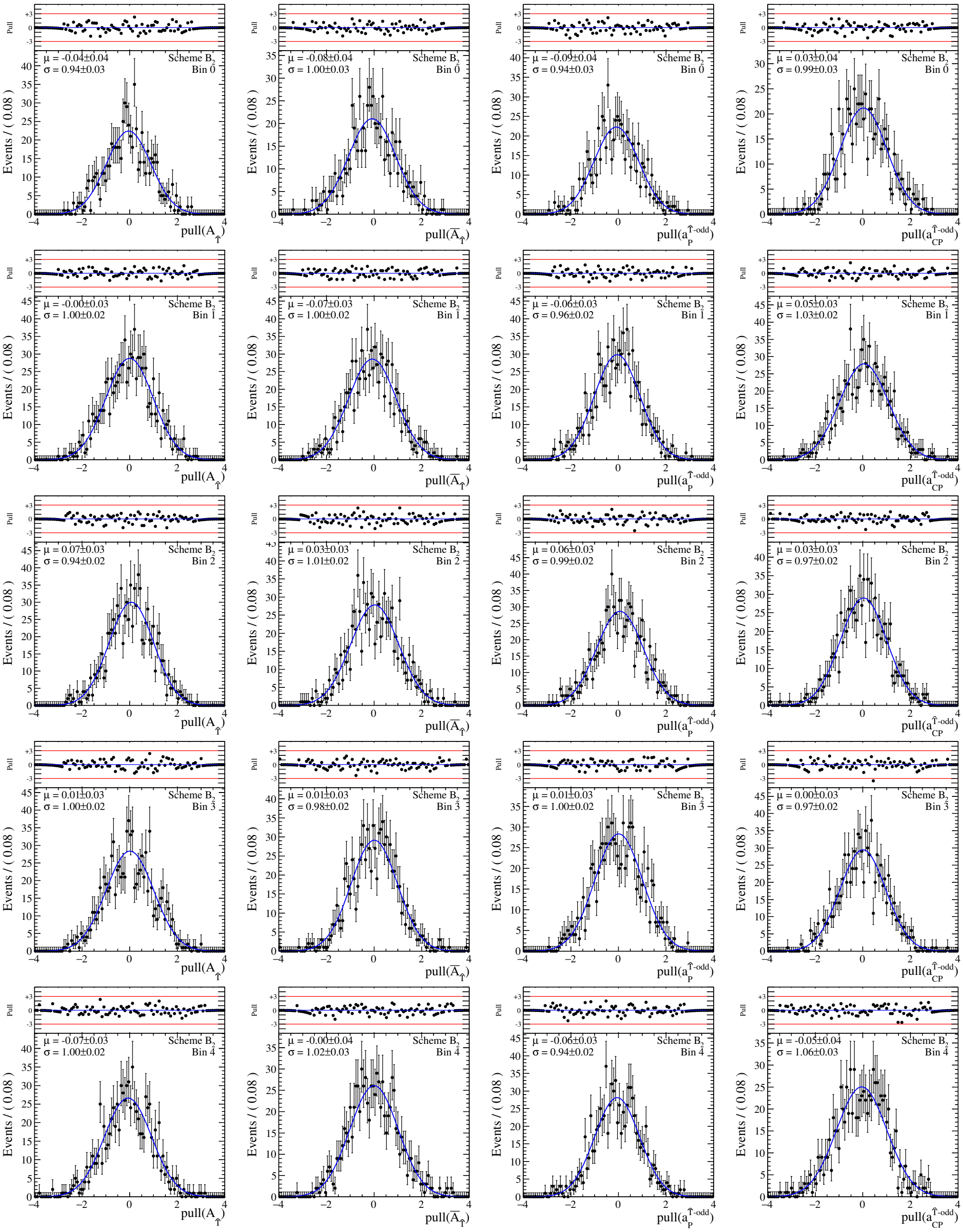

Figure A.15: Pull distributions for asymmetries in B_2 binning scheme for bins from 0 to 4.

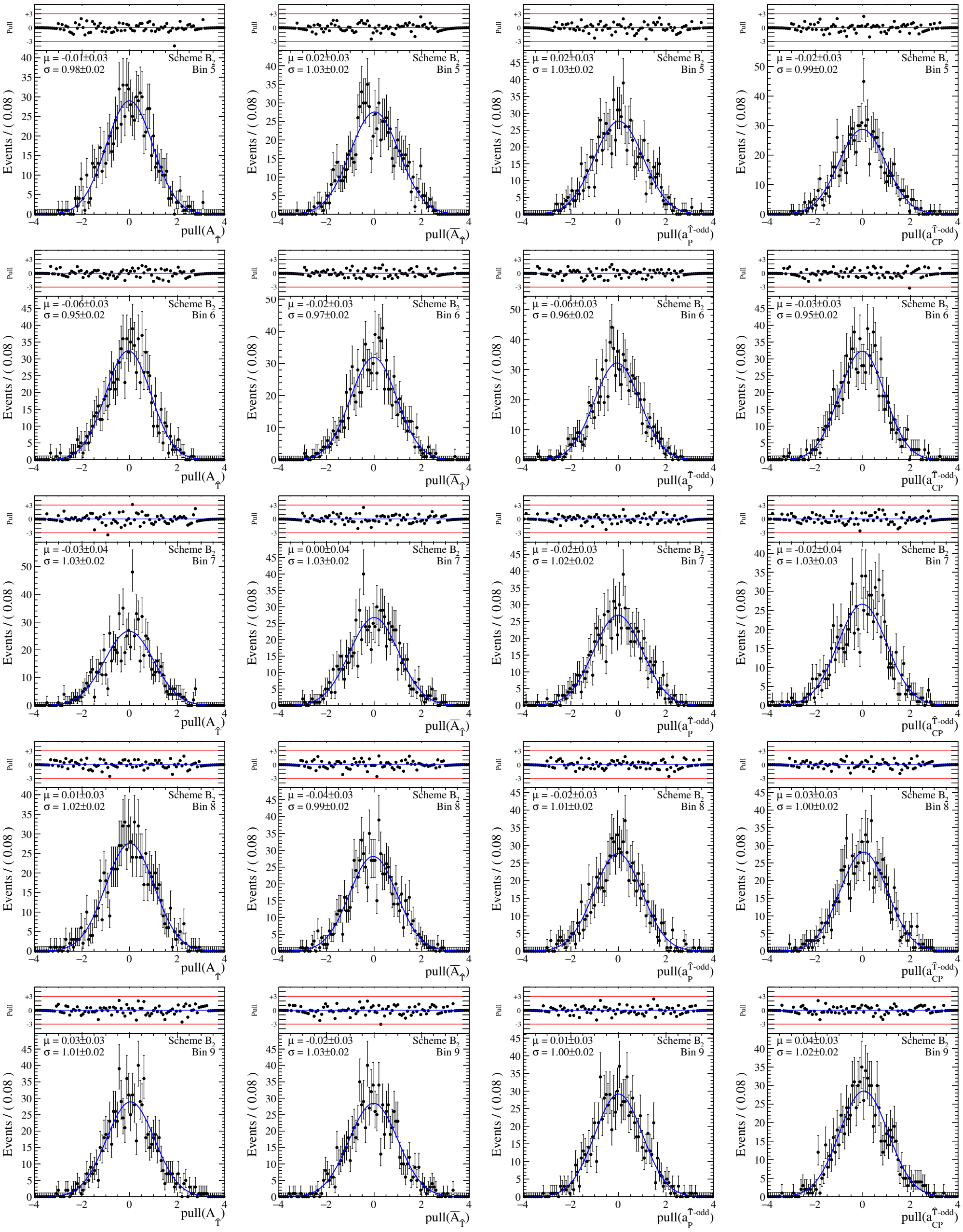

Figure A.16: Pull distributions for asymmetries in B_2 binning scheme for bins from 5 to 9.

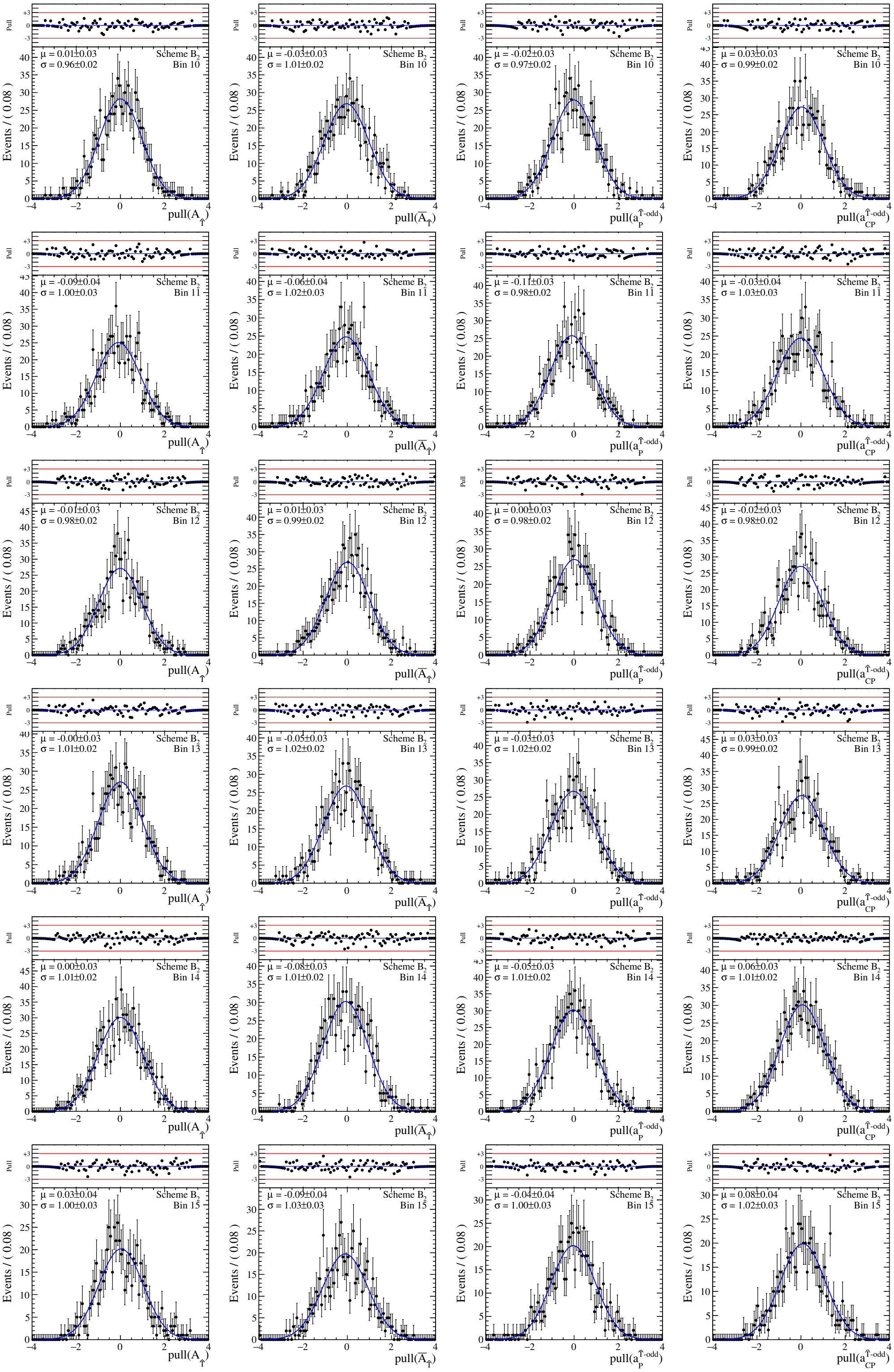

Figure A.17: Pull distributions for asymmetries in B_2 binning scheme for bins from 10 to 15.

APPENDIX B

Part II

B.1 Discrete ambiguities

From Equations (9.1) and (9.2) we observe that, if all the three components of the final polarization vector are measured, the g and d factors can be extracted simultaneously with the initial polarization s_0, up to discrete ambiguities. If $\{s_0,\ g',\ d\}$ is a solution, where $g' = (g-2)/2$ is the anomalous magnetic moment, then

$$\left\{-s_0,\ g' \pm \frac{n\pi}{\gamma\theta_C},\ d\left(1 \pm \frac{n\pi}{\gamma\theta_C}\frac{1}{g'}\frac{\cos\Phi - 1}{\cos\Phi + 1}\right)\right\},$$

$$\left\{s_0,\ g' \pm \frac{m\pi}{\gamma\theta_C},\ d\left(1 \pm \frac{m\pi}{\gamma\theta_C}\frac{1}{g'}\right)\right\}, \tag{B.1}$$

are also solutions, with n (m) an odd (even) integer. Performing a simultaneous fit to the angular distributions in bins of γ will resolve the ambiguity.

B.2 Spin time evolution for positively charged baryons

The time evolution of the spin-polarization vector for a particle with charge q in an electromagnetic field, as a function of the proper time τ, is given by the Thomas-Bargmann-Michel-Telegdi (T-BMT) equation [203, 204, 205],

$$\frac{da^\mu}{d\tau} = \frac{g\mu_B}{\hbar}\left[F^{\mu\nu}a_\nu + \left(a_\alpha F^{\alpha\beta}u_\beta\right)\frac{u^\mu}{c^2}\right] - \left(a_\alpha\dot{u}^\alpha\right)\frac{u^\mu}{c^2} - \frac{d\mu_B}{\hbar}\left[F^{*\mu\nu}a_\nu + \left(a_\alpha F^{*\alpha\beta}u_\beta\right)\frac{u^\mu}{c^2}\right], \tag{B.2}$$

where $F^{\mu\nu}$ is the electromagnetic tensor, $a^\mu = (a^0, \mathbf{a})$ is the spin 4-pseudovector, and $p^\mu = mu^\mu = (E/c, \mathbf{p})$ is the momentum 4-vector. For homogeneous fields, the velocity derivative is given by the Lorentz force,

$$\dot{u}^\mu \equiv \frac{du^\mu}{d\tau} = \frac{q}{mc}F^{\mu\nu}u_\nu. \tag{B.3}$$

In the rest frame of the particle, $a^\mu = (0, \mathbf{s})$, $p^\mu = (mc, \mathbf{0})$, where $\mathbf{s}$ is the non-relativistic spin-polarization vector. Therefore, in any frame $a^\mu p_\mu = 0$ and $a_\mu a^\mu = -\mathbf{s}^2$.

In a frame comoving with respect to the particle rest frame where the particle has velocity $\boldsymbol{\beta} = \mathbf{p}/m\gamma$, *e.g.* the laboratory frame, a^μ is given by [206, 207]

$$\mathbf{a} = \mathbf{s} + \frac{\gamma^2}{\gamma+1}(\boldsymbol{\beta}\cdot\mathbf{s})\boldsymbol{\beta}\ ,\ \ a^0 = \boldsymbol{\beta}\cdot\mathbf{a} = \gamma(\boldsymbol{\beta}\cdot\mathbf{s}), \tag{B.4}$$

where the components of the momentum 4-vector are $p^0 = \gamma mc^2$ and $\mathbf{p} = \gamma m\boldsymbol{\beta}c$. Substituting in the covariant Equation (B.2), the spin precession equation is [206, 207, 208, 209],

$$\frac{d\mathbf{s}}{dt} = \mathbf{s} \times \boldsymbol{\Omega} \ , \quad \boldsymbol{\Omega} = \boldsymbol{\Omega}_{\mathrm{MDM}} + \boldsymbol{\Omega}_{\mathrm{EDM}} + \boldsymbol{\Omega}_{\mathrm{TH}}, \tag{B.5}$$

where t is the time in the laboratory frame, and the precession angular velocity vector $\boldsymbol{\Omega}$ has been split into three contributions,

$$\begin{aligned}
\boldsymbol{\Omega}_{\mathrm{MDM}} &= \frac{g\mu_B}{\hbar}\left(\mathbf{B} - \frac{\gamma}{\gamma+1}(\boldsymbol{\beta}\cdot\mathbf{B})\boldsymbol{\beta} - \boldsymbol{\beta}\times\mathbf{E}\right), \\
\boldsymbol{\Omega}_{\mathrm{EDM}} &= \frac{d\mu_B}{\hbar}\left(\mathbf{E} - \frac{\gamma}{\gamma+1}(\boldsymbol{\beta}\cdot\mathbf{E})\boldsymbol{\beta} + \boldsymbol{\beta}\times\mathbf{B}\right), \\
\boldsymbol{\Omega}_{\mathrm{TH}} &= \frac{\gamma^2}{\gamma+1}\boldsymbol{\beta}\times\frac{d\boldsymbol{\beta}}{dt} = \\
&= \frac{q}{mc}\left[\left(\frac{1}{\gamma}-1\right)\mathbf{B} + \frac{\gamma}{\gamma+1}(\boldsymbol{\beta}\cdot\mathbf{B})\boldsymbol{\beta} - \left(\frac{1}{\gamma+1}-1\right)\boldsymbol{\beta}\times\mathbf{E}\right],
\end{aligned} \tag{B.6}$$

corresponding to the MDM, EDM and Thomas precession. The electric and magnetic fields, $\mathbf{E}$ and $\mathbf{B}$, respectively, are expressed in the laboratory frame.

For a neutral particle ($q = 0$) the Thomas precession term, arising from Lorentz forces, does not contribute and we obtain the classical equation, $d\mathbf{s}/d\tau = \boldsymbol{\mu} \times \mathbf{B}^* + \boldsymbol{\delta} \times \mathbf{E}^*$, where $\mathbf{E}^*$ and $\mathbf{B}^*$ are the external fields in the rest frame of the particle [206]. Equations (B.5) and (B.6) can be generalized to account for field gradient effects as described in Reference [210, 211].

For $\mathbf{B} = 0$ and $q = +1$, Equation (B.6) simplifies to

$$\boldsymbol{\Omega} = \frac{2\mu'}{\hbar}\left(\mathbf{E}\times\boldsymbol{\beta}\right) + \frac{d\mu_B}{\hbar}\mathbf{E} + \frac{1}{\gamma+1}\frac{2\mu_B}{\hbar}\left(\mathbf{E}\times\boldsymbol{\beta}\right) - \frac{d\mu_B}{\hbar}\frac{\gamma}{\gamma+1}\left(\boldsymbol{\beta}\cdot\mathbf{E}\right)\boldsymbol{\beta}, \tag{B.7}$$

where

$$\mu' = \frac{g-2}{2}\frac{e\hbar}{2mc}, \tag{B.8}$$

is the anomalous magnetic moment for a spin-1/2 particle. Since we are dealing with ultra relativistic baryons with $\gamma \gtrapprox 500$ at 1 TeV energy, in first approximation the terms $\propto 1/\gamma$ are neglected.

We describe the particle trajectory in a bent crystal using radial coordinates [163], as shown in Figure B.1,

$$\begin{aligned}
x(t) &= \ \mathrm{const.}, \\
y(t) &= \rho(t)\cos(\Omega t), \\
z(t) &= \rho(t)\sin(\Omega t),
\end{aligned} \tag{B.9}$$

where Ω is the revolution frequency for the particle traversing the bent crystal. In our ultra-relativistic case it is well approximated by $\Omega \approx c/\rho_0$, where ρ_0 is the crystal curvature radius. The radius of the trajectory as a function of time is

$$\rho(t) = \rho_0' + a\cos(\Omega_k t + \delta), \tag{B.10}$$

where a, Ω_k and δ are the oscillation amplitude, frequency and phase, respectively; a and δ depend on the particle energy and incident angle, while Ω_k depends on the crystal potential and particle energy. The radial equilibrium position ρ_0' differs from the electric potential minimum position ρ_0, due to the centrifugal potential, avoiding periodical cancellations and therefore inducing spin precession [164]. The electric potential in the crystal around the minimum can be approximated as an harmonic potential,

$$V = \frac{k}{e}\frac{\left[\rho(t) - \rho_0\right]^2}{2}, \tag{B.11}$$

and the corresponding electric field is

$$\begin{aligned} E_x &= 0, \\ E_y &= -\frac{dV}{d\rho}\cos(\Omega t), \\ E_z &= -\frac{dV}{d\rho}\sin(\Omega t), \end{aligned} \tag{B.12}$$

where the oscillation frequency of the particle around its equilibrium position ρ_0' is $\Omega_k = \sqrt{kc^2/eW}$ with W being the particle energy. Typical values for the relevant quantities are $\rho_0 \sim 30\,\mathrm{m}$, $\Omega \approx c/\rho_0 \sim 10^7\,\mathrm{Hz}$, $a \sim 10^{-10}\,\mathrm{m}$, $k = 4 \times 10^{17}\,\mathrm{eV/\,cm^2}$ for a Si crystal, yielding $\Omega_k \sim 10^{13}\,\mathrm{Hz}$ for 1 TeV particles.

Substituting the radial coordinates and applying the ultra-relativistic approximation to Equation (B.7) we obtain:

$$\begin{aligned} \Omega_x &\approx \frac{2\mu'}{\hbar}(E_y\beta_z - E_z\beta_y) = \frac{2\mu'}{\hbar}\left(-\frac{dV}{d\rho}\frac{\rho\Omega}{c}\right), \\ \Omega_y &\approx \frac{d\mu_B}{\hbar}\left[E_y - (\boldsymbol{\beta}\cdot\mathbf{E})\,\beta_y\right] = -\frac{d\mu_B}{\hbar}\frac{dV}{d\rho}\cos(\Omega t) + \frac{d\mu_B}{\hbar}\frac{dV}{d\rho}\frac{\dot\rho}{c^2}\left[-\rho\Omega\sin(\Omega t) + \dot\rho\cos(\Omega t)\right], \\ \Omega_z &\approx \frac{d\mu_B}{\hbar}\left[E_z - (\boldsymbol{\beta}\cdot\mathbf{E})\,\beta_z\right] = -\frac{d\mu_B}{\hbar}\frac{dV}{d\rho}\sin(\Omega t) + \frac{d\mu_B}{\hbar}\frac{dV}{d\rho}\frac{\dot\rho}{c^2}\left[\rho\Omega\cos(\Omega t) + \dot\rho\sin(\Omega t)\right]. \end{aligned} \tag{B.13}$$

In absence of EDM, *i.e.* $d = 0$, the spin precession inside the bent crystal occurs in the yz plane with the following spin time evolution [163],

$$\mathbf{s}(t) = \left\{ \begin{array}{l} s_x(t) = 0 \\ s_y(t) = s_0\cos(\omega t) \\ s_z(t) = s_0\sin(\omega t) \end{array} \right. , \tag{B.14}$$

for the initial condition $\mathrm{s}_0 = (0, s_0, 0)$ and where $\omega \approx 2\mu' E(\rho_0')/\hbar$ is the precession frequency. The spin precession angle defined in Equation (9.1) is $\Phi = \omega\bar{t}$, where $\bar{t}$ is the time needed to traverse the crystal. In presence of a non-zero EDM the spin precession is no longer confined to the yz plane, generating a s_x spin component otherwise not present,

$$\frac{ds_x}{dt} = s_y\Omega_z - s_z\Omega_y = \frac{d\mu_B}{\hbar}\frac{dV}{d\rho}s_0\left\{-\sin\left[(\omega+\Omega)t\right] + \frac{\dot\rho\rho\Omega}{c^2}\cos\left[(\omega+\Omega)t\right] + \frac{\dot\rho^2}{c^2}\sin\left[(\omega+\Omega)t\right]\right\}. \tag{B.15}$$

To derive Equation (B.15), EDM effects are assumed to be small compared to the MDM effects, *i.e.* $d \ll (g-2)$, and therefore $\Omega_y, \Omega_z \ll \Omega_x$. We neglect terms of order $\dot\rho/c$ where

$$\dot\rho = -a\Omega_k\sin(\Omega_k t + \delta) \sim a\Omega_k \sim 10^3\,\mathrm{m/s}, \tag{B.16}$$

since the second term of Equation (B.15) is about $\dot{\rho}\rho\Omega/c^2 \sim \dot{\rho}/c \sim 3\times10^{-4}$ and the third term is about $\dot{\rho}^2/c^2 \sim 9\times10^{-8}$. We demonstrate that $\Omega \ll \omega$ by requiring the electric force to be identical to the centripetal force,

$$\frac{m\gamma c^2}{\rho_0'} = eE(\rho_0'), \tag{B.17}$$

and obtain $\omega \approx \frac{2\mu'}{\hbar}E(\rho_0') \sim 10^{10}\,\mathrm{Hz} \gg \Omega \sim 10^7\,\mathrm{Hz}$.

Then, Equation (B.15) simplifies as

$$\frac{ds_x}{dt} = \frac{d\mu_B}{\hbar}\left(-\frac{dV}{d\rho}\right)s_0\sin(\omega t), \tag{B.18}$$

and the time evolution is

$$s_x(t) = -\frac{d\mu_B}{\hbar}E(\rho_0')\int_0^t \sin(\omega t')dt' - \frac{d\mu_B}{\hbar}\frac{ka}{e}\int_0^t \cos(\Omega_k t' + \delta)\sin(\omega t')dt'. \tag{B.19}$$

The second integral is negligibly small since $\Omega_k \gg \omega$ and its fast oscillation averages the integral to zero. The calculation can be decomposed into two analytically integrable terms proportional to $\sin(\Omega_k t')\sin(\omega t')$ and $\cos(\Omega_k t')\sin(\omega t')$. Assuming $\Omega_k \gg \omega$, the maximum value of this integral is

$$\sim \frac{d\mu_B}{\hbar}\frac{ka}{e\Omega_k} \sim 2\frac{d}{g-2}\xi, \tag{B.20}$$

where $\xi = \mu' ka/\hbar e\Omega_k \lesssim 10^{-2}$ and terms proportional to ξ were neglected to derive Equation (B.14) [163]. Finally we obtain the time evolution of the polarization vector in presence of a non-negligible EDM,

$$\mathbf{s}(t) = \begin{cases} s_x(t) \approx s_0\dfrac{d}{g-2}\left[\cos(\omega t) - 1\right] \\ s_y(t) \approx s_0\cos(\omega t) \\ s_z(t) \approx s_0\sin(\omega t) \end{cases}. \tag{B.21}$$

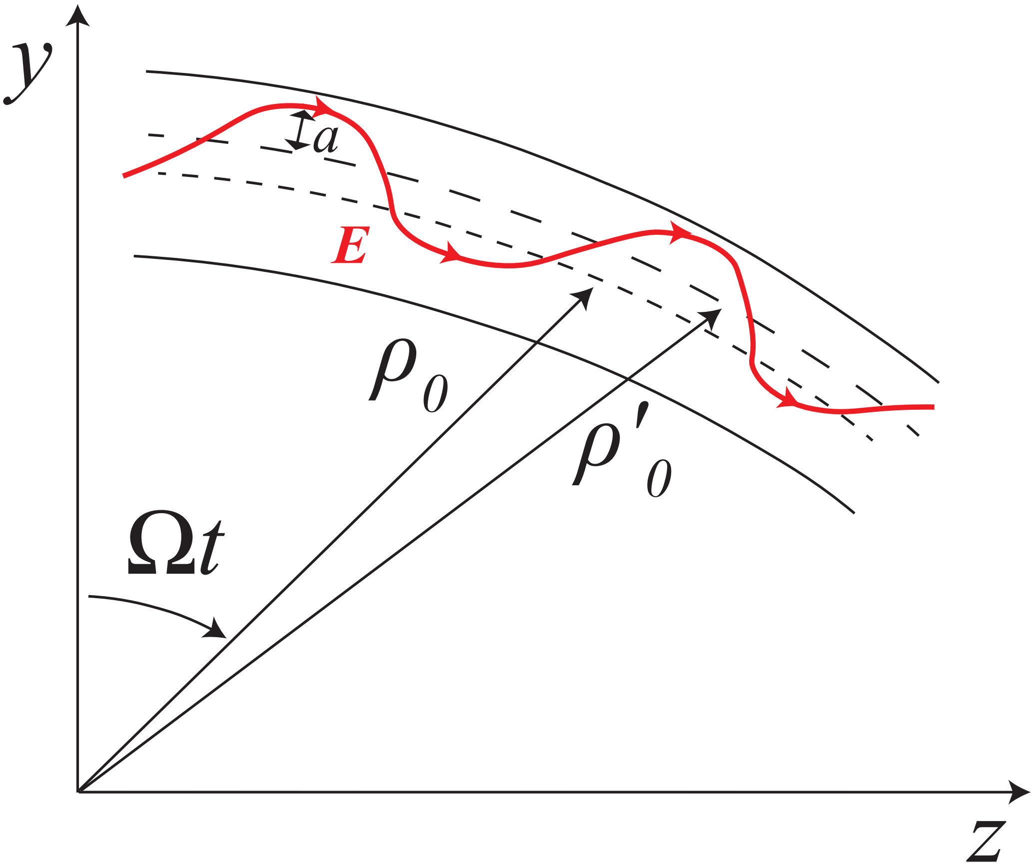

Figure B.1: Radial coordinates definition: ρ_0 is the radius corresponding to the minimum of the harmonic electric potential; ρ'_0 represents the radial equilibrium position of the electric and centrifugal potential. The red curve represents the particle trajectory inside the crystal in presence of the radial electric field $\mathbf{E}$, a is the oscillation amplitude and Ω the revolution frequency.

Bibliography

[1] L. Canetti, M. Drewes, and M. Shaposhnikov, *Matter and Antimatter in the Universe*, New J. Phys. **14** (2012) 095012, `arXiv:1204.4186`.

[2] M. S. Sozzi, *Discrete Symmetries and CP Violation*, Oxford Graduate Texts, Great Clarendon Street, Oxford OX2 6DP, 2008.

[3] J. M. Cline, *Baryogenesis*, `arXiv:hep-ph/0609145`.

[4] R. H. Cyburt, *Primordial nucleosynthesis for the new cosmology: Determining uncertainties and examining concordance*, Phys. Rev. D **70** (2004) 023505.

[5] W. Hu and S. Dodelson, *Cosmic microwave background anisotropies*, Ann. Rev. Astron. Astrophys. **40** (2002) 171, `arXiv:astro-ph/0110414`.

[6] W. Bernreuther, *CP violation and baryogenesis*, Lect. Notes Phys. **591** (2002) 237, `arXiv:hep-ph/0205279`.

[7] A. D. Sakharov, *Violation of CP Invariance, C Asymmetry, and Baryon Asymmetry of the Universe*, JETP **5** (1967) 24.

[8] G. 't Hooft, *Symmetry Breaking through Bell-Jackiw Anomalies*, Phys. Rev. Lett. **37** (1976) 8.

[9] F. R. Klinkhamer and N. S. Manton, *A saddle-point solution in the Weinberg-Salam theory*, Phys. Rev. D **30** (1984) 2212.

[10] R. L. Garwin, L. M. Lederman, and M. Weinrich, *Observations of the Failure of Conservation of Parity and Charge Conjugation in Meson Decays: the Magnetic Moment of the Free Muon*, Phys. Rev. **105** (1957) 1415.

[11] J. H. Christenson, J. W. Cronin, V. L. Fitch, and R. Turlay, *Evidence for the* 2π *Decay of the* K_2^0 *Meson*, Phys. Rev. Lett. **13** (1964) 138.

[12] P. Huet and E. Sather, *Electroweak baryogenesis and standard model CP violation*, Phys. Rev. **D51** (1995) 379, `arXiv:hep-ph/9404302`.

[13] R. F. Streater and A. S. Wightman, *PCT, Spin and Statistics, and All That*, Benjamin, New York, 1964. doi: 10.1126/science.145.3631.475.

[14] C. S. Wu *et al.*, *Experimental Test of Parity Conservation in Beta Decay*, Phys. Rev. **105** (1957) 1413.

[15] M. Goldhaber, L. Grodzins, and A. W. Sunyar, *Helicity of Neutrinos*, Phys. Rev. **109** (1958) 1015.

[16] N. Cabibbo, *Unitary Symmetry and Leptonic Decays*, Phys. Rev. Lett. **10** (1963) 531.

[17] S. L. Glashow, J. Iliopoulos, and L. Maiani, *Weak Interactions with Lepton-Hadron Symmetry*, Phys. Rev. D **2** (1970) 1285.

[18] J. J. Aubert *et al.*, *Experimental Observation of a Heavy Particle J*, Phys. Rev. Lett. **33** (1974) 1404.

[19] J. E. Augustin *et al.*, *Discovery of a Narrow Resonance in e^+e^- Annihilation*, Phys. Rev. Lett. **33** (1974) 1406.

[20] M. Kobayashi and T. Maskawa, *CP Violation in the Renormalizable Theory of Weak Interaction*, Prog. Theor. Phys. **49** (1973) 652.

[21] S. W. Herb *et al.*, *Observation of a Dimuon Resonance at 9.5 GeV in 400-GeV Proton-Nucleus Collisions*, Phys. Rev. Lett. **39** (1977) 252.

[22] CDF Collaboration, F. Abe *et al.*, *Observation of top quark production in $\bar{p}p$ collisions*, Phys. Rev. Lett. **74** (1995) 2626, `arXiv:hep-ex/9503002`.

[23] D0 Collaboration, S. Abachi *et al.*, *Search for high mass top quark production in $p\bar{p}$ collisions at $\sqrt{s} = 1.8$ TeV*, Phys. Rev. Lett. **74** (1995) 2422, `arXiv:hep-ex/9411001`.

[24] Argus Collaboration, H. Albrecht *et al.*, *Observation of B0 - anti-B0 Mixing*, Phys. Lett. B **192** (1987) 245.

[25] CDF Collaboration, A. Abulencia *et al.*, *Observation of B0(s) - anti-B0(s) Oscillations*, Phys. Rev. Lett. **97** (2006) 242003, `arXiv:hep-ex/0609040`.

[26] LHCb Collaboration, R. Aaij *et al.*, *Observation of $D^0 - \overline{D}^0$ oscillations*, Phys. Rev. Lett. **110** (2013), no. 10 101802, `arXiv:1211.1230`.

[27] BaBar Collaboration, B. Aubert *et al.*, *Observation of CP violation in the B^0 meson system*, Phys. Rev. Lett. **87** (2001) 091801, `arXiv:hep-ex/0107013`.

[28] Belle Collaboration, K. Abe *et al.*, *Observation of large CP violation in the neutral B meson system*, Phys. Rev. Lett. **87** (2001) 091802, `arXiv:hep-ex/0107061`.

[29] LHCb collaboration, R. Aaij *et al.*, *First observation of CP violation in the decays of B_s^0 mesons*, Phys. Rev. Lett. **110** (2013), no. 22 221601, `arXiv:1304.6173`.

[30] C. Jarlskog, *Commutator of the Quark Mass Matrices in the Standard Electroweak Model and a Measure of Maximal* CP *Nonconservation*, Phys. Rev. Lett. **55** (1985) 1039.

[31] L. Wolfenstein, *Parametrization of the Kobayashi-Maskawa Matrix*, Phys. Rev. Lett. **51** (1983) 1945.

[32] CDF collaboration, T. A. Aaltonen *et al.*, *Measurements of direct CP-violating asymmetries in charmless decays of bottom baryons*, Phys. Rev. Lett. **113** (2014) 242001, `arXiv:1403.5586`.

[33] LHCb collaboration, R. Aaij *et al.*, *Searches for $\mathit{\Lambda}_b^0$ and $\mathit{\Xi}_b^0$ decays to $K_S^0 p\pi^-$ and $K_S^0 pK^-$ final states with first observation of the $\mathit{\Lambda}_b^0 \to K_S^0 p\pi^-$ decay*, JHEP **04** (2014) 087 LHCb-PAPER-2013-061, CERN-PH-EP-2014-012, `arXiv:1402.0770`.

[34] LHCb collaboration, R. Aaij *et al.*, *Observation of the $\mathit{\Lambda}_b^0 \to J/\psi p\pi^-$ decay*, JHEP **07** (2014) 103 LHCb-PAPER-2014-020, LHCb-PAPER-2014-115, `arXiv:1406.0755`.

[35] LHCb collaboration, R. Aaij *et al.*, *Observations of $\mathit{\Lambda}_b^0 \to \mathit{\Lambda} K^+\pi^-$ and $\mathit{\Lambda}_b^0 \to \mathit{\Lambda} K^+K^-$ decays and searches for other $\mathit{\Lambda}_b^0$ and $\mathit{\Xi}_b^0$ decays to $\mathit{\Lambda} h^+h^-$ final states*, JHEP **05** (2016) 081 LHCb-PAPER-2016-004, CERN-EP-2016-038, `arXiv:1603.0041`.

[36] LHCb collaboration, R. Aaij *et al.*, *Observation of the decay $\mathit{\Lambda}_b^0 \to pK^-\mu^+\mu^-$ and search for CP violation*, JHEP **06** (2017) 108 LHCb-PAPER-2016-059, CERN-EP-2017-032, `arXiv:1703.0025`.

[37] LHCb, R. Aaij *et al.*, *Search for CP violation in $\Lambda_b^0 \to pK^-$ and $\Lambda_b^0 \to p\pi^-$ decays*, Phys. Lett. **B787** (2018) 124, `arXiv:1807.0654`.

[38] LHCb collaboration, R. Aaij *et al.*, *Measurement of matter-antimatter differences in beauty baryon decays*, Nature Physics **13** (2017) 391 LHCb-PAPER-2016-030, CERN-EP-2016-212, `arXiv:1609.0521`.

[39] LHCb collaboration, R. Aaij *et al.*, *Search for CP violation using triple product asymmetries in $\mathit{\Lambda}_b^0 \to pK^-\pi^+\pi^-$, $\mathit{\Lambda}_b^0 \to pK^-K^+K^-$, and $\mathit{\Xi}_b^0 \to pK^-K^-\pi^+$ decays*, JHEP **08** (2018) 039 LHCb-PAPER-2018-001, CERN-EP-2018-081, `arXiv:1805.0394`.

[40] LHCb collaboration, R. Aaij *et al.*, *Measurement of B^0, B_s^0, B^+ and $\mathit{\Lambda}_b^0$ production asymmetries in 7 and 8 TeV pp collisions*, Phys. Lett. **B774** (2017) 139 LHCb-PAPER-2016-062, CERN-EP-2017-036, `arXiv:1703.0846`.

[41] LHCb collaboration, R. Aaij *et al.*, *Search for CP violation in $\mathit{\Lambda}_c^+ \to pK^-K^+$ and $\mathit{\Lambda}_c^+ p\pi^-\pi^+$ decays*, JHEP **03** (2018) 182 LHCb-PAPER-2017-044, CERN-EP-2017-316, `arXiv:1712.0705`.

[42] LHCb collaboration, R. Aaij *et al.*, *Search for CP violation in $D^0 \to \pi^-\pi^+\pi^0$ decays with the energy test*, Phys. Lett. **B740** (2015) 158 CERN-PH-EP-2014-251, LHCb-PAPER-2014-054, `arXiv:1410.4170`.

[43] M. Gronau and J. L. Rosner, *Triple product asymmmetries in Λ_b and Ξ_b decays*, Phys. Lett. **B749** (2015) 104, `arXiv:1506.0134`.

[44] Y. K. Hsiao and C. Q. Geng, *Direct CP violation in $\mathit{\Lambda}_b^0$ decays*, Phys. Rev. **D91** (2015) 116007, `arXiv:1412.1899`.

[45] W. Bensalem, A. Datta, and D. London, *New physics effects on triple product correlations in $\mathit{\Lambda}_b^0$ decays*, Phys. Rev. **D66** (2002) 094004, `arXiv:hep-ph/0208054`.

[46] W. Bensalem and D. London, *T odd triple product correlations in hadronic b decays*, Phys. Rev. **D64** (2001) 116003, `arXiv:hep-ph/0005018`.

[47] G. C. Branco, L. Lavoura, and J. P. Silvaa, *CP Violation*, Clarendon Press, Oxford, UK, 1999.

[48] W. Bensalem, A. Datta, and D. London, *T violating triple product correlations in charmless $\mathit{\Lambda}_b^0$ decays*, Phys. Lett. **B538** (2002) 309, `arXiv:hep-ph/0205009`.

[49] A. J. Bevan, *C, P, and CP asymmetry observables based on triple product asymmetries*, `arXiv:1408.3813`.

[50] G. Durieux and Y. Grossman, *Probing CP violation systematically in differential distributions*, `arXiv:1508.3054`.

[51] G. Valencia, *Angular correlations in the decay B→VV and CP violation*, Phys. Rev. D **39** (1989) 3339.

[52] A. Datta and D. London, *Triple-product correlations in B –¿ V1 V2 decays and new physics*, Int. J. Mod. Phys. **A19** (2004) 2505, `arXiv:hep-ph/0303159`.

[53] G. Durieux and Y. Grossman, *Probing CP violation systematically in differential distributions*, Phys. Rev. D **92** (2015) 076013.

[54] E. M. Purcell and N. F. Ramsey, *On the Possibility of Electric Dipole Moments for Elementary Particles and Nuclei*, Phys. Rev. **78** (1950) 807.

[55] J. H. Smith, E. M. Purcell, and N. F. Ramsey, *Experimental limit to the electric dipole moment of the neutron*, Phys. Rev. **108** (1957) 120.

[56] ACME collaboration, J. Baron *et al.*, *Order of Magnitude Smaller Limit on the Electric Dipole Moment of the Electron*, Science **343** (2014) 269, `arXiv:1310.7534`.

[57] Muon g-2 collaboration, G. W. Bennett *et al.*, *An Improved Limit on the Muon Electric Dipole Moment*, Phys. Rev. **D80** (2009) 052008, `arXiv:0811.1207`.

[58] Belle collaboration, K. Inami *et al.*, *Search for the electric dipole moment of the tau lepton*, Phys. Lett. **B551** (2003) 16, `arXiv:hep-ex/0210066`.

[59] J. M. Pendlebury *et al.*, *Revised experimental upper limit on the electric dipole moment of the neutron*, Phys. Rev. **D92** (2015), no. 9 092003, `arXiv:1509.0441`.

[60] W. C. Griffith *et al.*, *Improved Limit on the Permanent Electric Dipole Moment of Hg-199*, Phys. Rev. Lett. **102** (2009) 101601.

[61] V. F. Dmitriev and R. A. Sen'kov, *Schiff moment of the mercury nucleus and the proton dipole moment*, Phys. Rev. Lett. **91** (2003) 212303, `arXiv:nucl-th/0306050`.

[62] L. Pondrom *et al.*, *New Limit on the Electric Dipole Moment of the Λ Hyperon*, Phys. Rev. **D23** (1981) 814.

[63] Muon g-2 collaboration, J. Grange *et al.*, *Muon (g-2) Technical Design Report*, tech. rep., 2015.

[64] J-PARC g-2/EDM collaboration, N. Saito, *A novel precision measurement of muon g-2 and EDM at J-PARC*, AIP Conf. Proc. **1467** (2012) 45.

[65] V. Anastassopoulos *et al.*, *A Storage Ring Experiment to Detect a Proton Electric Dipole Moment*, 2015, 2015.

[66] JEDI collaboration, J. Pretz, *Measurement of electric dipole moments at storage rings*, Physica Scripta **2015** (2015), no. T166 014035.

[67] I. B. Khriplovich, *Feasibility of search for nuclear electric dipole moments at ion storage rings*, Phys. Lett. **B444** (1998) 98, `arXiv:hep-ph/9809336`.

[68] CPLEAR, A. Angelopoulos *et al.*, *First direct observation of time reversal noninvariance in the neutral kaon system*, Phys. Lett. **B444** (1998) 43.

[69] BaBar collaboration, J. P. Lees *et al.*, *Observation of Time Reversal Violation in the B^0 Meson System*, Phys. Rev. Lett. **109** (2012) 211801, `arXiv:1207.5832`.

[70] J. Bernabeu and F. Martinez-Vidal, *Colloquium: Time-reversal violation with quantum-entangled B mesons*, Rev. Mod. Phys. **87** (2015) 165, `arXiv:1410.1742`.

[71] F. J. Botella *et al.*, *On the search for the electric dipole moment of strange and charm baryons at LHC*, Eur. Phys. J. C **77** (2017) 181, `arXiv:1612.0676`.

[72] V. G. Baryshevsky, *The possibility to measure the magnetic moments of short-lived particles (charm and beauty baryons) at LHC and FCC energies using the phenomenon of spin rotation in crystals*, Phys. Lett. **B757** (2016) 426.

[73] UA9 collaboration, L. Burmistrov *et al.*, *Measurement of Short Living Baryon Magnetic Moment using Bent Crystals at SPS and LHC*, Tech. Rep. CERN-SPSC-2016-030. SPSC-EOI-012, CERN, Geneva, Jun, 2016.

[74] M. Pospelov and A. Ritz, *Electric dipole moments as probes of new physics*, Annals Phys. **318** (2005) 119, `arXiv:hep-ph/0504231`.

[75] E761 collaboration, D. Chen *et al.*, *First observation of magnetic moment precession of channeled particles in bent crystals*, Phys. Rev. Lett. **69** (1992) 3286.

[76] A. Hayreter and G. Valencia, *Constraints on anomalous color dipole operators from Higgs boson production at the LHC*, Phys. Rev. **D88** (2013) 034033, `arXiv:1304.6976`.

[77] F. Sala, *A bound on the charm chromo-EDM and its implications*, JHEP **03** (2014) 061, `arXiv:1312.2589`.

[78] D. Chang, W.-Y. Keung, C. S. Li, and T. C. Yuan, *QCD Corrections to CP Violation From Color Electric Dipole Moment of b Quark*, Phys. Lett. **B241** (1990) 589.

[79] Y. T. Chien *et al.*, *Direct and indirect constraints on CP-violating Higgs-quark and Higgs-gluon interactions*, JHEP **02** (2016) 011, `arXiv:1510.0072`, [JHEP02,011(2016)].

[80] A. Wirzba, *Electric dipole moments of the nucleon and light nuclei*, Nucl. Phys. **A928** (2014) 116, `arXiv:1404.6131`.

[81] M. Nowakowski, E. A. Paschos, and J. M. Rodriguez, *All electromagnetic form-factors*, Eur. J. Phys. **26** (2005) 545, `arXiv:physics/0402058`.

[82] F.-K. Guo and U.-G. Meissner, *Baryon electric dipole moments from strong CP violation*, JHEP **12** (2012) 097, `arXiv:1210.5887`.

[83] R. Escribano and E. Masso, *Constraints on fermion magnetic and electric moments from LEP-1*, Nucl. Phys. **B429** (1994) 19, `arXiv:hep-ph/9403304`.

[84] A. E. Blinov and A. S. Rudenko, *Upper Limits on Electric and Weak Dipole Moments of tau-Lepton and Heavy Quarks from e^+e^- Annihilation*, Nucl. Phys. Proc. Suppl. **189** (2009) 257, `arXiv:0811.2380`.

[85] A. G. Grozin, I. B. Khriplovich, and A. S. Rudenko, *Upper limits on electric dipole moments of tau-lepton, heavy quarks, and W-boson*, Nucl. Phys. **B821** (2009) 285, `arXiv:0902.3059`.

[86] W. Dekens *et al.*, *Unraveling models of CP violation through electric dipole moments of light nuclei*, JHEP **07** (2014) 069, `arXiv:1404.6082`.

[87] N. Sharma, H. Dahiya, P. K. Chatley, and M. Gupta, *Spin* $1/2^+$, *spin* $3/2^+$ *and transition magnetic moments of low lying and charmed baryons*, Phys. Rev. **D81** (2010) 073001, `arXiv:1003.4338`.

[88] A. Pich and E. de Rafael, *Strong CP violation in an effective chiral Lagrangian approach*, Nucl. Phys. **B367** (1991) 313.

[89] B. Borasoy, *The electric dipole moment of the neutron in chiral perturbation theory*, Phys. Rev. **D61** (2000) 114017, `arXiv:hep-ph/0004011`.

[90] A. Faessler, T. Gutsche, S. Kovalenko, and V. E. Lyubovitskij, *Implications of R-parity violating supersymmetry for atomic and hadronic EDMs*, Phys. Rev. **D74** (2006) 074013, `arXiv:hep-ph/0607269`.

[91] A. A. Anselm and D. Diakonov, *On Weinberg's Model of CP Violation in Gauge Theories*, Nucl. Phys. **B145** (1978) 271.

[92] S.-L. Zhu, W.-Y. P. Hwang, and Z.-S. Yang, *The* Σ_c *and* Λ_c *magnetic moments from QCD spectral sum rules*, Phys. Rev. **D56** (1997) 7273, `arXiv:hep-ph/9708411`.

[93] H. Georgi, *Generalized dimensional analysis*, Phys. Lett. **B298** (1993) 187, `arXiv:hep-ph/9207278`.

[94] N. Yamanaka, *Analysis of the Electric Dipole Moment in the R-parity Violating Supersymmetric Standard Model*, PhD thesis, Osaka U., Res. Ctr. Nucl. Phys., 2013, doi: 10.1007/978-4-431-54544-6.

[95] K. Jungmann, *Searching for electric dipole moments*, Annalen Phys. **525** (2013), no. 8-9 550.

[96] M. Lamont, *EDM at storage rings. Physics Beyond Colliders workshop, March 2017. https://indico.cern.ch/event/608491/*, .

[97] A. Cordero-Cid, J. M. Hernandez, G. Tavares-Velasco, and J. J. Toscano, *Bounding the top and bottom electric dipole moments from neutron experimental data*, J. Phys. **G35** (2008) 025004, `arXiv:0712.0154`.

[98] J. Bramante, A. Delgado, L. Lehman, and A. Martin, *Boosted Higgses from chromomagnetic b's:* $b\bar{b}h$ *at high luminosity*, Phys. Rev. **D93** (2016), no. 5 053001, `arXiv:1410.3484`.

[99] D. Atwood and A. Soni, *Chiral perturbation theory constraint on the electric dipole moment of the* Λ *hyperon*, Phys. Lett. **B291** (1992) 293.

[100] Y.-P. Kuang *et al.*, *Testing Anomalous Color-Electric Dipole Moment of the c-Quark from* $\psi' \to J/\psi + \pi^+ + \pi^-$ *at Beijing Spectrometer*, Phys. Rev. **D85** (2012) 114010, `arXiv:1202.3042`.

[101] M. König, M. Neubert, and D. M. Straub, *Dipole operator constraints on composite Higgs models*, Eur. Phys. J. **C74** (2014), no. 7 2945, `arXiv:1403.2756`.

[102] M. Gorbahn and U. Haisch, *Searching for* $t \to c(u)h$ *with dipole moments*, JHEP **06** (2014) 033, `arXiv:1404.4873`.

[103] G. Panico and A. Pomarol, *Flavor hierarchies from dynamical scales*, JHEP **07** (2016) 097, `arXiv:1603.0660`.

[104] S.-M. Zhao *et al.*, *The one loop contributions to* $c(t)$ *electric dipole moment in the CP violating BLMSSM*, Eur. Phys. J. **C77** (2017), no. 2 102, `arXiv:1610.0731`.

[105] Z. Z. Aydin and U. Erkarslan, *The Charm quark EDM and singlet P wave charmonium production in supersymmetry*, Phys. Rev. **D67** (2003) 036006, `arXiv:hep-ph/0204238`.

[106] X.-J. Bi *et al.*, *The c-quark EDM and production of* h_c *in* e^+e^- *annihilation*, `arXiv:hep-ph/0412360`.

[107] D. A. Demir and M. B. Voloshin, *b-quark electric dipole moment in supersymmetry and CP-odd bottomonium formation*, Phys. Rev. **D63** (2001) 115011, `arXiv:hep-ph/0012123`.

[108] R. Martinez and G. Valencia, *Top and bottom tensor couplings from a color octet scalar*, Phys. Rev. **D95** (2017), no. 3 035041, `arXiv:1612.0056`.

[109] M. Baumgart, D. Stolarski, and T. Zorawski, *Split supersymmetry radiates flavor*, Phys. Rev. **D90** (2014), no. 5 055001, `arXiv:1403.6118`.

[110] R. Dhir, C. S. Kim, and R. C. Verma, *Magnetic Moments of Bottom Baryons: Effective mass and Screened Charge*, Phys. Rev. **D88** (2013) 094002, `arXiv:1309.4057`.

[111] J. P. Miller, E. de Rafael, and B. L. Roberts, *Muon (g-2): Experiment and theory*, Rept. Prog. Phys. **70** (2007) 795, `arXiv:hep-ph/0703049`.

[112] E. Norrbin and T. Sjostrand, *Production and hadronization of heavy quarks*, Eur. Phys. J. **C17** (2000) 137, `arXiv:hep-ph/0005110`.

[113] LHCb collaboration, R. Aaij *et al.*, *Measurement of* $\sigma(pp \to b\bar{b}X)$ *at* $\sqrt{s} = 7$ TeV *in the forward region*, Phys. Lett. **B694** (2010) 209, `arXiv:1009.2731`.

[114] LHCb Collaboration, R. Aaij *et al.*, *Measurement of b-hadron production fractions in* 7 TeVpp *collisions*, Phys. Rev. **D85** (2012) 032008, `arXiv:1111.2357`.

[115] Heavy Flavor Averaging Group (HFAG), Y. Amhis *et al.*, *Averages of b-hadron, c-hadron, and* τ*-lepton properties as of summer 2014*, `arXiv:1412.7515`.

[116] *LHCb : Technical Proposal*, Tech. Proposal, CERN, Geneva, 1998.

[117] LHCb Collaboration, A. Nobrega *et al.*, *LHCb reoptimized detector design and performance : Technical Design Report*, tech. rep., 2003.

[118] The LHCb Collaboration, *The LHCb Detector at the LHC*, Journal of Instrumentation **3** (2008), no. 08 S08005.

[119] LHCb Collaboration, P. R. Barbosa-Marinho *et al.*, *LHCb VELO (VErtex LOcator): Technical Design Report*, Technical Design Report LHCb, CERN, Geneva, 2001.

[120] J. Gassner, F. Lehner, and S. Steiner, *The mechanical Design of the LHCb Silicon Trigger Tracker*, Tech. Rep. LHCb-2004-110. CERN-LHCb-2004-110, CERN, Geneva, Aug, 2010.

[121] J. Gassner, F. Lehner, and S. Steiner, *The Production, Assembly and Testing of the LHCb Silicon Trigger Tracker*, Tech. Rep. LHCb-2004-109. CERN-LHCb-2004-109, CERN, Geneva, Jul, 2005.

[122] LHCb Collaboration, P. R. Barbosa-Marinho *et al.*, *LHCb inner tracker: Technical Design Report*, Technical Design Report LHCb, CERN, Geneva, 2002. revised version number 1 submitted on 2002-11-13 14:14:34.

[123] LHCb Collaboration, P. R. Barbosa-Marinho *et al.*, *LHCb outer tracker: Technical Design Report*, Technical Design Report LHCb, CERN, Geneva, 2001.

[124] LHCb Collaboration, S. Amato *et al.*, *LHCb magnet: Technical Design Report*, Technical Design Report LHCb, CERN, Geneva, 2000.

[125] J. Andre *et al.*, *Status of the lhcb magnet system*, Applied Superconductivity, IEEE Transactions on **12** (2002) 366.

[126] J. Andre *et al.*, *Status of the lhcb dipole magnet*, Applied Superconductivity, IEEE Transactions on **14** (2004) 509.

[127] M. Losasso *et al.*, *Tests and field map of lhcb dipole magnet*, Applied Superconductivity, IEEE Transactions on **16** (2006) 1700.

[128] LHCb Collaboration, S. Amato *et al.*, *LHCb RICH: Technical Design Report*, Technical Design Report LHCb, CERN, Geneva, 2000.

[129] LHCb Collaboration, S. Amato *et al.*, *LHCb calorimeters: Technical Design Report*, Technical Design Report LHCb, CERN, Geneva, 2000.

[130] I. Machikhiliyan and the LHCb calorimeter group, *Current status and performance of the lhcb electromagnetic and hadron calorimeters*, Journal of Physics: Conference Series **293** (2011), no. 1 012052.

[131] LHCb Collaboration, P. R. Barbosa-Marinho and otehrs, *LHCb muon system: Technical Design Report*, Technical Design Report LHCb, CERN, Geneva, 2001.

[132] LHCb Collaboration, *LHCb muon system: addendum to the Technical Design Report*, Technical Design Report LHCb, CERN, Geneva, 2003.

[133] LHCb Collaboration, *LHCb muon system: second addendum to the Technical Design Report*, Technical Design Report LHCb, CERN, Geneva, 2005. Submitted on 9 Apr 2005.

[134] LHCb collaboration, *Prompt charm production in pp collisions at* $\sqrt{s} = 7\,\mathrm{TeV}$, LHCb-CONF-2010-013.

[135] LHCb collaboration, R. Aaij *et al.*, *Measurement of the inelastic pp cross-section at a centre-of-mass energy of* $\sqrt{s} = 7$ *TeV*, `arXiv:1412.2500`.

[136] LHCb Collaboration, R. Antunes-Nobrega *et al.*, *LHCb trigger system: Technical Design Report*, Technical Design Report LHCb, CERN, Geneva, 2003. revised version number 1 submitted on 2003-09-24 12:12:22.

[137] V. V. Gligorov, C. Thomas, and M. Williams, *The HLT inclusive B triggers*, .

[138] M. Kucharczyk, P. Morawski, and M. Witek, *Primary Vertex Reconstruction at LHCb*, Tech. Rep. LHCb-PUB-2014-044. CERN-LHCb-PUB-2014-044, CERN, Geneva, Sep, 2014.

[139] R. Frühwirth, *Application of kalman filtering to track and vertex fitting*, Nuclear Instruments and Methods in Physics Research Section A: Accelerators, Spectrometers, Detectors and Associated Equipment **262** (1987), no. 2 444 .

[140] L. Breiman, J. H. Friedman, R. A. Olshen, and C. J. Stone, *Classification and regression trees*, Wadsworth international group, Belmont, California, USA, 1984.

[141] T. Likhomanenko *et al.*, *LHCb Topological Trigger Reoptimization*, J. Phys. Conf. Ser. **664** (2015), no. 8 082025, `arXiv:1510.0057`.

[142] W. D. Hulsbergen, *Decay chain fitting with a Kalman filter*, Nuclear Instruments and Methods in Physics Research A **552** (2005) 566, `arXiv:physics/0503191`.

[143] M. De Cian, S. Farry, P. Seyfert, and S. Stahl, *Fast neural-net based fake track rejection in the LHCb reconstruction*, Tech. Rep. LHCb-PUB-2017-011. CERN-LHCb-PUB-2017-011, CERN, Geneva, Mar, 2017.

[144] LHCb, R. Aaij *et al.*, *LHCb Detector Performance*, Int. J. Mod. Phys. **A30** (2015), no. 07 1530022, `arXiv:1412.6352`.

[145] R. Aaij *et al.*, *Selection and processing of calibration samples to measure the particle identification performance of the LHCb experiment in Run 2*, EPJ Tech. Instrum. **6** (2019), no. 1 1, `arXiv:1803.0082`.

[146] A. Hoecker *et al.*, *TMVA - Toolkit for Multivariate Data Analysis*, ArXiv Physics e-prints (2007) `arXiv:physics/0703039`.

[147] R. Kohavi, *A study of cross-validation and bootstrap for accuracy estimation and model selection*, in *Proceedings of the 14th International Joint Conference on Artificial Intelligence - Volume 2*, IJCAI'95, (San Francisco, CA, USA), pp. 1137–1143, Morgan Kaufmann Publishers Inc., 1995.

[148] M. Pivk and F. R. Le Diberder, *sPlot: A statistical tool to unfold data distributions*, Nucl. Instrum. Meth. **A555** (2005) 356, `arXiv:physics/0402083`.

[149] K. S. Cranmer, *Kernel estimation in high-energy physics*, Comput. Phys. Commun. **136** (2001) 198, `arXiv:hep-ex/0011057`.

[150] L. Breiman, J. H. Friedman, R. A. Olshen, and C. J. Stone, *Classification and regression trees. wadsworth*, Belmont, CA (1984).

[151] L. Anderlini *et al.*, *The PIDCalib package*, Tech. Rep. LHCb-PUB-2016-021. CERN-LHCb-PUB-2016-021, CERN, Geneva, Jul, 2016.

[152] T. Skwarnicki, *A study of the radiative cascade transitions between the Upsilon-prime and Upsilon resonances*, PhD thesis, Institute of Nuclear Physics, Krakow, 1986, DESY-F31-86-02.

[153] M. Rosenblatt, *Remarks on some nonparametric estimates of a density function*, Ann. Math. Statist. **27** (1956) 832.

[154] J. D. Richman, *An Experimenter's Guide to the Helicity Formalism*, .

[155] Particle Data Group, M. Tanabashi *et al.*, *Review of particle physics*, Phys. Rev. D **98** (2018) 030001.

[156] LHCb collaboration, R. Aaij *et al.*, *Measurements of the $\mathit{\Lambda}_b^0 \to J/\psi\,\mathit{\Lambda}$ decay amplitudes and the $\mathit{\Lambda}_b^0$ polarisation in pp collisions at $\sqrt{s} = 7\,\mathrm{TeV}$*, Phys. Lett. **B724** (2013) 27, `arXiv:1302.5578`.

[157] ATLAS, G. Aad *et al.*, *Measurement of the parity-violating asymmetry parameter α_b and the helicity amplitudes for the decay $\mathit{\Lambda}_b^0 \to J/\psi\,\mathit{\Lambda}$ with the ATLAS detector*, Phys. Rev. **D89** (2014), no. 9 092009, `arXiv:1404.1071`.

[158] CMS, A. M. Sirunyan *et al.*, *Measurement of the Λ_b polarization and angular parameters in $\Lambda_b \to J/\psi\,\Lambda$ decays from pp collisions at $\sqrt{s} = 7$ and 8 TeV*, Phys. Rev. **D97** (2018), no. 7 072010, `arXiv:1802.0486`.

[159] V. V. Baublis *et al.*, *Measuring the magnetic moments of short-lived particles using channeling in bent crystals*, Nucl. Instrum. Meth. **B90** (1994) 112.

[160] V. M. Samsonov, *On the possibility of measuring charm baryon magnetic moments with channeling*, Nucl. Instrum. Meth. **B119** (1996) 271.

[161] M. Jacob and G. C. Wick, *On the general theory of collisions for particles with spin*, Annals Phys. **7** (1959) 404.

[162] V. M. Biryukov *et al.*, *Crystal Channeling and Its Application at High-Energy Accelerators*, Springer-Verlag Berlin Heidelberg, 1997.

[163] V. G. Baryshevsky, *Spin rotation and depolarization of high-energy particles in crystals at Hadron Collider (LHC) and Future Circular Collider (FCC) energies and the possibility to measure the anomalous magnetic moments of short-lived particles*, 2015.

[164] I. J. Kim, *Magnetic moment measurement of baryons with heavy flavored quarks by planar channeling through bent crystal*, Nucl. Phys. **B229** (1983) 251.

[165] V. L. Lyuboshits, *The Spin Rotation at Deflection of Relativistic Charged Particle in Electric Field*, Sov. J. Nucl. Phys. **31** (1980) 509.

[166] E. Bagli *et al.*, *Electromagnetic dipole moments of charged baryons with bent crystals at the LHC*, Eur. Phys. J. **C77** (2017), no. 12 828, `arXiv:1708.0848`.

[167] C. Loizides, *Glauber modeling of high-energy nuclear collisions at the subnucleon level*, Phys. Rev. **C94** (2016), no. 2 024914, `arXiv:1603.0737`.

[168] LHCb collaboration, *Framework TDR for the LHCb Upgrade: Technical Design Report*, CERN-LHCC-2012-007. LHCb-TDR-012.

[169] S. Redaelli, *Experience with multi-TeV beam channeling and crystal extraction at the LHC,* Physics beyond collider kickoff workshop, CERN, 6-7 September, 2017.

[170] G. Apollinari, O. Brüning, T. Nakamoto, and L. Rossi, *High Luminosity Large Hadron Collider HL-LHC*, CERN Yellow Report (2015), no. 5 1, `arXiv:1705.0883`.

[171] C. Patrignani, *Review of Particle Physics*, Chin. Phys. **C40** (2016), no. 10 100001.

[172] PHENIX collaboration, A. Adare *et al.*, *Measurement of High-p_T Single Electrons from Heavy-Flavor Decays in $p + p$ Collisions at $\sqrt{s} = 200$ GeV*, Phys. Rev. Lett. **97** (2006) 252002, `arXiv:hep-ex/0609010`.

[173] B. A. Kniehl and G. Kramer, *D^0, D^+, D_s^+, and Λ_c^+ fragmentation functions from CERN LEP1*, Phys. Rev. **D71** (2005) 094013, `arXiv:hep-ph/0504058`.

[174] M. Lisovyi, A. Verbytskyi, and O. Zenaiev, *Combined analysis of charm-quark fragmentation-fraction measurements*, Eur. Phys. J. **C76** (2016), no. 7 397, `arXiv:1509.0106`.

[175] L. Gladilin, *Fragmentation fractions of c and b quarks into charmed hadrons at LEP*, Eur. Phys. J. **C75** (2015), no. 1 19, `arXiv:1404.3888`.

[176] E791 collaboration, E. M. Aitala *et al.*, *Multidimensional resonance analysis of $\Lambda_c^+ \to pK^-\pi^+$*, Phys. Lett. **B471** (2000) 449, `arXiv:hep-ex/9912003`.

[177] E. Braaten, Y. Jia, and T. Mehen, *The Leading particle effect from heavy quark recombination*, Phys. Rev. Lett. **89** (2002) 122002, `arXiv:hep-ph/0205149`.

[178] J. C. Anjos, J. Magnin, and G. Herrera, *On the intrinsic charm and the recombination mechanisms in charm hadron production*, Phys. Lett. **B523** (2001) 29, `arXiv:hep-ph/0109185`.

[179] G. Herrera and J. Magnin, *Lambda(c) / anti-Lambda(c) production asymmetries in p p and pi- p collisions*, Eur. Phys. J. **C2** (1998) 477, `arXiv:hep-ph/9703385`.

[180] LHCb, R. Aaij *et al.*, *Precision Measurement of the Mass and Lifetime of the Ξ_b^- Baryon*, Phys. Rev. Lett. **113** (2014), no. 24 242002, `arXiv:1409.8568`.

[181] Y. Amhis *et al.*, *Averages of b-hadron, c-hadron, and τ-lepton properties as of summer 2016*, `arXiv:1612.0723`.

[182] G. H. Arakelyan, C. Merino, and Yu. M. Shabelski, *Midrapidity hyperon production in pp and pA collisions from low to LHC energies*, Eur. Phys. J. **A52** (2016), no. 1 9, `arXiv:1509.0521`.

[183] NA61/SHINE, A. Aduszkiewicz *et al.*, *Production of Λ-hyperons in inelastic p+p interactions at 158* GeV/*c*, Eur. Phys. J. **C76** (2016), no. 4 198, `arXiv:1510.0372`.

[184] H. Kichimi *et al.*, *Inclusive Study of Strange Particle Production in p p Interactions at 405-GeV/c*, Phys. Rev. **D20** (1979) 37.

[185] STAR, J. Adams *et al.*, *Strange anti-particle to particle ratios at mid-rapidity in $\sqrt{s_{NN}} = 130$ GeV Au+Au collisions*, Phys. Lett. **B567** (2003) 167, `arXiv:nucl-ex/0211024`.

[186] LHCb collaboration, *LHCb Trigger and Online Technical Design Report*, CERN-LHCC-2014-016. LHCb-TDR-016.

[187] LHCb collaboration, R. Aaij *et al.*, *LHCb detector performance*, Int. J. Mod. Phys. **A30** (2015) 1530022, `arXiv:1412.6352`.

[188] HyperCP, Y. C. Chen *et al.*, *Measurement of the alpha asymmetry parameter for the $\Omega^- \to \Lambda K^-$ decay*, Phys. Rev. **D71** (2005) 051102, `arXiv:hep-ex/0502043`.

[189] D. M. Woods *et al.*, *Polarization of Ξ^- and Ω^- hyperons produced from neutral beams*, Phys. Rev. **D54** (1996) 6610.

[190] K. B. Luk *et al.*, *Polarization of Ω^- hyperons produced in 800-* GeV *proton-beryllium collisions*, Phys. Rev. Lett. **70** (1993) 900.

[191] M. Jezabek, K. Rybicki, and R. Rylko, *Experimental study of spin effects in hadroproduction and decay of Λ_c^+*, Phys. Lett. **B286** (1992) 175.

[192] P. M. Ho *et al.*, *Production polarization and magnetic moment of $\overline{\Xi}^+$ anti-hyperons produced by 800-* GeV/c *protons*, Phys. Rev. Lett. **65** (1990) 1713.

[193] L. H. Trost *et al.*, *New Measurement of the Production Polarization and Magnetic Moment of the Ξ^- Hyperon*, Phys. Rev. **D40** (1989) 1703.

[194] R. Rameika *et al.*, *Measurements of Production Polarization and Decay Asymmetry for Ξ^- Hyperons*, Phys. Rev. **D33** (1986) 3172.

[195] K. J. Heller *et al.*, *Polarization of Ξ^0 and Λ hyperons produced by 400-* GeV/c *protons*, Phys. Rev. Lett. **51** (1983) 2025.

[196] W. Scandale *et al.*, *Observation of channeling for 6500* GeV/c *protons in the crystal assisted collimation setup for LHC*, Phys. Lett. **B758** (2016) 129.

[197] J. P. Lansberg *et al.*, *A Fixed-Target ExpeRiment at the LHC (AFTER@LHC) : luminosities, target polarisation and a selection of physics studies*, PoS **QNP2012** (2012) 049, `arXiv:1207.3507`.

[198] W. Scandale *et al.*, *Observation of channeling for 6500 GeV/ c protons in the crystal assisted collimation setup for LHC*, Phys. Lett. B **758** (2016) 129.

[199] T. Pierog *et al.*, *EPOS LHC: Test of collective hadronization with data measured at the CERN Large Hadron Collider*, Phys. Rev. **C92** (2015), no. 3 034906, `arXiv:1306.0121`.

[200] T. Sjostrand, S. Mrenna, and P. Z. Skands, *PYTHIA 6.4 Physics and Manual*, JHEP **05** (2006) 026, `arXiv:hep-ph/0603175`.

[201] T. Sjostrand, S. Mrenna, and P. Z. Skands, *A Brief Introduction to PYTHIA 8.1*, Comput. Phys. Commun. **178** (2008) 852, `arXiv:0710.3820`.

[202] LHCb collaboration, *LHCb Tracker Upgrade Technical Design Report*, CERN-LHCC-2014-001. LHCb-TDR-015.

[203] L. H. Thomas, *The motion of a spinning electron*, Nature **117** (1926) 514.

[204] L. H. Thomas, *The kinematics of an electron with an axis*, Phil. Mag. **3** (1927) 1.

[205] V. Bargmann, L. Michel, and V. L. Telegdi, *Precession of the polarization of particles moving in a homogeneous electromagnetic field*, Phys. Rev. Lett. **2** (1959) 435.

[206] J. D. Jackson, *Classical Electrodynamics*, Wiley, 1998.

[207] E. Leader, *Spin in particle physics*, vol. 15, Camb. Monogr. Part. Phys. Nucl. Phys. Cosmol., 2011.

[208] T. Fukuyama and A. J. Silenko, *Derivation of Generalized Thomas-Bargmann-Michel-Telegdi Equation for a Particle with Electric Dipole Moment*, Int. J. Mod. Phys. **A28** (2013) 1350147, `arXiv:1308.1580`.

[209] A. J. Silenko, *Spin precession of a particle with an electric dipole moment: contributions from classical electrodynamics and from the Thomas effect*, Phys. Scripta **90** (2015), no. 6 065303, `arXiv:1410.6906`.

[210] R. H. Good, *Classical Equations of Motion for a Polarized Particle in an Electromagnetic Field*, Phys. Rev. **125** (1962) 2112.

[211] E. M. Metodiev, *Thomas-BMT equation generalized to electric dipole moments and field gradients*, 2015, 2015.

Acknowledgments

This is the last page dedicated to the acknowledgments and the people who supported me during this work. Some of them are not so good in english (me neither) and I prefer to write this last page in Italian.

Ecco qua, finalmente una pagina scritta in italiano direte voi. Questa è la vostra pagina, quella dedicata a voi che mi avete supportato lungo tutto il mio percorso universitario, iniziato ormai quasi 10 anni fa. Non posso che iniziare con la mia famiglia: i miei genitori Daniela e Stefano e mia sorella Michela. Questo traguardo è anche merito vostro, senza il vostro aiuto morale ed economico non sarei mai diventato quello che sono e non avrei mai potuto coronare quelli che sono i miei sogni. Sarò sempre riconoscente a mamma e papà per i loro sforzi nel crescermi, per avermi insegnato i valori della vita, per avermi fatto viaggiare un sacco, per avermi sempre spronato a migliorare per dare sempre il meglio e per avermi fatto capire l'importanza dello studio. Poi la mia inadeguatezza nel lavoro manuale ha fatto il resto, quando mio papà tornava a casa da mia mamma, dopo una giornata passata ad aiutarlo in officina, e si lamentava: "Speriamo che quel ragazzo studi, perché lì non ce lo vedo proprio". Ho studiato, forse fin troppo, con quasi 30 anni sulle spalle sono ancora qua a studiare, ma è quello che ho voluto, quello che mi piace e quello che vorrei fare. E poi la mia sorellina, o forse sarebbe meglio dire sorellona, che è davvero la migliore del mondo. Perché non è semplicemente una sorella, è anche una persona eccezionale come ne ho conosciute poche e che ammiro. Nei momenti di difficoltà lei c'era sempre, li ha capiti, mi è stata accanto e mi ha aiutato a risollevarmi più forte di prima. Ed è per questo che so che su di lei potrò sempre contare, che lei ci sarà sempre per me, ed io ci sarò sempre per lei.

E poi non posso che ringraziare Emma (preferisco questo al tuo vero nome Emma Maria). Ormai ci conosciamo da un po', ma sembra di stare insieme da anni. Mai avrei pensato di incontrare una persona come te, con così tanti interessi in comune e la stessa visione di vita. In così poco tempo abbiamo costruito qualcosa di unico per cui pensavo ci volessero anni. Abbiamo un sacco di progetti insieme e con un po' più di tempo piano piano li realizzeremo tutti. Aspettami a Como (suona come una minaccia ma non lo è)! Con questo non montarti troppo la testa perché resti pur sempre una sconosciuta, la mia sconosciuta. E poi grazie alla tua famiglia per avermi accolto e fatto sentire come a casa.

Un altro grazie a tutti i miei amici speciali di Piacenza. In particolare a Matteo e Giuseppe che hanno condiviso con me, in questo percorso universitario, ogni momento di gioia e di sconforto. Con voi sono cresciuto ed abbiamo passato insieme mille avventure. Ci siamo conosciuti da bambini/ragazzi e siamo ancora insieme ora che siamo diventati uomini. Grazie di cuore. Un grosso in bocca al lupo per te, Giuseppe, e per il figlio che stai aspettando.

Ultimi ma non ultimi grazie a tutti i miei colleghi, più amici che colleghi, con cui lavoro insieme ogni giorno. Accumunati dalla stessa passione, più che un lavoro lo considero un divertimento. Un grazie speciale a Nicola che oltre ad essere il mio supervisor per me resta un punto di riferimento perchè, tramite la sua curiosità, voglia di fare ed il suo spirito innovativo mi ha insegnato cosa vuol dire essere un vero ricercatore.